UNIVERSIDAD COMPLUTENSE DE MADRID

FACULTAD DE CIENCIAS FÍSICAS

TESIS DOCTORAL

Quatum optics applied to superconducting quantum links

Óptica cuántica aplicada a enlaces cuánticos superconductores

MEMORIA PARA OPTAR AL GRADO DE DOCTOR

PRESENTADA POR

Guillermo Federico Peñas Fernández

DIRIGIDA POR

Juan José García Ripoll

Ricardo Puebla Antunes

Universidad Complutense de Madrid
Facultad de Ciencias Físicas
Programa de Doctorado en Física

QUANTUM OPTICS APPLIED TO SUPERCONDUCTING QUANTUM LINKS

ÓPTICA CUÁNTICA APLICADA A ENLACES CUÁNTICOS SUPERCODUCTORES

Autor:

Guillermo Federico Peñas Fernández

Directores:

Juan José García Ripoll

Ricardo Puebla Antunes

CSIC
Consejo Superior de Investigaciones Científicas

Diciembre 2024

A mi familia,
a mis amigos.

Abstract

Scaling up quantum computers is a formidable task [Pre18, CKJ+20]. Quantum systems are extremely delicate and sensitive to environmental interactions [Nie02]. Ever since the first theoretical proposals for their construction in the early 1990s [CZ95], many platforms have arisen, and several of the original challenges addressed. However, while the first proof-of-concept quantum computers are already a reality, the question of how to scale up these prototypes to the dimensions needed for fault-tolerant computing remains largely open.

Distributed Quantum Computing (DQC) emerged as an alternative to expand the size and capabilities of quantum computers. The key idea is to distribute computations and memory across multiple medium-sized nodes, similar to classical computing. While this approach reduces cross-talk and control line overhead from placing many qubits on a single chip, it introduces new challenges. A distributed architecture needs fast, reliable, and synchronized information exchange between nodes to function effectively. In this thesis, we advocate for quantum state transfer, first proposed in [CZKM96], as a fundamental operation for transmitting quantum information deterministically and on demand. This constitutes the foundation of what we refer to as *quantum state transfer networks*, of which pioneering experimental realizations already exist [LLC+19, MSK+20, QLN+23]. In these networks, quantum information is transmitted by mapping states from stationary qubits to propagating ones. This requires strong and finely tuneable light-matter interactions, which make superconducting circuits an ideal platform for implementation.

The objective of this thesis is twofold. First, we construct a theoretical quantum optical model of a complete *state transfer network based on microwave quantum links* with the goal of understanding and providing theoretical insights for state-of-the-art experimental work. Secondly, we propose and design novel protocols and mitigation strategies for overcoming some of the most critical challenges affecting this platform nowadays.

Through detailed modeling of the experiments, we identified sources of error that are often overlooked in the superconducting circuits literature, such as wavepacket distortion caused by non-linear dispersion relations and non-uniform couplings. These limitations add on top of the commonly recognized issues, such as poor measurement fidelities, limited qubit coherence times, and the challenge of maintaining the entire network at cryogenic temperatures [BGGW21]. Beyond these imperfections, the field also faces ongoing challenges, particularly the need for multiplexing information through quantum links and the generation and distribution of entanglement across the network. Addressing both error mitigation and protocol design is crucial for building a functional, scalable quantum state transfer network.

Equipped with the tools of quantum optics and building on the complete modeling of existing experiments, we addressed both issues. By accurately characterizing the emission process and exploiting the explicit relationship between the couplings and the shape of the produced electromagnetic field, we were able to leverage the flexibility of the light-

matter couplings for various purposes. Through careful engineering of the phase profile, we designed a family of predistorted photons that are resilient to propagation distortions. This method applies to any quantum communication channel, provided the distortion behavior of the photon within the channel is known.

We also developed two strategies to increase the quantum link's information capacity. The first mechanism aims at increasing the computational space of the waveguide by designing photons that are orthogonal in the time domain, such that at the same frequency one could have several distinguishable wavepackets. The second consists of making use of the big operational frequency bands available in the experiments. By placing the carrier frequencies apart from each other, and carefully studying the cross-talk and overlap effects, we were able to predict that tens or even hundreds of flying qubits can be transmitted with current setups at extremely low error rates. Thus, we conclude that there is plenty of room in the bandwidth offered by microwave quantum links, the main remaining challenge being the ability to connect those many solid state qubits to the extremes.

Finally, once the realistic design and control of the quantum links is well understood, we focused on the application of these state transfer networks to the distribution of entanglement. We conceived and designed a novel operation, which we termed fractional quantum state transfer, demonstrating theoretically and through numerical simulations the deterministic generation of multipartite entanglement. By concatenating several of these fractional operations, we proposed two distinct protocols that enable entanglement distribution across all nodes of an arbitrary quantum network without requiring measurements. This approach is particularly advantageous for superconducting circuit architectures, where measurements tend to be slower compared to other platforms.

We conclude that state transfer networks based on microwave quantum links are a practical and effective solution and a promising avenue for quantum information processing in general when considering appropriate design protocols and mitigation strategies.

Resumen

El escalado de las arquitecturas de computación cuántica es una tarea formidable [Pre18, CKJ+20]. Los sistemas cuánticos son extremadamente delicados y sensibles a las interacciones con el entorno [Nie02]. Desde las primeras propuestas teóricas para su construcción a principios de la década de 1990 [CZ95], han surgido muchas plataformas y se han abordado varios de los desafíos originales. Sin embargo, aunque los primeros prototipos de ordenadores cuánticos son ya una realidad, la cuestión de cómo escalar estos dispositivos a las dimensiones necesarias para la computación tolerante a fallos sigue siendo en gran medida un problema abierto.

La Computación Cuántica Distribuida (DQC, por sus siglas en inglés) surgió como una alternativa para expandir el tamaño y las capacidades de los ordenadores cuánticos. El núcleo de la idea es distribuir las computaciones y la memoria entre múltiples nodos de tamaño mediano, similar a como se hace en computación clásica. Aunque este enfoque reduce las interferencias y la sobrecarga de las líneas de control al limitar la cantidad de cúbits en un solo chip, también plantea nuevos desafíos. Una arquitectura distribuida necesita un intercambio de información rápido, fiable y sincronizado entre nodos para funcionar eficazmente. En esta tesis, abogamos por la transferencia de estados cuánticos, propuesta por primera vez en [CZKM96], como una operación fundamental para transmitir información cuántica de manera determinista y bajo demanda. Esto constituye la base de lo que denominamos *redes de transferencia de estados cuánticos*, de las cuales ya existen realizaciones experimentales pioneras [LLC+19, MSK+20, QLN+23]. En estas redes, la información cuántica se transmite mapeando estados de cúbits estacionarios a cúbits propagantes. Esto requiere interacciones luz-materia fuertes y controlables con un alto grado de precisión, lo que convierte a los circuitos superconductores en una plataforma ideal para su implementación.

El objetivo de esta tesis es doble. Primero, construimos un modelo teórico de óptica cuántica de una *red de transferencia de estados basada en enlaces cuánticos de microondas* con el fin de comprender en profundidad los trabajos experimentales más avanzados del campo y proporcionar conocimientos teóricos para su mejora. En segundo lugar, proponemos y diseñamos nuevos protocolos y estrategias de mitigación para superar algunos de los desafíos más críticos que afectan a esta plataforma en la actualidad.

A través de la modelización detallada de los experimentos, identificamos fuentes de error que a menudo se pasan por alto en la literatura de circuitos superconductores, como la distorsión de los paquetes de onda a causa de la propagación y acoplos no uniformes. Estas limitaciones se suman a los problemas comúnmente reconocidos, como las bajas fidelidades en la medida, los limitados tiempos de coherencia de los cúbits y el desafío de mantener toda la red a temperaturas criogénicas [BGGW21]. Más allá de estas imperfecciones de ingeniería, el campo también enfrenta desafíos conceptuales, particularmente la necesidad de multiplexar información a través de enlaces cuánticos y la generación y distribución de entrelazamiento. Abordar tanto la mitigación de errores como el diseño de protocolos es

crucial para construir una red funcional y escalable de transferencia de estados cuánticos.

Equipados con las herramientas de la óptica cuántica y basándonos en la modelización completa de los experimentos existentes, abordamos ambos problemas. Al caracterizar con precisión el proceso de emisión y aprovechar la relación explícita entre los acoplos y la forma del campo electromagnético emitido, hemos podido aprovechar el alto nivel de control de las interacciones para varios propósitos. A través de una ingeniería cuidadosa del perfil de fase, diseñamos una familia de fotones predistorsionados que son resilientes a las distorsiones de propagación. Este método se aplica a cualquier canal de comunicación cuántica, siempre que se conozca el comportamiento de distorsión del fotón dentro de dicho canal.

También desarrollamos dos estrategias para aumentar la capacidad de información de los enlaces cuánticos. El primer mecanismo tiene como objetivo aumentar el espacio computacional de la guía de ondas diseñando fotones ortogonales en el dominio temporal, de manera que a la misma frecuencia se puedan tener varios paquetes de ondas distinguibles. El segundo consiste en aprovechar los grandes anchos de banda disponibles en los experimentos. Al separar las frecuencias centrales de los paquetes de onda y estudiar cuidadosamente los efectos de interferencia y solapamiento, hemos podido predecir que decenas o incluso cientos de cúbits propagantes pueden ser transmitidos en los equipos actuales con tasas de error extremadamente bajas. Por lo tanto, concluimos que aún queda un amplio margen por explotar en el ancho de banda de los enlaces cuánticos de microondas, siendo ahora el principal desafío conectar un gran número de cúbits de estado sólido a los extremos de la guía de ondas.

Finalmente, nos hemos centrado en la aplicación de estas redes de transferencia de estados a la distribución de entrelazamiento. Concebimos y diseñamos una nueva operación, que denominamos transferencia de estados cuánticos fraccionada, demostrando tanto teóricamente como mediante simulaciones numéricas la generación determinista de entrelazamiento multipartito. Al concatenar varias de estas operaciones fraccionadas, proponemos dos protocolos distintos que permiten la distribución de entrelazamiento entre todos los nodos de una red cuántica arbitraria sin necesidad de realizar medidas. Este enfoque es particularmente ventajoso para arquitecturas de circuitos superconductores, donde las mediciones tienden a ser más lentas en comparación con otras plataformas.

Concluimos que las redes de transferencia de estados basadas en enlaces cuánticos de microondas son una solución práctica y eficaz, y una vía prometedora para el procesamiento de información cuántica en general, teniendo en cuenta los protocolos de diseño y estrategias de mitigación apropiadas.

List of publications

PUBLICATIONS

This thesis has given rise to the following peer-reviewed articles and preprints:

P1 **Guillermo F. Peñas**, Ricardo Puebla, Tomás Ramos, Peter Rabl and Juan José García-Ripoll, *Universal deterministic Quantum Operations in Microwave Quantum Links*, Phys. Rev. Applied **17**, 054038 (2022).

P2 **Guillermo F. Peñas**, Ricardo Puebla and Juan José García-Ripoll, *Improving quantum state transfer: correcting non-Markovian and distortion effects.*, Quantum Sci. Technol. **8**, 045026 (2023).

P3 **Guillermo F. Peñas**, Ricardo Puebla and Juan José García-Ripoll, *Multiplexed quantum state transfer in waveguides*, Phys. Rev. Research **6**, 033294 (2024).

P4 **Guillermo F. Peñas**, Ricardo Puebla and Juan José García-Ripoll, *Deterministic multipartite entanglement via fractional state transfer across quantum networks.* arXiv:2408.01177 (2024).

Other publications/preprints outside the scope of this thesis

– Francisco Escudero, David Fernández-Fernández, Gabriel Jaumà, **Guillermo F. Peñas**, and Luciano Pereira *Hardware-Efficient Entangled Measurements for Variational Quantum Algorithms*, Phys. Rev. Applied **20**, 034044 (2023).

List of Figures

Contents

1 Thesis Overview

Quantum computing (QC) holds the potential to completely revolutionize the way we model and understand the physical world. The history of the field can be traced back to 1982, when Feynman realized that the impracticality of simulating quantum systems with classical devices could be overcome by the utilization of a quantum computer [Fey82]. Shortly after Feynman's conference, still in the 1980s, Bennett and Brassard proposed a protocol to share a private key between parties in a provable robust way [BB84] giving birth to the field of quantum cryptography. Building on the ideas of this protocol, the same authors designed a way to teleport a quantum state from one place to another [BBC$^+$93], at the cost of exchanging classical information through an auxiliary channel. Interestingly from a historical perspective, this protocol exploited the apparent paradox found by Einstein, Podolski, and Rosen in the 1930s with which they tried to prove the incompleteness of the quantum theory [EPR35]. The whole field finally exploded in the 1990s when Shor realized that a quantum computer could efficiently factorize large prime numbers [Sho94] and therefore break the RSA encryption scheme [RSA78]. Just the following year, Cirac and Zoller demonstrated that it was possible in principle to construct a universal quantum computer using atoms and lasers [CZ95]. Ever since these seminal proposals, many applications have been put forward. In particular, there is a consensus that quantum computation, if realized to unleash its full potential, will have an enormous influence in the fields of chemistry, pharmaceutics [MEA$^+$20], material science [BBMC20], complexity theory [BV97] and several others.

After these hallmark contributions, the 2000s and 2010s have mostly been devoted to their implementation. Throughout the last quarter of a century, many platforms for quantum information processing have been proposed and tested in the laboratory. Among these we can name trapped ions [BCMS19], cold atoms [WDE$^+$23], photonic computers [FSS18], Nitrogen-vacancy centers [DMD$^+$13], semiconductor quantum dots [GTK$^+$21] and superconducting circuits [BGGW21]. It turns out that scaling up any of these architectures to the number of coherent qubits that are needed for a universal fault-tolerant quantum computer is extremely challenging [Sho96, Got98]. In this thesis, we will focus our attention on superconducting circuits, but most of the difficulties encountered and proposed solutions may be also relevant to other platforms.

Superconducting circuits for quantum computing emerged in the early 2000s [BVJ$^+$98, NPT99, LBS$^+$03] and quickly gained significant attention. They leveraged techniques developed in the field of circuit quantum electrodynamics (cQED)[BGGW21], which itself arose from cavity-QED[MD02]. In cavity-QED, atoms are placed inside high-quality optical cavities, resulting in exceptionally strong light-matter couplings [Kim98]. Superconducting circuits inherited this key feature from cavity-QED [WSB$^+$04, KYG$^+$07, SHK$^+$08], and in fact, have achieved the most extreme coupling regimes to date [NDH$^+$10, FLM$^+$10, YFA$^+$17]. Another appealing aspect of this paradigm is its dimensions and operating

regime. Unlike real atoms, which are on the nanometer scale, superconducting circuits are several micrometers in size and operate in the microwave frequency range. This allows for the direct application of much of the existing knowledge from integrated electronics. Additionally, their larger size results in significant dipole moments, which enhances the light-matter interaction and controllability. However, these properties also pose challenges. Being each component on the micrometer scale, an entire chip spans millimeters, making it quite a large piece of material to keep cool at the cryogenic temperatures required for these systems to operate. Moreover, the large light-matter coupling leads to cross-talk between components [MMMJ20]. Currently, there is wide consensus that it will not be feasible shortly to host the millions of qubits required for error correction on a single chip [FMMC12].

The difficulty of scaling up a single chip led to the proposal of distributed quantum computing (DQC) [Kim08, MRR+14, WEH18]. This platform-independent paradigm involves building multiple medium-sized quantum computational nodes connected via communication channels, as opposed to attempting to construct one massive chip that handles all memory and computations. It is natural to think of this computing paradigm, since in some sense, it is how classical computers work. In a classical von Neumann architecture [von45], a universal computer is composed of a processing unit (itself subdivided into several components) and a memory unit, both of which continuously exchange bits in the form of traveling electromagnetic pulses.

We choose to categorize the efforts of distributing the computational tasks across multiple spatially separated nodes into two broad families: *Quantum teleportation networks* [BPM+97, KW19] and *Quantum state transfer networks* [RNH+12, ABP+18]. From an information-theoretic perspective, both approaches are equivalent. Despite their distinct inner mechanisms, both can be used to transmit quantum states and distribute entanglement among the network's nodes. The choice between them depends on the specifics of the platform.

Quantum teleportation networks share entangled qubit states across the network, using quantum teleportation protocols—i.e., local measurements and exchange of classical information—to implement operations across distant qubits. They are based on the foundational result of quantum teleportation [BBC+93], which was first experimentally validated in [BPM+97]. This kind of protocol has been successfully implemented with Nitrogen-vacancy centers [TKK+19, HPB+22], trapped ions [RHR+04, BCS+04, SKO+06], and it is central to photonic quantum computers [OFV09]. More speculatively, these networks have been proposed as the base technology for a quantum internet [WEH18]. Quantum state transfer networks, on the other hand, map the quantum states from the solid state *localized qubits* at the nodes to *propagating qubits* (in the form of one or more traveling photons, phonons, or other extended quantum degrees of freedom) that then travel through the links. They are based on the deterministic quantum state transfer protocol [CZKM96]. In the last decade, several pioneering experiments around the world have paved the way towards a realistic implementation of quantum state transfer networks with superconducting quantum links. Among these, we can name the first that were able to distribute entanglement deterministically across nodes in the same cryostat [ABP+18, CZN+18]. Also, those which achieved deterministic quantum state transfer among different nodes within the same refrigerator [ZCS+19, LLC+19, QLN+23], or between spatially separated ones [MSK+20, BTZ+21, SSK+23].

The decision to pursue teleportation or quantum state transfer networks largely depends on the hardware, as each approach imposes different demands. Teleportation networks require the faithful distribution of many entangled pairs, performing measurements, and classical communication channels to convey the outcomes of those measurements. One proposed solution for reliable entanglement distribution is *entanglement purification* or *dis-*

tillation [BBPS96, BDSW96, BBP$^+$96]. The core idea behind entanglement purification is to extract a smaller number of high-fidelity entangled pairs from a larger set of less reliable, noisy pairs. However, this process can be resource-intensive. If qubit coherence times and transmission fidelities are not high, many initial entangled pairs may be required. This challenge is further exacerbated if measurement fidelities are poor, as the distillation protocol itself demands additional measurements. Moreover, both distillation and entanglement distribution are inherently probabilistic processes. In summary, this paradigm is better suited for platforms where generating numerous copies of entangled states is feasible and where high measurement fidelities can be achieved [PEW$^+$15].

Unlike teleportation schemes, quantum state transfer networks do not require measurements or the exchange of classical information. Additionally, it is not necessary to distribute entangled pairs across the network a priori. However, this approach demands a high degree of controllability. Strong and finely tunable coupling mechanisms are essential to ensure the high-fidelity and rapid transfer of quantum information between solid-state devices and bosonic excitations. This paradigm is therefore better suited for platforms where strong couplings can be achieved, quantum information can be transmitted reliably and deterministically through the channels, and measurement fidelities pose a limitation. Superconducting circuits are an exemplary hardware that meets these requirements [BGGW21].

The aforementioned pioneering experiments in superconducting circuits suggest that this paradigm is feasible, demonstrating several key operations required to build a scalable state transfer network. However, the field still lacks a comprehensive model that covers all necessary components and operations, identifies the main bottlenecks, and addresses the most critical sources of errors. Our main goal in this thesis is to develop a comprehensive quantum optical modelization of a near-term quantum state transfer network based on superconducting circuits. Taking the previous experiments as a departing point, we aim to use the techniques of quantum optics to evaluate the required operation fidelities, identify the current sources of errors, propose mitigation strategies, and design novel protocols for quantum information processing. Our vision is to construct a functional and scalable quantum state transfer network using superconducting microwave quantum links.

In the first part, we focused our attention on the modelization of the experimental setup of [MSK$^+$20]. For that, we derived a complete quantum optical Hamiltonian description of a distributed superconducting architecture. One of the standing problems in the field consists of understanding how well the quantum state transfer protocol [CZKM96], conceived under ideal conditions, behaves when subject to real-world imperfections, such as non-linear dispersion relations and non-uniform couplings. We found that these mechanisms are relevant and have to be taken into account to aim for bellow fault-tolerant threshold errors. In the same vein, the protocol [CZKM96] is usually implemented in the above experiments through a technique called wavepacket shaping, essentially a scheme to map the quantum state from localized to propagating qubits. However, wavepacket shaping relies on some approximations that do not always apply to the physical systems under consideration, which also leads to errors. In Chapters 3 and 4 we provide a comprehensive analysis of all these issues. We discovered how considering these real-world effects (most notably non-linear dispersion relations and non-Markovian dynamics) impacts fidelity in non-obvious ways, assessed the appropriate operating regimes, and provided quantitative metrics and scaling analyses.

In the second part, we designed correction strategies to mitigate the effect of the studied imperfections. One of the inescapable consequences of having large light-matter couplings is that the generated photons have a big spectral width. This is not necessarily a negative trait, as it means that photons are generated quickly. However, it does make them more susceptible to propagation and scattering distortions. Some experiments have addressed

this issue by emitting very narrow, quasi-adiabatic wavepackets [LLC+19], which slows down the protocol. In contrast, we have developed a novel technique that, through a detailed study of the distortion process, injects a predistorted photon into the waveguide. This predistorted photon is shaped to compensate for errors in advance. As a result, this technique enables high-fidelity quantum communication between nodes without sacrificing speed, as it operates with broadband photons.

Another central challenge in the field is multiplexation of quantum information. Quantum state transfer networks, as well as any other candidate for scaling up quantum computing, have to show their ability to store, manipulate, and send large numbers of qubits. This thesis presents two distinct contributions directed towards this goal. First, on the modelization front, we have conducted an in-depth study of the physics beyond the single excitation case. This included developing a Python library for efficiently simulating states with multiple excitations, which would otherwise be intractable. We have open-sourced this library for the benefit of the entire community. Second, on the design front, we have proposed two protocols to increase the information capabilities of the quantum link, *mode multiplexing* and *frequency multiplexing*. Mode multiplexing leverages the flexibility of coupling schemes in superconducting quantum links to engineer photons that are orthogonal in the time domain, allowing for their discrimination even if they share the same carrier frequency. Frequency multiplexing, on the other hand, involves sending wavepackets simultaneously at different carrier frequencies. While this approach is commonly used in classical optical fibers, it poses new challenges when applied to microwave photons in superconducting quantum links. Using the aforementioned Python library, we established tight fidelity bounds for this type of multiplexing and assessed the channel capacity for several tens of qubits below the error correction threshold.

Lastly, any candidate for distributed quantum computing must be able to distribute entanglement. Entanglement, which can be viewed as a resource, is essential in a distributed architecture for performing non-local operations such as gates and measurements. Some of the pioneering experiments in superconducting quantum networks presented above have already demonstrated entanglement distribution [ABP+18, CZN+18, KMW+18]. For example, in [KMW+17], entanglement is generated by preparing a superposition state in one node and transferring it to another node with a 50% chance, resulting in a Bell state.

In contrast, we proposed in Chapter 7 an innovative method for deterministically distributing genuine multipartite entanglement across the network. Our method, based on the *fractional quantum state transfer operation*, enables the creation of an N-particle entangled state by allocating a single excitation across all these nodes. By combining various fractional transfers, we can create different types of entangled states. We have also developed theoretical tools to implement this protocol with a range of coupling schemes and network topologies.

In conclusion, we believe that the comprehensive modeling of superconducting quantum links using quantum optics tools, as presented in this thesis, adds significant value to the field of state transfer networks and represents a step forward toward achieving a fully scalable quantum computer. Additionally, the problems identified in this work, along with the proposed solutions and designed protocols, offer notable insights to guide future experiments and theoretical efforts.

Superconducting circuits, a platform for distributed quantum computing 2

Superconducting circuits are an ideal platform for quantum state transfer networks. Because of their size, they have large dipolar moments, which result in strong light-matter couplings. This, together with advanced microwave techniques, allows for good controllability, which is precisely what the protocol of deterministic quantum state transfer needs.

In what follows, we will introduce the different components of a superconducting circuit network using the language of quantum optics. The exposition will closely follow the references [BGGW21] and [Rip22]. It is convenient that the theory describing the interaction of atoms and light in the visible regime [SZ97, GZ15] so well applies to superconducting circuits and the electromagnetic field in the microwave regime, because it means that most of the theoretical background was established decades ago.

Some promising proposals rely on using the big light-matter couplings achievable with circuits to produce microwave photons and then transduce them to the optical regime [LRSS20, LSB$^+$20, SHR$^+$22]. This approach holds great potential because it takes advantage of all the techniques from the mature field of integrated photonics [WSLT20]. However, this is not the path to be studied in this thesis. Instead, we will consider a setup in which all the components work at cryogenic temperatures in the microwave regime. Emission, propagation, and absorption of information throughout the network will happen in these conditions. This paradigm also enjoys good health nowadays and there have been several different experimental proposals connecting different nodes inside the same refrigerator [KKT$^+$18], [ZCB$^+$21], or across spatially-separated refrigerators through a cryogenic waveguide [MSK$^+$20, SSK$^+$23].

The setup that we will argue in favor of throughout the whole thesis is that depicted pictorially in Fig. 2.1a, in which several distributed quantum computing nodes are connected through quantum links of very different sizes, comprising communications inside the same fridge as well as far-apart ones. The type of computing node we are considering is illustrated in Fig. 2.1b, which shows a real superconducting quantum computing node from A. Wallraff's lab at ETH Zurich [MSK$^+$20]. The microscopic image displays all the components that we will describe theoretically in this chapter: the resonators, represented by simple curved cables (shown in green and yellow), the central superconducting nonlinear element (colored in red), and the various coupling and drive lines.

We decided to structure the chapter in the following manner. In Section 2.1, we introduce the essential components needed to construct a theoretical quantum computing machine, following the criteria outlined by DiVincenzo [DiV00]. After that, in Section 2.2 we lay out the basic components to build a superconducting quantum computing node, these are, the resonator—Subsection 2.2.1—, and the qubit—Subsection 2.2.2—. After having presented these essential pieces, we devote Section 2.3 to study different coupling regimes

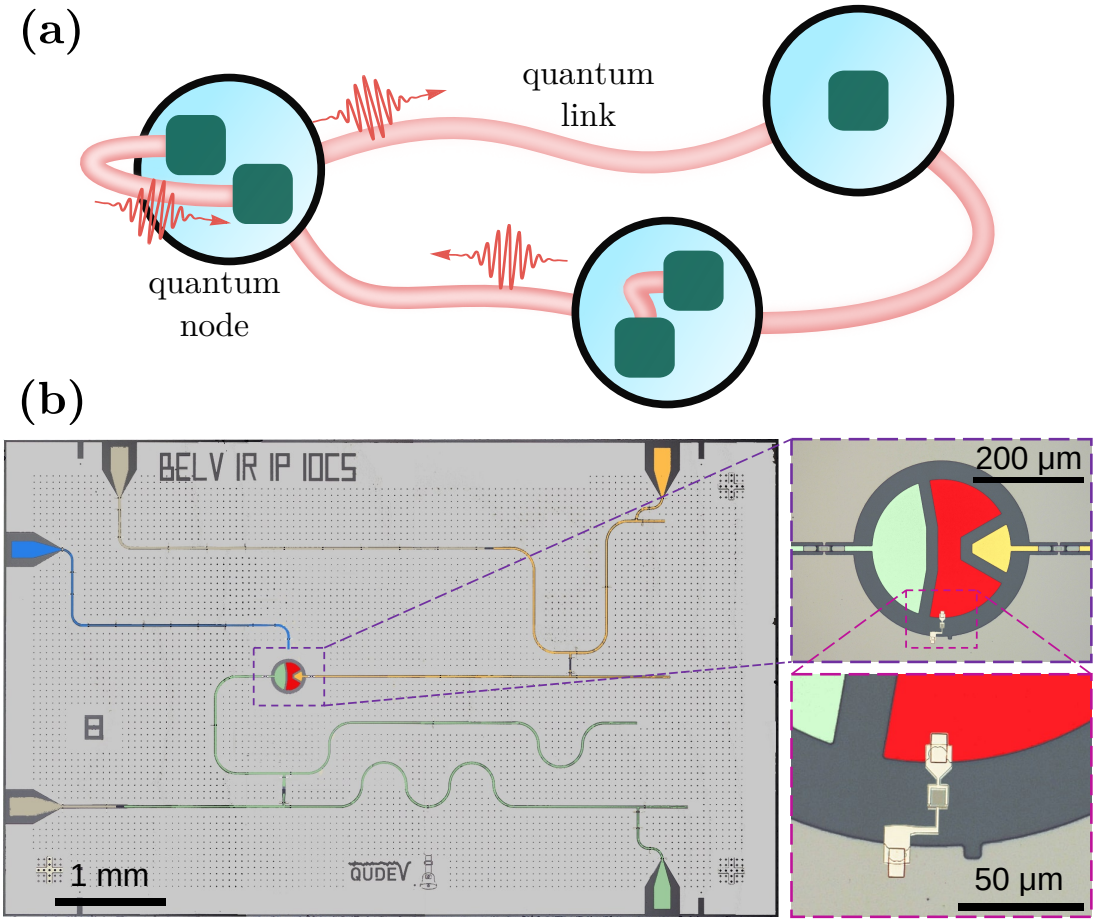

Figure 2.1: Superconducting quantum network architectures. (a) Sketch of a quantum network, where multiple quantum nodes are connected via quantum links of different lengths, allowing for an inter- and intra-node bidirectional exchange of quantum information via photon pulses. (b) False color photograph of a chip from the experiment [MSK+20] showing the transmon island (red), the drive line (blue), the readout circuitry (green), and the transfer circuitry (yellow). The purple inset shows a microscope image of the transmon qubit, after deposition of the Josephson junctions. The pink inset presents an enlarged view of the Josephson junctions, see scale bars for reference.

between them, Subsection 2.3.1 explores the static resonant regime, Subsection 2.3.2 the situation of dynamical couplings, and Subsection 2.3.3 the off-resonant one. Finally, as a last ingredient to build a superconducting quantum network we present, in Section 2.4 the concept of a superconducting quantum link that allows for communication among the different nodes of the network.

2.1 Necessary components of a quantum computer

Some basic concepts of quantum information theory bear great importance and will play a central role in this thesis. The idea is to present them now so that they are clear before digging into the particular protocols and proposals. The exposition will follow the standard reference in the field [NC00].

In the year 2000, David DiVizenzo introduced five criteria that every quantum computer should meet [DiV00], and they have become a cornerstone in the field. We will follow

them making the necessary definitions when needed, and, in the following subsection, we will show how they can be met using superconducting circuits.

1. *A scalable system with a well-characterized qubit.* The **qubit**, short for "quantum bit," is the fundamental unit of quantum information, analogous to the bit in classical computing. However, unlike a classical bit which can exist in one of two states (either 0 or 1), a qubit can exist in a state that is a superposition of both 0 and 1. Mathematically, a qubit can be represented by the quantum state vector

$$|\psi\rangle = \alpha\,|0\rangle + \beta\,|1\rangle\,, \tag{2.1}$$

   where α and β are complex numbers, which ensure that the state is normalized. Physically, a qubit can be realized in many different ways, everything that is needed is a quantum state which can only exist in two different states.

2. *The ability to initialize the state of the qubits to a simple fiduciary state.* Typically, and definitely for the case of superconducting circuits, this fiduciary initial state will be the vacuum state $|0\rangle$.

3. *Long relevant decoherence times.* **Decoherence time** is the duration after which a quantum system loses its genuinely quantum properties. This can happen for a variety of reasons. The excitation might leave the qubit altogether, this is governed by the decay time T_1. More subtly, the noise can cause information about the relative phase between α and β in Eq. (2.1) to get lost, which is dictated by the dephasing time T_2. All the relevant times that affect coherence must be as long as possible. In Section 4.2 of Chapter 4, we will detail how to characterize the errors stemming from the finite T_1 and T_2 values, when considering experimental imperfections.

4. *A universal set of quantum gates.* A **quantum logic gate** is a basic quantum circuit operating on a small number of qubits. They are the fundamental building blocks of quantum circuits, much like logic gates are for classical digital circuits. Quantum gates are essential for performing computations in quantum computing and are mathematically represented by unitary matrices. A gate that acts on n qubits is represented by a $2^n \times 2^n$ unitary matrix. An important result is that a **universal set of quantum gates** can be built only with a very small number of one and two-qubit gates. This means that only with these very simple operations, any imaginable quantum operation in any state can be implemented. One example of such a set consists of the one qubit rotations $R_x(\theta), R_y(\theta), R_z(\theta)$, the phase flip $P(\phi)$ and the controlled-not gate. In Chapter 4 we show how one such universal set can be constructed using only basic distributed network operations.

5. *A qubit-specific measurement capability.* For the quantum computer to output any information, it is essential to measure the qubits after all the desired logic operations have been performed on them.

2.2 Components of a superconducting quantum computer

A minimal superconducting quantum computing node needs at least two physical devices and a way to couple them. In increasing level of complexity, it first needs a resonator, which is a basic circuit component that behaves as a harmonic oscillator. Then, it requires a qubit, which will be realized as a non-linear circuit component. This nonlinearity is essential to allow for selective targeting of a single transition and not others, something that is not possible with a linear harmonic oscillator.

2.2.1 Superconducting resonators

The first circuit component that we are going to focus our attention on is a quantum LC oscillator. This device can be realized in a variety of ways, and it is always characterized by its inductance L and capacitance C. This system presents an oscillatory behavior whose natural frequency is $\omega_r = 1/\sqrt{LC}$. In the particular example that we are focusing on in this thesis, they are coplanar waveguide resonators, essentially a single conducting track printed onto a dielectric substrate [BGGW21, GFB$^+$08]. The green and yellow curves in Fig. 2.1 are coplanar waveguide resonators. The energy is given by the following Hamiltonian,

$$H_{LC} = \frac{Q^2}{2C} + \frac{\Phi^2}{2L}, \tag{2.2}$$

where $Q(t)$ is the charge in the capacitor, and $\Phi(t)$ is the flux traversing the inductor. Their respective relations with current and voltage are

$$Q(t) = \int_{t_0}^{t} dt' I(t'), \quad \Phi(t) = \int_{t_0}^{t} dt' V(t'). \tag{2.3}$$

The relevant feature to us here is that the Hamiltonian (2.2) corresponds to a harmonic oscillator and that, from a quantum mechanical perspective, these charge and flux operators obey[1]

$$[\Phi, Q] = i. \tag{2.4}$$

This canonical commutation relations allow us to define annihilation and creation operators in the following way

$$\Phi = \sqrt{\frac{1}{2\omega_r C}}(a^\dagger + a), \tag{2.5}$$

$$Q = i\sqrt{\frac{\omega_r C}{2}}(a^\dagger - a). \tag{2.6}$$

In terms of these operators, the previous Hamiltonian now becomes

$$H_{LC} = \omega_r(a^\dagger a + 1/2). \tag{2.7}$$

We will drop the constant quantity $\omega/2$ throughout the rest of the thesis since it simply corresponds to an energy shift.

Large macroscopic LC circuits also exhibit oscillatory behavior without the need for a quantum mechanical description. For the quantum effects to become apparent, the system has to operate in a regime where the thermal fluctuations are much smaller than the energy separation between levels, mathematically, $k_B T \ll \hbar\omega_r$. This imposes a strict condition on the operating temperature: for a typical microwave frequency of $\omega_r = 2\pi \times 1$ GHz, temperatures below 50 mK are required. In addition to these cryogenic temperatures, large quality factors are required, but nowadays values of $Q \approx 10^5 - 10^8$ are achieved in the laboratory without difficulty [FWS$^+$05, RPA$^+$16].

Microwave resonators are of uttermost importance in circuit QED, as they are essential to measuring qubits [BHW$^+$04, CDG$^+$10], shaping photons [PHE$^+$14, ZPB$^+$15], and several other tasks. However, they do not serve as a qubit. They are linear devices and, as such, the spectrum of (2.7) is equispaced, and therefore no individual transitions can be targeted independently. For that, some kind of non-linearity has to be included.

[1] We will, throughout the whole thesis, consider $\hbar = 1$.

2.2.2 Superconducting qubits

As mentioned in the previous subsection, realizing a qubit requires a quantum system where two specific states can be selectively addressed. Even restricting ourselves to superconducting circuits, several different embodiments of qubits can be found. Throughout this thesis, we will consider the **transmon** as the paradigmatic superconducting circuit qubit [BGGW21].

To understand the physics of the transmon it is necessary first to study the broader concept of a **charge qubit** and the parts of which it is made. A charge qubit (also known as Cooper pair box) is a qubit whose basis states are charge states, and they were first envisioned in [BVJ+98, NPT99, LBS+03]. This means that the states represent the presence or absence of excess Cooper pairs on a superconducting island. The fact that one can define such states relies on the so-called **Josephson junctions**, which are two pieces of superconducting material separated by some dielectric. This configuration establishes a potential through which some Cooper pairs can tunnel. The pink inset of Fig. 2.1 shows a real-world picture of the deposited dielectric material on top of the superconducting island.

The transmon qubit is one specific clever realization of the previous concept, conceived in a way that minimizes charge noise. First realized by the Yale group [KYG+07, SHK+08], the Hamiltonian describing such system is

$$H_T = 4E_c \left(n - n_g\right)^2 - E_J \cos(\phi). \tag{2.8}$$

The quantity E_J is the Josephson energy, and it represents the energy associated with the coherent tunneling of Cooper pairs across the junction. On the other hand, E_C is the charging energy, and it is related to the total capacitance of the circuit. The operator n represents the number of quanta, and as usual, the bigger its eigenvalue, the bigger the energy of the system. Also, Eq. (2.8) contains the term n_g, which represents a charge offset, this can come from desired sources, such as an intentional gate voltage $V_g = Q_g/C_g$, or undesired ones, such as environmental interactions. This is so because the relation between the number and charge operators is just $n_g = Q_g/2e$. Finally, ϕ is a rescaled flux traversing the inductor, and it is an essential term for the Hamiltonian (2.8) to display a non-linear behavior and depart from the completely harmonic spectrum of the LC resonator displayed in the previous subsection. Let us recall that in the harmonic case, the inductor flux appears as Φ^2 in the Hamiltonian (2.2), which ensures the linear behavior and differs substantially from the cosine term in Eq. (2.8).

The spectrum of H_T is controlled by the ratio E_J/E_C. When $E_J/E_C \ll 1$ the situation corresponds to the first attempts of charged qubits referred to at the beginning of the Section [NPT99], which are very sensitive to the term n_g and therefore not robust to external disturbances. The regime $E_J/E_C \approx 1$ was explored in [VAC+02], and finally $E_J/E_C \gg 1$ is the transmon regime, which was first reached in [KYG+07]. Fig. 2.2a shows how the spectrum of the Hamiltonian changes as a function of the ratio E_J/E_C. In the transmon regime, it is observable how the energy levels flatten out and get distributed anharmonically (solid lines in Fig. 2.2a), this is analogous to atomic energy levels, and it is the reason why these circuits are often called *artificial atoms*.

The transmon qubit presents a challenging trade-off, while the robustness against n_g increases with E_J/E_c, the anharmonicity decreases. The anharmonicity parameter $\alpha = E_{12} - E_{01}$ is the difference in energy between the two lowest transitions, and it is a critical feature of any charge qubit. The fact that made the transmon the most popular physical realization of a qubit in superconducting circuits is that, while the reduction in charge noise is exponential with E_J/E_c, the loss of anharmonicity is algebraic $(E_J/E_c)^{-1/2}$ [KYG+07, SHK+08]. This makes it possible to find a regime in which the decoherence gets dramatically reduced while the anharmonicity is kept large enough

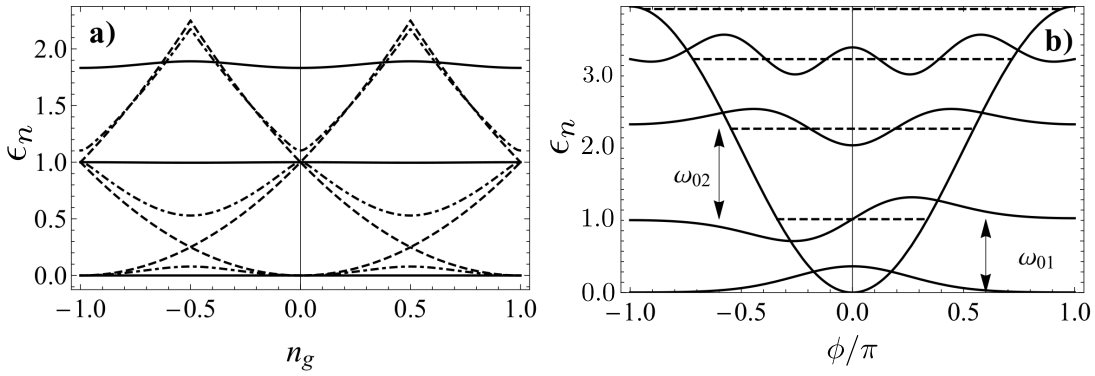

Figure 2.2: Spectrum of the transmon qubit and first few eigenfunctions. a) Eigenenergies $\epsilon_n = (E_n(n_g) - E_0(0)/\omega_{01})$ (for the first three levels, $n = 0, 1, 2$) of the qubit Hamiltonian presented as a function of the effective offset charge n_g for different ratios of $E_J/E_c = 0.02$ (dashed), 2 (dot-dashed) and 16 (solid). The energies are referred to the transition energy E_{01} evaluated at the degeneracy point $n_g = 0.5$. The dashed line corresponds to the charge qubit regime, in which one already has anharmonicity, but the charge fluctuations are large. As the ratio keeps increasing the fluctuations concerning n_g become smaller until finally in the transmon regime (solid line) they are negligible. b) For a transmon with $E_J/E_C = 16$, we plot the energy levels relative to the ground state $\epsilon n(0)$, together with the nonlinear inductive potential $E_J \cos(\phi)/\omega_{01}$. On top of each level, we plot the eigenfunctions, shifted and scaled arbitrarily.

to guarantee high-fidelity manipulations. For a value of $E_J/E_c = 16$, inside the transmon regime, we show in Fig. 2.2b the energies of the four lowest energy levels together with their corresponding eigenfunctions.

In the transmon regime $E_J/E_C \gg 1$, the term n_g can be dropped because the energy of the level flattens and does not depend on this parameter. Doing so, and truncating the Hamiltonian (2.8) up to fourth order in ϕ leads to

$$H'_T = 4E_C n^2 + \frac{1}{2}E_J\phi^2 - \frac{1}{4!}E_J\phi^4. \tag{2.9}$$

Now, rewriting this Hamiltonian in terms of creation and annihilation operators $b, b^\dagger$ defined through

$$\phi = \left(\frac{2E_C}{E_J}\right)^{1/4}\left(b^\dagger + b\right)$$
$$n = \frac{i}{2}\left(\frac{E_J}{2E_C}\right)^{1/4}\left(b^\dagger - b\right)$$

results into

$$H'_T = \sqrt{8E_C E_J}b^\dagger b - \frac{E_C}{12}\left(b^\dagger + b\right)^4 \approx \omega_q b^\dagger b - \frac{E_C}{2}b^\dagger b^\dagger b b, \tag{2.10}$$

where in the last step we have only kept the terms having the same number of b $b^\dagger$ operators, following [BGGW21], and where the natural frequency of the system is $\omega_q = \sqrt{8E_C E_J} - E_C$.

Finally, focusing only on the two lowest energy levels of the transmon $|g\rangle$ and $|e\rangle$, which amounts to making the changes $\hat{b}^\dagger \to \sigma^+ = |e\rangle\langle g|$ and $\hat{b} \to \sigma^- = |g\rangle\langle e|$ transforms the previous Hamiltonian into

$$H_{2ls} = \omega_q \sigma^+ \sigma^-, \tag{2.11}$$

which is the standard expression of a 2-level system Hamiltonian, or, in other words, a qubit.

2.3 Qubit-resonator couplings for gates and measurements

Some form of coupling between the resonator and the qubit is essential such that they can affect each other. In the particular case of superconducting circuits, many control tasks on the qubit, including all measurements, are made through the resonator. In particular, in the quantum computing node photograph of Fig. 2.1b, the yellow resonator is used for transferring population in and out of the qubit (cf. Subsection 2.3.1), and the green resonator for measuring the state of the qubit via an out of resonance coupling (cf. Subsection 2.3.3).

2.3.1 Resonant regime

Having the Hamiltonians for both the resonator and the transmon qubit, the next step is to couple them. This can be done in two different ways, *capacitively* or *inductively*, in either case, the resulting Hamiltonian has the same form, the so-called *spin boson model* [LCD+87]

$$H = \omega_q \sigma^+ \sigma^- + \omega_r a^\dagger a + g(\sigma^+ + \sigma^-)(a + a^\dagger), \tag{2.12}$$

where the coupling constant g changes depending on whether it is capacitive or inductive [Rip22]. The physics of the spin-boson model is very rich. When instead of considering a single mode a, one considers a collection of modes a_k, it constitutes one of the paradigmatic models for studying dissipation in quantum systems. The specific instance of the single-mode spin-boson model considered here is usually referred to as the *Quantum Rabi model*, due to its connection with the Rabi problem in nuclear magnetic resonance [Rab37].

When the natural frequencies of the elements involved ω_q, ω_r are much larger than the typical couplings of the system, the conditions for the rotating wave approximation hold. In this situation, the terms $\sigma^+ a^\dagger$, $\sigma^- a$ oscillate much faster than the relevant timescales of the problem, and therefore their effect becomes negligible. In this situation, one arrives at the Jaynes-Cummings Hamiltonian [JC63],

$$H_{\mathrm{JC}} = \omega_q \sigma^+ \sigma^- + \omega_r a^\dagger a + g(\sigma^+ a + \sigma^- a^\dagger). \tag{2.13}$$

The Hamiltonian given by Eq.(2.13) is ubiquitous in quantum optics and captures the physics of an excitation being coherently exchanged between the atom and the resonator. It is important to note that the Hamiltonian (2.13), unlike the Quantum Rabi model (2.12) preserves the number of excitations, which will be of central importance to this thesis. This means that the eigenstates of the Hamiltonian are also eigenstates of the number operator $n = a^\dagger a$. This fact implies that the number of excitations present in the initial condition of the problem will be preserved. This, in turn, allows for a simplification of the problem as the different blocks of the Hilbert space containing different numbers of excitations do not get mixed, see Chapter 3 for a thorough discussion of this method.

In the resonant condition $\omega_q = \omega_r$, it gives rise to the so-called *Rabi oscillations*. These describe a process in which the two-level system and the resonator exchange an excitation back and forth, and are an important benchmark of quantum behavior. The Jaynes-Cummings model is exactly solvable and, despite its simplicity, offers valuable insights into the quantum nature of light. Indeed, some of the most used benchmarks for the quantum regime are directly derived from this model. We devote the rest of this subsection to their study.

To confidently know that we are manipulating quantum information in this context, we have to ensure that we are working in the strong coupling regime. This is the regime

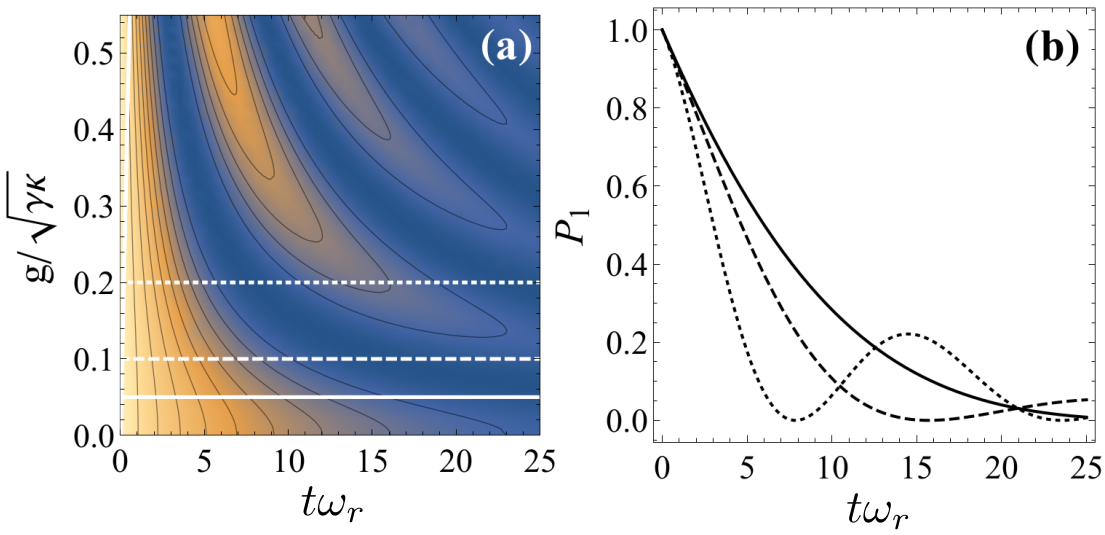

Figure 2.3: Dynamics in the weak and strong coupling regimes of a JC model. (a) Excited state population for the cavity-qubit system starting in the $|e,0\rangle$ state, that is, qubit excited and no photons in the cavity. The horizontal axis represents time in units of the system's natural frequency and the vertical coupling strength over losses. (b) Horizontal cuts for $g = 0.05\gamma$, 0.1γ and 0.2γ. Plots use $\omega_r = \omega_q = 1$, $\gamma = \kappa = 0.1$. Figure borrowed from [Rip22].

in which the coupling between qubit and cavity is larger than the intrinsic losses of the system $|g| \gg \kappa, \gamma$, where κ is the linewidth of the cavity and it dictates how fast it leaks excitations to the environment. Whereas γ represents the losses of the qubit. We can study the dynamics of the JC model with losses employing the following master equation [Rip22]

$$\partial_t \rho = -i\left[H_{\mathrm{JC}}, \rho\right] + \frac{\gamma}{2}(2\sigma^- \rho \sigma^+ - \sigma^+\sigma^-\rho - \rho\sigma^+\sigma^-) + \frac{\kappa}{2}(2a\rho a^\dagger - a^\dagger a\rho - \rho a^\dagger a). \quad (2.14)$$

Because the JC Hamiltonian preserves the number of excitations, we can project our density matrix onto a specific sector with a fixed number of excitations $\rho_N(t) = P_N \rho(t) P_N$, where P_N is precisely the operator which projects the full density matrix onto the subspace of size containing N excitations. Doing so, the previous master equation becomes [Rip22]

$$\partial_t \rho_N = -i\left[H_{\mathrm{eff}}\rho_N\right] + \kappa a \rho_{N+1} a^\dagger + \gamma \sigma^- \rho_{N+1} \sigma^+, \quad (2.15)$$

$$H_{\mathrm{eff}} = H_{\mathrm{JC}} - i\frac{\gamma}{2}\sigma^+\sigma^- - i\frac{\kappa}{2}a^\dagger a. \quad (2.16)$$

As previously mentioned, the dynamics of this model is integrable for any number of excitations. We choose now as our initial condition $\rho_1(0) = |e,0\rangle\langle e,0|$, this is, the emitter in its excited state and zero photons in the cavity. The solution in this case takes the form

$$|\psi(t)\rangle = c_e(t)\,|e,0\rangle + c_g(t)\,|g,1\rangle\,, \quad (2.17)$$

which is an unnormalized state that loses population as it leaks into the environment. The coefficients $c_e(t)$, $c_g(t)$, which can be comprised into the vector $\mathbf{c}(t)$, follow the dynamics

$$\mathbf{c}(t) = e^{-i\frac{1}{2}(\omega_q - \omega_r)t - \frac{1}{4}(\kappa+\gamma)t}\left[\cos(\bar{\Omega}t)\mathbb{I} - i\sin(\bar{\Omega}t)\bar{\mathbf{v}}\cdot\sigma\right]\mathbf{c}(0), \quad (2.18)$$

where σ is a vector containing all Pauli matrices as its components, and the vector $\bar{\mathbf{v}}$ and the Rabi frequency $\bar{\Omega}$ are respectively

$$\bar{\mathbf{v}} = \left(\frac{g}{\bar{\Omega}}, 0, \frac{\omega_q - \omega_r}{2\bar{\Omega}} + i\frac{\kappa-\gamma}{4\bar{\Omega}}\right), \quad \bar{\Omega} = \sqrt{g^2 + \left(\frac{\omega_q - \omega_r}{2} + i\frac{\kappa-\gamma}{4}\right)^2}. \quad (2.19)$$

The norm of the state $|\psi(t)\rangle$ decreases exponentially, $\mathrm{Tr}(\rho_1(t)) = ||\psi(t)\rangle||^2 \propto e^{-\frac{1}{4}(\kappa+\gamma)t}$, pointing to the fact that population from the excited state is lost irreversibly to the environment.

Besides this behavior of exponential losses, there are also oscillations between $|e,0\rangle$ and $|g,1\rangle$. We could determine the regime in which we are operating by looking at the interplay between the damping and the oscillatory dynamics. To ensure that we are in the quantum regime, *Rabi-like oscillations* must be observed, these are the coherent exchange of excitations between the qubit and the resonator. This interplay is precisely what is shown in Fig. 2.3. The evolution dynamics starting from the initial state $|e,0\rangle$ is shown for different values of the ratio $g/\sqrt{\gamma\kappa}$. It is observed that when in the *weak coupling regime* $g \ll \gamma, \kappa$, the dissipation dominates, and no oscillation is observed, this is evident from the horizontal cut displayed by the solid line in Fig. 2.3b. On the other hand, when in the *strong coupling regime* $g \gg \gamma, \kappa$ the oscillations become visible (dotted line in Fig. 2.3b). In this situation, we can ensure that a coherent interaction between the quantum elements is occurring.

The first observations of Rabi-oscillations in a cavity-atom system were made by Serge Haroche and his group [RBH01, Har13] using high-quality factor microwave cavities. Nowadays, the strong coupling regime, evidenced by the observation of these oscillations is routinely achieved in circuit QED experiments coupling microwave resonators to superconducting qubits, [MSK$^+$20, KKT$^+$18, LLC$^+$19].

Before closing this subsection on the resonant cavity-qubit regime, it is instructive to clarify that the master equation formalism, such as that displayed in Eq. (2.14) will not be used almost anywhere in this thesis. Although it is a very powerful theoretical tool and it incredibly helps to study losses and open dynamics in general in quantum systems, it has the drawback that one misses most information regarding the environment. As will be explained in more detail in Section 2.4 and especially throughout Chapter 3, one of the main objectives of the present study is to assess the performance of quantum links and understand the behaviors of the fields inside them. Because of this reason, the collection of modes comprising the quantum link will be explicitly taken into account.

2.3.2 Tunable couplers

Another central idea of this thesis is that of wavepacket shaping, which will be described at length in Chapter 3. It essentially consists in deterministically shaping the outgoing photon using a time-dependent coupling. What is relevant to note now, is that the Hamiltonian (2.13) suffices to implement this technique as long as the coupling g changes with time, that is $g \longrightarrow g(t)$. Within the field of circuit QED several proposals enable time-dependent couplings, some of them make use of the upper energy levels of the transmon [ZPB$^+$15, PHE$^+$14], others use intermediary transmons that then get traced out [YEA$^+$23], and yet others effectively tune the coupling between the node and the quantum link [CNR$^+$14, KM19, GYC$^+$24].

Throughout most of the thesis, we will work with the assumption that the coupling between the qubit and the resonator can be tuned in time, that is, we will treat it as a time-dependent function $g(t)$. Moreover, we will not only tune its amplitude but also its phase, that way, we will assume that, in general, $g(t) \in \mathbb{C}$. This last requirement will sometimes be relaxed, but it will be central in Chapter 5 when we attempt to correct distortion by engineering phases on the control. Because in the following we will just assume that we have this time-dependent $g(t)$ at hand, we will devote this subsection to detail one specific way this can be achieved in a distributed superconducting architecture.

We choose to focus on the implementation put forward in [PHE+14], and [ZPB+15], in which they arrive at an effective $g(t)$ through applying a microwave drive to a transmon-resonator node. This approach is appealing because it does not require changing the qubit frequency, or the coupling, which minimizes the number of circuit components.

In the scheme proposed in [ZPB+15] the amplitude and phase tunability is achieved by a mechanism known as cavity assisted Raman process, which is well known in the atomic physics literature [GE90, CKSG91, AB95, Wu96]. The core of the concept is to use an external coherent drive with a time dependent-amplitude that induces an effective coupling $g(t)$ between two levels of the transmon qubit and the resonator. The idea is that, through a two-photon process, and mediated by a third level that will be traced out, the two levels under interest get coupled with the cavity field. As we will see, having access to the amplitude and phase of the drive, will allow us to control the amplitude and phase of the coupling.

To explain how this cavity-assisted Raman process works in this context it is illustrative to go back to the picture of the transmon as an anharmonic oscillator, c.f. Eq. (2.10). The three lowest energy levels are $|g\rangle$, $|e\rangle$, and $|f\rangle$, and their respective energy differences $E_{ge} = \omega_q$, $E_{ef} = \omega_q + \alpha$, with α negative in this case. A display of the different energy levels can be seen in Fig. 2.4. The resonator, on the other hand, is a harmonic oscillator with energy ω_r. The transmon and resonator are in the dispersive regime, that is, $\Delta_{qr} = \omega_q - \omega_r \gg g$, and therefore the exchange of excitations between them is suppressed. Together with this, the idea is to apply a drive to the qubit with a frequency $\omega_d = 2\omega_q + \alpha - \omega_r$, which corresponds to the difference between the $|f0\rangle$ and $|g1\rangle$ states. Such drive is of the form

$$\Omega(t) = \Omega_0(t)\cos\left(\omega_d t - \varphi(t)\right), \tag{2.20}$$

which has the corresponding complex drive strength $\Omega(t) = \Omega_0(t)\mathrm{e}^{\mathrm{i}\varphi(t)}$ with slowly varying amplitude $\Omega_0(t)$ and phase $\varphi(t)$. In reality, the frequency one has to consider is a bit more involved than ω_d, because one has to compensate for the difference in AC Stark shift suffered by $|f0\rangle$ and $|g1\rangle$. However, such technicality is not very relevant here, and we refer to [ZPB+15] for these details.

The Hamiltonian of this system, in a frame rotating at the frequency of the drive ω_d, is $H = H_{\mathrm{JC}} + H_d$, where

$$H_{\mathrm{JC}} = (\omega_r - \omega_d)a^\dagger a + (\omega_q - \omega_d)b^\dagger b + \frac{\alpha}{2}b^\dagger b^\dagger b b + g(ab^\dagger + a^\dagger b), \tag{2.21}$$

and

$$H_d = \frac{\Omega_0(t)}{2}\left(\mathrm{e}^{\mathrm{i}\varphi}b + \mathrm{h.c.}\right). \tag{2.22}$$

The idea now is to get to an effective qubit-cavity Hamiltonian with a dynamical coupling $g(t)$ by writing H in the eigenbasis of H_{JC} and performing perturbation theory on H_d. Following [ZPB+15] we label the eigenstates of H_{JC} as $|i,j\rangle_D$ ($i = g, e, f, \ldots$ and $j = 0, 1, 2, \ldots$), whereby the subscript D we refer to the *dressing* caused by the static coupling g. Oppositely, we will use $|i,j\rangle = |i\rangle \otimes |j\rangle$ for the bare qubit-resonator states. Looking at the energy levels of the JC ladder in the rotating frame, panel (b) of Fig. 2.4, we can see that the only relevant transitions are those involving the resonant states $|g, l+1\rangle_D$ and $|f, l\rangle_D$. Keeping only these terms is analogous to the rotating wave approximation performed to go from the spin-boson to the Jaynes-Cummings Hamiltonian. Finally, writing H_d in the $|i,j\rangle_D$ basis and truncating as just stated, one obtains

$$H_d \approx \sum_l \frac{\Omega_0(t)}{2}|g, l+1\rangle_D\langle f, l|_D\left\{\langle g, l+1|_D\left(\mathrm{e}^{\mathrm{i}\varphi(t)}b + \mathrm{e}^{-\mathrm{i}\varphi(t)}b^\dagger\right)|f, l\rangle_D\right\}. \tag{2.23}$$

Now, because the qubit and resonator are in the dispersive regime (i.e. they are far off resonance, $g/(\omega_q - \omega_r) \ll 1$), we can treat the term $g(ab^\dagger + a^\dagger b)$ in H_{JC} as a perturbation

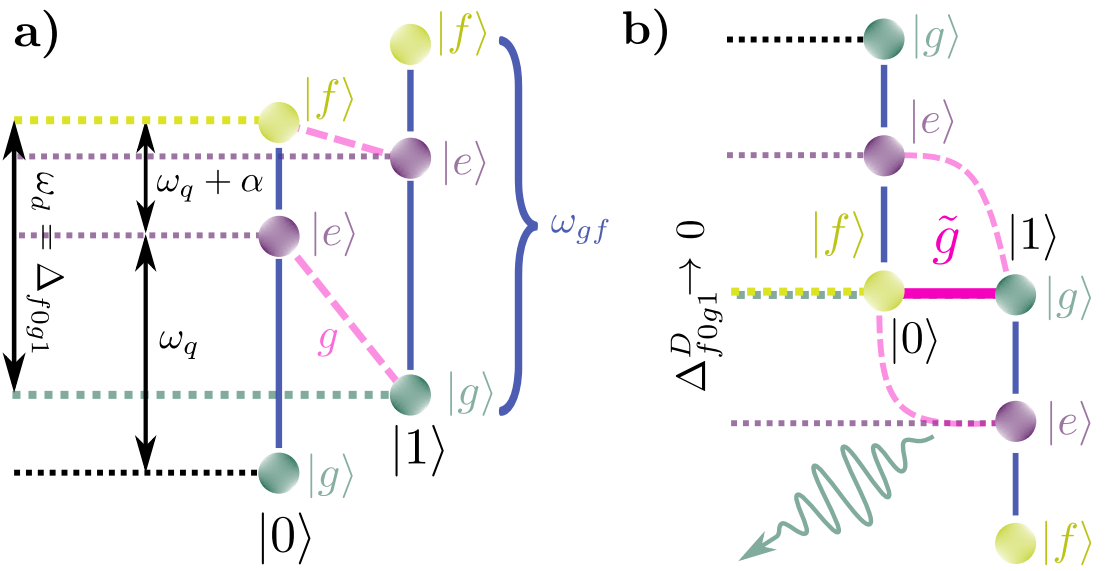

Figure 2.4: Energy level diagram of the transmon-resonator system in the laboratory frame a), and in a frame rotating at the drive frequency ω_d, b). In panel a) we show the different energy gaps between the three lowest levels of the transmon and define the quantity Δ_{f0g1} as the energy difference between the $|f0\rangle$ and $|g1\rangle$ states. This value of Δ_{f0g1} corresponds to that of ω_d defined in the main text. Panel b) shows how, in the rotating frame at the drive frequency, the energy difference between the $|f0\rangle_D$ and $|g1\rangle_D$, that is, Δ^D_{f0g1} vanishes. The effective coupling $\tilde{g}$ can be understood as a second-order cavity-assisted Raman process, indicated by the pink dashed lines. Also, the blue curvy arrow represents a photon being emitted when the system undergoes the transition from $|f0\rangle$ to $|g1\rangle$ and then spontaneously decays to $|g0\rangle$.

and obtain an expression for $|i,j\rangle_D$ in terms of $|i,j\rangle$ at first order in g. Doing this allows us to calculate the effective coupling as

$$\tilde{g}_l(t) \equiv \langle g, l+1|_D \; H_d \, |f,l\rangle_D \approx g\Omega_0(t) e^{i\varphi(t)} \sqrt{\frac{l+1}{2}} \frac{\alpha}{\Delta_{qr}(\Delta_{qr}+\alpha)} \,. \tag{2.24}$$

And now, defining the lowering operators for the dressed states as

$$\tilde{\sigma} \equiv \sum_l |g,l\rangle_D \langle f,l|_D \,, \qquad \tilde{a} \equiv \sum_{l,j} \sqrt{l+1} \; |j,l\rangle_D \langle j,l+1|_D \,, \tag{2.25}$$

we can express the driving Hamiltonian

$$\tilde{H}_d \approx \tilde{g}_l(t) \tilde{a}^\dagger \tilde{\sigma}_l + \tilde{g}_l^*(t) \tilde{a} \tilde{\sigma}_l{}^\dagger . \tag{2.26}$$

We will, throughout the rest of the thesis, consider $l = 0$ in the previous expression, therefore, focusing our attention on the $|f0\rangle_D$, $|g1\rangle_D$ transition and taking as the time-dependent coupling $\tilde{g}_{l=0}(t)$, we get

$$\tilde{g}_0(t) \approx g\Omega_0(t) e^{i\varphi(t)} \frac{\alpha}{\sqrt{2}\Delta_{qr}(\Delta_{qr}+\alpha)} \,. \tag{2.27}$$

Two things are important to bear in mind, first, that restricting our attention to the $|f0\rangle_D$, $|g1\rangle_D$ transition amounts to having again a Jaynes-Cummings Hamiltonian (cf. Eq. (2.13)), given that the anharmonicity α is big enough and the other levels do not play

any role. In the following, we will treat our system as described by Eq. (2.13) but with a time-dependent tunable coupling. Second, from Eq. (2.24), and its particular case with $l = 0$ (2.27), it is evident that both the strength of the coupling and its complex phase can be tuned through $\Omega_0(t)$ and $\varphi(t)$. The ability to tune these quantities will be essential for the content of this thesis, as all the protocols that we will propose need the modulation of the amplitude, and many of them also of the phase.

2.3.3 Dispersive regime

The resonant regime bears great importance due to the possibility of exchanging excitations coherently. However, there is another important regime that takes place when qubit and resonator are far out of resonance. This is the so-called dispersive regime. For instance, in the microscopic photograph of Fig. 2.1b, the readout resonator (depicted in yellow), and the transmon qubit (depicted in red) are in this situation. This is the case because superconducting qubits are usually measured with a far detuned resonator, as we will explain in the following.

The dispersive regime refers to the scenario where the detuning between the qubit and the resonator is large compared with the coupling strength ($\Delta_{qr} = \omega_q - \omega_r \gg g$). In this regime, it is useful to perform a Schrieffer-Wolf transformation [SW66, BDL11] on the Hamiltonian (2.13) [BHW$^+$04, KYG$^+$07]. The Schrieffer–Wolff is a unitary transformation that determines an effective (often low-energy) Hamiltonian by decoupling weakly interacting subspaces. In the case under consideration, this effective Hamiltonian becomes

$$H_{\text{eff}} = (\omega_r + \chi\sigma^z)\, a^\dagger a + \frac{1}{2}(\omega_q + \chi)\sigma^z, \tag{2.28}$$

where the dispersive parameter χ is

$$\chi = \frac{g^2}{\omega_q - \omega_r}.$$

The effective Hamiltonian (2.28) indicates that the frequency of the resonator moves up when the qubit is excited ($\sigma^z |e\rangle = s_+ |e\rangle$) and down when the qubit is in the ground state ($\sigma^z |g\rangle = s_- |g\rangle$), where $s_\pm = \pm 1$. This last term is particularly interesting, because, as was realized in [BHW$^+$04, WSB$^+$05, SWB$^+$05], it can be used to determine the state of the qubit without destroying it. Likewise, as will be shown in Chapter 4, this same dependence can be used to engineer gates between remotely located qubits.

The technique to determine the state of the qubit making use of Eq. (2.28) receives the name of dispersive measurement and is widespread nowadays, being the most popular measuring protocol in superconducting circuits. The method consists of sending a microwave pulse and studying its phase upon reflection from the dispersively coupled cavity. It is known from scattering theory [Nav22] that the amplitude of the reflected field with frequency ω_t is

$$R_{\omega_t} = \frac{i(\omega_r - \omega_t) - \kappa/2}{i(\omega_r - \omega_t) + \kappa/2} \approx e^{i\phi_s(\omega_t)}, \tag{2.29}$$

where $\phi_s(\omega_t)$ is the phase acquired. Now, driving the pulse resonantly with the cavity $\omega_r = \omega_t$, and incorporating the fact that the frequency is dependent on the state of the qubit $s_\pm = \pm 1$ the phase change results in

$$R_{\omega_t} = \frac{is_\pm\chi - \kappa/2}{is_\pm\chi + \kappa/2} \approx e^{i(\pi + \delta\phi_s s_\pm)}. \tag{2.30}$$

The term $\delta\phi_s$ is the difference in the scattering phase of the tone depending on whether the qubit is in its excited or ground state. This last expression provides the state of the qubit by detecting the phase of the scattered field. This phase goes as

$$\tan\left(\pi + \delta\phi_s s_\pm\right) \approx \frac{\chi s_\pm}{\kappa}, \tag{2.31}$$

from which $s_\pm$ reveals the information about the qubit's state in the z-basis.

2.4 Superconducting quantum link

The final aim of this chapter is to arrive at the complete Hamiltonian of a superconducting quantum network. For that, the missing part at this point is to join the quantum computing nodes via quantum links.

The lumped circuit element for a quantum link is that of a transmission line, which can be seen as a set of coupled resonators [BGGW21], and whose Hamiltonian, written in terms of the creation and annihilation operators takes the form

$$H_{\mathrm{Q}L} = \sum_m \omega_m b_m^\dagger b_m. \tag{2.32}$$

Eq. (2.32) describes the physics of a multimode resonator that holds m different modes at frequency ω_m. How these frequencies are distributed, i.e. the *dispersion relation*, depends on the specific physical implementation of the transmission line and will be of great importance throughout this thesis. For the most part, we will work with a superconducting WR90 rectangular microwave guide [Dav12], as is the case in the experiment reported in [MSK$^+$20], which greatly inspires the model developed here. The TE_{10m} modes frequencies of this waveguide are distributed according to

$$\omega_m = c\sqrt{(\pi/l_1)^2 + (m\pi/L)^2}, \tag{2.33}$$

which depend on the vacuum speed of light c, the broad wall dimension $l_1 = 2.286$ cm and the wave number $k_m = m\pi/L$. This dispersion relation gives rise to very interesting physics, as it presents non-linearities and the mass-like term $(\pi/l_1)^2$ which opens a band gap. When not explicitly stated, this is the waveguide and dispersion relation that we will be using. However, for the sake of generality, we will at moments offer examples of other dispersion relations, such as linear, quadratic, or cosine-like. Albeit outside the scope of this thesis, it is worth mentioning that the difficulties arising from non-linear dispersion relations are not unique to superconducting circuits and microwave photons. They pose a challenge in many platforms in the wider field of quantum technologies such as magnons [BGL$^+$21], coupled cavity arrays [ACAS16], or topological waveguides [OPA$^+$19] among others.

Now, once we have particularized the quantum link Hamiltonian (2.32) and a specific dispersion relation (2.33), the final step is to take the Jaynes-Cummings Hamiltonian for a computing node (cf. Eq. (2.13)) and join the two of them. For that, we need a term that couples the resonator mode to the collection of waveguide modes, the term $G_{m,j}$ in Fig. 2.5. This resonator-waveguide coupling amplitude can be deduced from each cavity's decay rate κ_j and the parity of the stationary modes as [Nav22, Rip22]

$$G_{m,j} = \cos\left(\frac{m\pi x_j}{L}\right)\sqrt{\kappa_j v_g \omega_m/(2\Omega_{\mathrm{R}j}L)}. \tag{2.34}$$

The prefactor before the integral is related to the parity of the stationary waveguide modes, and will in practice always take the values ± 1 since the computing node is either located at $x_j = 0$ or at $x_j = L$. The group velocity inside the transmission line is denoted as

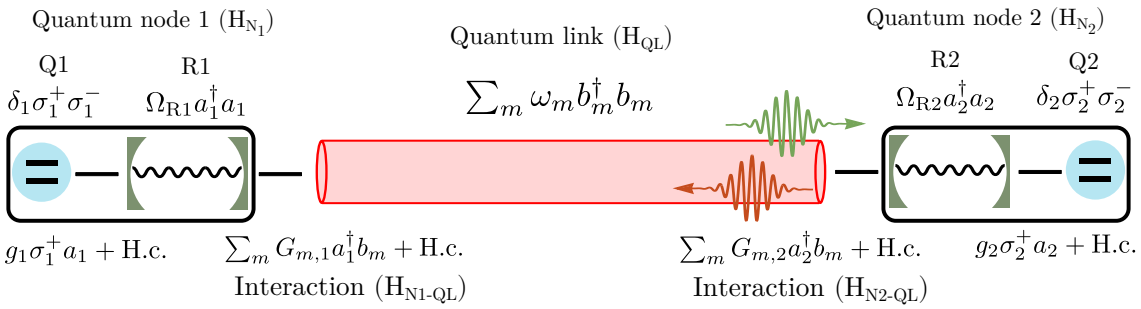

Figure 2.5: Minimal Network represented by the Hamiltonian (2.35) consisting of two nodes connected through a quantum link. Each of the nodes is composed of a qubit-cavity system. The system is bidirectional, and the structure of the couplings makes it possible for both nodes to emit and absorb excitations independently.

v_g and is defined as the derivative of the dispersion relation at the working frequency. Finally, it is important to note that the strength of the coupling is not the same for all the stationary modes but that it has a dependence $G_{m,j} \propto \sqrt{\omega_m}$. With all this into account, the complete Hamiltonian of the kind of quantum network we propose in this thesis is the following

$$
\begin{aligned}
H &= H_{\mathrm{QL}} + \sum_j \left[H_{\mathrm{N}_j} + H_{\mathrm{N}_j - QL}\right], \quad \text{with} \\
H_{\mathrm{N}_j} &= \delta_j \sigma_j^+ \sigma_j^- + \Omega_{\mathrm{R}j} a_j^\dagger a_j + g_j(t)\sigma_j^+ a_j + g_j^*(t)\sigma_j^- a_j^\dagger, \\
H_{\mathrm{QL}} &= \sum_m \omega_m b_m^\dagger b_m, \\
H_{\mathrm{N}_j - QL} &= \sum_m G_{m,j}\left(b_m^\dagger a_j + \text{H.c.}\right).
\end{aligned}
\tag{2.35}
$$

Each quantum node contains a qubit and a cavity H_{N_j} with a time-dependent coupling $g_j(t)$ that can be tuned for wavepacket engineering [KMW+17, MSK+20] (cf. Subsection 2.3.2). The waveguide H_{QL} hosts a family of modes with frequencies ω_m, which connect both cavities through a static coupling $H_{\mathrm{N}_j - QL}$. The a_j and b_m are Fock operators for the resonators and waveguide modes respectively, and we use spin-1/2 Pauli matrices $\sigma_j^+ = |1\rangle_j\langle 0|_j$ for the qubits, as detailed in Subsection 2.2.2.

We compute the group velocity $v_g = \mathrm{d}\omega(k)/\mathrm{d}k$ at the frequency closest to both cavities $\omega_c = \omega(k_c) \simeq \Omega_{\mathrm{R1}} = \Omega_{\mathrm{R2}}$, which we assume identical. We choose a gauge in which the resonator-waveguide coupling $G_{m,j} \in \mathbb{R}$ whereas $g_j(t) \in \mathbb{R}$ or $\mathbb{C}$ depending on the situation. All couplings between qubits, resonators and waveguide, as well as their intrinsic energies respect a hierarchy of interactions which justifies the rotating-wave approximation $|\Omega_{\mathrm{R}j} - \delta_j| \ll |\Omega_{\mathrm{R}j} + \delta_j|$, and $|g_j|, |\kappa_j| \ll \omega_m, \Omega_{\mathrm{R}j}, \delta_j$.

We choose to work at the X-band of the waveguide ($8 - 12$ GHz) as it is usual in experiments [MSK+20, KMW+17]. For typical parameters $\delta_{1,2}, \omega_{1,2} \sim 2\pi \times 8.4$ GHz, $\kappa_j \sim$ MHz, the group velocity of the central mode is $v_g = c\sqrt{1 - (\pi c/a\omega)^2} \approx 2c/3$.

A relevant parameter is the free spectral range (FSR) $\Delta\omega_m = \omega_{m+1} - \omega_m$, which is the frequency separation between adjacent waveguide modes and it is inversely proportional to L. We will refer to it by FSR or $\Delta\omega_m$ indistinctively. The interplay between κ_j and $\Delta\omega$ will prove relevant in later developments. The decay rate of the resonator κ will ultimately determine the maximum frequency width of the emitted wavepacket, and whether the ratio κ/FSR is big or small will determine if the picture resembles more that of a continuum of modes or of a coherent interaction between the resonator and one single waveguide mode.

The model described by Hamiltonian (2.35) will guide us through most of the thesis, and the parameters specified in the previous paragraphs will serve as the standard. However, depending on the specific problem we are tackling, we will include variations of it. For instance, in Chapter 6, when exploring how to increase the information capacity of quantum links, we will allow more than one qubit and resonator per computing node. In another example, when distributing entanglement across different network topologies in Chapter 7, we will consider situations in which not one but many quantum links depart from the same computing node.

2.5 Summary

Finally, in the last five to ten years, several leading laboratories around the world have started implementing protocols that fall under what we have named quantum state transfer networks, namely the precise control of qubit photon interactions to create deterministically wavepackets on demand. Although these experiments differ from one another, the communication channels are different, some use additional resonators for filtering purposes and so on, all of them can be described with the formalism presented in this chapter. To the best of our knowledge, the leading experimental efforts in the field up to date are: from the group at Yale [PHB$^+$14, CZN$^+$18, ABP$^+$18, BTZ$^+$21], from the group at the University of Chicago [ZCS$^+$19, LLC$^+$19, CZB$^+$20], from the group at ETH Zurich [KMW$^+$17, BGC$^+$18, MSK$^+$20, SSK$^+$23], from the group at UCBerkley [RSM$^+$14], from the group at the University of Tokyo [KKT$^+$18], from the group at Chalmers University [SCC$^+$22, YEA$^+$23, ESK$^+$24], and from the group at Tsinghua University in Beijing [QLN$^+$23].

Throughout the following chapters, we will put forward our protocols and ideas, but always with a look at these experiments. We will use them as guides to assess losses and imperfections, and we will compare our ideas with the ones already implemented in them. This is especially true in the case of the experiments of the ETH Zurich group, since this thesis was conceived as part of a joint project in which to propose novel methods for implementation in their distributed superconducting setup.

Wavepacket engineering as a primitive for distributed computing

3

As pointed out in Chapter 1, the main objective of this thesis is to build the framework for a quantum state transfer network based on superconducting circuits. The main primitive for that is quantum state transfer, and the way to achieve it will be following the seminal proposal by Cirac and collaborators dating back to 1996 [CZKM96]. In it, the authors propose a way to map the quantum state of a solid-state qubit to a flying one, that then travels through some medium until it reaches another node.

The present chapter focuses on a specific part of the protocol proposed in [CZKM96], which, as we shall see, allows for much more than just state transfer. The problem under consideration consists of how to map the quantum state of one emitter to a traveling photon in a waveguide, and conversely to convert a flying photonic qubit into a stationary one hosted in a computing node. The technique to achieve this, called *wavepacket shaping* or *wavepacket engineering*, consists of the dynamical control of the emitter-waveguide coupling $g(t)$ such that the electromagnetic field acquires a particular target shape. Wavepacket shaping has an interest in itself as it allows for the creation of entanglement between a stationary and a flying qubit, as already demonstrated experimentally [RNH$^+$12, PHE$^+$14, ZPB$^+$15, FWC$^+$17, MKLR19]. When also applied at other nodes of the network, the emitted wavepacket can be absorbed, achieving deterministic quantum state transfer between distant qubits [KMW$^+$17, ABP$^+$18, CZN$^+$18, MSK$^+$20]. There already exist two experimental PhD theses on how to apply these techniques to the particular context of superconducting quantum networks [Kur19], [Mag21]. These works will motivate experimentally many of the ideas that will be presented in this and subsequent chapters.

It is worth noting that whereas the original proposal imposes a time-symmetric shape for the wavepacket, this restriction is not necessary, and the aforementioned works achieve state transfer with non-symmetric as well as symmetric wavepackets. What is however unavoidable for wavepacket shaping to work is the ability to engineer time-dependent light-matter couplings, a requirement that many laboratories around the world meet nowadays ordinarily [YEA$^+$23, SSK$^+$23]. This last point was already commented on in Chapter 2 when presenting the Hamiltonian model (2.35).

Also, there is a conceptual difference between the original proposal and the methods we describe in this chapter. Because in [CZKM96], they achieved the transfer by imposing a dark state condition (no population in the quantum link upon reflection), the dynamics of the emitter and the receiver get connected. This leads them to require that the wavepacket is time-symmetric, or, in a less restrictive way, that the absorption control is the time-reversed of the emission one. In reality, no connection between $g(t)_{\text{emission}}$ and $g(t)_{\text{absorption}}$ has to be imposed. Everything works more clearly if one only focuses on the relation

between the incoming field and the corresponding $g(t)$ (in the case of absorption), or the relation between the desired outgoing field and its related $g(t)$ (in the case of emission). This way, the whole problem reduces to computing the differential equations backward or forward, but with the nodes treated as independent. Because of this simplification in the formalism, we can compute controls $g(t)$ even analytically in relevant situations that had been previously overlooked, such as the presence of extra resonators between the computing nodes and the quantum link.

This chapter is divided into two well-differentiated parts. In the first one—Section 3.1—we present the Wigner-Weisskopf ansatz, and show how it can be used to go from equations for operators to equations for complex scalar coefficients. Besides this simplification, this ansatz also allows for a dramatic reduction of the dimensionality of the problem. After that, but still in the same section, we introduce the Markov approximation and input-output theory. These allow for a further simplification of the equations of motion by decoupling the dynamics of the different nodes of the network. In the second part—Section 3.2—we will make use of the simplified decoupled model to obtain analytical expressions for the time-dependent controls $g(t)$. Explicit formulae for the couplings $g(t)$ will be given in a variety of physical situations and for several different target wavepacket shapes. These generalizations are not trivial. As we will see, allowing for arbitrary phase profiles or including extra cavities as filters modify the methods and controls in a non-obvious fashion.

3.1 Wigner-Weisskopf ansatz, the Markov approximation and input-output theory

The rotating wave light-matter Hamiltonian given by Eq. (2.35) preserves the number of excitations. This makes it possible to fix the number of quanta in the initial state in a way that will be preserved throughout the whole dynamics. The so-called Wigner-Weisskopf ansatz builds precisely on this idea. It is the most general initial state for a given number of excitations. The rest of the chapter will be centered around the single excitation Wigner-Weisskopf ansatz, which we will use to study the dynamics of an emitter that leaks into an environment. The most general one-excitation state within a system described by the Hamiltonian (2.35) is

$$|\Psi(t)\rangle = \left[\sum_{j=1,2}\left(q_j(t)\sigma_j^+ + c_j(t)a_j^\dagger\right) + \sum_k \psi_k(t)b_k^\dagger\right]|\mathbf{0}\rangle\,. \tag{3.1}$$

The operators σ_j^+, $a_j^\dagger$ and $b_k^\dagger$ represent the possibility that an excitation is created in the qubit j, the cavity j or the waveguide mode k respectively, when acting upon the vacuum $|\mathbf{0}\rangle$. The coefficients $q_j(t)$, $c_j(t)$, and $\psi_k(t)$ are complex numbers that determine the field in each of the system's components. For example, the quantity $|\psi_3(t)|^2$ corresponds to the probability of finding the excitation in the third waveguide mode, while $\sum_k |\psi_k(t)|^2$ represents the probability of finding the excitation in the waveguide altogether.

Now, the convenience of defining the ansatz (3.1) becomes evident when imposing it upon the Schrödinger equation together with the Hamiltonian (2.35). When doing so, the general equation for operators transforms into a set of coupled linear differential equations

$$i\dot{q}_j(t) = \delta_j q_j(t) + g_j(t)c_j(t), \tag{3.2}$$

$$i\dot{c}_j(t) = \Omega_{\mathrm{R}j}c_j(t) + g_j^*(t)q_j(t) + \sum_k G_{k,j}\psi_k(t), \tag{3.3}$$

$$i\dot{\psi}_k(t) = \omega(k)\psi_k(t) + \sum_{j=1,2} G_{k,j}c_j(t), \tag{3.4}$$

which can be summarized as

$$i\frac{d}{dt}\left|\Psi(t)\right\rangle = H_{1\text{exct}}\left|\Psi(t)\right\rangle, \tag{3.5}$$

whereby $H_{1\text{exct}}$ we are denoting only the part of the initial Hamiltonian that acts on the 1 excitation subspace, an operator whose matrix representation is much smaller than that of the full problem Hamiltonian H. The Eqs. (3.2) to (3.4) are comparatively easy to handle, and since they are linear, we can solve them using the matrix exponential operator, which is numerically very efficient. In our particular case, in which the Hamiltonian depends explicitly on time, we can write the evolution operator as

$$U(t_i, t_{i-1}) = e^{-iH_i\Delta t},$$

and then obtain the wavefunction at any time

$$\Psi(t_i) = U(t_i, t_{i-1})\Psi(t_{i-1}).$$

The key realization that makes this process very efficient, made by [HA10] and later refined by [AH11] is that we do not have to compute the full $N \times N$ matrix exponential U. Rather, it is sufficient to only compute the result of the product $U(t_i, t_{i-1})\Psi(t_{i-1})$, which is of size $N \times 1$, as it is the exponential of an $N \times N$ matrix acting on a vector.

For the problem of wavepacket shaping, only the dynamics of one node containing the emitter and the resulting field are of interest. Because of that, it is convenient to find a way to decouple the different emitters in Eqs. (3.2) to (3.4). This can be done in a context in which the medium connecting the different nodes, the *bath*, has a memory time much shorter than the typical energies of the different elements. This physical regime, called a *Markovian environment*, allows one to perform the so-called *Markov approximation*, which is ubiquitous in quantum optics [GZ15, Rip22]. It is important to pause for a moment here and consider the implications of doing this step. From a physical point of view, performing this approximation means that all relevant timescales of our problem are much longer than that of the environment. In other words, the validity of the method will be worsened as we push towards faster protocols and dynamics. In particular, we will have to come back to this point in Chapter 5 where we realized that for the quick controls and cavity fields needed there, this approximation in the way it is performed here no longer applies. See [dA17] for a thorough review of non-Markovian dynamics in quantum systems.

The first step towards a Markovian model of Eqs. (3.2)-(3.4) is to integrate the field variables $\psi_k(t)$ in Eq. (3.4) and substitute them into Eq. (3.3), arriving at

$$\dot{c}(t) = -ig^*(t)q(t) - i\tilde{\xi}_{\text{in}}(t) - \int_{t_0}^{t} d\tau K(t-\tau)c(\tau). \tag{3.6}$$

As it is standard in the quantum optics literature, $\tilde{\xi}_{\text{in}}(t) = \sum_k G_k e^{-i\tilde{\omega}(k)(t-t_0)}\psi_k(t_0)$ is the *input* field which represents the electromagnetic field that arrives to the emitter from the past state of the environment. The term $K(t-\tau) = \sum_k G_k^2 e^{-i\tilde{\omega}_k(t-\tau)}$ is referred to as the kernel and it contains information on how the state of the emitter affects the state of the field. It is also useful to define implicitly the *spectral function*, which is the Fourier transform of the memory function

$$K(t) = \sum_k G_k^2 e^{-i\tilde{\omega}_k(t-\tau)} = \frac{1}{2\pi}\int J(\bar{\omega})e^{-i\bar{\omega}t}d\bar{\omega}. \tag{3.7}$$

The equations we are considering in the present calculation assume only one qubit and one resonator per computing node, when more of these interacting quantities are placed

together, the expressions for the Kernel and spectral function get modified. This situation will be studied in detail in Chapter 6.

Proceeding now analogously to appendix B of [Rip22] (Eq. B.26), we can separate the time evolution of $c(t)$ as a slow contribution $c(t) = c_{\text{slow}}(t)e^{-i\omega' t} = c_{\text{slow}}e^{-i\omega t}e^{-i\omega' t}$ with an unknown frequency ω', and a fast one. Performing this step, and introducing $u = t-\tau$, the kernel integral in Eq. (3.6) becomes

$$c_{\text{slow}}e^{-it\omega}\int_0^{+\infty} duK(u)e^{i\omega' u}e^{-i\omega' t}. \tag{3.8}$$

The core of the Markov approximation relies on this *separation of time scales*. Assuming that the memory time of the bath is much shorter than all other characteristic times, or mathematically, that the kernel approaches a delta function, the integral (3.8) becomes local in time

$$c(t)\int_0^{+\infty} duK(u)e^{i\omega' u} = (i\delta\omega + \frac{1}{2}\kappa)c(t), \tag{3.9}$$

where $c_{\text{slow}}(t)e^{-i\omega' t} = c(t)$. The quantities $i\delta\omega$ and κ are the Lamb shift and decay rate, respectively. They are related to the spectral function by the following relations, which are very useful for calculations [DCPGR15]

$$\delta\omega = \frac{1}{2\pi}\int i\ \text{PV}\left(\frac{1}{\omega'-\omega}\right)J(\omega)d\omega, \tag{3.10}$$

$$\frac{\kappa}{2} = \frac{1}{2\pi}\int \pi\delta\left(\omega'-\omega\right)J(\omega)d\omega. \tag{3.11}$$

When combining all this, the initial equations for the coefficients (3.2) to (3.4), can be simplified to

$$\dot{q}(t) = -ig(t)c(t), \tag{3.12}$$

$$\dot{c}(t) = -ig^*(t)q(t) - i\tilde{\xi}_{\text{in}}(t) - (i\delta\omega + \frac{1}{2}\kappa)c(t). \tag{3.13}$$

The Lamb shift $\delta\omega$ constitutes a change in frequency of the cavity due to its interaction with the environment [Nav22], which in this particular case is represented by the mode structure of the waveguide. As we will see in Chapter 4, the value of the Lamb shift is not a mere technicality, on the contrary, it is a relevant effect that has to be accounted for and precisely computed. The decay rate κ replaces the complicated term $\sum_k G_{k,j}\psi_k(t)$ in Eq. (3.3), a term in which the details of the frequency modes of the environment, and the cavity-waveguide capacitive coupling are present. Instead, the Markovian decay rate κ represents a picture in which all the information regarding the environment has been lost, and what remains is a cavity that leaks excitations to this medium at an exponential rate.

The previous simplification comes, however, at a price. That of losing the connection present in the full model between, for example, an excitation in the qubit, and the shape of the electromagnetic field generated upon emission. This is so because all the details about the intricate mode structure of the waveguide, or environment in general, have been washed out. Luckily, there is a solution to this, the so-called *input-output relations* [Yur84, GC85]. The concept is that it is possible to replicate the procedure to obtain (3.12) but using initial conditions from the far future ($t_f \longrightarrow \infty$), instead of from some past time, as has been done in the previous paragraphs. This leads to an equation for the cavity field of the form

$$\dot{c}(t) = -ig^*(t)q(t) - i\tilde{\xi}_{\text{out}}(t) - (i\delta\omega - \frac{1}{2}\kappa)c(t). \tag{3.14}$$

This cavity field however, has to coincide with the one predicted by the previous procedure, that is, we can subtract Eq. (3.13) from Eq. (3.14), and the only terms that survive are those of κ, the only ones that changed sign between both calculations. This yields the really simple relation

$$\tilde{\xi}_{\text{out}}(t) = \tilde{\xi}_{\text{in}}(t) - i\kappa c(t). \tag{3.15}$$

There is, however, one last issue to be resolved. The dimensions of $\tilde{\xi}$ are not the right ones. If instead of doing the calculation with coefficients (complex scalars) we do it with operators, see for instance [Rip22], we realize that $\left[\tilde{\xi}^{\text{op}}_{\text{in}}(t), \tilde{\xi}^{\text{op}}_{\text{in}}(t')\right] = \kappa\delta(t-t')$. Therefore, they do not satisfy causal commutation relations and can not be considered proper field operators, to fix this we introduce new field operators $\xi^{\text{op}}(t) = \tilde{\xi}^{\text{op}}(t)/\sqrt{\kappa}$. These translate into our equation for coefficients as

$$\xi_{\text{out}}(t) = \xi_{\text{in}}(t) - i\sqrt{\kappa}c(t). \tag{3.16}$$

Now, bringing together the equation for the field coefficients $\xi(t)$ with Eqs. (3.12) one arrives at the set of equations that will lead all the remaining sections in the chapter

$$\dot{q}(t) = -ig(t)c(t), \tag{3.17}$$

$$\dot{c}(t) = -ig^*(t)q(t) - i\sqrt{\kappa}\xi_{\text{in}}(t) - (i\delta\omega + \frac{1}{2}\kappa)c(t), \tag{3.18}$$

$$\xi_{\text{out}}(t) = \xi_{\text{in}}(t) - i\sqrt{\kappa}c(t). \tag{3.19}$$

These equations deal solely with one node and constitute the appropriate tool for obtaining the time-dependent coupling $g(t)$ in terms of some desired target wavepacket.

The Eqs. (3.17)-(3.19) will be a very important tool throughout the thesis, unlike Eqs. (3.2)-(3.4), they are manageable analytically and offer valuable insights between the fields $\xi(t)$ and the rest of dynamical quantities. Under the input-output relation, Eq. (3.19), we can keep track of the incoming and outgoing fields while at the same time resorting to the Markov approximation and forgetting about all intricacies related to the environment.

It is important, before we go on, to state the assumption on which Eqs. (3.17)-(3.19) rely, as their validity will be a much-discussed topic in the forthcoming chapters. The input-output theory assumes a continuum of modes, therefore it is expected to apply when the frequency width $\tilde{\kappa}$ of the wavepackets $\xi(t)$ is much greater than the frequency separations of these modes, or, in the language presented in Chapter 2, when $\tilde{\kappa} \gg \text{FSR}$. As we will discover in Chapter 4, there are situations in which the previous condition is not respected and the input-output relations still hold. On top of this, to arrive at Eqs. (3.17), (3.18), we made use of the Markov approximation, which assumes that the time scales of all the terms that we keep are much slower than those of the environment. As we will see in Chapter 5, this is no longer the case when one tries to imprint chirps and non-trivial phase profiles in the wavepacket, and the Markov approximation in such cases will have to be amended.

3.2 Reverse engineering the dynamical equations

This section aims to propose a target wavepacket shape and reverse engineer the equations to obtain an analytical expression for $g(t)$. The starting point for this task is the Markovian equations derived in the previous section, Eqs. (3.17)-(3.19). The shape of the control $g(t)$ depends on the target wavepacket and also on the physical setup. In the following subsections, different physical scenarios will be studied, and for each of them, different wavepackets proposed.

3.2.1 Real valued controls, $g(t) \in \mathbb{R}$.

The easiest possible scenario is that in which $g(t)$ is a real-valued function of time, and therefore no tuning of the phase is necessary. Albeit its simplicity, many insights can be extracted from this example. Indeed, this first case will reveal an intrinsic physical limitation regarding the speed at which the photon can be emitted that will be present in one form or another throughout the whole thesis.

3.2.1.1 Qubit-cavity node.

Most experiments in this realm of superconducting quantum links place a transfer resonator between the qubit and the waveguide [ABP$^+$18, KMW$^+$18, MSK$^+$20], thus using qubit-cavity computational nodes. Furthermore, this scheme is necessary to achieve the effective time-dependent coupling $g(t)$ as described in Section 2.3.2 of the previous chapter. Because of this reason, this is the configuration that we will explore in more depth. However, other configurations are also feasible and deserve attention, the next subsection will treat the case of a node with an additional cavity; and, in Chapter 7 we will briefly discuss the situation of a qubit directly coupled to the waveguide.

Recall that the objective is to reverse engineer the equations of motion to obtain the $g(t)$ that produces the target wavepacket $\xi_{\text{out}}(t)$. Hence, the initial state of the field will be the vacuum, therefore $\psi_k(t_0) = 0 \implies \xi_{\text{in}}(t) = 0$. Furthermore, imposing that $g(t) \in \mathbb{R}$ and setting without loss of generality the Lamb shift equal to zero, the Eqs. (3.17), (3.18) for the qubit and the cavity become

$$\dot{q}(t) = -ig(t)c(t) \tag{3.20}$$

$$\dot{c}(t) = -ig(t)q(t) - \frac{\kappa}{2}c(t). \tag{3.21}$$

writing $\tilde{c}(t) = -ic(t)$, the parameters $q(t)$ and $\tilde{c}(t)$ are also real, and the outgoing photon, given by Eq. (3.19) is

$$\xi_{\text{out}}(t) = \sqrt{\kappa}\tilde{c}(t). \tag{3.22}$$

The probability that the excitation remains in the qubit or resonator is $\left[q^2(t) + \tilde{c}^2(t)\right]$, therefore the time evolution of this quantity becomes

$$\frac{d}{dt}\left[q^2(t) + \tilde{c}^2(t)\right] = -\kappa\tilde{c}^2(t). \tag{3.23}$$

This single equation can be solved formally from an initial arbitrary time t_0 as

$$q^2(t) = q^2(t_0) - \tilde{c}^2(t) - \kappa\int_{t_0}^{t} d\tau\ \tilde{c}^2(\tau) \tag{3.24}$$

$$= q^2(t_0) - \frac{1}{\kappa}\xi^2_{\text{out}}(t) - \int_{t_0}^{t} d\tau\ \xi^2_{\text{out}}(\tau), \tag{3.25}$$

where Eq. (3.22) relating the outgoing wavepacket with the cavity field was used in the second line.

This previous expression sets a constraint in the pulses that can be produced, since the left-hand side is a probability, it imposes that

$$0 \leq \frac{1}{\kappa}\xi^2_{\text{out}}(t) + \int_{t_0}^{t} d\tau\xi^2_{\text{out}}(\tau) \leq 1. \tag{3.26}$$

The expression given by Eq. (3.26) limits the slope of the photon envelopes, restricting the ones that can be created with this method to have an edge that raises at most as an

exponential. For this reason, photons with, for example, Gaussian envelopes cannot be produced. This limitation on how fast the wavepacket envelope can raise (or fall) will be present throughout the whole thesis and will determine, for example, in Chapter 5 how much distortion can be corrected.

Having $q^2(t)$, it is direct to obtain the pulse using the relation

$$g(t) = \frac{\sqrt{\kappa}\dot{q}(t)}{\xi(t)}, \tag{3.27}$$

where for simplicity we have dropped the label *out* from the output field. From now on, $\xi(t)$ will denote the output field, in other words, the target wavepacket.

The first example of a wavepacket we present is the hyperbolic secant wavepacket, which is widely used in the literature. [Mag21, Kur19, MSK+20, SSK+23]. This wavepacket is easy to handle analytically—it is only composed of exponential functions—and it permits the maximization of the bandwidth allowed by the cavity, its expression in frequency space is

$$|\xi\rangle = \int d\omega f(\omega) b_\omega^\dagger |\mathbf{0}\rangle, \quad \text{with} \quad f(\omega) = \sqrt{\frac{\pi}{2\tilde{\kappa}}}\,\mathrm{sech}\left(\frac{\pi(\omega-\omega_c)}{\tilde{\kappa}}\right). \tag{3.28}$$

This wavepacket is defined by the central frequency ω_c, which we will also refer to as *carrier frequency*, and its effective linewidth $\tilde{\kappa}$. This last quantity is bounded by the restriction (3.26), which imposes that it is always smaller than the cavity's decay rate $\tilde{\kappa} \leq \kappa$. When the equality holds, the wavepacket maximizes the allowed bandwidth, as stated before. The Fourier transform of the wavepacket given by Eq. (3.28) provides its shape in the time domain

$$\xi(t) = -\sqrt{\frac{\tilde{\kappa}}{4}}\,\mathrm{sech}\left(\frac{\tilde{\kappa}t}{2}\right), \tag{3.29}$$

ensuring that $\int_{-\infty}^{\infty} dt|\xi(t)|^2 = 1$. Applying the previous procedure with such a wavepacket shape, the resulting control is

$$g(t;\tilde{\kappa},\kappa) = \frac{\kappa - \tilde{\kappa}\tanh(\tilde{\kappa}t/2)}{2\sqrt{(1+e^{-\tilde{\kappa}t})\kappa/\tilde{\kappa}-1}}. \tag{3.30}$$

In particular, when $\tilde{\kappa} = \kappa$, that is, when the bandwidth of the photon saturates the limit imposed by Eq. (3.26), the control simplifies and also follows a hyperbolic secant

$$g(t;\kappa) = \frac{\kappa}{2}\mathrm{sech}(\kappa/2t). \tag{3.31}$$

This nice relation between a hyperbolic wavepacket and hyperbolic control $g(t)$ will be exploited many times in the subsequent chapters. The hyperbolic secant photon with maximum width and its associated control will be the benchmarks with which we will first test all the proposed protocols. Also, as it will become clear, different methods and purposes will require other shapes.

Another wavepacket shape that bears interest is a Lorentzian one, defined by

$$\xi(t) = \sqrt{\frac{\tilde{\kappa}}{\pi(1+\tilde{\kappa}^2t^2)}}, \tag{3.32}$$

which following the previous steps leads to a different protocol $g(t)$, which adopts the form

$$g(t) = \frac{\tilde{\kappa}(1+(\tilde{\kappa}t)^2)^{-3/2}(\kappa - 2\tilde{\kappa}^2t + \kappa\tilde{\kappa}^2t^2)}{\sqrt{2\tilde{\kappa}}\sqrt{\kappa\pi - 2\tilde{\kappa}(1+(\tilde{\kappa}t)^2)^{-1} - 2\kappa\,\arctan(\tilde{\kappa}t)}}. \tag{3.33}$$

3.2.1.2 Inclusion of a Purcell filter. Qubit-cavity-filter node.

The Purcell effect is the enhancement of the spontaneous emission rate of a quantum system by its environment. In particular, when a cavity is coupled dispersively to an emitter, as described by Eq. (2.28), a new channel for emission appears spoiling the coherence properties of the qubit. This mechanism is of critical relevance in superconducting circuits because the dispersive coupling is essential for measuring [BGB09], [JSM+14]. To mitigate this effect it is customary to include an auxiliary cavity that blocks the decay channel, what is called a Purcell filter (Chapter 4 discusses in quantitative terms how much the Purcell decay affects the concrete model proposed in this thesis). The inclusion of an extra cavity does have an impact, as the field emitted by the qubit will now have to traverse two resonators before being poured into the waveguide. In the following, we will study how the inclusion of this new element transforms the control $g(t)$. To the best of our knowledge, this has not been studied elsewhere, and it is relevant, because most superconducting circuit experiments use Purcell filters, and the modifications in the control shape, as we will see, are substantial.

To account for the extra cavity, the equations of motion of the effective model (3.19) have to be transformed. We add the new equation for the population in the filter, with coefficient $d(t)$, and the coupling between filter and cavity g_p. Analogously as before, the rotations in the complex plane, $q(t) = i\tilde{q}(t)$ and $d(t) = i\tilde{d}(t)$ make all the coefficients real-valued

$$\dot{\tilde{q}}(t) = -g(t)c(t), \tag{3.34}$$

$$\dot{c}(t) = g(t)\tilde{q}(t) + g_p\tilde{d}(t), \tag{3.35}$$

$$\dot{\tilde{d}}(t) = -g_p c(t) - \kappa/2\tilde{d}(t). \tag{3.36}$$

Analogously as before, the time evolution of the excitation's probability to remain in the qubit-cavity-filter system is

$$\frac{d}{dt}\left[\tilde{q}^2(t) + c^2(t) + \tilde{d}^2(t)\right] = -\kappa\tilde{d}^2(t). \tag{3.37}$$

The input-output relation gives $\xi(t) = \sqrt{\kappa}\tilde{d}(t)$, and the expression given by Eq. (3.24) transforms to

$$\tilde{q}^2(t) = \tilde{q}^2(t_0) - c^2(t) - \frac{\xi^2(t)}{\kappa} - \int_{t_0}^{t} d\tau\ \xi^2(\tau), \tag{3.38}$$

which again is a limitation to how steep can the photon envelope be.

Now solving for the field in the cavity

$$\dot{\tilde{d}}(t) = -g_p c(t) - \kappa/2\tilde{d}(t) \quad \Rightarrow \quad c(t) = -\frac{1}{g_p}\left(\frac{\dot{\xi}(t)}{\sqrt{\kappa}} + \frac{\sqrt{\kappa}}{2}\xi(t)\right) \tag{3.39}$$

and plugging it in the previous equation for the qubit, the equation for the control in this case becomes

$$g(t) = \frac{\sqrt{\kappa}\ \dot{\tilde{q}}(t)}{\xi(t)}.$$

For the sake of comparison, we will now aim at producing the same wavepacket as in the previous subsection, and see how the inclusion of the filter cavity changes the resulting $g(t)$. Such wavepacket is

$$\xi(t) = -\sqrt{\frac{\tilde{\kappa}}{4}}\ \mathrm{sech}\left(\frac{\tilde{\kappa}t}{2}\right) = -\sqrt{\frac{\kappa}{4\eta}}\mathrm{sech}\left(\frac{\kappa t}{2\eta}\right). \tag{3.40}$$

Where we introduced the parameter η which relates the photon effective bandwidth $\tilde{\kappa}$ with the decay rate of the cavity κ. The idea is that $\eta \geq 1$ such that by $\tilde{\kappa} = \kappa/\eta$ the effective bandwidth $\tilde{\kappa}$ is always smaller than κ. The first difference concerning the case without a filter is that because now both q and c appear in the equation for the modulus, we have a restriction for the values κ can take in terms of g_p. For the proposed wavepacket the field in the cavity is

$$c(t) = \frac{\kappa \mathrm{sech}(\kappa t/(2\eta))\left(\eta - \tanh(\kappa t/(2\eta))\right)}{4\eta^{3/2} g_p}, \tag{3.41}$$

and since $0 \leq c^2(t) \leq 1 \ \forall t$ we find

$$\kappa \leq \frac{16\sqrt{2}}{\sqrt{\frac{8+\eta\left(8\sqrt{8+\eta^2}+\eta\left(20+\eta\left(\sqrt{8+\eta^2}-\eta\right)\right)\right)}{\eta^3 g_p^2}}}. \tag{3.42}$$

Having the wavepacket $\xi(t)$, and the form of the field $c(t)$ we can easily obtain using Eq. (3.38) the field in the qubit $\tilde{q}^2(t)$. Again, this quantity must be bounded between 0 and 1, which results in the following condition for κ

$$\kappa \leq \frac{\sqrt{2}\eta \left(\frac{2+\sqrt{\eta(5\eta-4)^3}+\eta(11\eta-14)}{\eta-1}\right)^{1/2} g_p}{(1+\eta)^{3/2}}. \tag{3.43}$$

This physics is quite different from that observed in the scenario with just qubit and cavity. It essentially means that coupling two resonators comes with constraints when it comes to engineering a particular wavepacket. In particular, for the easiest case of $\eta \to 1$, the previous condition simplifies to

$$\kappa \leq 2g_p.$$

There are analytical expressions for the control $g(t)$ corresponding to the proposed hyperbolic secant photon, and also for a Lorentzian profile. We choose however to avoid writing them explicitly here since the expressions are intricate and not too informative.

Finally, Fig.3.1 illustrates the difference in the control functions, $g(t)$, required to generate the same wavepacket described by Eq.(3.40) in two different scenarios. In one, solid green line, the system is composed of one qubit, one Purcell filter, and one cavity, so it obeys Eqs. (3.44) and the parameters for κ, η and g_p are chosen such that the restrictions (3.41) and (3.42) are respected. The other control $g(t)$, dashed orange line, is the one obtained by considering the same wavepacket in a node with only one cavity and one qubit. The main difference is that in the case of the Purcell filter, the control remains open, which can be interpreted as an extra time that is needed so that the excitation can leave through both resonators. It is worth noting that, with another choice of parameters or of photon shape for the situation of only qubit and cavity, the obtained control could have also been left open. The converse however is not true, the control $g(t)$ with a Purcell filter must always remain open.

3.2.2 Complex valued controls, $g(t) \in \mathbb{C}$.

Allowing $g(t)$ to take complex values is essential for correcting distortion, see Chapter 5; for creating orthogonal spatial wavepacket modes, see Chapter 6; and for other potential applications, such as emitter-photon-receiver mismatches.

In order to find the pulse when $g(t) \in \mathbb{C}$, the Eqs. (3.20) have to be generalized to

$$\dot{q}(t) = g(t)\tilde{c}(t) \tag{3.44}$$

$$\dot{\tilde{c}}(t) = -g^*(t)q(t) - \kappa\tilde{c}(t)/2. \tag{3.45}$$

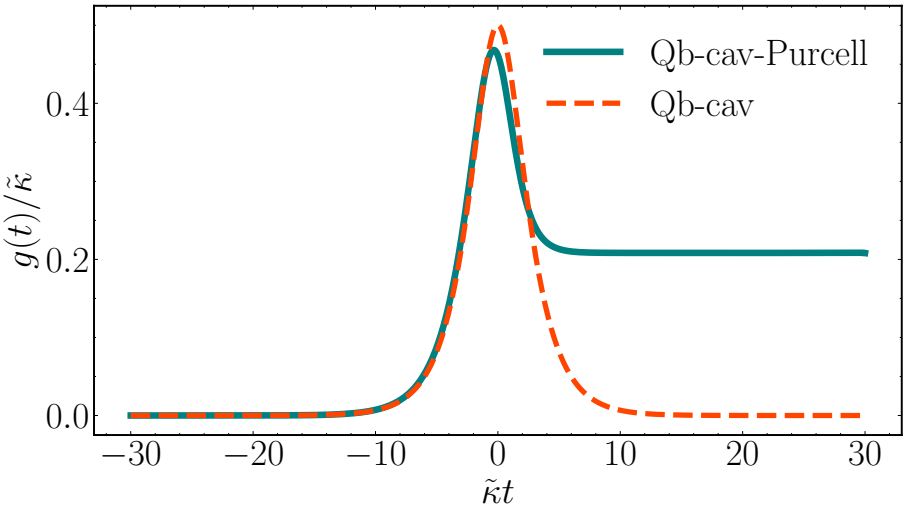

Figure 3.1: Difference between controls for creating the photon $\xi(t) = -\sqrt{\tilde{\kappa}/4}\,\mathrm{sech}(\tilde{\kappa}t/2)$ with $\tilde{\kappa} = 2\pi 19.23$ MHz. In the case with Purcell filters, the parameters are $\kappa_{\mathrm{cav}} = 2\pi 130$ MHz, $\eta = 6.76$, $g_p = 2\pi 25$ MHz. In the case with only one qubit and one cavity $\kappa_{\mathrm{cav}} = 2\pi 19.23$ MHz, $\eta = 1$.

The input-output relation for the field does not change $\xi(t) = \sqrt{\kappa}\tilde{c}(t)$. Now, the key difference between the current procedure compared with the previous subsections is that it is mandatory to keep track of the modulus and phase of all quantities at all times. This is the only way to engineer a control that now has two degrees of freedom instead of just one. For that, we make the following definitions for the fields in the cavity and the qubit

$$\tilde{c}(t) = e^{r(t)-i\theta(t)}, \tag{3.46}$$

$$q(t) = e^{x(t)-i\sigma(t)}, \tag{3.47}$$

from which it follows

$$\dot{q}(t) = (\dot{x}(t) - i\dot{\sigma}(t))q(t) = g(t)\tilde{c}(t) \tag{3.48}$$

$$\dot{\tilde{c}}(t) = (\dot{r}(t) - i\dot{\theta}(t))\tilde{c}(t) = -g^*(t)q(t) - \kappa\tilde{c}(t)/2. \tag{3.49}$$

Solving for $\tilde{c}(t)$ in the last equation,

$$\tilde{c}(t) = \frac{-g^*(t)q(t)}{\dot{r}(t) - i\dot{\theta}(t) + \kappa/2} \tag{3.50}$$

and plugging it into Eq. (3.48), one obtains

$$(\dot{x}(t) - i\dot{\sigma}(t)) = g(t)\tilde{c}(t)/q(t) = -\frac{|g(t)|^2}{\dot{r}(t) - i\dot{\theta}(t) + \kappa/2}. \tag{3.51}$$

This equation is important as it isolates the phase and the modulus of the qubit field. These quantities are not obvious to obtain because they can not be readily extracted from the equation for the modulus, as in the previous subsection. On the other hand, by the input-output relation, the phase and modulus of the cavity field, $r(t), \theta(t)$ respectively, are related to those of the proposed wavepacket. There is a way to proceed now by isolating the real and imaginary parts of Eq. (3.51)

$$\dot{x}(t) = -\frac{|g(t)|^2(\dot{r}(t) + \kappa/2)}{(\dot{r}(t) + \kappa/2)^2 + \dot{\theta}^2(t)}, \tag{3.52}$$

$$\dot{\sigma}(t) = \frac{|g(t)|^2\dot{\theta}(t)}{(\dot{r}(t) + \kappa/2)^2 + \dot{\theta}^2(t)}. \tag{3.53}$$

Making the quotient between these two equations, the qubit phase can be written as an ordinary differential equation which can be integrated

$$\dot{\sigma}(t) = -\frac{\dot{\theta}(t)\dot{x}(t)}{(\dot{r}(t) + \kappa/2)}. \tag{3.54}$$

And finally, once we solve for the phase $\sigma(t)$ we can compute the control similarly to all previous cases, that is, by dividing the qubit and cavity fields

$$g(t) = \frac{\dot{q}(t)}{\tilde{c}(t)} = \frac{(\dot{x}(t) - i\dot{\sigma}(t))e^{x(t)-i\sigma(t)}}{e^{r(t)-i\theta(t)}}. \tag{3.55}$$

The logic is the following. Given a target wavepacket $\xi(t)$, we can compute $r(t)$ and $\theta(t)$. Recall that $r(t) = \log|\tilde{c}(t)|$, while $\theta(t)$ is its phase. Having $|\xi(t)|^2$ (or what is the same,$r(t)$) we compute $|q(t)|$ from

$$|q(t)|^2 = |q(t_0)|^2 - \frac{|\xi(t)|^2}{\kappa} - \int_{t_0}^{t} d\tau |\xi(\tau)|^2. \tag{3.56}$$

This allows us to determine $x(t) = \log|q(t)|$. Then, we use Eq. (3.54) to compute $\sigma(t)$, so that we have all the ingredients to plug in Eq. (3.55) and find $g(t)$.

Keep in mind however that the equation for the qubit phase (3.54) has an intricate form and does not seem easy to solve analytically. While we can always find a numerical solution, it is desirable to not lose the intuition of how the phase of the qubit field, and ultimately of the control $g(t)$ depend on the target wavepacket. The next section is precisely devoted to that.

3.2.3 Explicit relation between wavepacket shape and control.

The expression derived at the end of the last subsection (Eq. (3.55)) already gives a recipe for obtaining a control $g(t) \in \mathbb{C}$, albeit a bit involved, as it is not straight forward to compute it. Both to gain intuition and to improve the computational toolbox, it would be convenient to have an explicit expression. Defining the control as $g(t) = |g(t)|e^{i\varphi(t)}$, the aim is to obtain closed expressions for the modulus and the phase solely in terms of wavepacket variables. We will break up Eq. (3.55) into equations for the phase and modulus and obtain from them simple analytical expressions.

The derivation of these formulas requires the separation of the wavepacket expression into amplitude and phase

$$\xi(t) = f(t)e^{-i\beta(t)}, \tag{3.57}$$

with $f(t), \beta(t) \in \mathbb{R}$, with the caveat that $f(t)$ may take negative values. Removing the sign dependence of $\xi(t)$ from $\beta(t)$ eases the calculations, as otherwise $\beta(t)$ may undergo discontinuous jumps whenever $\xi(t)$ changes sign. Next, defining $F(t) = \int_{t_0}^{t} d\tau |\xi(\tau)|^2 = \int_{t_0}^{t} d\tau f^2(\tau)$ allows rewriting Eq. (3.24) as

$$x(t) = \log|q(t)| = \frac{1}{2}\log\left[1 - \frac{1}{\kappa}f^2(t) - F(t)\right] \tag{3.58}$$

and thus, its derivative as

$$\dot{x}(t) = -\frac{\dot{f}(t)f(t) + \kappa/2\ f^2(t)}{\kappa(1 - F(t)) - f^2(t)}. \tag{3.59}$$

Now, this last expression gives $\dot{x}(t)$, whereas Eq. (3.54) provides the expression for the qubit field phase. Finally, this facilitates the modulus of the expression for the control (3.55)

$$|g(t)| = e^{x(t)-r(t)}[\dot{x}^2(t) + \dot{\sigma}^2(t)]^{1/2}. \tag{3.60}$$

Now, plugging in the expressions,

$$|g(t)| = \sqrt{\frac{(\dot{f}(t) + \kappa/2\ f(t))^2 + (\dot{\beta}(t)\ f(t))^2}{\kappa(1-F(t)) - f^2(t)}}, \tag{3.61}$$

which is the desired formula explicitly relating the control modulus with exclusively wavepacket variables, the envelope $f(t)$, and the phase $\beta(t)$.

The phase of the control $\varphi(t)$ is more problematic. Firstly, the phase of the rotated cavity filed $\theta(t)$ is not exactly $\beta(t)$ because of the choice that $f(t)$ changes sign. The input-output relation connecting the target wavepacket with the cavity field is, in this case,

$$f(t)e^{-i\beta(t)} = \sqrt{\kappa}\tilde{c}(t). \tag{3.62}$$

At this point, since $\tilde{c}(t) = e^{r(t)-i\theta(t)}$, we identify the phase in the resonator as $\theta(t) = \beta(t) + \phi_f$. Where ϕ_f accounts for the sign of $f(t)$, that is, $\xi(t) = |f(t)|e^{-i\beta - i\phi_f}$, where $\phi_f = \pi$ for $f(t) < 0$ and $\phi_f = 0$ for $f(t) > 0$.

Then, from $g(t) = i\dot{q}(t)/c(t)$ we have

$$\varphi(t) = \beta(t) + \phi_f + \text{atan}(\dot{\sigma}(t)/\dot{x}(t)) - \sigma(t). \tag{3.63}$$

There is no simple expression for $\sigma(t)$, but it can be left in an integral form. Expressing everything in terms of the proposed photon, the phase of the control becomes

$$\varphi(t) = \beta(t) + \phi_f + \text{atan}\left(\frac{\dot{\beta}(t)f^2(t)}{-(\dot{f}(t)f(t) + \kappa/2f^2(t))}\right) - \int_{t_0}^{t} d\tau \frac{\dot{\beta}(\tau)f^2(\tau)}{\kappa(1-f(\tau)) - f^2(\tau)}. \tag{3.64}$$

This last equation is still quite involved, but it is a closed relation between solely wavepacket variables $(\beta, f, \tilde{\kappa})$ and the phase of the control. Even though it might not look intuitive, having this kind of relation is important, when, for example, relating the modulus and phase of the microwave drive that induces the coupling discussed in Chapter 2. Being able to relate the physical magnitudes explored there, namely $\Omega_0(t)$ and $\varphi(t)$ in Eq. (2.27), with our $|g(t)|$ and $\varphi(t)$ given by Eqs. (3.61), and (3.64) respectively is very valuable. We believe that the fidelity of cutting-edge experiments such as [MSK$^+$20, SSK$^+$23] could be improved by explicitly making use of these relations.

3.3 Summary

In this chapter, we have established the framework of wavepacket engineering. We have explicitly shown how to obtain particular controls $g(t)$ from a target wavepacket under a variety of scenarios. In particular, the ability to make complex controls has many applications that will become clear later in the thesis. The fact that we can engineer the modulus and phase of the coupling according to Eqs. (3.61), (3.64) will be essential to correcting distortion in nonlinear waveguides, the main topic of Chapter 5. A complex control $g(t)$ will also be required to create orthogonal wavepackets and increase the computational space of the channel, as will be shown in Chapter 6. But before we jump into those applications, we will devote the following chapter to studying in depth the real-world limitations of this theory and the validity of all approximations we have made. We will do so by landing all these concepts in a specific implementation and doing careful simulations comparing the simplified model with the complete set of dynamical equations.

Design of a universal set of distributed gates 4

In this chapter, we develop a general framework for implementing distributed quantum gates. For this, we use the realistic setup introduced at the end of Chapter 2: a quantum network composed of bidirectional quantum links connecting distant nodes. Our proposal works both for inter- and intra-node communication and handles scenarios ranging from the few to the many modes limit of the quantum link. This includes intrasystem links like those in [CZB+20] and meter scale microwave networks such as [KMW+17] and [MSK+20]. We can design fast and reliable state transfer protocols in every regime of operation. Combined with a detailed understanding of the scattering process, this enables the engineering of two sets of deterministic universal distributed quantum gates. These gates can be implemented in quantum networks without requiring entanglement distribution or measurements.

The design of the gates builds upon two physical processes, photon-based state transfer and photon-cavity scattering. Both state transfer and photon scattering are foundational elements of a deterministic distributed quantum toolbox. The idea is to use these two primitives to design a universal family of distributed quantum gates. The propagating photon state transfer follows the seminal work by Cirac et al. [CZKM96], whereas the scattering gate is inspired by [DK04].

The core of the analysis develops analytically and numerically demonstrates the implementation of the gates in a scenario with realistic waveguides. We consider the real-world limitations that hinder the fidelity of both state transfer and photon cavity scattering. The case of state transfer by means of wavepacket shaping is studied in particular detail, paying attention to how each source of error affects it and comparing it with other methods in a variety of scenarios. We find that wavepacket shaping outperforms adiabatic-like protocols [VVN+17, CZB+20, LLC+19] and direct-SWAP-like ones [SMB06] for any waveguide length once one accounts for the imperfections.

The realization that wavepacket shaping works so well for both long and short waveguides is somewhat surprising, and it stems from the fact that input-output theory describes accurately the physics of these systems in those two regimes. In previous works, it was assumed that wavepacket shaping would only work in the long waveguide limit, in which the mode structure resembles the continuum [CZKM96, VVN+17]. By extending the regime of applicability of input-output theory, we could use the techniques of wavepacket shaping developed in Chapter 3 for any waveguide length and therefore design very general families of distributed quantum gates. With this knowledge, we are able to identify optimal points of operation both for the state-transfer and scattering gates with resulting infidelities of $1 - F \approx 10^{-2} - 10^{-3}$.

The chapter is organized as follows. In Section 4.1 we define and explore the two different physical mechanisms that will be the foundations of the distributed gates, photon-based quantum state transfer (Subsection 4.1.1), and photon-cavity scattering (Subsec-

tion 4.1.2). After that, in Section 4.2 we benchmark these primitives and assess their feasibility. First, by studying with semi-analytical tools the main sources of imperfections (Subsection 4.2.1), and after that, by carrying out detailed simulations and comparisons with other state-of-the-art strategies of both quantum state transfer (Section 4.2.2) and photon phase scattering (Section 4.2.3). Finally, Section 4.3 uses the knowledge gained in the previous sections to build two families of distributed quantum gates, one based solely on quantum state transfer (cf. Subsection 4.3.1) and the other on wavepacket shaping plus photon scattering (cf. Subsection 4.3.2).

4.1 Primitive operations for distributed quantum gates

Quantum state transfer via wavepacket shaping [CZKM96] and collisional photon phase-imprinting [DK04] are the building blocks for the distributed gates that we will propose towards the end of the chapter. In this section, we will present both of them in an ideal scenario without considering losses.

4.1.1 Quantum state transfer via wavepacket shaping

In chapter 3 we presented the idea of engineering a control related to a one-to-one correspondence with a wavepacket shape. It was pointed out that this correspondence meant that the photon could either be emitted or absorbed, depending on the initial state of the field and the emitter. It turns out that this wavepacket shaping technique based on input-output theory can be used to implement deterministic quantum state transfer in the way this was designed by Cirac and collaborators in Ref. [CZKM96].

Deterministic quantum state transfer as put forward in the mentioned seminal work describes the process whereby quantum information is physically moved between distant qubits, as described by the operation:

$$(\alpha\,|0\rangle_1 + \beta\,|1\rangle_1) \otimes |0\rangle_2 \xrightarrow{\mathcal{T}} |0\rangle_1 \otimes (\alpha\,|0\rangle_2 + \beta\,|1\rangle_2). \tag{4.1}$$

This notion of state transfer, elaborated upon in Ref. [CEHM99] and first empirically validated in [RNH$^+$12], is based on the exchange of a single photon. The central idea put forward in [CZKM96] is that one can ensure a zero reflection of the emitted photon by imposing it to be time-symmetrical and applying at the second node the time reversal of the emission control. Within this framework, an excitation $|1\rangle_1$ from qubit Q1 is converted to a photon by wavepacket shaping. Then, this photon is captured by cavity R2 and qubit Q2. To achieve this photon emission and absorption, the temporal modulation of the couplings $g_1(t)$ and $g_2(t)$ is essential, ensuring that $g_2(t) = g_1(-t + t_d)$, where t_d is some delay time to be adjusted depending on the situation. The condition that the wavepacket is time symmetrical has been relaxed in further works [VVN$^+$17] and we now know that it suffices $g_2(t) \equiv g_{\text{absorption}}(t)$ is related to the incoming wavepacket, independently of the emission control.

On top of the symmetric condition, it has long been assumed that quantum state transfer through wavepacket shaping would only work in the continuum limit, where the mode structure of the propagating channel resembles that of free space. This assumption aligns with the established limits of input-output theory. Recall that the entire model for designing the control $g(t)$, developed in Section 3.2, is based on this theory, which inherently works in a continuous framework. We will, however, apply the same techniques to situations in which very few modes participate and show that wavepacket shaping still works very well in these regimes. This result is important since it implies that wavepacket shaping can be applied in almost any regime. Furthermore, we will show in Subsection 4.2.2.1

that this technique outperforms other protocols in the very few mode regimes in which it was suspected to fail.

But before jumping to the scattering process and the comparison between protocols, we will devote the following subsection to particularizing the time-dependent controls $g_j(t)$ that we will use for emission and absorption throughout the chapter. This is important because there are infinitely many wavepackets that can be created, with different shapes and durations.

For the sake of simplicity, we will use in this chapter a limited set of real and time reverse symmetric controls. This allows us to focus on the design of gates, the experimental limitations, and the realistic modelization of waveguides and circuit components, without loss of generality. We will thus follow the derivation of Section 3.2.1.1 in Chapter 3. The treatment of the dynamics will be fully Markovian, following Eqs. (3.20). The aim is to create the already presented, commonly used [Mag21, VVN+17], sech profile photon

$$|\xi\rangle = \int d\omega f(\omega) b_\omega^\dagger |\mathbf{0}\rangle\,, \quad \text{with} \quad f(\omega) = \sqrt{\pi/(2\tilde{\kappa})}\text{sech}(\pi(\omega-\omega_c)/\tilde{\kappa}). \tag{4.2}$$

As explained in Chapter 3, the photon bandwidth $\tilde{\kappa}$ must be smaller than or equal to the decay rate of the cavity that produces it, $\tilde{\kappa} \leq \kappa_1$. When equality holds, the hyperbolic secant photon maximizes the frequency bandwidth provided by the cavity. The temporal width of this family of photons is $\sigma_t = \pi/(\sqrt{3}\tilde{\kappa})$, which is obtained by computing the Fourier transform of Eq. (4.2). They are generated by the qubit-resonator coupling (cf. Section 3.2.1.1)

$$g(t;\tilde{\kappa},\kappa) = \frac{\kappa - \tilde{\kappa}\tanh(\tilde{\kappa}t/2)}{2\sqrt{(1+e^{-\tilde{\kappa}t})\kappa/\tilde{\kappa}-1}}. \tag{4.3}$$

In an optimal scenario, the interaction ensures that the photon is completely captured by the second resonator, R2. If we use as the emitting control $g_1(t) = g(t+t_d/2;\tilde{\kappa},\kappa_1)$, this occurs when the coupling condition $g_2(t) = g(-t+t_d/2;\tilde{\kappa},\kappa_2)$ is met and $\tilde{\kappa} \leq \kappa_2$ holds true. To achieve the fastest implementation of the protocol, the maximum qubit-resonator coupling value is determined to be $\max_t\{g_{1,2}(t)\} = \kappa_{1,2}/2$.

The delay between controls t_d is adjusted to correspond with the propagation time of the photon in the waveguide, that is, $t_d = t_p \equiv L/v_g$. However, this quantity may change when other mechanisms, such as photon scattering, are present. The protocol unfolds over a duration $t \in [-T, T]$, chosen to avoid significant cut-offs of the sech-pulse control. In this context, the initial and final values of the coupling, $g_1(-T)/\tilde{\kappa}$ and $g_2(T)/\tilde{\kappa}$, are constrained to less than 10^{-5}. To accomplish this, the total time of the protocol, $2T$, is calibrated based on the inherent temporal scale of the system, according to the formula $2T = t_p + 10/\tilde{\kappa}$. Further discussions will demonstrate that such small coupling values at the outset are not a prerequisite for achieving high fidelities.

It is worth noting that this control can handle asymmetric networks where $\kappa_2 \neq \kappa_1$ without any problem. Also, it enables the creation of photons with reduced bandwidth, characterized by a factor $\eta = \kappa_1/\tilde{\kappa} \geq 1$, enhancing their robustness against imperfections. However, producing such narrow-bandwidth photons requires a longer protocol duration by a factor of η, presenting a balance between reducing distortions and mitigating decoherence. The interplay between these different kinds of imperfections will be treated in detail in Subsection 4.2.1, where we will also provide analytical estimates.

4.1.2 Photon phase via scattering

Besides the already presented quantum state transfer, another key element for building photonic networks is the collisional scattering operation introduced by Duan and

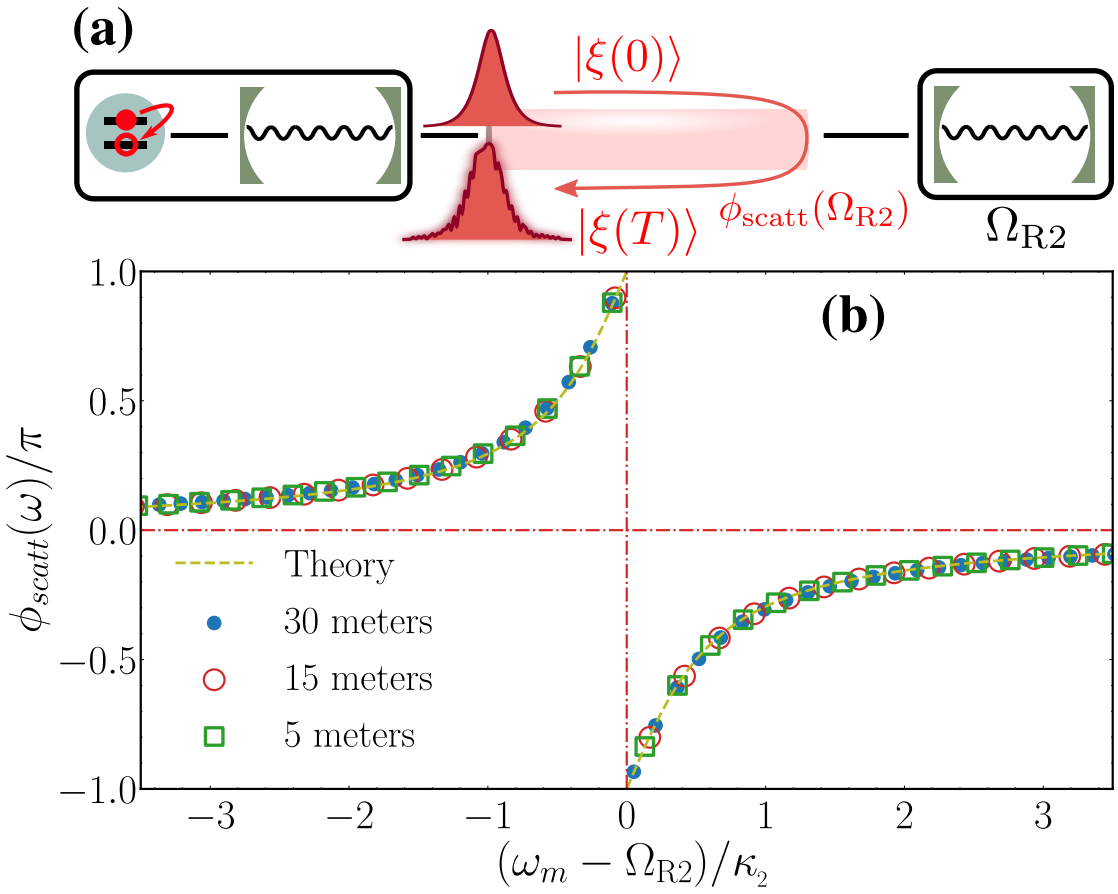

Figure 4.1: (a) Schematic illustration of a photon scattering process, where the photon interacts with R2, which results in a phase $\phi_{scatt}(\Omega_{\text{R2}})$ imprinted on the photon. (b) Phase gained by each mode of frequency ω_m of the QL after a scattering process with R2 with frequency Ω_{R2} and decay rate κ_2. The phase for each of the discrete modes (points) of a QL with $L = 30$, 15 and 5 meters with $\kappa_2/2\pi = 20$, 25 and 80 MHz, respectively, closely follows the theoretical expression (4.4) for any L and κ_2. Note that the spacing between the points is given by the free spectral range of the QL.

Kimble [DK04]. In this proposal, the photon acquires a controlled phase by a tailored photon-cavity interaction. This approach involves a traveling photon being reflected off a cavity, with the frequency of the cavity varying based on the state of a qubit coupled off-resonantly. Recall the dispersive limit Hamiltonian from Section 2.3.3. The phase of the reflected photon, which will be dependent upon the state of the qubit, is instrumental in executing various protocols. In particular, it will be central in our proposal of a distributed controlled phase gate detailed in Subsection 4.3.2.

We depict, in Fig. 4.1a, the configuration for observing the scattering phase. In this setup, a single photon generated by qubit Q1 at the first node travels and interacts with the second cavity, R2. The photon enters and exits R2 with its shape intact, undergoing only a phase shift. Initially, this study explores this phase shift for very long wavepackets or quasi-monochromatic photons. The focus is on how the phase shift varies with the detuning between the photon and the cavity.

According to the standard input-output formalism outlined in [GZ15], the output field scattered by a resonator R2 with frequency Ω_{R2} undergoes a linear transformation $b_{\text{out}} = e^{i\phi_{\text{scatt}}(\omega)} b_{\text{in}}$, which maintains the mode population while imprinting a frequency-

dependent phase shift, given by

$$e^{i\phi_{\text{scatt}}(\omega)} = \frac{i(\omega - \Omega_{\text{R2}}) + \kappa_2/2}{i(\omega - \Omega_{\text{R2}}) - \kappa_2/2}. \tag{4.4}$$

In this expression, ω represents the frequency of the incident photon, κ_2 is the decay rate of R2, and the equation is applicable in the context of an infinitely long waveguide.

Numerical verification confirms the applicability of the relation (4.4) for each discrete mode ω_m of the quantum link. By generating monochromatic photons of the form $b_\omega^\dagger |\mathbf{0}\rangle$ and disconnecting the Q1-R1 coupling, it was observed that after a sufficiently long interaction period $T > t_p$, these photons returned to their original mode, exhibiting a phase shift $e^{i\phi_{\text{tot}}} b_\omega^\dagger |\mathbf{0}\rangle$. This observed phase, $\phi_{\text{tot}} = -\omega t + \phi_{\text{scatt}}(\omega)$, conveys both the free evolution of the mode, proportional to ωt, and the scattering component as described in Eq. (4.4).

In Fig. 4.6b, we present the scattering phase that each mode undergoes in waveguides ranging from $L = 5$m to 30m after removing the free evolution component ωt. Remarkably, the observed phase closely aligns with the theoretical prediction of Eq. (4.4), showing a high degree of accuracy across different waveguide lengths L and regardless of the second resonator's decay rate κ_2. This outcome indicates the reliability of input-output theory even in scenarios where its applicability might initially be questioned, similar to the findings in the quantum state transfer numerical experiments that will be presented in Subsection 4.2.2.

4.2 Benchmarking the primitives

We want to study how the previously proposed primitives, i.e., quantum state transfer and photon scattering, behave when considering real-world imperfections. For that, we will first, in Subsection 4.2.1, explore the main sources of imperfections affecting superconducting networks and propose heuristic explanations and semi-analytical scalings. Secondly, in Subsections 4.2.2 and 4.2.3, we will benchmark through careful simulations of state transfer via wavepacket shaping, and phase scattering imprinting respectively.

4.2.1 Experimental limitations and imperfections

Our idea is to design protocols that can be implemented in the near term, in particular, employing a superconducting platform. For this objective, it is important to assess the main sources of error and the way each of them would affect the fidelity of the primitives that we presented.

In the following, we enumerate the most pressing physical mechanisms that affect distributed superconducting architectures, stating in each case its magnitude and, when possible, ideas to mitigate them. We pay special attention to the process of propagation by distortion, as Chapter 5 will be mostly devoted to correcting this effect.

4.2.1.1 Lamb shifts

The Lamb shift is an energy shift that was first measured by Willis Lamb in the context of atomic physics [LR47]. It refers to the fact that the natural or *bare* frequency of an electromagnetically interacting object changes due to the coupling of this object with its environment. In the particular case of the setup presented in Chapter 3, the natural frequency of the resonator gets modified due to its interaction with the collection of waveguide modes, which play a role analogous to the environment. Although this is not critical for experimental implementation, since in the laboratory one always measures the already modified *dressed* frequency, it is important for calibration tasks and accurate simulations.

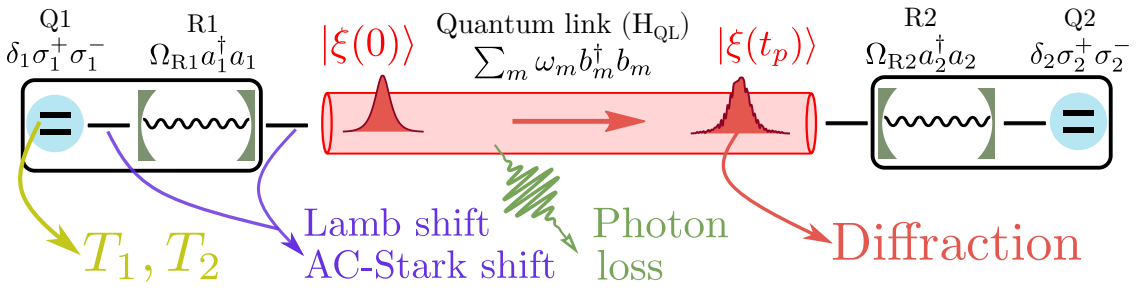

Figure 4.2: Setup proposed in Chapter 2 and strongly inspired by the experiment [MSK+20], in which we will analyze the sources of losses. The decoherence and dephasing times of the qubits are, respectively T_1, T_2. The Lamb shift affects the resonator frequencies, $\Omega_{R1,R2}$ since these are the objects in contact with the collection of waveguide modes ω_m. The dynamical coupling between the qubit and the resonator causes AC-Stark shifts that alter the frequencies $\delta_{1,2}$. Diffraction alters the shape of the wavepacket as it traverses the quantum link, this mechanism also applies in the situation of scattering, although not depicted here (cf. Fig. 4.1a). Finally, in any of the resonators, quantum link, or matching elements the photon may escape, a process modeled as photon loss.

There are two contributions to the Lamb shift in this context [DCPGR15], (i) the unequal coupling between the cavity and the different waveguide modes $G_{m,j} \propto \sqrt{\omega_m}$, and (ii) the curvature in the dispersion relation (refer to Section 2.4). This interaction alters the frequency of the resonator by a factor that λ_j, changing its bare frequency to the value $\Omega_{R_j}^D = \Omega_{R_j} + \lambda_j$. This last frequency is the dressed one we referred to in the previous paragraph as the one measured in the experiments, and to which the frequency of the qubit has to be adjusted. However, we can not do that *a priori* in the simulation, and instead, have to run a calibration procedure. This consists of starting with an excited qubit $q_1(-T) = 1$ and running a depletion simulation that transfers that excitation to the resonator and finally to the waveguide. In this simulation, we choose the Lamb shift λ_j to be a parameter and optimize over it aiming at maximum depletion.

Besides its relevance for accurate simulations, it is important to check from a theory standpoint that the Lamb shift does not present divergences in the regime under study. It is well known that the calculation of this quantity explodes to infinity in a variety of situations. Bear in mind that the mathematical expression given by Eq. (3.10) can diverge depending on the form of $J^{QO}(\omega)$ and therefore of the mode structure of the waveguide and the couplings G_k. The convergence of the model under study in this thesis was verified semi-analytically in [DCPGR15] and [GPRB+17], and is confirmed numerically in the present chapter. Also, pursuing this question gave rise to a Master thesis within our group, in which the convergence of Eq. (3.10) was studied in great detail.

Finally, the value of the Lamb shift might vary in time if the coupling $g(t)$ also does so. We will not pay attention to that fact in this chapter since all the controls are real and therefore do not have rapid phase changes. In the next chapter, however, we will explore complex controls $g(t) \in \mathbb{C}$ and, in that context, the dynamical nature of the Lamb shift and the effective decay rate will prove important. A detailed analysis of these mechanisms is provided in Section 5.2 of Chapter 5.

4.2.1.2 Distortion by propagation

The typical microwave photons produced by superconducting qubits have wide bandwidths, in the range of tens of MHz [KKT+18, MSK+20, SSK+23]. This presents advantages and disadvantages. On the one hand, large bandwidths mean fast emission times

and therefore fast protocols, on the other, these kinds of wavepackets are more prone to distortion. The wider the photon is in frequency space, the more sensitive it becomes to effects such as the non-linearity of the dispersion relation.

The distortion by propagation is important because it causes the photon to lose its original shape. At the core of state transfer via wavepacket shaping lies the idea of absorbing a photon with a control tailored for a particular shape. Therefore, if the arriving wavepacket is different from the supposed one, the absorption efficiency at the second node lowers. We evaluate this distortion through the overlap fidelity $|z|^2 = |\langle\tilde{\xi}(t_p)|\xi(t_p)\rangle|^2$. This overlap compares the ideal photon $|\xi(t_p)\rangle$, having traversed the waveguide for a duration t_p, against the distorted photon $|\tilde{\xi}(t_p)\rangle$, which would have followed a similar path in a waveguide with a non-linear dispersion relation. Mathematically we can define the evolution under a linear dispersion relation as $U(t)$ and under the realistic one as $\tilde{U}(t)$ and write

$$|\xi(t)\rangle = U(t)\,|\xi(0)\rangle\,, \tag{4.5}$$

$$|\tilde{\xi}(t)\rangle = \tilde{U}(t)\,|\xi(0)\rangle\,. \tag{4.6}$$

In the system under consideration, the realistic dispersion relation will be

$$\omega_m = c\sqrt{(\pi/l_1)^2 + (m\pi/L)^2}, \tag{4.7}$$

cf. Eq. (2.33) from Chapter 2.

For the scenario involving propagation, expanding the dispersion relation around the central frequency ω_c up to the second order yields

$$\omega(k) \approx v_g k + \frac{(\omega-\omega_c)^2}{2v_g^2} D, \tag{4.8}$$

where $v_g = \mathrm{d}\omega(k)/\mathrm{d}k|_{k_c}$ and $D = \mathrm{d}^2\omega(k)/\mathrm{d}k^2|_{k_c}$ denote the group velocity and curvature of the dispersion relation respectively at the central wave vector k_c. Using this approximation, we can compute $|z|^2$ up to second order in $\omega(k)$. The expression for this quantity after a one-way trip, that is, after an evolution time equal to the propagation time of the waveguide t_p is

$$|z|^2 = \left|\int d\omega |f(\omega)|^2 e^{-it_p(\omega-\omega_c)^2 D/(2v_g^2)}\right|^2 \approx 1 - \frac{L^2 D^2 \kappa^4}{180 v_g^6 \eta^4}. \tag{4.9}$$

As a reference, for the standard WR90 waveguide, utilized in [MSK+20, SSK+23], the curvature is of the order of $D \approx 10^6 \mathrm{m}^2/\mathrm{s}$. The expression given by Eq. (4.9) quantifies the distortion of the photon and the diminished state transfer probability. Notably, the relationship $1 - |z|^2 \propto \kappa^4/\eta^4$ suggests that photons with narrower bandwidths are less affected by the waveguide's dispersion curvature. A similar approach will be followed in Section 4.2.3 when quantifying the distortion due to limited bandwidth scattering.

4.2.1.3 Stark shifts

Depending on the strength and the speed of the change of the dynamical coupling $g(t)$, frequency modulations of the AC-Stark type occur. In practice, this effect is only relevant in the few modes limit, when the qubit-cavity system is mainly interacting with the closest frequency mode. In this regime, small shifts can alter the depletion efficiency of our protocol. We now present an analytical but heuristic derivation for estimating this effect.

We are focusing for this analysis on the setup pictured in Fig. 4.2, that is, qubit resonator nodes linked by a WR90 waveguide. Investigating the dressed states of the full

bosonic part, the R1-QL-R2 configuration, gives valuable insight into the long photon limit, that is, when the photon does not fit in the waveguide. This situation corresponds to the sech-like photon used in this chapter with $\tilde{\kappa}L < 2\pi v_g/\sqrt{3}$.

Diagonalizing the Hamiltonian yields

$$\Lambda^\dagger H_{\mathrm{R1-QL-R2}}\Lambda = \sum_n \tilde{\omega}_n c_n^\dagger c_n, \tag{4.10}$$

where c_n represents the annihilation operator of the dressed modes of the R1-QL-R2 ensemble. The central mode $\tilde{\omega}_0$ and its nearest counterparts, $\tilde{\omega}_{\pm 1}$ are of particular interest. These three mixed modes are close to the resonant condition $\tilde{\omega}_0, \tilde{\omega}_{\pm 1} \approx \delta_{1,2}$, and possess the largest resonator content.

In an ideal waveguide with a linear dispersion relation and constant coupling ($G_{m,j} \equiv G$), it is known that $\tilde{\omega}_0^{\mathrm{id}}$ coincides with the frequency of both resonators $\Omega_{\mathrm{R1,R2}}$. The frequencies of the adjacent modes, $\tilde{\omega}_{\pm 1}^{\mathrm{id}}$, separate from $\tilde{\omega}_0^{\mathrm{id}}$ by $\pm\sqrt{2}G$. The small frequency separation between the two adjacent states makes them relevant for the dynamics [VVN+17]. A realistic dispersion relation modifies these expressions by an amount of the order of the Lamb shift found numerically while inducing an asymmetry in the resonator content of the dressed modes. Meaning that $\tilde{\omega}_{+1}$ and $\tilde{\omega}_{-1}$ are not at the same distance from $\tilde{\omega}_0$ anymore.

Including now the qubits, we can write the Hamiltonian of the full system in the diagonal bosonic dressed states basis as

$$H = \sum_n \tilde{\omega}_n c_n^\dagger c_n + \sum_{j=1,2} \delta_j \sigma_j^+ \sigma_j^- + g_j(t)\sigma_j^+ \left(\sum_n \beta_n^j c_n\right) + \mathrm{H.c.},$$

where the $a_j^\dagger$ have been transformed to the dressed mode representation through the unitary matrix Λ, which acts as $a_j^\dagger \to \sum_n \beta_n^j c_n$. Adopting the Wigner-Weisskopf ansatz $|\psi(t)\rangle = [\sum_{i=1,2} \sigma_i^+ q_i(t) + \sum_n c_n^\dagger d_n(t)]\,|\mathbf{0}\rangle$, shows that the sum of probabilities $|q_1(t)|^2 + |q_2(t)|^2 + |d_0(t)|^2 \approx 1$ in the long photon limit. This means that during the whole protocol, the excitation is either in one of the qubits or in the central resonant mode. Yet, there is still a small contribution given by the two adjacent dressed modes $\tilde{\omega}_{\pm 1}$ so that the single-mode approximation is not completely valid. As an example, for $L = 5$, $\kappa = 2\pi \times 1$ MHz we find $\max_t \left(|d_{-1}(t)|^2 + |d_{+1}(t)|^2\right) \approx 0.02$. The rest of the modes barely participate in the dynamics (populations smaller than 10^{-10}), this behavior was already observed in [VVN+17]. To the contrary, and as expected, in the short-photon limit, many dressed modes participate.

In the long photon limit, where only three or fewer modes participate, the dynamics are slow enough that adiabatic elimination is justified. The equation of motion for each dressed mode coefficient m is

$$\dot{d}_m(t) = -i\tilde{\omega}_m d_m(t) - ig_1(t)\beta_m^1 q_1(t) - ig_2(t)\beta_m^2 q_2(t), \tag{4.11}$$

whereby imposing $\dot{d}_m(t) = 0$ (adiabatic condition), one arrives to

$$d_m(t) = -\frac{g_1(t)\beta_m^1 q_1(t) + g_2(t)\beta_m^2 q_2(t)}{\tilde{\omega}_m}. \tag{4.12}$$

Substituting now in the equation for the coefficient of the qubit 1 we obtain

$$\dot{q}_1(t) = -i\delta_1 q_1(t) - ig_1(t)\sum_{n\neq m} \beta_n^1 d_n(t) + i\frac{g_1(t)g_2(t)}{\tilde{\omega}_m}\beta_m^1\beta_m^2 q_2(t) + i\frac{g_1^2(t)|\beta_m^1|^2}{\tilde{\omega}_m} q_1(t). \tag{4.13}$$

That is, for all the adiabatically eliminated modes we find a time-dependent Stark shift to the qubits' frequencies that amounts to

$$\tilde{\delta}_j(t) = \delta_i - \sum_m \frac{g_i^2(t)|\beta_m^i|^2}{\tilde{\omega}_m}, \tag{4.14}$$

and a flip-flop term between qubits that goes as $g_1(t)g_2(t)\beta_m^1\beta_m^2/\tilde{\omega}_m$.

On the other hand, a small frequency mismatch $(\delta_i - \tilde{\delta}_i)$ in a coherent and resonant transfer of excitations leads to a residual population $F_{st} \approx 1 - \frac{(\delta_i - \tilde{\delta}_i)^2}{4g^2}$, in a situation in which $|(\delta_i - \tilde{\delta}_i)/g| \ll 1$, where g is the coupling between emitter and receptor.

In the long photon limit, we can approximate $\sum_m |\beta_m^i|^2/\tilde{\omega}_m \approx 1/\tilde{\omega}_0$ and $g_1(t) \approx \tilde{\kappa}$. Doing so, the detuning given by Eq. (4.14) becomes $|\tilde{\delta}_i(t) - \delta_i| = \tilde{\kappa}^2/\tilde{\omega_0}$. It is worth stressing that, unlike the propagation by distortion, this estimation does not depend on the length of the waveguide or diffraction properties, and in addition, it scales as $\tilde{\kappa}^2 = \kappa^2/\eta^2$ rather than κ^4/η^4 as the diffraction limit.

4.2.1.4 Relaxation, dephasing and photon loss

All the errors considered in the previous subsections are of the coherent type, that is, all of them preserve the number of excitations and involve an exchange of information only within the initially chosen subspace. There is, however, a different family of errors, those in which the excitation is lost or, more generally, in which the information is exchanged with an environment. These errors are called incoherent and are more difficult to deal with since retrieving the information is effectively impossible.

One obvious approach is to try to make better qubits and components at the hardware level, such that their rate of losses to the environment is minimal. A lot of effort is being currently put into this, and proposing novel types of qubits and coupling schemes is an active field of research. On the other hand, a more quantum information theoretical approach consists of codifying the information in logical qubits composed of many physical ones using error correction techniques [Sho95, Ter15].

Besides the errors in the qubit, there is also the possibility that the photon escapes once in the resonators, in the waveguide, or in any of the matching elements. We refer to all these scenarios as photon loss, depicted with the green photon flying away in Fig. 4.2. Although this is an important source of error in the systems under study we choose to not focus on it, since, as far as we know, there are no theoretical tools that can improve it and it remains mainly an engineering challenge. Also, any time this kind of error occurs it results in a random catastrophic loss, which yields zero fidelity for that specific realization. This means that a fair way to take it into account would be to multiply the final fidelity by an error probability, which does not have to be taken into account beforehand.

Contrary to photon loss in other parts of the experiment, we do take into account qubit decay, first, because making better qubits is a separate problem in which theoretical advancements may play a role, and second, because different protocols populate the qubits very differently. This means that one way in which one protocol may outperform the other is by how much time they leave the excitation within the qubit. This will become evident in Section 4.2.2.1, and also in Chapter 7 in the context of different protocols for entanglement distribution.

To assess this effect, the duration τ for which the qubits remain populated is calculated as follows:

$$\tau = \int_{-T}^{T} dt \left(|q_1(t)|^2 + |q_2(t)|^2 \right),$$

where the integration spans the entire protocol duration. The time T_1 sets a characteristic timescale in which the excitation is lost. Averaging over many realizations, mathematically, the fidelity diminishes by a factor $e^{-\tau/T_1}$.

Finally, we model qubit dephasing as a random uncertainty in each of the qubit frequencies obeying a Gaussian distribution. For a single realization, the frequency of the ith qubit is shifted according to $\delta_i \to \delta_i + \delta\omega_i$ with

$$p(\delta\omega) = \frac{1}{\sqrt{2\pi}\sigma} e^{-\delta\omega^2/(2\sigma^2)}. \tag{4.15}$$

The dephasing time T_2 is related to the standard deviation of the Gaussian distribution as $\sigma = \sqrt{2}/T_2$. Assuming an equal T_2 for all the qubits, this results in an independent and identically distributed fluctuation $\delta\omega_i$ for all qubits in the network.

4.2.2 Benchmarking state transfer via wavepacket shaping

Let us now discuss a realistic numerical study of state transfer in a scenario that contemplates most of the imperfections discussed before. The study is based on a Wigner-Weisskopf model such as the one described by Eq. (3.1), with which we will explore the limits of transferring one excitation from qubit 1 to qubit 2 located at the opposite node.

In this study, a simulation of the state transfer protocol $\mathcal{T}$ was executed, implementing numerically the evolution with the Hamiltonian (2.35). A very important parameter to consider in these simulations is the number of waveguide modes, however, it does not make sense to fix it for all lengths since this would imply very different frequency windows. Instead, what we do is fix an operation band of 4 GHz, that is, much bigger than the wavepacket width $\tilde{\kappa} \sim$ MHz and adapt the number of modes to this requirement. In the case of a 30 m waveguide, the free spectral range is of ~ 3 MHz so we will consider 2000 modes, in the case of $l = 5$ m, the free spectral range increases to ~ 20 MHz, and therefore, 500 modes suffice.

The simulation starts with the initial condition $q_1(-T) = 1$. Hence, the quantum state transfer efficiency can be quantified as $|q_2(T)|^2$, the population of the second qubit at the end of the protocol. Displayed in Fig. 4.3b, the transfer efficiency is plotted as a function of the cavity bandwidth, $\kappa = \kappa_{1,2}$, across various waveguide lengths ($L = 1, 5$, and 30 m). The simulation uses photons at maximum bandwidth, $\tilde{\kappa} = \kappa$. For the 30 m scenario, it also extends to photons with reduced bandwidth, $\tilde{\kappa} = \kappa/4$ (equivalent to $\eta = 4$), to explore the effect of narrowed photons on transfer efficiency.

There are two different tendencies in Fig. 4.3b which correspond to the two different regimes of operation, the *short photon limit* and the *long photon limit*. In the *short photon limit*, when $\kappa/\eta \gtrsim 2\pi v_g/(\sqrt{3}L)$, the photon fits entirely within the quantum link. In this regime the state transfer fidelity is primarily limited by waveguide diffraction, approximated as $|q_2(T)|^2 \approx |z|^2 \sim \kappa^4/\eta^4$, cf. Eq. (4.9). Producing narrower photons ($\tilde{\kappa} < \kappa$, $\eta > 1$) significantly increases the fidelity by a factor of η^{-4} (cf. Fig. 4.3b) while slowing down the transfer process, increasing its duration proportionally by a factor of η.

Conversely, in the *long photon limit*, $\kappa/\eta \lesssim 2\pi v_g/(\sqrt{3}L)$, and the wavepacket does not fit within the waveguide. Under these circumstances, the input-output theory that justifies the control mechanism detailed in Eq. (4.3) is not expected to apply. This is because, in this limit, the photon in frequency space is narrower than the free spectral range, that is, it can resolve the discrete nature of the waveguide, interacting only with very few modes. This seems far away from the application regime of the wavepacket shaping regime, which assumes a frequency continuum. Because of this, the literature assumes that in this situation, only slow adiabatic-like protocols work [VVN$^+$17, KKT$^+$18]. Our approach, however, is to follow the spirit of analytical continuation and just apply the controls $g(t)$ obtained with the continuous theory to this apparently far-off regime.

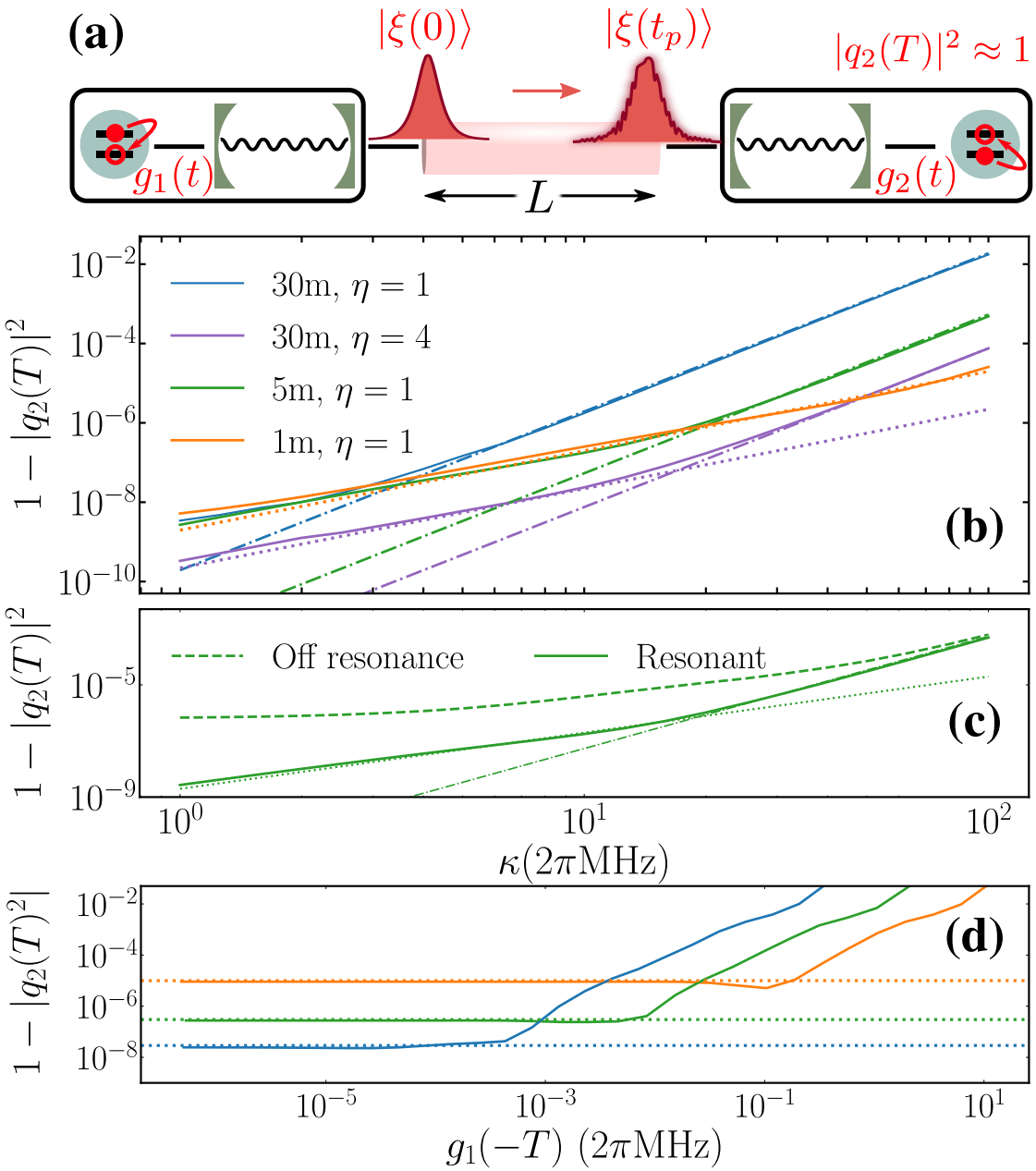

Figure 4.3: (a) Schematic illustration of the quantum state transfer protocol: By applying the controls $g_{1,2}(t)$ one can transfer the excitation from Q1 to Q2 via a photon propagating through the quantum link that distorts it, and thus, $|q_2(T)|^2 \approx 1$ at the end of the protocol. Panel (b) shows the quantum state transfer efficiency $1 - |q_2(T)|^2$ as a function of κ for three different quantum link lengths ($L = 30$, 5 and 1 m), and distinct photon bandwidths, $\eta = 1$ and $\eta = 4$. The dashed-dotted lines correspond to the limit imposed by diffraction, cf. Eq. (4.9) (short photon limit). The dotted lines represent the length-independent limit (long photon limit). The crossover between these regimes takes place when $2\sigma_t \approx t_p$, i.e., $\kappa/\eta \approx 2\pi v_g/(\sqrt{3}L)$. Panel (c) shows the impact in quantum state transfer efficiency when the resonant condition is not met, that is, $\Omega_{\text{R1}} = \Omega_{\text{R2}} = \omega_c$ (resonant) versus $\Omega_{\text{R1},R2} = \omega_c + \Delta\omega_c/2$ (off-resonant), i.e., R1 and R2 lie in between two TE_{10m} modes. Panel (d) shows the impact that a truncation of the control $g(t)$ has on the quantum state transfer efficiency, for $\kappa = 2\pi \times 90, 18, 3$ MHz and $L = 1$, 5 and 30 m, respectively (same style as in (b)). This indicates that the diffraction limit can be reached already with $g_1(-T) \approx 2\pi \times 10^{-3}$ or 10^{-1} MHz, depending on the parameters.

Contrary to what the literature suggests, we prove that wavepacket shaping leads to high efficiencies in quantum state transfer within the long photon limit, using the controls $g_{1,2}(t)$ outlined in Eq. (4.3). Furthermore, we identified that the coherent error is coming from the AC-Stark shifts. As studied in Subsection 4.2.1.3, a time-dependent control of the type we are using in this simulation leads to a dynamical detuning proportional to $\tilde{\kappa}$, which in turn affects the absorption efficiency by $1 - |q_2(T)|^2 \sim \kappa^2/\eta^2$. This error mechanism is independent of the waveguide length. This behavior is validated by the results shown by the dotted line in Fig. 4.3b for $\eta = 1$ across different lengths ($L = 30\text{m}, 5\text{m}, 1\text{m}$).

The efficiency of state transfer in the long photon limit is highly dependent on achieving a resonant condition between the resonators R1, R2, and the closest mode of the waveguide ($\Omega_{R1} = \Omega_{R2} = \omega_c$). This requirement is depicted in Fig. 4.3c, which shows a significant decrease in fidelity when this resonance condition is not met. This behavior is expected, since in this regime the photon is narrower in frequency than the separation between modes, and therefore the emission can not be complete if the wavepacket is centered between two modes. This dependence between the central frequency of the wavepacket and those of the waveguide modes is not relevant in the short photon regime. In such case, the frequency width of the wavepacket $\tilde{\kappa} >$ FSR, and therefore it always has modes to decay to.

It is possible to optimize the duration of the protocol by investigating the state transfer fidelity as a function of the sech-pulse duration, this is studied in Fig. 4.3d. This involves shortening the protocol duration $2T$, causing the initial value of the control to rise from $g_1(-T)/\kappa \approx 10^{-5}$ to $g_1(-T)/\kappa \approx 1$. As depicted in Fig. 4.3d, there is a threshold for $g_1(-T)$ beyond which the transfer efficiency reaches a saturation point, corresponding to the diffraction limit. This observation suggests that the previously assumed necessity of $g_1(-T)/\kappa \lesssim 10^{-5}$ is too conservative. In practice, as reported in experiments like that in [MSK+20], values of $g_1(-T)/\kappa$ within the 10^{-2} to 10^{-1} range are likely adequate for achieving high-fidelity in quantum operations, marking a significant flexibility in protocol timing for efficient quantum state transfer. It all indicates that the duration previously proposed of $2T = t_p + 10/\tilde{\kappa}$ is indeed too long, and that good fidelities can be obtained with durations of only $2T = t_p + 1/\tilde{\kappa}$.

4.2.2.1 Comparison with adiabatic and direct SWAP protocols

The remarkable performance of the pulse shaping method in the long photon limit offers an interesting comparison point with state-of-the-art adiabatic-like protocols from previous studies [VVN+17, CZB+20, LLC+19], as well as with the direct-SWAP gate approach detailed in [SMB06]. The comparison with STIRAP protocols is particularly interesting, the acronym derives from Stimulated Raman adiabatic passage and is a technique that draws on strategies from atomic physics for transferring excitations between atoms in a Λ configuration [VRSB17]. is implemented through the time-dependent control functions

$$g_1(t) = g_0 \sin((t+T)\pi/(4T)), \quad \text{and} \quad g_2(t) = g_0 \cos((t+T)\pi/(4T)), \tag{4.16}$$

starting with $g_1(-T) = 0$ and $g_2(-T) = g_0$, as applied in [CZB+20]. This method can achieve perfect state transfer from Q1 to Q2 in the adiabatic condition where T is much greater than $1/g_0$. Also, the g_0 parameter is not free, as it has to always remain below the free spectral range.

Eq. (4.16) is not unique, in the same way that many controls can be used for wavepacket shaping, the same holds for STIRAP. The proposal of [VS97] uses the following set of equations,

$$g_1(t) = g_0 \sin^2((t+T)\pi/(4T)), \quad \text{and} \quad g_2(t) = g_0 \cos^2((t+T)\pi/(4T)), \tag{4.17}$$

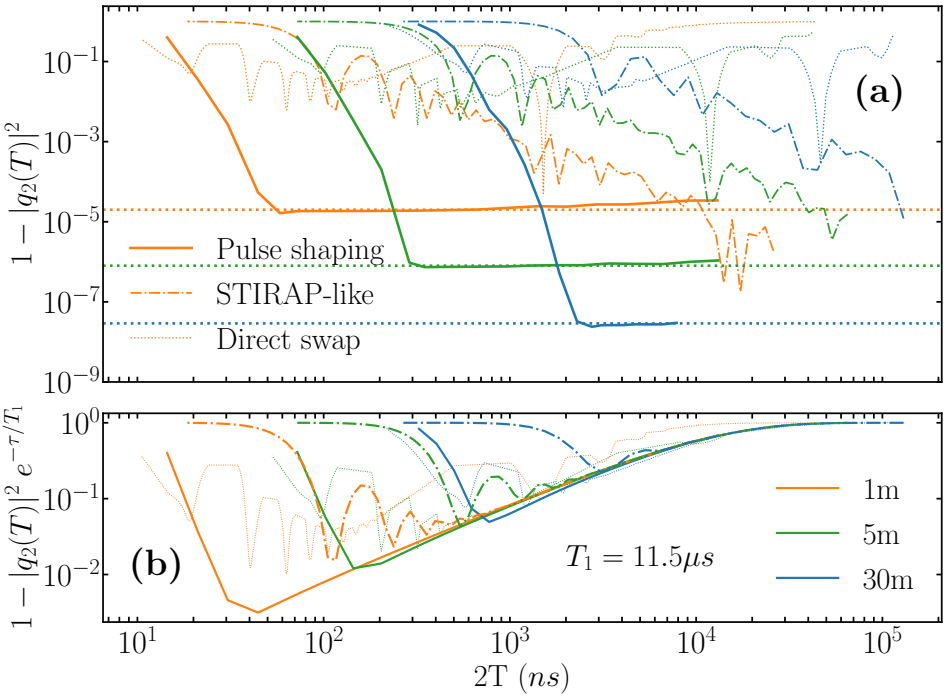

Figure 4.4: (a) Comparison of the quantum state transfer efficiency $1 - |q_2(T)|^2$ as a function of the protocol duration for the direct swap, STIRAP-like and pulse shaping following Eq. (4.3), for $L = 1$, 5, and 30 m; and $\Delta\omega_c \approx \kappa = 2\pi \times 90$, 18 and 3 MHz, respectively. The horizontal dotted lines correspond to the efficiency limit posed by the wavepacket distortion (cf. Eq. (4.9)), to which the pulse shaping saturates. (b) State transfer efficiency for the same three protocols but including a finite coherence time of the qubits of $T_1 = 11.5\mu s$, following Ref. [CZB+20]. The decoherence has been introduced according to $1 - |q_2(T)|^2 e^{-\tau/T_1}$.

which are similar to the previous but differ in that $dg_{1,2}(\pm T)/dt = 0$. The switching off and on is now smoother, making the STIRAP more *adiabatic*. We will show in the two figures of this subsection that both STIRAP protocols defined through Eqs. (4.16) and (4.17) perform more poorly than wavepacket shaping.

However, there is yet another approach besides wavepacket shaping and STIRAP, the direct-SWAP gate. This involves maintaining constant couplings $g_{1,2} = g$ to get an approximate quantum state transfer in a time frame defined by $gt \approx \pi$, as proposed in [SMB06]. This method represents a more straightforward approach compared to the adiabatic STIRAP-like protocol.

Following the parameters used in [CZB+20], we set the decay rates of the resonators equal to the free spectral range $\kappa = \kappa_{1,2} = \Delta\omega_c$, and choose $g_0 = \kappa/5.26$, a ratio dictated by the adiabatic condition discussed in the supplemental material of [CZB+20]. We then proceed to compare the efficiency of our pulse shaping method under Eq. (4.3) with that of a STIRAP-like protocol as the protocol duration increases, as illustrated in Fig. 4.4a. As anticipated, while the fidelity of the pulse shaping approach reaches a limit due to wavepacket distortion as per Eq. (4.9), this saturation level is achieved much faster compared to the STIRAP-like method, leading to an advantage of two orders of magnitude in terms of protocol speed.

Additionally, this study explores the fidelity of a direct-SWAP protocol by experimenting with different coupling strengths g. The goal is to identify the optimal duration for quantum state transfer (Fig. 4.4a). The comparison shows that pulse shaping and STIRAP-like methods maintain efficiency across a range of times. In contrast, the direct-

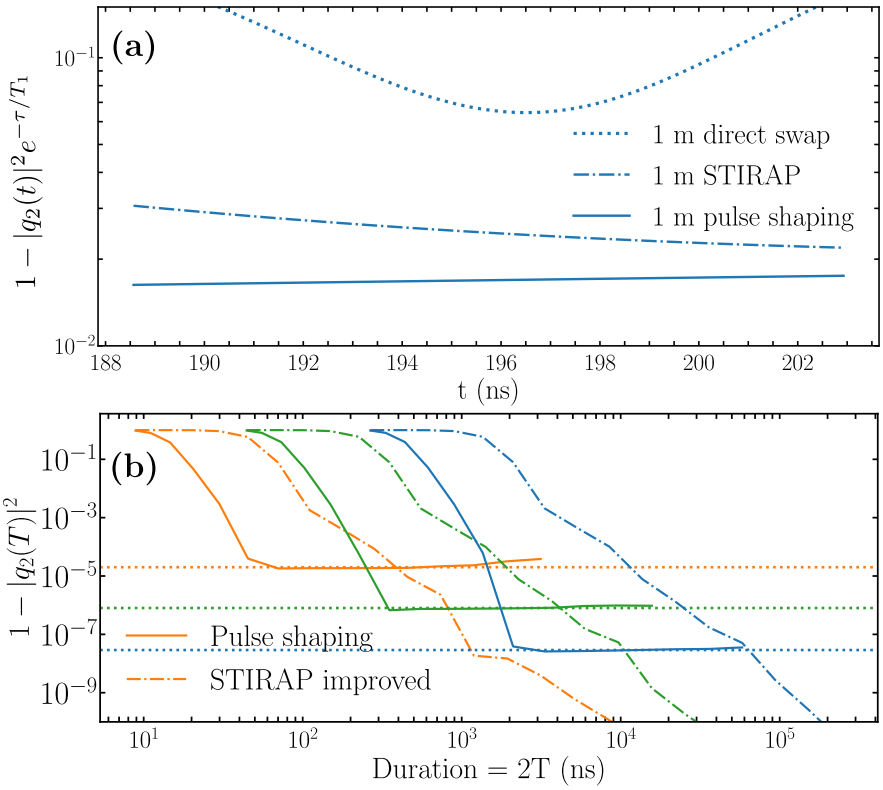

Figure 4.5: (a) Robustness of each of the three protocols studied in this manuscript against slight variations of the protocol time for $\kappa = 2\pi \times 90$ MHz $\approx \Delta\omega_c$ and a $L = 1$ m waveguide. The lines plotted correspond to a single simulation of those shown in Fig. 7.8(b) around the 200 ns point. It can be seen that whereas the pulse shaping and the STIRAP (solid and dotted-dashed lines respectively) are robust, the direct SWAP (dotted line) undergoes large variations even for just a few nanoseconds. (b) Comparison of the quantum state transfer efficiency $1 - |q_2(T)|^2$ as a function of the protocol duration for an improved STIRAP-like protocol and pulse shaping following Eq. (4.3), for $L = 1$, 5, and 30 m, as in Fig. 7.8(a). The horizontal dotted lines correspond to the efficiency limit posed by the wavepacket distortion (cf. Eq. (4.9)), to which the pulse shaping saturates.

SWAP method's success depends highly on hitting the optimal timing precisely. Despite this, the direct-SWAP method does not achieve greater fidelity than pulse shaping.

The distinction in protocol duration is significant when incorporating decoherence effects. While STIRAP avoids diffraction effects and can theoretically achieve perfect transfer with sufficiently prolonged controls, its slower pace makes it more prone to decoherence effects. For illustration, Fig. 4.4b showcases a realistic protocol scenario incorporating all imperfections and assuming a qubit lifetime of $T_1 = 11.5\mu$s, in line with cutting-edge experimental benchmarks [CZB+20]. Including decoherence (T_1-errors), the considerable difference in the duration of the protocols leads to a substantial fidelity advantage for the faster pulse shaping method, exceeding STIRAP by more than an order of magnitude.

As outlined in [SMB06], executing a SWAP gate involves utilizing constant and always-on couplings g_1 and g_2, assumed here for simplicity to be equal ($g_1 = g_2 = g$). When $g \ll G$, that is, when the coupling between qubit and cavity is much smaller than that of cavity-waveguide, the interaction between Q1 and Q2 effectively occurs through a single mode, allowing for an approximate quantum state transfer within a time frame of $gt \approx \pi$. To maximize transfer efficiency, one must identify the optimal timing where the population $|q_2(t)|^2$ reaches its peak, as depicted in Fig. 4.4a. This characteristic makes the direct-

SWAP fidelity vulnerable to timing inaccuracies, thus being less robust than STIRAP-like or pulse-shaping methods. This vulnerability is highlighted in Fig. 4.5a for a given example, displaying the variation of $|q_2(t)|^2 e^{-\tau/T_1}$—with $T_1 = 100\ \mu$s—around the optimal time, and presenting it together the more stable outcomes of pulse shaping and STIRAP.

Finally, to close up this comparison between methods we show the last version of the *more adiabatic* STIRAP, defined through Eqs. (4.17) instead of the control equations defined by (4.16). This effect is depicted in Fig. 4.5b, where g_0 is set to $\kappa/2$. Again, while pulse shaping is ultimately limited by propagation distortion and the improved STIRAP is not, the former reaches its limiting fidelity in a much shorter time than the latter.

4.2.3 Benchmarking photon scattering phase

While the total phase acquired by each mode $\phi_{\text{tot}}(\omega)$ coincides with the theoretical result, it is important to recognize that this total phase is composed of two distinct parts: the phase due to propagation and the scattering phase, neither of which behaves linearly with the quasi momentum of the photon. This non-linearity, especially noticeable in the curvature of the scattering phase depicted in Fig. 4.6b, plays a role similar to photon diffraction.

To explore the impact of distortion on a photon generated by the first node with the control $g(t)$ defined by Eq. (4.3), we describe the initial state of the photon as $|\xi(t=0)\rangle = \int f(\omega) b_\omega^\dagger |\mathbf{0}\rangle \, \mathrm{d}\omega$, where $f(\omega) = \sqrt{\pi/(2\tilde{\kappa})}\,\mathrm{sech}(\pi(\omega-\omega_c)/\tilde{\kappa})$ and $\kappa_{1,2} = \kappa$. After the photon travels a sufficient distance, defined by a time longer than the propagation time ($T > t_p$), it is fully scattered by the second resonator, which then returns to its empty state. According to the theoretical framework, this interaction results in the photon undergoing a frequency-dependent phase shift of the form

$$|\xi(T)\rangle = \int f(\omega) e^{-iT\omega} e^{i\phi_{\text{scatt}}(\omega)} b_\omega^\dagger |\mathbf{0}\rangle \, \mathrm{d}\omega. \tag{4.18}$$

For wavepackets that are narrowly centered around the frequency ω_c, the scattering phase $\phi_{\text{scatt}}(\omega)$ can be approximated by expanding it to the second order around $(\omega - \omega_c)$. This gives the expression

$$\phi_{\text{scatt}}(\omega) \approx \phi_{\text{scatt}}(\omega_c) + \phi'(\omega_c)(\omega - \omega_c) + \frac{1}{2}\phi''(\omega_c)(\omega - \omega_c)^2.$$

Here, the zeroth-order term is the average phase the photon experiences, relevant when the bandwidth is nearly zero. The first-order derivative, $\phi'_{\text{scatt}}(\omega) = 4\kappa/(\kappa^2 + 4(\Omega_{\text{R2}} - \omega)^2)$, reflects a delay owing to the photon's absorption and subsequent remission by R2. This implies that the total round-trip time of the scattered photon will be $T = 2t_p + \phi'(\omega_c)$, with t_p being the propagation time L/v_g.

The second-order term,

$$\phi''_{scatt}(\omega) = \frac{32\kappa(\Omega_{\text{R2}} - \omega)}{(\kappa^2 + 4(\Omega_{\text{R2}} - \omega)^2)^2},$$

accounts for the curvature of the phase profile. This curvature will be the main cause of distortion of the photon shape upon scattering.

To compute the magnitude of this distortion, the actual scattered photon, represented by $|\xi(T)\rangle$, is compared with an ideal photon, $|\tilde{\xi}(T)\rangle$, which undergoes no distortion but simply experiences a delay and an average scattering phase, $\bar{\phi}_{\text{scat}} \simeq \phi_{\text{scat}}(\omega_c)$. The fidelity of this transformation can be determined by examining the overlap between these two-photon states. This calculation incorporates not only the curvature of the phase profile

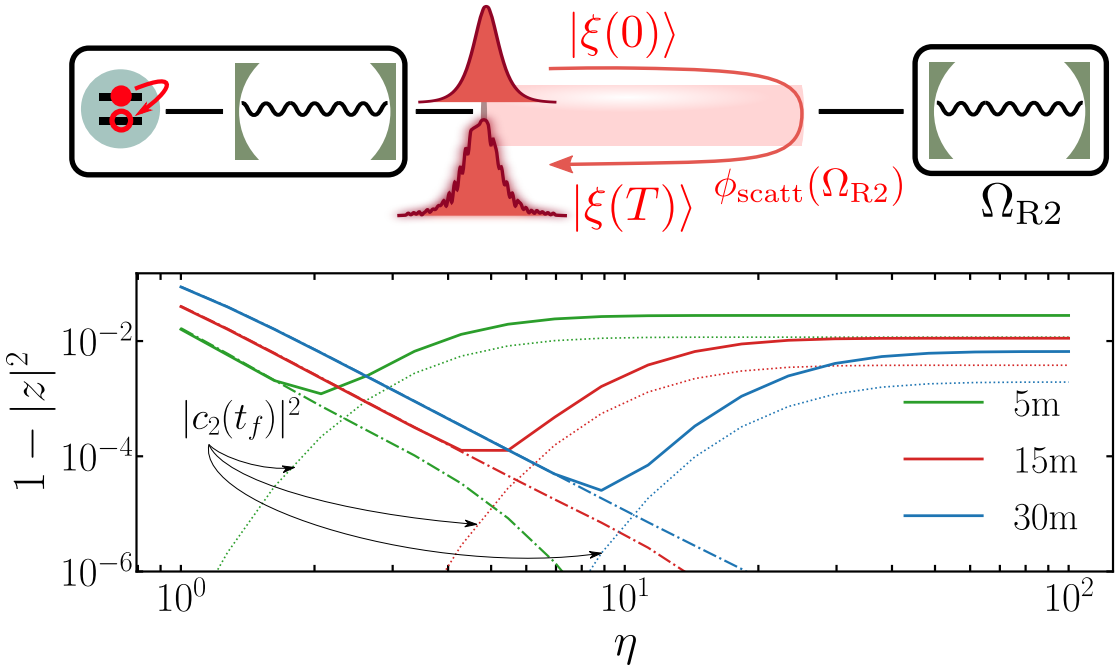

Figure 4.6: Distortion of a realistic wavepacket due to the phase profile $\phi_{scatt}(\omega)$ as well as due to the residual population that remains in the R2 (dotted lines) for different length but with $\kappa = 2\pi \times 100$ MHz. Solid lines correspond to the numerical simulation compared to the ideal photon after scattering $|z|^2 = |\langle\tilde{\xi}(T)\,|\psi(T)\rangle\,|^2$, while the dashed-dotted lines have been obtained using the theoretical expression (4.4), $|z|^2 = |\langle\tilde{\xi}(T)\,|\xi(T)\rangle\,|^2$. Note that for $\eta \lesssim 10$, $1-|z|^2 \sim \eta^{-4}$ as predicted by Eq. (4.19), while quantum links with larger length L are more prone to distortion due to propagation (cf. Section 4.1.1). For $\eta \gg 1$ one enters the long-photon limit where the photon does not fit within the quantum link and residual populations remain (see main text for further details).

but also the effects of propagation through the waveguide,

$$|z|^2 = \left|\langle\tilde{\xi}(T)|\xi(T)\rangle\right|^2 = \left|\int d\omega\ |f(\omega)|^2 e^{i(\phi''_{scatt}(\omega_c) - TD/v_g^2)(\omega-\omega_c)^2/2}\right|^2$$
$$\approx 1 - \frac{\kappa^4}{45\eta^4}\left(\frac{\phi''_{scatt}(\omega_c)}{2} - \frac{TD}{2v_g^2}\right)^2. \tag{4.19}$$

We have tested our theoretical predictions against numerical simulations of the scattering process, using a fixed resonator frequency. Later, in Section 4.3.2, the frequency will depend on the state of the qubit, but for now, we arbitrarily set $\omega_c - \Omega_{\text{R2}} = \kappa(1/2 + 1/\sqrt{2})$ so that the resulting phase gained by the photon upon scattering is $\phi_{scatt}(\omega_c) = -\pi/4$ (cf. Fig. 4.6b), while $\phi''_{scatt}(\omega_c) = 2(1-\sqrt{2})/\kappa^2$.

We calculate $|z|^2$ using two approaches to compare our analytical second-order perturbation theory with simulation data. First, we compute the overlap between the ideal, undistorted wavepacket $|\tilde{\xi}(T)\rangle$ and the wavepacket from the numerical simulation $|\psi(T)\rangle = e^{-iT(H_{QL}+H_{N_2-QL})}\,|\psi(0)\rangle$, where $|\psi(0)\rangle$ represents the initial state with a photon in the quantum link and an empty resonator R2 ($c_2(0) = 0$). Then, we measure how well this ideal $|\tilde{\xi}(T)\rangle$ agrees with the theoretically derived wavepacket, $|\xi(T)\rangle = \sum_m e^{-iT\omega_m} e^{i\phi_{scatt}(\omega_m)} f(\omega_m) b_m^\dagger\,|\mathbf{0}\rangle$, with $\phi_{scatt}(\omega)$ specified by Eq. (4.4).

As Fig. 4.6 reveals, achieving minimal distortion and accurate alignment with the scattering phase requires the bandwidth of the scattered photons, $\tilde{\kappa}$, to be narrower than

the decay rate κ_2 of the second resonator, or equivalently, $\eta > 1$. Within this parameter range, the observed infidelities agree well with theoretical predictions, and demonstrate a consistent decrease as the factor $\eta = \kappa_2/\tilde{\kappa}$ increases, until reaching a minimum bandwidth that is dependent on the length of the waveguide L.

After this minimum, the infidelity starts to increase again, as the system enters the long-photon limit. Specifically, as η expands further, the temporal width of the photon $\sigma_t = \pi\eta/(\sqrt{3}\kappa)$ exceeds the node-to-node propagation time $\sigma_t \gtrsim t_p$. In such a scenario, the photon does not fit completely within the waveguide, leading to a significant change in dynamics. The resonator R2 fails to empty entirely, retaining some population even well after the interaction period $T = 2t_p + \phi_{scatt}(\omega_c)$. This results in a decrease in the norm of the scattered wavepacket, resulting in the observed spoiling of the fidelity.

In summary, the dynamics of a photon generated by node Q1-R1 and interacting with a second resonator R2 at a different node follow input-output theory predictions. Building from the initial proposal in [DK04], our investigations emphasize the importance of considering the shape and duration of the wavepacket, as well as the distance between nodes. For practical scenarios, the long-photon limit is not too relevant, as operationally, photons of intermediate size ($\sigma_t \lesssim t_p$) are needed. This size range enables clear differentiation between the emission and scattering phases of the photon, and its potential reabsorption by the Q1-R1 node, as detailed in Section 4.3.2.

4.3 Distributed quantum gates design

Based on the findings of the previous two sections, we propose two novel methods for achieving a distributed quantum gate across nodes in a quantum network. The first method relies on quantum state transfer, where a flying qubit is sent through the bidirectional channel. The second method introduces a passive approach that obviates the need for node synchronization, implementing the gate through photon scattering processes.

4.3.1 Quantum gate transfer

The *quantum gate transfer* protocol leverages state transfer to distribute a quantum operation across the network, analogous to distributing an entangled state. This process is encapsulated by the formula

$$U_{1,3} \otimes \mathrm{I}_2 := \mathcal{T}_{1,2}^{\dagger} U_{2,3} \mathcal{T}_{1,2}. \tag{4.20}$$

It involves a sequence of two state transfer steps—$\mathcal{T}_{1,2}$ from Eq. (4.1) and its reverse, $\mathcal{T}_{2,1}$—flanking a two-qubit gate $U_{2,3}$ executed between qubits Q2 and Q3 at the second node, as depicted in Fig. 4.7a.

The second state transfer protocol essentially substitutes the classical communication necessary for a gate based on quantum teleportation. Even though the speed of our proposal is upper bounded by $v_p \approx 2c/3$, the overall performance of this direct operation could surpass that of the mixed quantum-classical method. This advantage can be relevant in particular in superconducting circuits, where state transfer can achieve high fidelity, and the additional processes required for quantum state distillation introduce significant errors.

The fidelity of the gate transfer can be estimated by a lower bound expressed as

$$F = \left[F_{\mathrm{st}} \exp(-\tau/T_1)\right]^2 F_{2,3}. \tag{4.21}$$

The term $F_{2,3}$ denotes the fidelity of the operation within a single node, $U_{2,3}$. The term $F_{\mathrm{st}} = |q_2(T)|^2$ represents the fidelity of a single state transfer step, and T_1 is the single qubit

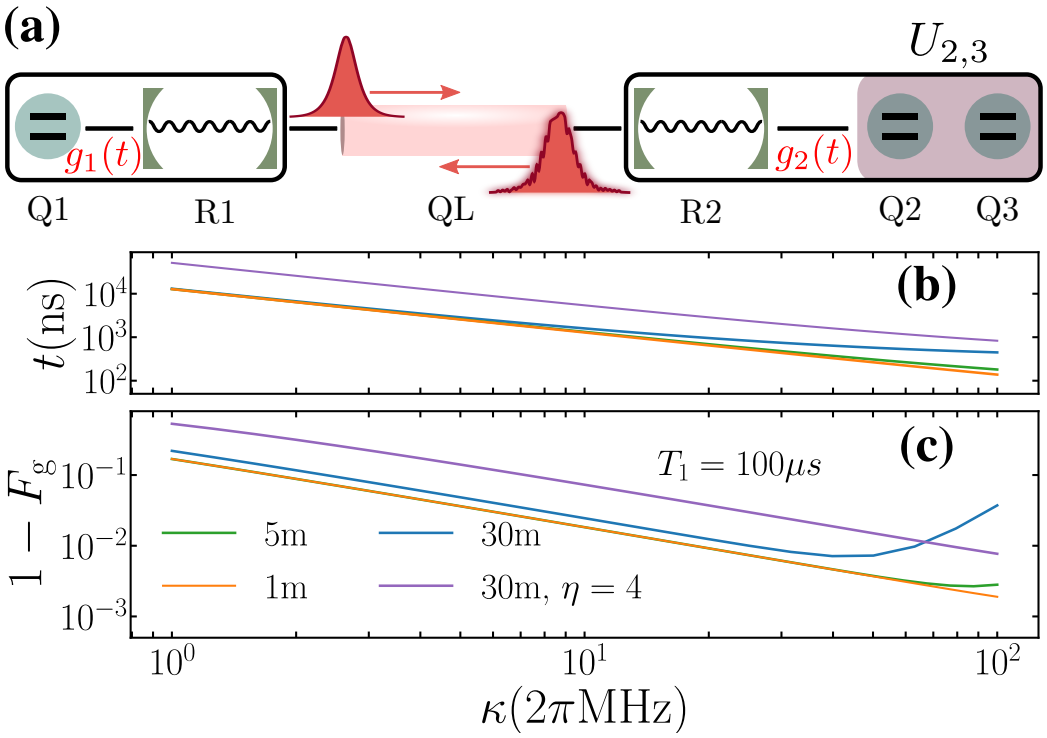

Figure 4.7: (a) Schematic illustration of a quantum gate transfer between Q1 and Q3, as given in Eq. (4.20), that involves two state transfer operations and a two-qubit gate $U_{2,3}$ on qubits within the same node. (b) Duration of the gate transfer protocol $t = 2 \times 2T$, assuming that the local gate implemented at the second node is instantaneous, for three different waveguide lengths with $\eta = 1$ (omitted in the legend) and one case with $L = 30$ m and $\eta = 4$. For small, κ the propagation time is negligible, and the limitation comes from the time-dependent control $g(t)$ and all lines with $\eta = 1$ overlap. (c) Fidelity of the process for the same set of parameters, where a trade-off between protocol duration and distortion of the wave packet is observed, specially in the $L = 30$ m, $\eta = 1$ case.

decoherence time (including effects from other potential decoherence sources like non-radiative decay). Here, τ indicates the duration for which the qubits hold their population during a single quantum state transfer event, as detailed in Subsection 4.2.1.4.

Examining the contribution to the fidelity that only depends on the state transfer and qubit decay from the simulation values of Section 4.1.1, we observe, as illustrated in Fig. 4.7b, that the quantum gate transfer presents an optimal operational point. This balance point depends on the trade-off between distortion errors and the decoherence stemming from the duration of the protocol. In practical settings, especially with shorter waveguides designed to link fridges or chips within the same cooling unit, the gate transfer achieves competitive fidelities in the range of $1 - F \sim 10^{-2} - 10^{-3}$. Importantly, these control methods facilitate faster operations compared to adiabatic population transfers, a point highlighted in Section 4.1.1 and evidenced in Fig. 4.4.

The fidelity of the gate transfer can be enhanced by shortening the protocol duration, $2T$. The results shown in Figs. 4.7(b)-(c) were derived by ensuring that the fidelity for each data point is limited by the propagation-induced distortion. As mentioned previously, adhering strictly to this limitation may not always be practical for actual implementations. When T_1 is more restrictive than the diffraction limit, it is beneficial to shorten the protocol even if it worsens depletion, as minimizing the decoherence error becomes the priority. To demonstrate this, we tailored the protocol duration for a set of specific parameters —

$L = 30$ m, $\kappa = 2\pi \times 3$ MHz, $T_1 = 100$ μs — and achieved a gate fidelity of $F_g \approx 10^{-2}$. This represents a 5-fold improvement over the fidelity achieved using a less optimized protocol duration $2T$.

4.3.2 Controlled-phase gate

The operation of the gate transfer demands synchronization between the sender and receiver nodes. A more straightforward gate can be devised where only the initial node Q1-R1 emits and subsequently reabsorbs a photon, which becomes entangled with the second node. This approach leverages the photon-cavity scattering phases discussed in Ref. [DK04] and Section 4.1.2. In this simplified protocol, active control is only required at the first node, while the second node influences the process through a resonance frequency $\Omega_{\mathrm{R2}} + \chi\sigma_2^z$, which varies based on the state of the second qubit (Q2 as depicted in Fig. 4.8a).

To test the performance of this protocol, we emit a photon to transfer the state of qubit Q1 into a traveling photon, denoted by $|\xi_{\mathrm{in}}\rangle$. This photon moves along the link and eventually interacts with the second node, during which it gains a qubit-state-dependent scattering phase. The mathematical expression of this process is

$$|\xi_{\mathbf{in}}\rangle \left(\alpha\,|0\rangle_2 + \beta\,|1\rangle_2\right) \rightarrow \left(|\xi_{\mathbf{out}}\rangle\,|0\rangle_2\,\alpha e^{-i\varphi_0} + |\xi_{\mathbf{out}}\rangle\,|1\rangle_2\,\beta e^{-i\varphi_1}\right).$$

After scattering, the photon, now $|\xi_{\mathrm{out}}\rangle$, gets reabsorbed by the first node, again using the same mechanisms of wavepacket shaping. By adjusting the resonance center Ω_{R2} and the displacement χ, we create a scenario where $\varphi = \varphi_1 - \varphi_0 = \pi$. This setup, upon the reabsorption of the photon, creates a controlled-phase gate between Q1 and Q2, represented as

$$U_{\mathbf{cp}} = \exp\left[-i\frac{1}{2}(\sigma_1^z + 1) \otimes \frac{\pi}{2}\sigma_2^z\right]. \tag{4.22}$$

First, let us consider the setup described in Ref. [DK04] and illustrated in Fig. 4.8a, where the second node features a single cavity influenced by a qubit through a dispersive frequency shift. This interaction is governed by the Hamiltonian [KKT+18, BGC+18], see also the discussion in Chapter 2

$$H_{\mathrm{Node2}} = \delta_2\sigma_2^+\sigma_2^- + (\Omega_{R2} + \chi\sigma_2^z)a_2^\dagger a_2. \tag{4.23}$$

Here, the frequency of the second resonator R2 is modified to $\Omega_{R2,x} = \Omega_{R2} + (-1)^{x+1}\chi$ based on the state $|x \in \{0,1\}\rangle$ of the second qubit Q2. The parameter χ depends on the coupling strength g_2 between Q2 and R2, and their frequency difference $\Delta = \delta_2 - \Omega_{\mathbf{R2}}$. The application of the dispersive limit as detailed in Eq. (4.23) requires the condition $\Delta \gg g_2$, a regime easily achieved in various experimental settings.

As outlined in Ref. [DK04] and further explored in Section 4.1.2, when a quasi-monochromatic photon interacts with R2, it undergoes a phase shift $b_\omega^\dagger\,|\mathbf{0}\rangle\,|x\rangle \rightarrow e^{i\phi(\omega,x)}b_\omega^\dagger\,|\mathbf{0}\rangle\,|x\rangle$. The change in phase $\phi(\omega, x)$ depends on the frequency of the second resonator $\Omega_{R2,x}$ (cf. Eq. (4.4)). Setting the parameters to $\omega_c = \Omega_{R2}$ and $\chi = \kappa_2/2$, the phase difference tied to different qubit states is $\phi(\omega_c, x) = (-1)^{x+1}\pi/2$. This configuration achieves the target controlled-z gate operation by making $\varphi_{id} = \pi$, as shown in Fig. 4.8b.

The study performed in Section 4.1.2 suggests that the first node is limited to generating photons within a finite bandwidth, making them susceptible to diffraction effects from both the waveguide and the curvature of the scattering profile. These imperfections can be quantified as

$$|z_x|^2 \approx 1 - \frac{\kappa_1^4}{45\eta^4}\left(\frac{t_p D}{v_g^2} + (-1)^x\frac{2}{\kappa_2^2}\right)^2. \tag{4.24}$$

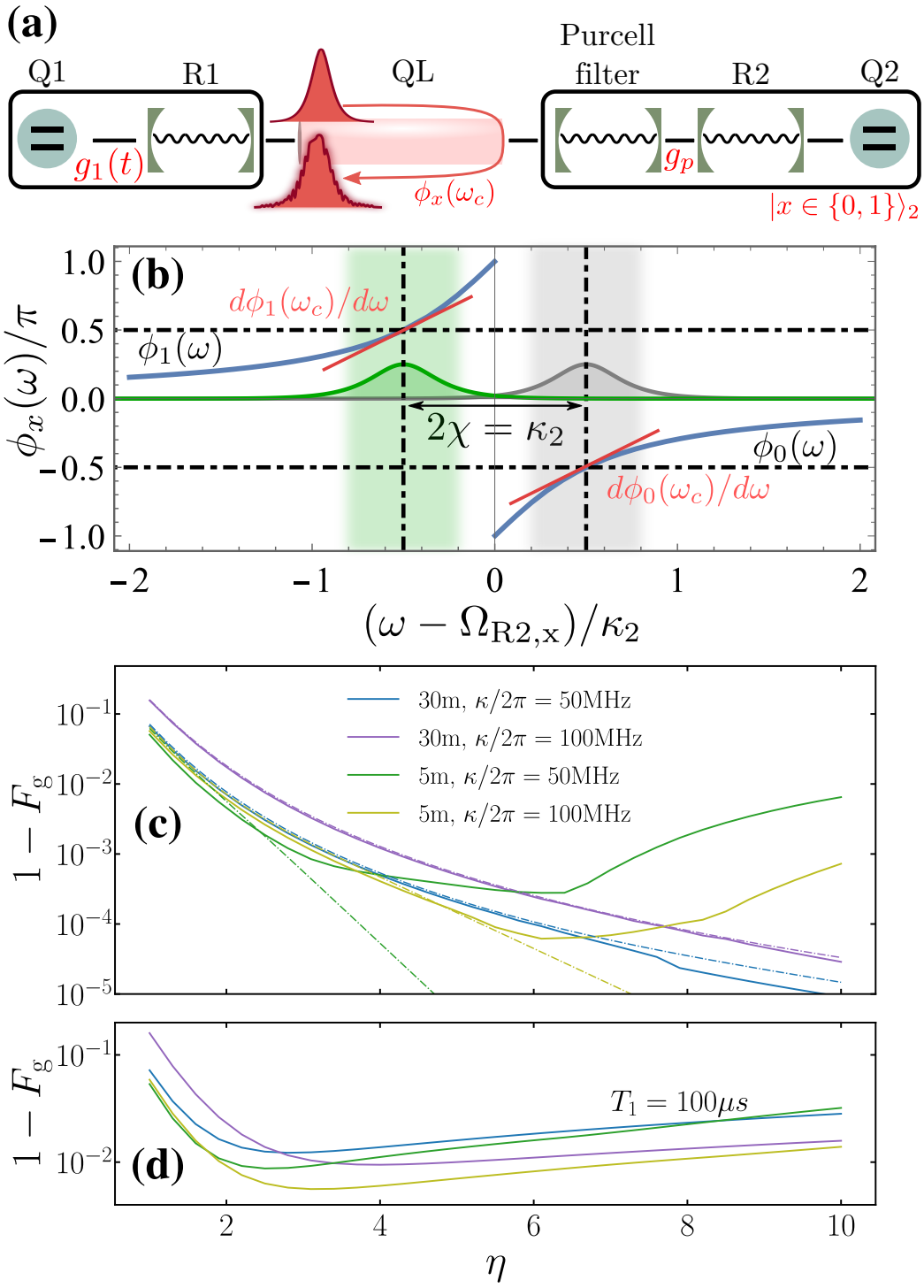

Figure 4.8: (a) Schematic illustration for the realization of a controlled-phase gate, where the phase of the scattered photon depends on the Q2's state, $|x \in \{1,0\}\rangle$. (b) Phase profile $\phi_x(\omega)$ as a function of the detuning of the incident photon for the effective R2 frequency. (c) Infidelity of the controlled-phase gate $1 - F_g$ for two different L and κ. The quantity F_g is calculated according to Eq. (4.25) of the main text. The solid lines correspond to the numerical simulations optimizing χ so one can access the long-photon regime, while the theoretical predictions (dashed lines) are calculated from the joint diffraction and scattering expressions. Neither decoherence times nor the effect of the Purcell filter are considered. (d) Results for $1 - F_g$ for the same set of parameters but including coherence times and a Purcell filter between the quantum link and R2. We set $g_2/\Delta = 0.1$ and 0.125 for $\kappa = 2\pi \times 100$ and 50 MHz with $g_p/\Delta = 0.03$ and 0.04, respectively.

This equation highlights an asymmetry, $|z_1| \geq |z_0|$, indicating that for $x = 1$, the scattering and propagation distortions counterbalance, whereas for $x = 0$, they add up. Utilizing z_x and the phase difference φ, we derive a lower bound for the gate fidelity compared to the perfect gate operation U_{cp}, as:

$$F_g = \begin{cases} \frac{|z_0|^2 \sin^2 \varphi}{(1+r^2+2r\cos\varphi)}, & \text{if} \quad \frac{(1+r\cos\varphi)}{(1+r^2+2r\cos\varphi)} \leq 1, \\ |z_0|^2, & \text{otherwise,} \end{cases} \tag{4.25}$$

where $r \equiv |z_0|/|z_1| \leq 1$ is defined.

In our setup with $\kappa_{1,2} = \kappa$, we conducted numerical simulations of the gate operation. The Q2-R2 node, being passive, is characterized by a fixed coupling $g_2(t) = g_2$, which enables the dispersive interaction detailed in Eq. (4.23). For the Q1-R1 node, a symmetric pulse governs the emission and reabsorption phases with the following functional form

$$g_1(t) = \begin{cases} g(t + t_d/2; \tilde{\kappa}, \kappa), & \text{for } t \in [-T, 0], \\ g(-t + t_d/2; \tilde{\kappa}, \kappa), & t \in [0, T]. \end{cases} \tag{4.26}$$

The value of the delay is set to $t_d = 2L/v_g + 2/\kappa$, which accounts for both the propagation time of the photon and the delay from scattering, as discussed in Section 4.1.2.

The data shown in Fig. 4.8c demonstrates that gate fidelity agrees closely with the theoretical predictions. Fidelity diminishes with increasing waveguide length and with the ratio $\eta = \kappa/\tilde{\kappa}$, which compares the bandwidth of the photon to the curvature of the scattering phase. Notably, the gate fidelity reaches very good values for moderate η, at the expense of protocol duration. As previously mentioned, the gate continues to perform well even when the assumptions of the input-output theory no longer apply. Yet, in the long-photon domain—defined as $\eta \gtrsim 2$ or 5 for $L = 5$m, 10m respectively—the optimal value for χ diverges from the expected $\chi = \kappa/2$ and requires semi-analytical corrections. Furthermore, when the width of the photon is more than twice the length of the quantum link, the emission and absorption controls overlap, precluding perfect reabsorption as inferred from Eq. (4.26).

In this setup, we explore the intrinsic limitations of quantum gates due to scattering processes. A notable issue arises from the dispersive interaction between the qubit and cavity in standard superconducting qubit models, leading to Purcell-induced decay in data qubit Q2, represented by $\gamma_\kappa = \kappa_2(g_2/\Delta)^2$ [BGB09, JSM+14]. This decay, previously unaddressed, can significantly affect gate fidelity. An effective mitigation strategy involves using a Purcell filter [SMK15, WKG+17, KMW+17], an additional resonator that substantially reduces the decay of the second qubit Q2 by effectively decoupling it from the transmission line. This approach, illustrated in Fig. 4.8a, can enhance qubit coherence dramatically, ensuring more accurate quantum gate operations.

In our analysis, we have integrated a resonant cavity that exhibits a decay rate of κ_2 when linked to the quantum link, and it interacts with R2 through a coupling strength denoted by g_p. The deployment of a filtering mechanism significantly curtails the decay rate of Q2 to $\gamma_\kappa \approx \kappa_2(g_2/\Delta)^2(g_p/\Delta)^2$, under the assumption that $\Delta \gg g_2, G_2, \kappa_2$ [SMK15]. Additionally, the derived formula for the phase profile (see Eq. (4.22)) remains applicable, and the aggregate gate fidelity is obtained by adjusting the factor shown in Fig. 4.8c through multiplication by $e^{-(\tau/T_1 + T\gamma_\kappa)}$. Examining the set of non-optimized parameters displayed in Fig. 4.8d, we find that $1/\gamma_\kappa \gtrsim T_1$, where T_1 is specified as 100μs. Given these practical scenarios, it is feasible to execute a controlled-phase gate with an infidelity of $1 - F_g \approx 10^{-2}$.

4.4 Summary

In the first part of the analysis we showed that input-output theory, foundational for quantum device operation as shown in [CZKM96, DK04], remains valid even under large Free Spectral Range (FSR) and short quantum links, conditions previously thought unsuitable. Pulse shaping proves effective in regimes with short links or few relevant modes, outperforming traditional adiabatic approaches and enabling rapid operations constrained only by cavity bandwidth.

We proposed two different distributed quantum gates, one based solely on quantum state transfer and the other on wavepacket shaping plus a collisional scattering phase. Both these gates are specially suited for implementation in superconducting quantum networks since they do not require entanglement distribution, measurements, or the exchange of classical information. All these mechanisms are costly in a superconducting platform. The gate based only on state transfer via wavepacket shaping is quite straightforward to implement in experiments where the primitive has already been demonstrated, such as [KMW$^+$17, KKT$^+$18, MSK$^+$20, SSK$^+$23], however, it demands perfect synchronization between nodes and at least three qubits. On the other hand, the collisional controlled-phase gate, while in principle requiring more ingredients and being more challenging to implement, has some clear advantages. First, the node with the control qubit is passive, and therefore no dynamical $g(t)$ nor perfect synchronization is needed. Second, it suffices to have two qubits, the target and the control for the complete action of the gate, saving up valuable resources, especially thinking of scalability. Under realistic coherence times, between 20 μs and 100 μs, our analysis shows gate fidelities ranging from $1 - F = 10^{-2}$ to 10^{-3}. This performance suggests such gates offer better fidelities than those based on entanglement distribution plus measurements.

Based on our findings, we posit that quantum networks composed of superconducting qubits and waveguides offer a viable foundation for executing quantum operations across both long-distance (inter-node) and short-distance (intra-node) quantum processors. We anticipate that forthcoming theoretical advancements, notably in techniques such as chirping [CGBM$^+$21] and quantum control [SRS$^+$10, SRS$^+$11], will address the current challenges associated with propagation delays and Stark shifts. These developments are expected to enhance the efficiency and speed of quantum state transfer, further increasing the potential of these networks for quantum computing and communication applications.

Finally, setting aside photon loss and decoherence, the most pressing source of error we found in the present analysis is the distortion due to the propagation. This is especially so as we move towards longer links and faster emission protocols (broad bandwidth photons), which is one of the main goals of the field. Because of this, the next chapter will be devoted to the design of a strategy to mitigate this error, namely, to engineer wavepackets that are robust to this distortion by exploiting the flexible nature of the controls $g(t)$.

Mitigation of distortion and non-Markovian effects 5

In this chapter, we address the imperfections suffered by photons as they propagate on a waveguide, providing error mitigation strategies that are compatible with the photon generation and state transfer protocols from Chapters 3 and 4. The existing quantum-optical frameworks for the pitch-and-catch methods overlook two critical elements (i) the diffraction of photons as they propagate through a waveguide with some dispersion, and (ii) the non-Markovian signatures triggered by the dynamical nature of the couplings. Both these mechanisms are shown pictorially in Fig. 5.1a, the necessity for creating fast, broad-bandwidth wavepackets implies that they are more sensitive to the curvature of the dispersion relation, and the finite nature of the waveguide.

The first limitation, photon diffraction, is significant across numerous experimental setups involving microwave guides [MSK$^+$20, KMW$^+$17], photonic crystal arrays [YMHK19, BKK21], or spin-wave technologies [RVH$^+$16, CKW$^+$22]. Regarding the traces of non-Markovian dynamics [TKC14, LPB10], these are primarily observed in the frequency modulation of qubit-photon systems, leading to alterations in the shape of the transmitted wavepackets that deviate from standard input-output theory. Importantly, these errors increase with both expansion of the bandwidth of the flying qubits, and the length of the quantum link. A viable strategy to mitigate this involves the use of photons with extremely narrow bandwidths, such as is done in adiabatic quantum state transfer [Pel97, CYL$^+$07, YZZ08, Cla14, Tia12, ZCB$^+$21, BTZ$^+$21]. Nevertheless, such an approach inevitably slows down the photon generation process, making it less robust against qubit decay and dephasing.

The present chapter offers simultaneously mitigation strategies for both sources of error without sacrificing the speed of state transfer, which is especially important for long waveguides, such as those in [SSK$^+$23, QLN$^+$23]. The approach considers a fully-coherent transfer and solves the dispersion by imprinting the flying qubit with engineered phases and frequency chirps that compensate for the errors in the quantum link, this is summarized in panels c) and d) of Fig. 5.1. On top of this, the emission and reabsorption of the flying qubits are done using an improved input-output model, with corrected equations that go beyond the Markov approximation, the difference between using or not the improved model is represented schematically in Fig. 5.1b.

The chapter is structured into three parts. Section 5.1 explains how to implement the correction strategy by imprinting phases on the wavepacket. Section 5.2 revolves around how to implement such a correction strategy in a scenario with modifications that go beyond the Markov approximation. Finally, Section 5.3 centers on the implementation of the correction strategies in situations with real-world interest.

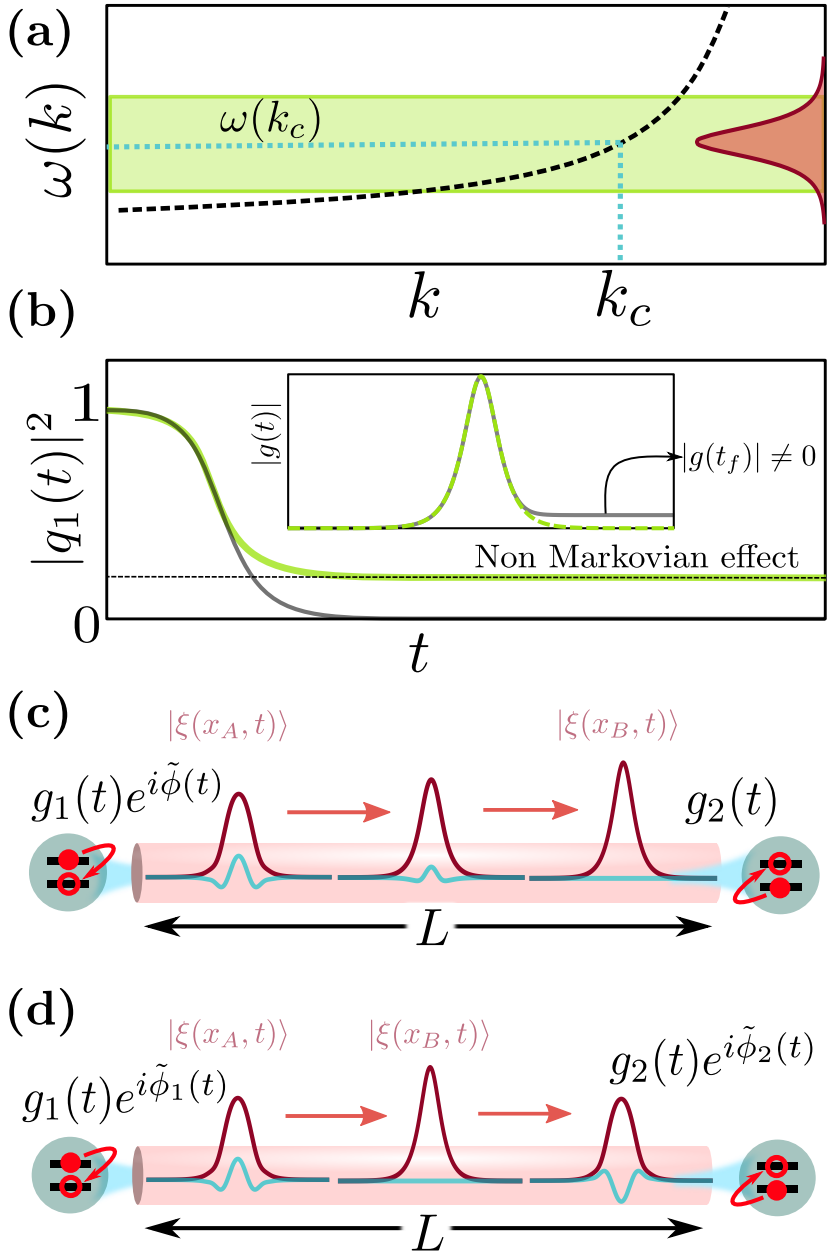

Figure 5.1: (a) Illustration of the two sources of imperfections that we tackle in this chapter, namely, that the fast-generated photons (wide in frequencies) are affected by both the curvature of the dispersion relation of the material through which they propagate and the edges of the frequency band within they are contained. (b) Neglecting non-Markovian effects leads to an imperfect depletion of the qubit excitation (green line). This stems from the revivals as the photon hits the end of the frequency band. In the inset we show the controls $g(t)$ for the two different cases: when non-Markovian corrections are taken into account, the control remains non-zero at the end and the depletion is perfect (gray line). Panels (c) and (d) show a sketch of the aim of this article, that is, to engineer complex controls, where both the phase and modulus are tuned dynamically. These control pulses yield photons robust to distortion that improve quantum state transfer. A phase is imprinted in these photons such that the propagation through the medium leads to a photon on the other end which can be absorbed with either a real control (cf. panel (c)) or with a complex control (cf. panel (d)).

5.1 Correction strategy

As considered in Chapter 3, we are interested in a single photon propagating through a quantum link. The setup is again the one described in previous chapters, in which the use of a Wigner-Weisskopf single excitation ansatz leads to Eqs. (3.2). Within this model, this chapter aims to design photons that are robust against distortion when traveling through a medium with a nonlinear dispersion relation, encapsulated in the term $\omega(k)$.

The main focus will be to mitigate the effects of the curvature of the WR90 waveguide thoroughly studied in the previous chapter, therefore the dispersion relation $\omega(k) \propto \sqrt{b + k^2}$ will center the discussion. This dispersion relation, and how the operation bandwidth compares to the photon bandwidth, is represented in Fig. 5.1a. Also, to show the generality of the method, the same techniques will be applied to a dispersion relation with negative curvature in Subsection 5.3.4.

The present approach aims to generate a target wavepacket form, $\xi_{\text{target}}(x_B, t)$, at a designated position x_B of the waveguide. In the presence of distortions, this goal can be achieved by generating the photons at the emitter position, $\xi_{\text{injection}}(x_A, t)$, with a different shape that, once subject to the actual distortions imposed by propagation, will become the target wavepacket. To analyze the wavepacket to be created, we must therefore understand the precise transformations experienced by the photon in the waveguide.

The wavepacket of interest at location x_B can be expressed as a sum of waveguide modes $\psi_\omega^{(B)}$, represented mathematically by

$$\xi_{\text{target}}(x_B, t) \approx \sum_\omega \psi_\omega^{(B)} e^{-i\omega t}. \tag{5.1}$$

In a scenario where the dispersion relation is linear, described by $\omega(k) = v_g|k|$, one can generate this profile by introducing a wavepacket with a similar shape, $\xi(x_B, t) \propto \xi(x_A, t - t_{\text{AB}})$, at the entry point of the quantum link x_A. Where, t_{AB} is the distance between x_A and x_B, divided by v_g. However, in the presence of generic dispersion relations $\omega(k)$, the shape of the wavepacket will change from x_A to x_B as depicted in Fig. 5.1c and d.

Without loss of generality, let us consider a semi-infinite line, with photons originating at $x_A = 0$ and moving right-wards with momentum k. Within this context, the expression of the field at various points on the path is given by

$$\xi(x, t) = \sum_k \psi_{\omega(k)} e^{ikx - i\omega(k)t}. \tag{5.2}$$

This formula demonstrates how the initial wavepacket shape and phase at point x_A, written as $\xi(x_A, t) = \sum_k \psi_{\omega(k)}^{(A)} \exp\{-i\omega(k)t\}$ correlates with the wavepacket $\xi(x_B, t)$ at any other location and time. By inverting this relation, the linear and non-linear contributions of the phase accumulated by the dispersion relation $\omega(k)$ separate into

$$\omega(k) = \omega(k_0) + v_g(k - k_0) + \omega_{\text{NL}}(k) \tag{5.3}$$

where $v_g = \partial\omega(k)/\partial k\big|_{k_0}$ is the group velocity, and $\omega_{\text{NL}}(k)$ represents the sum of all nonlinear terms in k. After rearranging, we arrive at the first conclusion of this chapter. That a specific shape of the input wavepacket (5.1) can create the desired photon shape at x_B

$$\xi_{\text{injection}}(t) := \xi(x_A, t) = \sum_k \psi_{\omega(k)}^{(B)} e^{+i\omega_{\text{NL}}(k)t_{\text{AB}}} e^{-i\omega(k)t}. \tag{5.4}$$

This adjustment in frequency space means the photon emitted does not retain the standard hyperbolic secant profile in position space at x_A. Rather, its initial amplitude and phase

are influenced by the nonlinear term $\omega_{\rm NL}(k)$, alongside the duration t_{AB} required for its travel from x_A to x_B.

Before jumping to the implementation of the predistorted wavepacket method, it is important to mention the two distinct strategies for the correction method, as illustrated in Fig. 5.1c and d. The first strategy, *predistortion* (i), (cf. Fig. 5.1c) consists of selecting x_A and x_B as the endpoints of the waveguide, ensuring that the photon achieves a perfect hyperbolic secant shape upon arrival. However, this approach might not always be practical, when the distance $|x_B - x_A|$ or the nonlinear coefficients $\omega_{\rm NL}$ are too large, the phase profile changes too fast and the $g(t)$ cannot be engineered. This is a consequence of the restriction on the derivative of the profile of the wavepacket (3.26). In such instances, the alternative strategy of *pre- and post-distortion* (ii), outlined in panel (d), becomes relevant. This method involves aiming for an optimal wavepacket at a midpoint B within the waveguide. It requires applying correction strategies at both the insertion and receiving endpoints.

The next subsection revolves around this point, namely, how much distortion can be corrected depending on the length of the waveguide, the width of the wavepacket, and the curvature of the dispersion relation.

5.1.1 Maximum correctable distortion

The photon injection mechanism does not allow arbitrary wavepackets to be generated. These wavepackets must satisfy some restrictions (cf. Eqs. (3.41), (3.42) from Chapter 3) that prevent us from creating arbitrary predistortions or correcting generic errors in the waveguide. This can be seen by developing a heuristic that produces sech photons and corrects up to the second order in the dispersion relation, that is, approximating $\omega_{\rm NL}(k)$ with a quadratic term.

This subsection details the second-order approximation of the non-linear dispersion relation for deriving $g(t)$ and the formula for the maximum correctable distortion. The approach begins by considering the continuum limit, which includes infinitely many modes, expressed as

$$\begin{aligned}\xi_{\rm dist}(t) &\simeq \int \mathrm{d}\omega \left(\frac{\partial\omega}{\partial k}\right)^{-1} \psi^{\rm id}(k) \exp\left\{i\omega_{\rm NL}(k(\omega))t_{\rm AB} - i\omega t\right\} \\ &= \int \mathrm{d}\omega \psi^{\rm id}(\omega) \exp\left\{i\omega_{\rm NL}(k(\omega))t_{\rm AB} - i\omega t\right\}.\end{aligned} \tag{5.5}$$

The wavepacket (5.5) is essentially the continuum limit of the one given by Eq. (5.4).

The next section will explain how to calculate the pulse $g(t)$ needed to generate a photon with a specific distortion D. For now, the focus is on determining the maximum value of this distortion parameter before the model breaks down. Consider a photon $|\xi(D)\rangle = \int d\omega b^\dagger_\omega f(\omega, D)\,|0\rangle$ where, following previous works, and without loss of generality we model as hyperbolic secant

$$f(\omega, D) = \sqrt{\frac{\pi}{2\kappa}}\mathrm{sech}\left(\frac{\pi\omega}{\kappa}\right) e^{-i\omega^2 D}. \tag{5.6}$$

For $D = 0$, after a Fourier transform, the resulting photon in time-space becomes $\xi(t) = \sqrt{\kappa/4}\,\mathrm{sech}(\kappa t/2)$. When $D \neq 0$, determining the time profile requires numerical methods. The goal is to produce a photon with $D \neq 0$ that, after traveling through a medium with a nonlinear dispersion relation, suffers a distortion with the opposite sign to that caused by the propagation.

To calculate $D_{\rm max}(\kappa)$ numerically, we hold κ constant and gradually increase the distortion starting from $D = 0$. The spirit of the calculation is the following, we take the

Markovian equations of motion (3.20) and try to invert them to obtain a $g(t)$ for wavepackets that are more and more distorted (this is what increasing D means). At some point, the condition $0 \leq |q(t)|^2 \leq 1$ (Eq. (3.26)) no longer holds, and we interpret this as the last physical photon that can be created. The greatest permissible value of D that meets this criterion is denoted as $D_{\max}(\kappa)$, which is depicted as blue dots in Fig. 5.2.

Additionally, a heuristic approach helps to establish the relationship $D_{\max}(\kappa)$. The leading order overlap between the distorted and ideal photons, expressed in terms of $D^2\kappa^4$, is represented by

$$|z|^2 = |\langle \xi(0)|\xi(D)\rangle|^2 = \left| \int d\omega \; f^*(\omega, 0) f(\omega, D) \right|^2 = \tag{5.7}$$

$$= \left| \int d\omega \; |f(\omega, 0)|^2 e^{-iD\omega^2} \right|^2 \approx 1 - \frac{D^2\kappa^4}{45} + O(D^4\kappa^8). \tag{5.8}$$

For a traveling photon in this context, the D parameter accounts for both the curvature of the dispersion relation and the propagation time. Using the formula above, $D = 3\sqrt{5}(1 - |z|^2)/\kappa^2$, the scaling $D_{\max} \propto \kappa^{-2}$ is determined. Setting $|z|^2 = 9/10$ agrees well with the numerical analysis, yielding $D_{\max} = 3/(2\sqrt{5}\kappa^2)$. Thus, $D_{\max}$ specifies the upper limit of D that can be imprinted on a photon, defining the maximum correctable distortion.

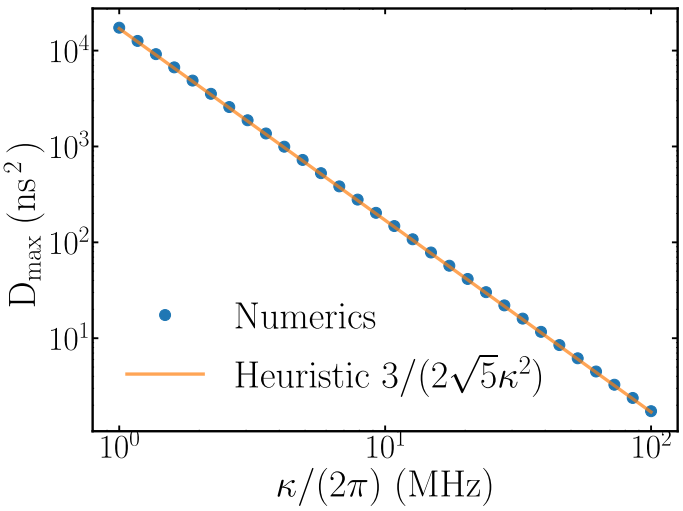

Figure 5.2: Maximum distortion that can be imprinted in a sech-photon using our formalism. The numerical simulations using a 3-level system (points) agree with the theoretical expression $D_{\max} = 3/(2\sqrt{5}\kappa^2)$.

Once it is understood how imprinting phases on a wavepacket can counter the effect of distortion, and that there is a limit to how much predistortion can be imprinted, it is time to explore how one can effectively design such photons. One of the first difficulties is that by making the control faster the applicability of the Markov approximation worsens, and therefore, further corrections have to be included.

5.2 Beyond Markov approximation

As we design more sophisticated photon generation controls, including strong predistortions, we approach the limits of validity of the Markov equations derived for this purpose (cf. Chapter 3). This section aims to extend the utility of those controls, including small corrections that allow us to correct the lowest-order non-Markovian effects.

The reason for the breaking of the Markov scenario is two-folded, first, strong predistortions force us to imprint rapid chirps onto the wavepacket, and second, engineering ever faster protocols makes broad bandwidth photons. This second fact is illustrated in Fig. 5.1a, namely that, when the wavepacket is too wide in frequency space, it starts resolving the mode structure of the waveguide and moving away from the purely Markovian scenario.

These rapid chirps and broad bandwidth photons are not adequately addressed in the framework of the Markov approximation. This approximation presumes that the cavity field $c(t)$ varies slowly around a central carrier frequency $\sim \Omega_R$. However, by revisiting the principles of input-output theory, we can incorporate corrections of the lowest order that account for a chirp in the modulation.

5.2.1 Dynamical beyond Markov approximation

Recall from Chapter 3 that the equation for the cavity field before the separation of timescales method is Eq. (3.6)

$$\dot{c}(t) = -ig^*(t)q(t) - i\tilde{\xi}_{\text{in}}(t) - \int_{t_0}^{t} d\tau K(t-\tau)c(\tau).$$

The expressions for $K(t-\tau)$ and $\tilde{\xi}_{\text{in}}$ are also given in Chapter 3 right after Eq. (3.6), but we reproduce them again here for the sake of clarity

$$\tilde{\xi}_{\text{in}}(t) = \sum_k G_k e^{-i\tilde{\omega}(k)(t-t_0)}\psi_k(t_0), \tag{5.9}$$

$$K(t-\tau) = \sum_k G_k^2 e^{-i\tilde{\omega}_k(t-\tau)}. \tag{5.10}$$

In a prototypical state transfer experiment, the waveguide has initially no field in it, i.e., $\psi_k(t_0) = 0$. Consequently, the equation for the cavity field becomes

$$\dot{c}(t) = -ig^*(t)q(t) - \Gamma(t), \tag{5.11}$$

where the source term $\Gamma(t)$ is defined as

$$\Gamma(t) = \int_{t_0}^{t} d\tau \ \sum G_k^2 e^{-i\tilde{\omega}(k)(t-\tau)}c(\tau) = \int_{t_0}^{t} d\tau \ K(t-\tau)c(\tau). \tag{5.12}$$

There might be a frequency shift due to the interaction (Lamb shift); to compensate for such shift we introduce $c(t) = c_{\text{s}}(t)e^{-i\delta\omega t}$, which leads to

$$\begin{aligned}\Gamma(t) &= \int_{t_0}^{t} d\tau \ \sum_k G_k^2 e^{-i\tilde{\omega}(k)(t-\tau)}c_{\text{s}}(\tau)e^{-i\delta\omega\tau} = \\ &= \int_{t_0}^{t} d\tau \ e^{-i(\tilde{\omega}(k)-\delta\omega)(t-\tau)}e^{-i\delta\omega t}c_{\text{s}}(\tau) = e^{-i\delta\omega t}\int_{t_0}^{\tau} d\tau \ K(t-\tau)c_{\text{s}}(\tau).\end{aligned} \tag{5.13}$$

Now, the Markov approximation, as it is done in Chapter 3 and exemplified by Eq. (3.9) presumes that the kernel $K(t-\tau)$ is a very peaked distribution around t and that therefore the previous integral is just local in time. The aim here is to explore what happens when this is not assumed.

Recall that we are in the rotating frame with respect to the resonator. Now, we introduce $U(t-\tau) = \int_{t_0}^{\tau} d\tau' K(t-\tau')$ and do integration by parts as

$$\begin{aligned}\int_{t_0}^{t} d\tau \ K(t-\tau)c_{\text{s}}(\tau) &= \int_{t_0}^{t} d\tau \ \frac{dU(t-\tau)}{d\tau}c_{\text{s}}(\tau) = \\ &= U(t-\tau)c_{\text{s}}(\tau)\Big|_{t_0}^{t} - \int_{t_0}^{t} d\tau \ U(t-\tau)\dot{c}_{\text{s}}(\tau).\end{aligned} \tag{5.14}$$

By definition $U(t-t_0)=0$, taking this into account and assuming that $\dot{c}_{\rm s}(t)$ varies slower than the integral of the memory kernel, we arrive at

$$e^{-i\delta\omega t}\int_{t_0}^{t} d\tau\ K(t-\tau)c_{\rm s}(\tau) \approx$$
$$c(t)\int_{t_0}^{t} d\tau\ K(t-\tau) - \dot{c}_{\rm s}(t)e^{-i\delta\omega t}\int_{t_0}^{t} d\tau \int_{t_0}^{\tau} d\tau' K(t-\tau'). \tag{5.15}$$

Now, making use of the fact that

$$\dot{c}(t) = \frac{d}{dt}\left[c_{\rm s}(t)e^{-i\delta\omega t}\right] = \dot{c}_{\rm s}(t)e^{-i\delta\omega t} - i\delta\omega c_s(t)e^{-i\delta\omega t} = \dot{c}_{\rm s}(t)e^{-i\delta\omega t} - i\delta\omega c(t),$$

we have

$$e^{-i\delta\omega t}\int_{t_0}^{t} d\tau\ K(t-\tau)c_{\rm s}(\tau) \approx c(t)K_1(t) - (\dot{c}(t) + i\delta\omega c(t))K_2(t) \tag{5.16}$$

with

$$K_1 = \int_{t_0}^{t} d\tau\ K(t-\tau), \tag{5.17}$$
$$K_2(t) = \int_{t_0}^{t} d\tau \int_{t_0}^{\tau} d\tau' K(t-\tau'), \quad \text{and} \tag{5.18}$$
$$K(t-\tau) = \sum_k G_k^2 e^{-i(\tilde{\omega}(k)-\delta\omega)(t-\tau)} \tag{5.19}$$

For a linear dispersion relation with $G_k \equiv G$ and $\tilde{\omega}(k) = k\Delta$, there is no Lamb shift ($\delta\omega = 0$), and the terms $K_1(t)$ and $K_2(t)$ can be easily computed. Indeed, following the calculation of Chapter 3, (cf. Eq. (3.11)), the first term corresponds just with the decay rate in Markovian scenario, $K_1(t) \approx \kappa/2$, while the second deserves its separate definition

$$\mathcal{N} = \int_{t_0}^{t} d\tau \int_{t_0}^{\tau} d\tau' K(t-\tau'). \tag{5.20}$$

It is important to note that the approximation in Eq. (5.15) depends on the dynamics. Thus, expanding the source term only up to the second order, one ends up with

$$\Gamma(t) \approx c(t)\int_{t_0}^{t} {\rm d}\tau K(t-\tau) + \dot{c}(t)\int_{t_0}^{t}\int_{t_0}^{\tau} {\rm d}\tau{\rm d}\tau' K(t-\tau') + \cdots \tag{5.21}$$

For the study that follows, only the first two terms of the expansion are relevant, since the order of magnitude of the third-order correction is smaller than other effects present in the system. Doing so, the expression of the source term becomes

$$\Gamma(t) \approx c(t)\left(i\delta\omega(t) + \frac{\kappa(t)}{2}\right) + \dot{c}(t)\mathcal{N}(t), \tag{5.22}$$

where the dynamical Lamb shift and the decay rate are linked to the kernel through $i\delta\omega(t) + \kappa(t)/2 = \int_{t_0}^{t} d\tau K(t-\tau)$, and the correction term $\mathcal{N}(t) = \int_{t_0}^{t} d\tau \int_{t_0}^{\tau} d\tau' K(t-\tau')$. As a result, non-Markovian effects manifest through a time-variable decay rate $\kappa(t)$ and Lamb shift, along with a first-order correction $\mathcal{N}(t) \neq 0$.

5.2.2 Pulse derivation

In the forthcoming sections, it will be shown that to design a control, adopting average values κ and $\mathcal{N}$ during the whole duration of the experiment is a good approximation. By taking these values constant, it becomes feasible to write down a modified equation for the cavity field. This, together with that of the qubit (which is unchanged by the first-order non-Markovian correction) takes the form

$$\dot{q}(t) = -ig(t)c(t) \tag{5.23}$$

$$\dot{c}(t) = \frac{1}{1-\mathcal{N}}\left(-ig^*(t)q(t) - \kappa c(t)/2\right), \tag{5.24}$$

where the resonant condition, $\delta = \Omega + \delta\omega$, is maintained. In this subsection, we provide the details for the derivation of $g(t)$ from the dynamical equations for the qubit and cavity field. Importantly, the non-Markovian parameter $\mathcal{N} \in \mathbb{C}$, and we will make the definition $\mathcal{N} = |\mathcal{N}|e^{i\phi_{\mathcal{N}}}$. The procedure is similar to that outlined in Section 3.2.2, replacing the equation for the cavity field to include the non-Markovian correction. This replacement changes the shape of the equations, but not the spirit of the derivation. That way, the equation for the qubit field becomes

$$|q(t)|^2 = |q(t_0)|^2 - \frac{(1-\mathcal{N})}{\kappa}\int_{t_0}^{t}\xi^*(\tau)\dot{\xi}(\tau)d\tau - \frac{(1-\mathcal{N}^*)}{\kappa}\int_{t_0}^{t}\xi(\tau)\dot{\xi}^*(\tau)d\tau - \int_{t_0}^{t}|\xi(\tau)|^2 d\tau. \tag{5.25}$$

Let us recall the definitions from Section 3.2.2, $\tilde{c}(t) = -ic(t) = e^{r(t)-i\theta(t)}$, $q(t) = e^{x(t)-i\sigma(t)}$, to keep track of the modulus and phase of all quantities. Additionally, we also recall the input-output relation $\tilde{c}(t) = \xi(t)/\sqrt{\kappa}$, where $\xi(t) := \xi(x_A, t)$ for simplicity.

Obtaining the modulus and the phase of the cavity field, $r(t)$ and $\theta(t)$ respectively, is straightforward once the wavepacket is known. The modulus of the qubit field is given by Eq. (5.25). However, recall from Section 3.2.2 that, when deriving a complex $g(t)$ the main difficulty was obtaining the phase of the qubit field $\sigma(t)$. Following exactly the same steps for arriving at Eq. (3.54), but dragging along the parameter $\mathcal{N}$, one arrives at

$$\dot{\sigma}(t) = -\dot{x}(t)\frac{\dot{\theta}(t)(1-|\mathcal{N}|\cos\phi_{\mathcal{N}}) + \dot{r}(t)|\mathcal{N}|\sin\phi_{\mathcal{N}}}{\dot{r}(t)(1-|\mathcal{N}|\cos\phi_{\mathcal{N}}) - \dot{\theta}(t)|\mathcal{N}|\sin\phi_{\mathcal{N}} + \kappa/2}, \tag{5.26}$$

and upon integrating $\sigma(t)$ numerically one has all the ingredients to construct the desired control.

It is interesting to explore a simplified example to highlight the fact that there still exist analytical expressions for the controls in this non-Markovian scenario.

A simple limiting case would be to emit a photon that has no imaginary part (for example, if we planned to correct all distortion at reception). Considering such a real pulse $\theta(t) = \sigma(t) = 0\ \forall t$, then

$$g(t) = \frac{\dot{x}(t)e^{x(t)}}{e^{r(t)}}, \tag{5.27}$$

where $r(t) = \log(|\xi(t)|/\sqrt{\kappa})$ and $x(t) = \log|q(t)|$. For $\xi(t) = \sqrt{\kappa/4}\mathrm{sech}(\kappa t/2)$, we find

$$g(t) = \frac{e^{\kappa t/(2-2\mathcal{N})}\kappa}{(1+e^{\kappa t/(1-\mathcal{N})})^2\sqrt{\mathcal{N}+(1-\mathcal{N})/(1+e^{\kappa t/(1-\mathcal{N})})^2}}. \tag{5.28}$$

When the Markovian parameter is zero $\mathcal{N} = 0$, one recovers the physics of the Markovian model studied in Chapters 3, and 4, and the standard pulse $g(t) = \kappa/2\mathrm{sech}(\kappa t/2)$. However, for $\mathcal{N} > 0$ the dynamics change, and to create a sech photon, the coupling remains opened $|g(t\to\infty)|^2 = \mathcal{N}$.

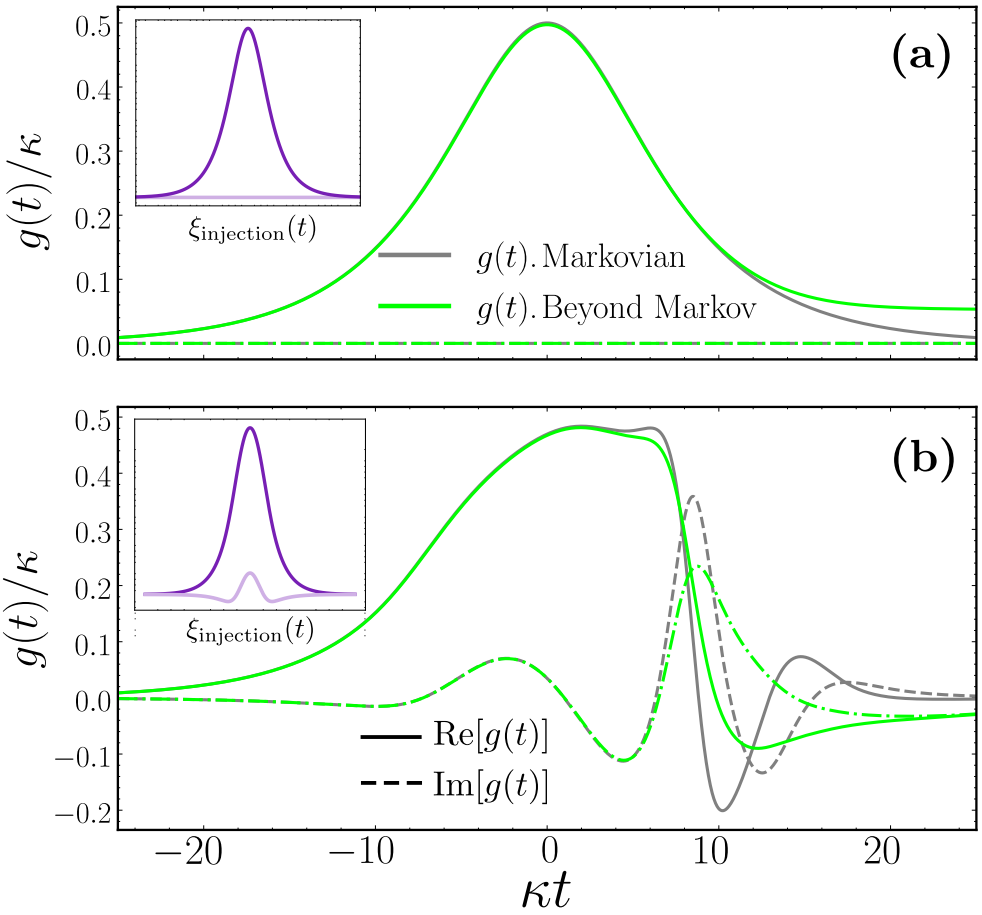

Figure 5.3: Time dependent controls $g(t)$ for different proposed injection wavepackets. Panel a) shows the result of proposing a sech photon. In this case, we have analytical expressions for both cases, the Markovian control (gray line) is just another hyperbolic secant, while the $g(t)$ obtained with the refined model (green line) is given by Eq. (5.28). In panel b) the proposed photon follows the Eq. (5.4) where the non-linear part of the dispersion relation has been kept quadratic, i.e., $\omega_{\text{NL}} \propto k^2$. In this case, no analytic expression exists, and the equation for the phase of the qubit field (5.26) has been integrated numerically.

The controls shown in Fig. 5.3 summarize the difference between using the Markovian model derived in Chapter 3 versus the first-order Markovian approximation presented here. Panel a) shows the control when the target wavepacket is hyperbolic secant, whereas in panel b) the target photon has an imaginary part equivalent to setting $\omega_{\text{NL}} \propto k^2$ in the equation for injected wavepacket (5.4). The insets show the real and imaginary parts of the injection wavepackets in each of the cases. The main qualitative differences introduced by the refinement are that i) the coupling remains opened (as remarked in the previous paragraph), and ii) the oscillations of the imaginary part get smoothed when imprinting phases on the wavepacket. This last trace is very convenient since it allows imprinting greater distortions than the purely Markovian theory.

5.3 Implementation of the correction strategy

The theoretical investigations in the previous sections have revealed two key findings. First, non-Markovian effects play a significant role, highlighting the need for protocols that

account for these influences when correcting diffraction. Second, the revised model, which incorporates non-Markovian effects, allows for accurate wavepacket engineering. This enables the mitigation of distortion by precisely imprinting the desired phase patterns onto the target photons. These findings will be validated through detailed numerical simulations, focusing on a practical application of the state transfer mechanism using circuit-QED elements.

5.3.1 Simulation parameters in WR90 waveguide

The detailed study of the setup of [MSK+20, SSK+23] done in Chapter 4 lead us to the conclusion that the propagation distortion was indeed playing a role. Because of this, we choose to test the method described in the previous sections first on a WR90 waveguide. This is, in the kind of waveguide used in these particular experiments.

Let us recall from Chapter 2 that the dispersion relation of this waveguide is [Dav12]

$$\omega(k_m) = c\sqrt{\left(\frac{\pi}{l_1}\right)^2 + k_m^2}, \tag{5.29}$$

where the k_m represents the wave numbers along the longer dimension of the waveguide, defined by $k_m = m\pi/L$ for $x \in [0, L]$, and l_1 denotes the width. The theory of capacitive couplings between the transfer resonators and the cavities allows for the derivation of the cavity-photon coupling coefficients $G_{m,j} = (-1)^{m(j-1)}\sqrt{\kappa_j v_g\, \omega(k_m)/(2\Omega_{\mathrm{R}j}L)}$ [Rip22], where κ_j are the experimental decay rates for the two transfer resonators. Recall Section 2.4 of Chapter 2.

The computational modeling of the experiments relies on two separate elements. First, a software was developed to generate the time-varying control functions, $g_j(t)$. In simple scenarios, such as a waveguide with a linear dispersion relation, the software uses analytical expressions for $g(t)$. For more complex scenarios, Runge-Kutta integration is employed. This method integrates Eq. (5.24) in the reverse temporal direction, starting from a specifically chosen predistorted wavepacket.

This study also incorporates a simulation of the entire set of dynamical equations of the full problem: Eqs. (3.2), (3.3), and (3.4). The approach uses a Trotterization technique to model the dynamics, accommodating a variety of dispersion relations, time-dependent controls, and any value of the length and free spectral range (FSR) of the waveguide. These simulations, which are numerically exact within the single-excitation subspace, evaluate the fidelity of the state transfer process. In general, this numerical implementation of the evolution dynamics is very similar to what was already used in Chapter 4 and produced the state transfer data shown in Figs. 4.5, 4.4, 4.8. Only technical improvements to accommodate that now $g(t) \in \mathbb{C}$, and some other minor changes were included. The main novelty of this chapter is the design of the distortion-correcting controls.

This subsection deals with two different simulation scenarios within the WR90 waveguide. First, inspired by [MSK+20], a waveguide with a length $L = 5$m, which supports 351 modes. Second, and thinking of a return trip in the setup of [SSK+23] a considerably longer $L = 60$m waveguide, which accommodates 4000 modes.

The inverse relationship between the free spectral range and the length of the waveguide imposes a difference in the number of modes between the two setups. It demands a greater number of modes for the 60m waveguide to maintain a bandwidth comparable to that of the 5m setup. In both experiments, we operated at the highest possible speeds i.e. $\tilde{\kappa} = \kappa$, leveraging the fact that the X-band in the WR90 waveguide is much wider than the typical wavepacket κ, as highlighted in [Dav12].

It is important to note that the simulations disregard decoherence effects to focus on improving the fidelity of coherent quantum state transfers. Nonetheless, it is relevant to

mention that, based on findings from [SSK+23, QLN+23], photon loss could potentially degrade the fidelity by up to 0.5% in a 60m waveguide. As discussed further below, this degree of loss is less significant than the infidelity caused solely by photon distortion in cryogenic superconducting waveguides.

However, before presenting the results for distortion correction in a full state transfer experiment, it is important to assess the fidelity of the effective non-Markovian model representing the dynamics of the full system.

5.3.2 Comparison between the non-Markovian model, and the full Hamiltonian

The simulation in this segment focuses on a single node, starting with the qubit in an initially populated state $q(0) = 1$. A broadband hyperbolic secant photon, characterized by $\kappa/(2\pi) = 200$ MHz, is introduced into a waveguide of length $L = 5$ m. This challenging experimental scenario enables rapid protocol execution and thorough investigation of the non-Markovian effects.

The first quantity we will pay attention to is $\Gamma(t)/c(t)$. Recall Eq. (5.12) for the definition of $\Gamma(t)$ and its simplified second order approximation, Eq. (5.22). It is important to remember that in a purely Markovian scenario, the mentioned ratio is just a constant complex number, namely,

$$\frac{\Gamma(t)}{c(t)} = i\delta\omega + \kappa/2 \tag{5.30}$$

with the real and imaginary parts representing the decay rate and the effective Lamb shift, respectively. This quantity is shown in the top two panels of Fig. 5.4 for two different situations.

When looking at a linear dispersion relation, the Lamb shift disappears. However, the ratio $\Gamma(t)/c(t)$ displays dynamic behavior instead of remaining static. Specifically, the real part of the ratio, $\mathrm{Re}(\Gamma(t)/c(t))$, oscillates around the predetermined decay rate κ, alternating below and above it depending on whether $\dot{c}(t)/c(t) > 0$ or $\dot{c}(t)/c(t) < 0$. For a non-linear dispersion relation, the average Lamb shift deviates from zero and exhibits fluctuations proportional to $\dot{c}(t)/c(t)$.

Utilizing the calculated values for $c(t)$ and $\Gamma(t)$, it is possible to deduce the magnitude of the non-Markovian correction parameter, denoted as $\mathcal{N}(t)$. Set κ and $\delta\omega$ to their mean values (indicated by the gray dashed lines in Fig. 5.4a and (b)), and compute

$$\mathcal{N}(t) = \left(\frac{\Gamma(t)}{c(t)} - \frac{\kappa}{2} - i\delta\omega\right)\frac{c(t)}{\dot{c}(t)}. \tag{5.31}$$

The calculated non-Markovian corrections for the emission process, which occurs over $t_{\text{emission}} \in (-12/\kappa, +12/\kappa)$, are depicted in Fig. 5.4c. At approximately $t = 0$, the population of the cavity peaks, making the $c(t)/\dot{c}(t)$ term in Eq. (5.31) singular, and thus the formula inapplicable. This effect is observable in Fig. 5.4c, where the absolute value of $\mathcal{N}$ exhibits a divergence around $\kappa t \approx 0$ and its phase undergoes rapid fluctuations between $-\pi$ and π. Nonetheless, during most times of the dynamics, $\mathcal{N}(t)$ remains roughly a constant complex value.

The departure from Markovian theory has significant implications. Such deviations suggest that a control $g(t)$, formulated under the strict Markovian framework, will inject photons $\xi_{\text{injection}}$ that differ from the anticipated profile ξ_{target}. These imperfections can be mitigated by employing non-Markovian models that incorporate a non-zero $\mathcal{N}$.

This approach has been numerically verified by evaluating the fidelity of the photon injection

$$F_{\text{pulse}} = |\langle \xi_{\text{target}} | \xi_{\text{injection}} \rangle|^2. \tag{5.32}$$

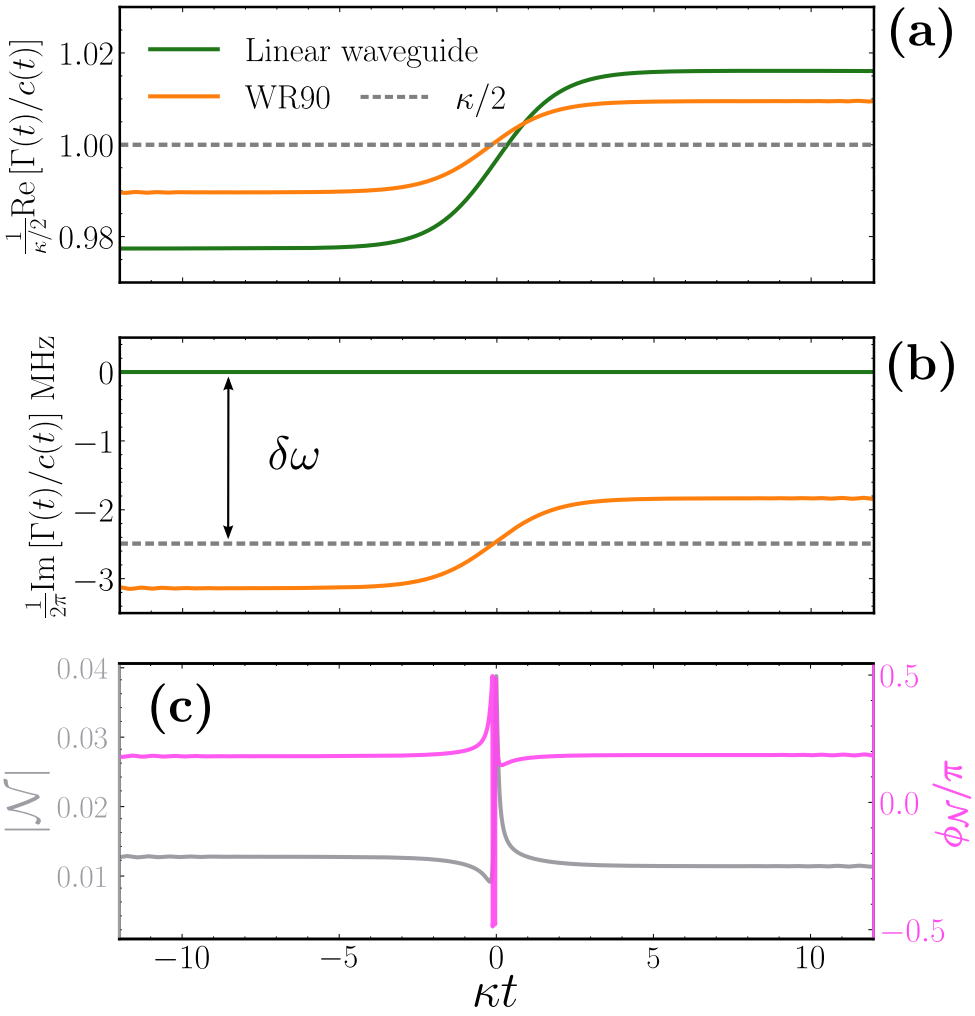

Figure 5.4: Real (a) and imaginary (b) part of $2/\kappa\ \Gamma(t)/c(t)$ for a linear waveguide with constant couplings $G_k = |G|$ (green line) and for a WR90 model (orange line). The real part gives an account for the decay rate, while the imaginary part refers to a Lamb shift. (c) Modulus and phase of the non-Markovian parameter $\mathcal{N} = |\mathcal{N}|e^{i\phi_{\mathcal{N}}}$ calculated from the two top panels according to Eq. (5.31). Note that, around $\kappa t \approx 0$, $\dot{c}(t) \longrightarrow 0$, leading to a singular behavior of $\mathcal{N}$, which is physically irrelevant. Parameters: $L = 5$m waveguide, $\kappa/(2\pi) = 200$ MHz, 5000 time steps, $g(t) \propto \mathrm{sech}(\kappa t)$.

Simulations with the complete Hamiltonian, applying controls $g(t)$ calculated via both Markovian and non-Markovian models, support this verification. Simulation data, depicted in Fig. 5.5 for waveguides of $L = 5$m and $L = 60$m with a linear dispersion relation, show that incorporating the non-Markovian parameter $\mathcal{N}$ significantly enhances the pulse fidelity by more than an order of magnitude.

This evidence reinforces the argument that integrating corrections beyond the Markov approximation leads to a model that reflects more accurately the physics of the entire system, thus enabling higher fidelity state transfer in practical settings.

5.3.3 Correcting distortion in a WR90 waveguide

This section demonstrates the significant enhancement of quantum state transfer fidelity achieved through our approach, using a WR90 waveguide. As outlined in Section 5.1, addressing distortion requires creating a wavepacket defined in Eq. (5.1).

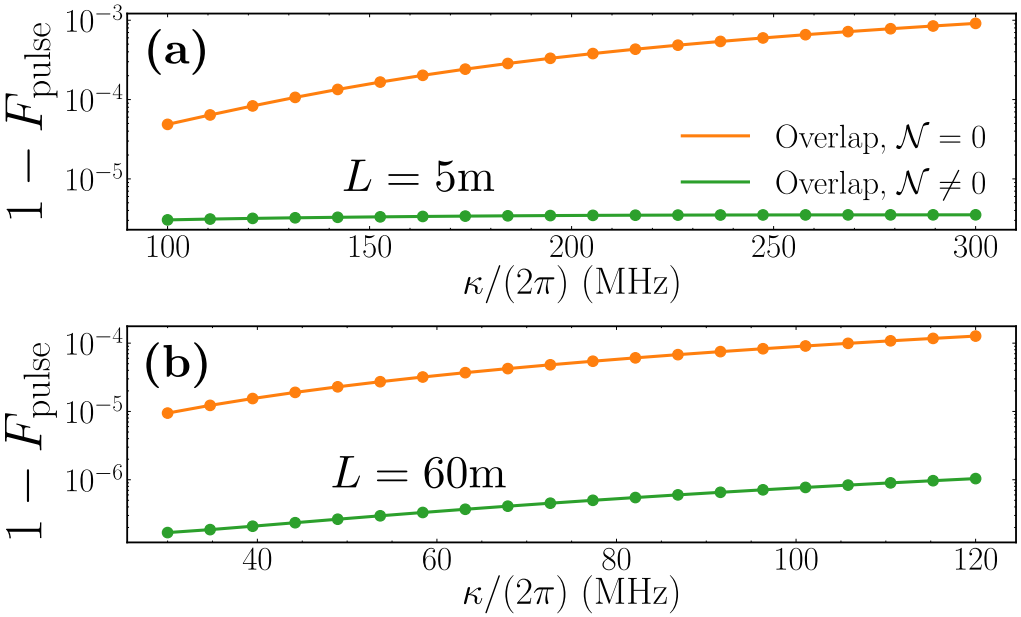

Figure 5.5: Infidelity $1 - F_{pulse}$ to quantify the faithfulness of the effective model for two different waveguide lengths $L = 5$ m (a) and $L = 60$ m (b). F_{pulse} is calculated according to Eq. (5.32) The control $g(t)$ is derived from a Markov model ($\mathcal{N} = 0$, orange lines) and the effective model including non-Markovian effects ($\mathcal{N} \neq 0$, green lines). The target field in every case is $\psi_{\text{target}}(t) = \sqrt{\kappa/4}\,\text{sech}(\kappa t/2)$. The output field has been reconstructed at the middle of the waveguide using Eq. (5.2) setting $x = L/2$. For $L = 5$ m, 351 modes, 2000 time steps have been used, and a protocol duration of $t_{5\text{m}} \in (-40/\kappa, +40/\kappa)$. For $L = 60$ m, 4000 modes, 2000 timesteps and $t_{60\text{m}} \in (-100/\kappa, +100/\kappa)$.

Approximating the dispersion relation (5.29) to second order around $(k - k_c)$, the resulting expression is

$$\omega(k) = \omega(k_c) + (k - k_c)v_g + \frac{1}{2}(k - k_c)^2 D_2, \tag{5.33}$$

where $D_2 = \frac{\partial^2 \omega(k)}{\partial k^2}\big|_{k_0}$ represents the curvature of the dispersion relation.

In our study, we adopt again the wavepacket $\psi_k^{\text{id}} = \sqrt{\frac{\pi}{2\kappa}}\text{sech}\left(\frac{\pi\omega(k)}{\kappa}\right)$. To adequately address correction up to second order, D_2, the wavepacket demands the following phase profile

$$\xi_{\text{injection}}(t) = \sum_k \psi_k^{\text{id}} e^{-i\omega(k)t} \exp\left(i\frac{1}{2}D_2(k - k_0)^2 t_{\text{AB}}\right), \tag{5.34}$$

where recall that the parameter t_{AB} is the propagation time from the emission point (x_A) to some other point (x_B). If we wanted to correct all distortion at emission, then t_{AB} would just be the propagation time of the waveguide. But other possibilities involving correction at emission and reception are also possible. These different approaches are shown pictorially in Fig. 5.1c and d.

Further, we define a normalized distortion parameter $D = D_2 t_{\text{AB}}/(2v_g^2)$. Computational analyses reveal that the phase configuration in Eq. (5.34) can be generated through a control $g(t)$, assuming $|D| \leq D_{max}$, where D_{max} is approximately $3/(2\sqrt{5}\kappa^2)$, as detailed in Subsection 5.1.1.

Considering the parameter regime shown in Fig. 5.6, i.e. $L = 5$ m and $\kappa/(2\pi) \sim 10^2$ MHz and a $L = 60$ m waveguide with $\kappa/(2\pi) \sim 10^1$ MHz, the values for the distortion

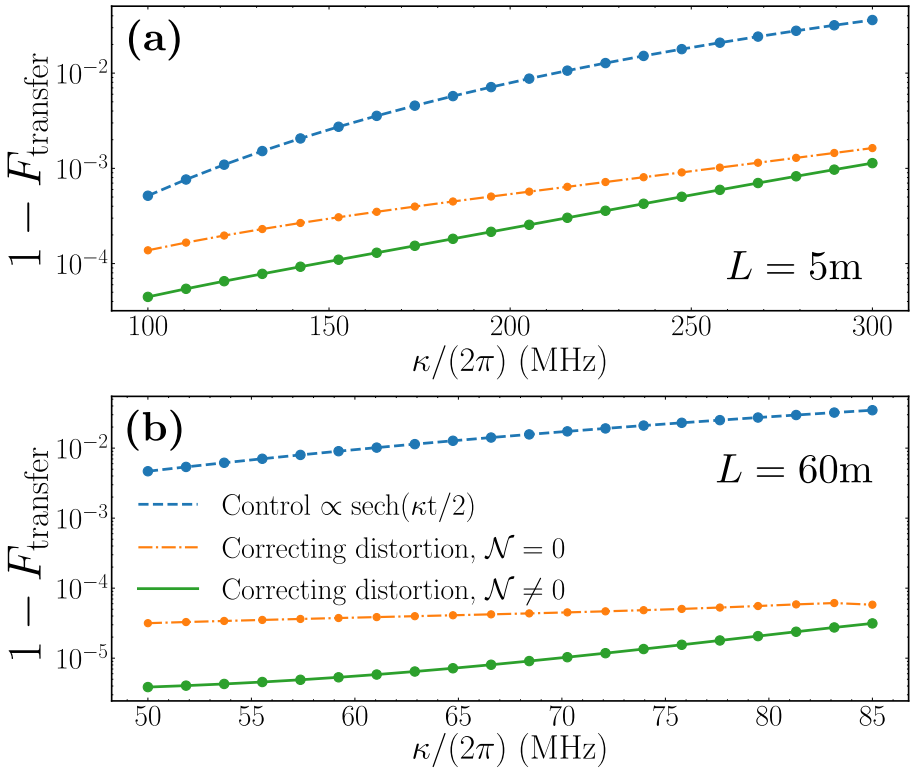

Figure 5.6: State transfer infidelity for a realistic WR90 waveguide. The dots are the actual points where the simulation was performed, whereas the lines are to be interpreted merely as guides to the eye. Blue lines correspond to the usual $g(t) = \kappa/2\ sech(\kappa t/2)$. Orange lines are obtained by trying to generate the corrected photon (5.34), obtaining the corresponding $g(t)$ with the effective Markovian model ($\mathcal{N} = 0$). Green lines correspond to the infidelity when the control to generate Eq. (5.34) is obtained, considering corrections beyond Markov ($\mathcal{N} \neq 0$). Both the blue and green lines are explained very accurately by an analytical calculation of the distortion, analogous to the one presented in [PnPR+22]. Panel (a) contains simulations for a 5 m waveguide whose parameters are 351 modes, 2000 time steps, and a protocol duration of $t_{5\text{m}} \in (-40/\kappa, +40/\kappa)$. A distortion of $D_{5\text{m}} = 0.33/2$ ns^{-2} at each of the nodes. The parameters of the panel (b) are 60 m waveguide 4000 modes, 2000 time steps and $t_{60\text{m}} \in (-100/\kappa, +100/\kappa)$. A distortion of $D_{60\text{m}} = 4.70/2$ ns^2 at each of the nodes.

parameter are $D_{5\text{m}} = 0.33$ ns^2 and $D_{60\text{m}} = 4.70$ ns^2. These values are larger than $D_{\max}$ but still smaller than $2D_{\max}$. Hence, one can employ the complex control to correct half the distortion on the emission process and half on the absorption, as discussed at the end of Section 5.1.

In Fig. 5.6 we show how our method compares to the usual wavepacket engineering done ignoring non-linear dispersion relations. We define the fidelity of state transfer as the probability that the second qubit absorbs the photon and gets excited at the end of the experiment t_f

$$F_{\text{transfer}} = |q_2(t_f)|^2. \tag{5.35}$$

The blue line corresponds to the state transfer fidelity using the usual Markovian control $g(t) = \kappa/2\ \text{sech}(\kappa t/2)$ [PnPR+22], obtained from an ideal wavepacket such as $\psi_k^{\text{id}} = \sqrt{\frac{\pi}{2\kappa}}\text{sech}\left(\frac{\pi\omega(k)}{\kappa}\right)$ without any predistortion of the phase. As expected, we obtain fidelities that decrease with increasing photon bandwidth. These infidelities are dominated by the photon wavepacket distortion, consistent with the estimations in Chapter 4.

The orange and green lines show the fidelity obtained using controls that have been obtained, proposing the $\xi_{\text{injection}}$ defined in Eq. (5.34). Both of them show much better fidelities than the case of the ideal photon. The orange line uses time-dependent controls obtained with the Markovian effective model, cf. Eqs. (3.17) and (3.18) in Chapter 3. The values to which this line saturates can be explained by the orange line in Fig. 5.5. Beware that the results of Fig. 5.5 can not be directly translated to Fig. 5.6, since $G_k = |G|$ in the first one, whereas $G_k \propto \sqrt{\omega_k}$ in the second.

Also, the generation of the target wavepacket (5.34) with a control $g(t)$ taking into account non-Markovian effects, that is, Eqs. (5.23) and (5.24) with $\mathcal{N} \neq 0$, leads to infidelities that are up to three orders of magnitude better than with the usually employed controls. As for the blue line, we stress again that the numerical results for the green line are accurately predicted by the theoretical model proposed in [PnPR$^+$22] provided that one accounts for the correction of the quadratic term.

Finally, let us mention that the proposed method can be applied to different quantum platforms, that is, to quantum links with distinct dispersion relations, either with positive or negative curvature. The following and final subsection is devoted to implementing correction strategies for a typical $\omega(k)$ of coupled arrays, such as those found in [CSP$^+$19, SLZ$^+$19, LH17].

5.3.4 Correcting distortion in a $\omega(k) \propto \cos(k)$ waveguide

In this section, we illustrate the adaptability of our approach to various platforms characterized by different dispersion relations $\omega(k)$. Employing the methodology outlined in the previous subsections, we conduct numerical simulations for state transfer through a medium with the following dispersion relation

$$\omega(k) = \omega_0 - 2J\cos(k). \tag{5.36}$$

This relation is representative of those found in coupled cavity array systems [CCCR16, SLZ$^+$19, LH17].

The group velocity and curvature of this waveguide are

$$v_g = \frac{\partial\omega(k)}{\partial k}\Big|_{k_0} = 2J\sin(k_0), \tag{5.37}$$

$$D_2 = \frac{\partial^2\omega(k)}{\partial k^2}\Big|_{k_0} = 2J\cos(k_0), \tag{5.38}$$

where k_0 represents the wave number at which the frequency of the waveguide mode equals that of the emitter, i.e. $\omega(k_0) \approx \delta_{1.2}$. Similar to the situation with the WR90 waveguide, both the curvature D_2 and the distance traveled determine the value of the distortion coefficient D.

To align with the frequency domain utilized for the WR90 waveguide, the parameters chosen are: $\omega_0/2\pi = 9.406$ GHz, $J/2\pi = 1.5$ GHz, and the waveguide length is set to 30 m, with emitters tuned to $\delta_{1,2}/2\pi = 10.406$ GHz. Consequently, the curvature of the dispersion relation in the operation band is negative (refer to Fig. 5.7a), unlike the positive curvature considered in the previous subsection. With these specifications, the distortion for a single trip in this waveguide totals $D = -1.343$ ns^2. The propagation time at the emitter frequency is $t_{\text{prop}} = 134.99$ ns, compared to $t_{\text{prop}} = 142.58$ ns observed in the WR90 waveguide.

The infidelity of state transfer is depicted in Fig. 5.7b. Similar to observations with the WR90 waveguide, the inclusion of a control function $g(t)$, which compensates for non-Markovian effects ($\mathcal{N} \neq 0$) and distortions in the wavepacket, improves the fidelity by

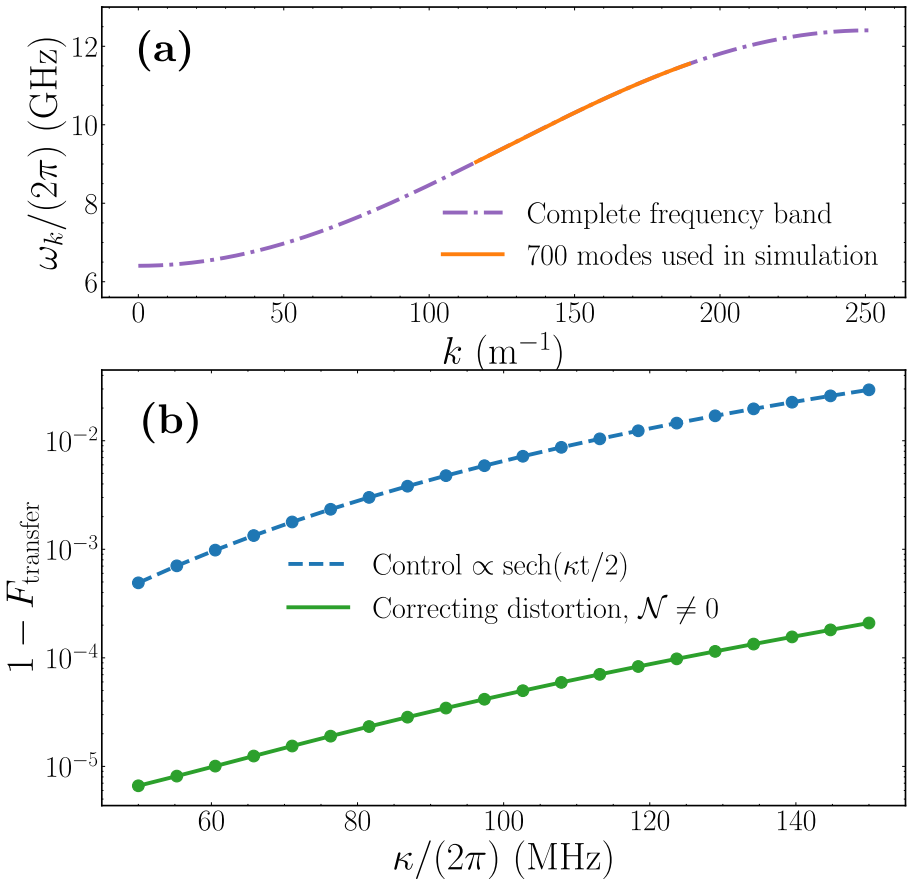

Figure 5.7: (a) Dispersion relation $\omega(k)$ given by Eq. (5.36) (dotted-dashed line). The region highlighted with a solid orange line corresponds to the 700 modes used for the simulation, and is centered around the emitter frequency $\delta/2\pi = 10.406$ GHz where $\omega(k)$ features a negative curvature. (b) State transfer infidelity for $\omega(k)$ (5.36). The points correspond to the numerical results, while the lines are guides to the eyes. In blue, the standard strategy without correction, $g(t) = \kappa/2$ sech$(\kappa t/2)$. In green, the infidelity when the control to generate (5.34) is obtained considering corrections beyond Markov ($\mathcal{N} \neq 0$), and correcting $D = -1.34/2$ ns^{-2} at each of the nodes.

two orders of magnitude. This enhancement underscores the adaptability of the proposed method for accelerating state transfers across different quantum platforms.

In conclusion, it is noteworthy that the method introduced herein is versatile and adaptable across various quantum systems, specifically to quantum links characterized by different dispersion relations, including those with either positive or negative curvature.

5.4 Summary

In this chapter, we introduce two relevant and sophisticated correction mechanisms to improve the fidelity of quantum state transfer in realistic waveguides. The core finding is that near-optimal quantum state transfer is feasible despite coherent distortions encountered within the quantum link. To compensate for the distortions that appear in a medium with non-linear dispersion relations, we derived a new set of control equations that both address the need for complex couplings, while introducing corrections beyond the usual Markovian theory. Both ingredients combine to reduce the infidelity of quantum state transfer for several orders of magnitude in scenarios of practical experimental inter-

est, such as circuit-QED experiments involving long quantum links as those employed in Refs. [SSK+23, QLN+23]. For short quantum links, i.e. in the few-mode limit, infidelities can also be reduced, where the correction would be noticeable in the case of strong non-linear dispersion relations. Note that, albeit adiabatic quantum state transfer is not limited by distortion, such slow protocols are more prone to decoherence, and wavepacket engineering performs similarly or better, even at short distances [PnPR+22].

In the context of shorter quantum links, particularly those in the few-mode regime, the improvements in fidelity are also substantial, especially under conditions of pronounced non-linear dispersion relations. It is important to note that while adiabatic quantum state transfer is not constrained by distortion, such slow protocols are generally more susceptible to decoherence, yet wavepacket engineering often provides equal or superior performance, even over shorter distances [PnPR+22].

This work opens various avenues for further research. From a fundamental perspective, it may be interesting to understand how the theory applies to more general platforms, from photonic crystals to magnonic waveguides. More generally, straightforward continuations include higher-order corrections to the Markovian limit, evidence of which already exists in these simulations. The most ambitious goal would be to push the speed limits of quantum state transfer, seeking interaction strengths and control speeds that challenge the constraints of the current model, such as the rotating-wave approximation.

Another natural extension to everything that has been laid out up until now is to consider multiple emitters sending multiple excitations through the quantum channel. Multiplexing information in these architectures will be essential for future development and scaling, however, everything in this and the previous chapter was single excitation physics. The next chapter delves in detail into the possibility of sending multiple photons and the challenges and obstacles that this poses.

Multiplexation of quantum information in waveguides

6

In this chapter, we present two techniques for multiplexing the communication through a microwave waveguide utilizing single-photon wavepacket shaping methods [PHE+13, FWC+17, KAS+23, YEA+23]. These approaches are examined within a distributed framework involving two remote nodes connected via a quantum link, as experimentally realized in state-of-the-art experiments [KMW+17, MSK+20, SSK+23, QLN+23, GYC+24].

The two multiplexing techniques that we have developed are *mode multiplexing* and *frequency multiplexing*. The first method consists of a spatiotemporal mode multiplexing strategy. This functions by engineering a control for producing a set of orthogonal modes that would work with current single-photon shaping systems [PHE+13, YEA+23]. This method expands the potential for constructing large photonic states [SCS+16, FKB+22] and broad quantum resources. However, it is impractical for communicating more than two qubits coupled resonantly because operating on two orthogonal photons sharing the same carrier frequency leads to interference and cross-talk effects.

The second method changes the focus and proposes a scenario where multiple emitters operate at different wavelengths while maintaining coherent dynamics. This frequency multiplexing technique effectively isolates unwanted interactions between emitters and identifies optimal operating regimes. A detailed study involving 2+2 qubits—two qubits at each of two separate computing nodes sharing a common quantum link—demonstrates the feasibility of simultaneously transferring two photonic qubits with high fidelity. Only a relatively small frequency separation, determined by the photon bandwidth, is required to achieve the excellent fidelities of single-photon state transfer studied in [PPGR23, PnPR+22]. A pessimistic extrapolation of the two-photon case to multiple emitters estimates the information capacity of the waveguide. This is understood as the bandwidth requirements to transmit a given number of qubits below a given overall infidelity. These estimates suggest that current setups support transferring tens of multiplexed qubits with minimal coherent errors, at levels compatible with fault-tolerant quantum computation.

The presentation of the two multiplexing techniques is organized into four sections. Section 6.1 presents the model and introduces the single and double excitation ansätze employed in the simulations. Section 6.2 presents the idea of mode multiplexing, elaborates on the theoretical framework for producing the target family of orthogonal wavepackets, and shares numerical results from quantum state transfer protocols. Section 6.3 explores frequency multiplexing, presenting in-depth numerical simulations of quantum state transfers using two photons to assess its efficacy and predict its scalability with increasing numbers of multiplexed photons and emitters. Lastly, Section 6.4 summarizes the key findings of this study and discusses possible future implications.

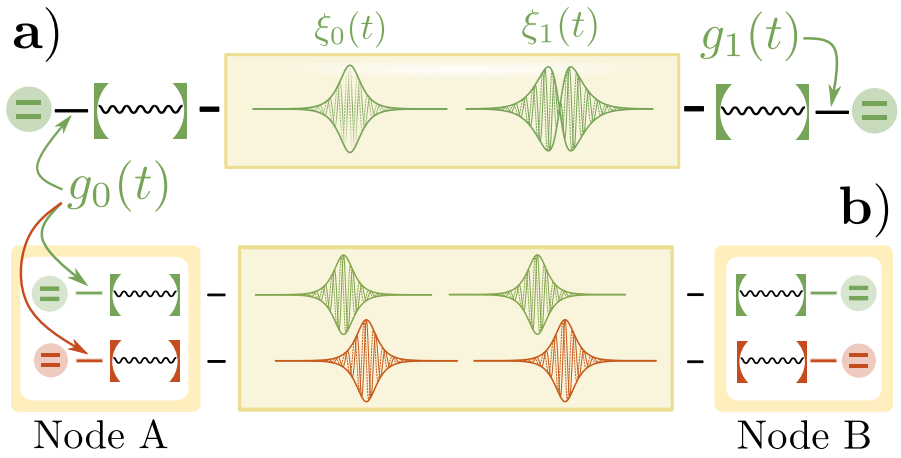

Figure 6.1: Schematic representation of the multiplexation protocols considered in this chapter, namely, mode (a) and frequency multiplexation (b) across a waveguide connecting two nodes. Mode multiplexation is illustrated in (a), where one can apply either $g_0(t)$ or $g_1(t)$ to produce a propagating photon, $\xi_0(t)$, or one that is orthogonal to it, $\xi_1(t)$. At the second node, one can selectively choose to interact with one or the other also by choosing the adequate control. Panel (b) refers to frequency multiplexing, illustrated for nodes containing two qubit-resonator systems each, and chosen to be pairwise resonant, $\delta_1 = \delta_3$ (green qubits), and $\delta_2 = \delta_4$ (red qubits). The photons travel concurrently and do not disturb each other because they have different central frequencies, exploiting the available bandwidth.

6.1 Model

This chapter aims to improve the information capacity of a waveguide-QED quantum link connecting two quantum processors. The proposed theoretical framework for the link assumes two quantum nodes attached to either end of an open waveguide. Each node is equipped with quantum registers comprising one or more qubits. These qubits are individually linked to the waveguide through distinct microwave cavities, serving as frequency filters. This arrangement has been previously implemented in cutting-edge experiments involving superconducting circuits [ELF+12, PHE+13, ZPB+15, KMW+17, MSK+20, SSK+23, QLN+23]. In this study, we expand upon this model to include multiple emitters at each of the two nodes (see Fig. 6.1).

The setup shown in Fig. 6.1 is a figurative representation of the two multiplexing techniques that are introduced in the following sections. First, Fig. 6.1a illustrates photons in orthogonal spatio-temporal wavefunctions. This corresponds to the mode multiplexing method for increasing the channel capacity. Second, Fig. 6.1b pictorially shows the idea of frequency multiplexing, that is, sending simultaneously two flying qubits at different central frequencies. This final proposal requires moving beyond the single-excitation ansatz and developing strategies to effectively manage multiple excitations.

In exploring multiplexing strategies, it is essential to extend the analysis beyond the limit of a single excitation. The smallest problem we need to analyze consists of two qubits per node, exchanging at most two photons. This corresponds to a Wigner-Weisskopf wavefunction with at most two excitations, which, due to the need to work with hundreds of frequency modes, lays at the limit of our computational capabilities—at least when working with exact diagonalization techniques. This two-excitation wavefunction model

is represented by

$$|\Psi(t)\rangle = \Bigg[\sum_{i\neq j} q_{i,j}(t)\sigma_i^+\sigma_j^+ + \sum_{i,j} \zeta_{i,j} c_{i,j}(t) a_i^\dagger a_j^\dagger + \sum_{m,n} \zeta_{m,n}\psi_{m,n}(t) b_m^\dagger b_n^\dagger + \sum_{i,j} q_{i,j}^c(t)\sigma_i^+ a_j^\dagger + \sum_{i,m} q_{i,m}^\psi(t)\sigma_i^+ b_m^\dagger + \sum_{i,m} c_{i,m}^\psi(t) a_i^\dagger b_m^\dagger \Bigg] |\mathbf{0}\rangle \,, \tag{6.1}$$

where $\zeta_{i,i} = 1/\sqrt{2}$, and otherwise 1. By analogy with the notation used for single excitations (cf. Chapter 3, Section 3.1), the terms $q_{i,j}(t), c_{i,j}(t)$, and $\psi_{m,n}(t)$ denote two excitations in the qubits, resonators, or the waveguide, respectively. The wavefunction further accounts for pairs of excitations in different combinations: one in a qubit and one in a filter represented by $q_{i,j}^c(t)$, qubit and waveguide mode $q_{i,m}^\psi(t)$, and a resonator and a waveguide mode $c_{i,m}^\psi(t)$. A critical constraint ensures that no individual qubit contains more than one excitation, as specified by the condition $i \neq j$ in the initial sum. The evolution of the state described in Eq. (6.1) under the general Hamiltonian of the system presented in Chapter 2, cf. Eq. (2.35), leads to a set of coupled differential equations akin to those in Eqs. (3.2)-(3.4).

The case of two excitations is still numerically tractable, as in this subspace of the Hilbert space the size of the evolution matrix scales as $N(N-1) \times N(N-1) \propto N^4$. In this context, N denotes the sum of all elements of the system, N_{qubits}, N_{cavities} and N_{WGmodes}, where the main overhead comes from the number of waveguide modes. Still, as will be shown in the numerical analysis, the 2 excitation ansatz permits simulations with as many as 500 waveguide modes without being too demanding computationally. Simulations will be run in a workstation with 38 cores. The same is not true, however, when scaling to the three excitation subspace, nor when increasing the number of modes. Let us recall again that the method we are using for computing the evolution never constructs the matrix itself, but only the action of the exponential of the matrix acting on the state vector. Without this method, the two excitation examples would already be at the limit of the aforementioned computational capabilities.

The formulation of the time-dependent couplings $g_j(t)$ differs depending on the chosen multiplexing strategy, which will be further elaborated in Section 6.2.1. Now, we turn our attention to the first of the approaches studied in this chapter, mode multiplexing, or the creation of electromagnetic modes that are orthogonal in the time domain.

6.2 Mode multiplexing

Multiplexing is the process of combining two or more information channels into a single transmission medium. This normally involves the use of various degrees of freedom in the channel to increase the capacity, e.g., the time at which the wavepackets are produced. In this section, we describe the first approach that we propose, introducing an additional spatio-temporal dimension, represented by the waveform of the photons traveling through the waveguide [see Fig. 6.1a].

The use of mode multiplexing requires us to generate and absorb photons in different waveforms. As explained in Subsection 6.2.1, each mode from an orthonormal basis $\{\xi_n(t)\}$ will be associated with one control for the emitter qubit and a slightly different one for the receiver qubit. The controls must be discriminative, ensuring that if the j-th qubit is intended to absorb a specific wavepacket shape, it completely rejects photons in orthogonal modes. As discussed in the following subsection, adopting multiple modes demands a departure from traditional wavepacket shaping methods [VVN$^+$17, MSK$^+$20, PnPR$^+$22, PCZL17], which typically involve real-valued positive wavepackets, in favor of more general

designs. These include the possibility of envelopes changing sign, or imprinting phases on demand, as discussed in Chapter 3.

6.2.1 Engineering orthogonal wavepackets

Let us denote as $\{\xi_n(t)\}$ the family of orthogonal modes in the multiplexed channel, where $n = 0, 1, \ldots$ indicates the mode index. These photonic modes form an orthonormal basis, expressed as

$$\langle \xi_n(t), \xi_m(t) \rangle = \int_{-\infty}^{\infty} dt\, \xi_n^*(t)\xi_m(t) = \delta_{n,m}. \tag{6.2}$$

Fulfilling this condition demands that certain modes exhibit non-trivial phase profiles, such as sign changes at specific points. This requirement challenges traditional wavepacket shaping methods that typically rely on real-valued functions for wavepackets and controls throughout their calculations. However, this limitation is not fundamental, complex controls of the form $g(t) \equiv |g(t)|e^{-i\varphi(t)}$ pose no theoretical challenge, and can be engineered with current technologies like qubit-cavity coupling systems [PHE+13].

This problem was tackled in Section 3.2.2 of Chapter 3, when the general equations for the modulus and phase of the control were derived in terms of a general wavepacket, these are Eqs. (3.61), and (3.64). The case of orthogonal wavepackets is a concrete example where this generalization is mandatory. There is no way to satisfy the orthogonal condition (6.2) if one does not allow the envelope to take negative values.

6.2.2 Orthogonal mode state transfer

The minimal instance of mode multiplexing is to communicate nodes through two orthogonal modes. The objective of this subsection is to numerically evaluate the effectiveness of a single-photon state-transfer protocol making use of two orthogonal modes. These modes are generated by the control functions $g_0(t)$ and $g_1(t)$, which were derived as outlined in Chapter 3 and are illustrated in Fig. 6.2.

This analysis aims to verify that quantum state transfer is feasible using any desired orthogonal mode while maintaining its selectivity. This is, whether we can reject an incoming photon with a probability of 100% by receiving it with a control $g_n(t)$ which is orthogonal to that which created it.

As customary in the literature [KMW+17, MSK+20, ABP+18, CZN+18], and also throughout this whole thesis, we start from a sech-pulse

$$\xi_0(t) = \sqrt{\frac{\kappa}{4}}\mathrm{sech}(\kappa t/2), \tag{6.3}$$

and construct the orthonormal family of photon wavepackets associated with it. One can obtain the first orthogonal photon mode by multiplying Eq. (6.3) by a first-degree monomial t. In this case, the orthogonality is guaranteed by the difference in symmetry between both functions, $\int \xi_1^*(t)\xi_0(t)\mathrm{d}t = 0$, this leads to

$$\xi_1(t) = \sqrt{\frac{3\kappa^3}{4\pi^2}}\mathrm{sech}(\kappa t/2)t. \tag{6.4}$$

A larger family of sech-orthogonal photons can be constructed by Gram-Schmidt orthogonalization. For the second orthogonal photon, we could naively increase the order of the monomial

$$\xi_{\perp_2}(t) = \sqrt{\frac{15\kappa^5}{28\pi^4}}\mathrm{sech}(\kappa t/2)t^2 \tag{6.5}$$

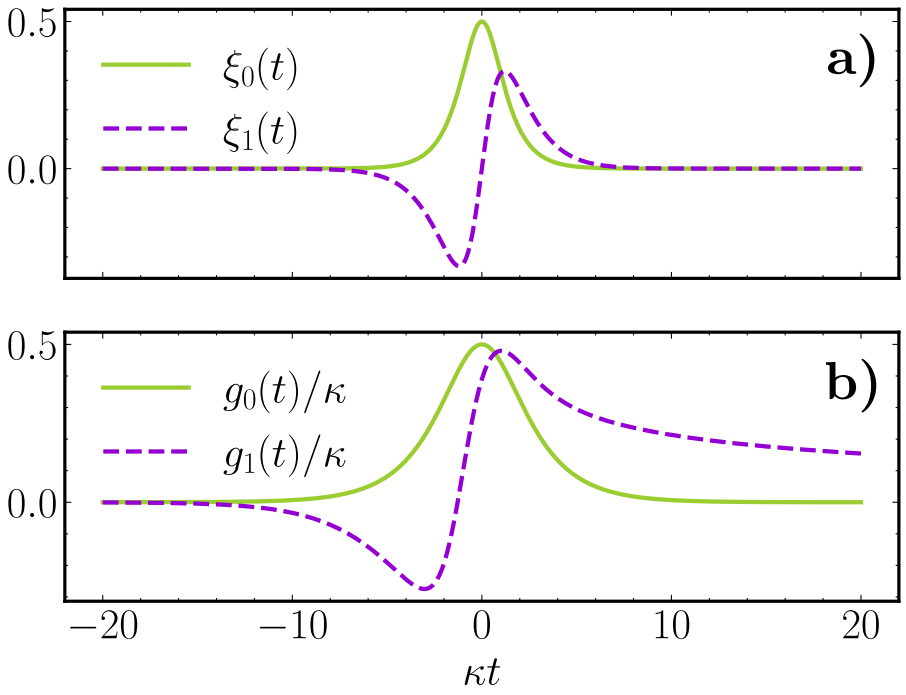

Figure 6.2: Panel a) shows the shape of the first two mutually orthogonal photons from the family $\xi_n(t) \propto \mathrm{sech}(t) \times t^n$, i.e. $\xi_0(t)$ and $\xi_1(t)$. Panel b) shows the corresponding controls to produce them, $g_0(t)$ and $g_1(t)$, respectively. These controls admit an analytical description and are obtained by plugging the wavepackets $\xi_0(t)$ and $\xi_1(t)$ into the Eqs. (3.61), and (3.64).

However, this function is not orthogonal to ξ_0. To ensure that the new proposed photon is orthogonal to all the others one can use the Gram-Schmidt method,

$$\xi_2(t) \propto \xi_{\perp_2} - \langle \xi_{\perp_2}, \xi_0 \rangle \, \xi_0 - \langle \xi_{\perp_2}, \xi_1 \rangle \, \xi_1, \tag{6.6}$$

finally finding $\xi_2(t)$ to be

$$\xi_2(t) = \frac{\sqrt{5\kappa}}{24\pi^2\kappa^2} \, \mathrm{sech}(\kappa t/2) \left(t^2 - \frac{\pi^2}{3\kappa^2} \right) \tag{6.7}$$

Naturally, this technique can be extended to consider polynomial corrections of arbitrary order.

Any of these photon shapes can be plugged into Eqs. (3.61) and (3.64), and obtain from there the analytical formulas of the controls to produce them. We will reproduce again here the formulas for the modulus and phase of the control in terms of the wavepacket for the sake of clarity, they are

$$|g(t)| = \sqrt{\frac{(\dot{f}(t) + \kappa/2 \; f(t))^2 + (\dot{\beta}(t) \; f(t))^2}{\kappa(1 - F(t)) - f^2(t)}}, \tag{6.8}$$

and

$$\varphi(t) = \beta(t) + \phi_f + \mathrm{atan}\left(\frac{\dot{\beta}(t) f^2(t)}{-(\dot{f}(t) f(t) + \kappa/2 f^2(t))} \right) - \int_{t_0}^{t} d\tau \frac{\dot{\beta}(\tau) f^2(\tau)}{\kappa(1 - f(\tau)) - f^2(\tau)}. \tag{6.9}$$

In all cases considered in this chapter, the wavepacket is real $\xi_n \in \mathbb{R}$, and we can set $f_n = \xi_n, \; \beta_n = 0$. The expressions for the controls of the first two orthogonal modes are

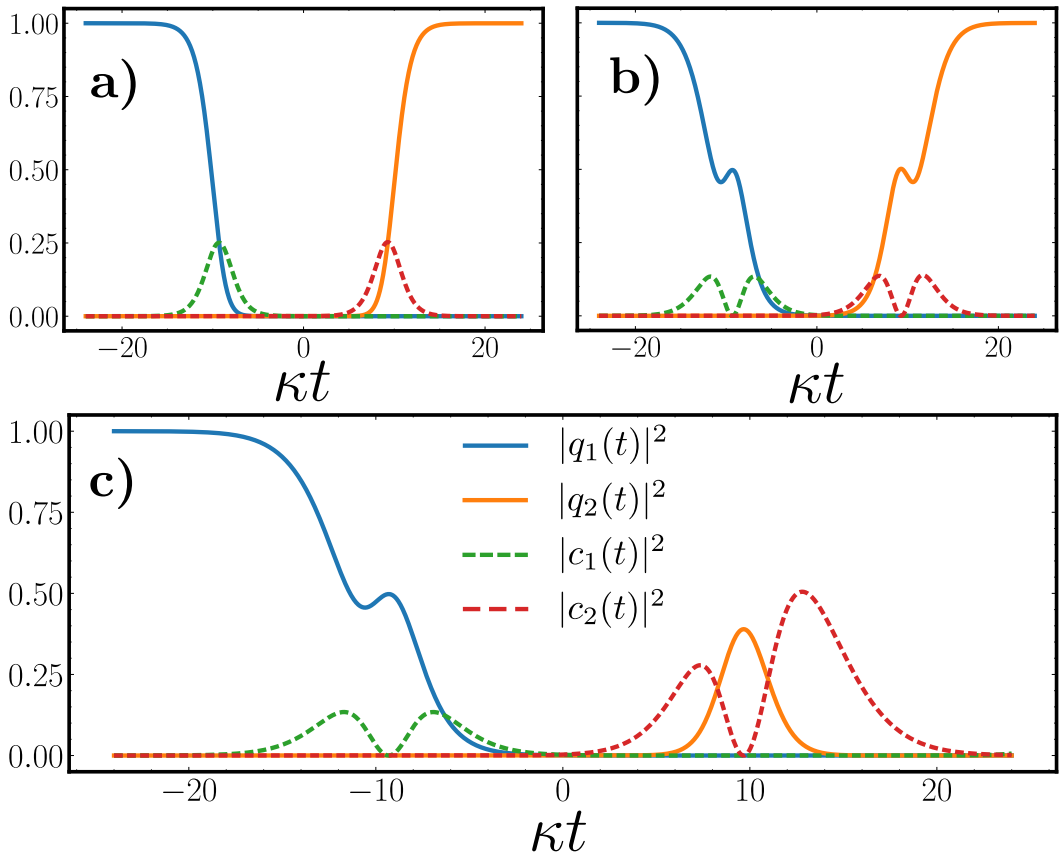

Figure 6.3: Quantum state transfer employing orthogonal wavepackets, showing the evolution of the populations of the qubits and transfer resonators. Panels a) and b) show a standard emission absorption protocol using the same controls at both ends, namely $g_0(t)$ in (a) and $g_1(t)$ in (b), resulting in a transfer efficiency in both cases well over 99%. Panel c) shows the dynamics when a photon $\xi_1(t)$ is emitted using $g_1(t)$, and we apply an orthogonal control $g_0(t)$ at the receiver end. The transfer efficiency in this case drops to $\approx 10^{-5}$. The simulation parameters are: $\delta_{1,2} = \omega_{1,2} = 2\pi \times 8.9$ GHz, $N_{\text{WG}} = 300$, $l_{\text{WG}} = 30$ m, and $\kappa_{1,2} = 2\pi \times 20$MHz.

given by

$$g_0(t) = \frac{\kappa}{2}\text{sech}(\kappa t/2), \text{ and} \tag{6.10}$$

$$g_1(t) = \frac{\kappa(1+e^{\kappa t}+\kappa t)\text{sech}(\kappa t/2)}{D_1}, \text{ where } \quad D_1 = \tag{6.11}$$

$$(1+e^{\kappa t})\sqrt{-8\text{Li}_2(-e^{-\kappa t})+\kappa t\left[2\kappa t+8\log(1+e^{-\kappa t})-\kappa t\text{sech}^2\left(\kappa t/2\right)\left(1+\sinh(\kappa t)\right)\right]},$$

with the special function $\text{Li}_n(x) = \sum_{k=1}^{\infty} x^k/k^n$. These controls are displayed in Fig. 6.2b and they produce the wavepackets $\xi_0(t)$ and $\xi_1(t)$ shown in Fig. 6.2a. Observe the change of sign in $\xi_1(t)$, a wavepacket of this nature cannot be generated by a non-negative coupling $g_1(t) = |g_1(t)|$. Nevertheless, the approach presented here still yields a smooth and real control, where the phase $\varphi(t) = 0, \pi$ merely indicates a sign shift in $g(t)$. The point at which the control changes sign is not obvious, since it depends on the profile of the wavepacket, and also on the more involved term $\dot{f}(t)f(t) + \kappa/2 f^2(t)$ in Eq. (3.64).

We have studied the transfer of information among two nodes using the previous modes. The first study relies on the transfer of a single qubit using either ξ_0 or ξ_1, with adequate

controls at the receiving port. In Fig. 6.3, we present the results of a numerical simulation for the single-qubit state-transfer protocol that incorporates two orthogonal modes in three different situations. The upper two panels illustrate that employing the same control, $g(t)$, at both ends of the system, results in a high-fidelity transfer. It is important to note that the state transfer is not perfect owing to wavepacket distortion effects, and the other source of imperfections detailed in Chapter 4. Although the correction methods proposed in Chapter 5 might enhance the results, they were omitted here to facilitate a direct comparison with the single-mode strategy.

The fidelity of the process is quantified by the probability of completely transferring the excited state of the emitting qubit at one end, $|q_1(0)|^2 = 1$, to the receiving qubit at the other, $|q_2(T)|^2$. The simulations depicted in Fig. 6.3 c) validate the selective aspect of the controls, which, when configured for a specific photon mode $\xi_0(t)$, effectively reject photons arriving in a different mode $\xi_1(t)$. Though not depicted, the reverse scenario with emission by $g_0(t)$ and absorption through $g_1(t)$ yields the same results. Finally, we note that the method is extensible to any arbitrary mode functions, $\xi_n(t)$.

It is important to note that the photon that is rejected undergoes significant distortion due to its interaction with the second qubit. Although the wavefront is not explicitly shown in Fig. 6.3c, it is possible to infer both the original wavepacket $|\xi_1(t)|^2 \propto \kappa_1|c_1(t)|^2$ and its altered form $|\xi_1(t)'|^2 \propto \kappa_2|c_2(t)|^2$ using input-output theory based on the population profiles of the cavities (dashed lines). There is a notable asymmetry in the distortion at the right-hand node, which makes the photon notably distinct from its original profile [cf. Fig. 6.3c, red dashed line]. We devote the next subsection to analyzing this effect and its possible implications in mode multiplexing.

6.2.3 Orthogonal mode state scattering

The distortion observed in Fig. 6.3c is completely accounted for by the interaction between the photon wavepacket and the resonant qubit-filter node. During the reflection, the photon, although being rejected, interacts with the qubit and undergoes a phase shift. This process was already studied in Chapter 4 and the distortion it causes is captured in Eq. (4.19). This section aims to examine what happens when a photon ξ scatters off a qubit-resonator node which is using a control $g(t)$ designed to absorb a different photon mode. The previous subsection already shows how the absorption gets completely suppressed, the objective now is to understand how this rejection affects the envelope of the wavepacket.

The analysis is based on numerical experiments with the two wavepacket shapes $\xi_{0,1}(t)$ (6.3)-(6.4) from the previous section. The study compares the scattering phases acquired by the two modes in frequency space. First, in an experiment with a bare resonator, and second, in a situation with a resonator-qubit using a time-dependent control $g(t)$. The numerical experiment is designed with broadband wavepackets so that the photon completely fits inside the waveguide. The idea is to compare the photon shape before and after scattering. This comparison is performed in frequency space, where the probability of the different waveguide modes is undisturbed and only scattering phases are acquired.

The data displayed in Fig. 6.4 illustrates the scattering phases after the interaction with a bare cavity— Panel a), top— and with a cavity and a qubit— Panel b), bottom—. The phases acquired by the interaction with a single resonator, shown in Fig. 6.4a are independent of the incoming mode, $\xi_0(t)$ or $\xi_1(t)$, and are compatible with the expected phases from an input-output theory calculation (cf. Section 4.1.2 of Chapter 4)

$$e^{i\phi_{scatt}(\omega)} = \frac{i(\omega - \Omega_{R2}) + \kappa_2/2}{i(\omega - \Omega_{R2}) - \kappa_2/2}. \tag{6.12}$$

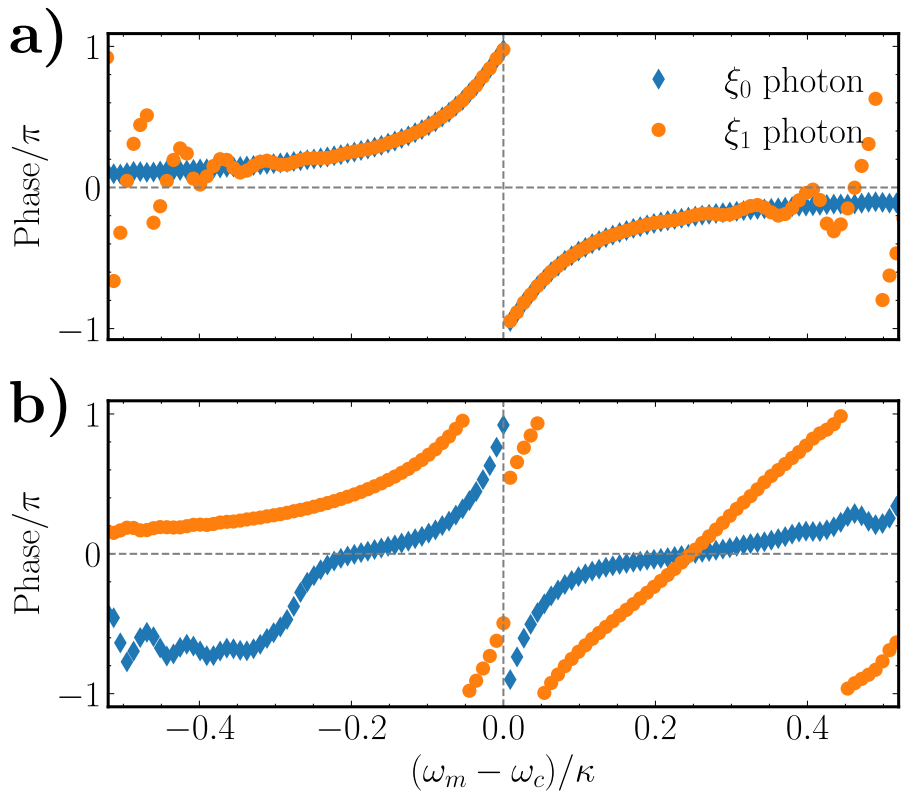

Figure 6.4: Orthogonal photonic modes scattering. Panel a) shows the result of comparing the ξ_0 and ξ_1 photons after scattering off a resonator with no active control. Panel b) shows the phases acquired by ξ_0 after scattering off a qubit-resonator system with dynamic coupling $g_1(t)$ (blue dots), and those acquired by ξ_1 when at the other end $g_0(t)$ is applied (orange dots). Parameters of the simulation: $l = 30$ m, $\kappa = 2\pi \times 60$ MHz. $N_{\text{WG}} = 300$ modes around a central frequency of $\omega_c = 2\pi \times 8.9$ GHz. Of those 300 modes only the 40 modes closest to the emitter's frequency are displayed, which correspond to a bandwidth of approximately κ.

Panel b) reveals a completely different behavior. It displays the phase acquired by a photon in mode $\xi_0(t)$ when the cavity-filter interaction follows protocol $g_1(t)$ (blue diamonds) and the phase acquired by a photon in mode $\xi_1(t)$ when $g_0(t)$ is used (orange dots). Now the scattering phases are affected by the type of control $g(t)$, imprinting a distortion that is markedly different from the photon-cavity collisional phase. This said, the phase profiles can still be computed and used to learn the shape of the reflected photon. This would allow for engineering controls that could fix this distortion.

The methods described in Chapter 5 for correcting distortion using $g(t) \in \mathbb{C}$ can be applied to this context. The core of the method relies on imprinting on-demand phases on the wavepacket to fix distortion, which is what this physics of scattering requires. This underpins the assertion that mode multiplexing applies to broadband-based protocols for generating high-dimensional photonic states, such as those proposed in [FKB+22].

6.2.4 Mode multiplexing conclusions

Nonetheless, while the multiplexing of a single photon mode is effective, generating two resonant photons in two orthogonal modes simultaneously proves unfeasible. The use of two resonant emitters, each equipped with their distinct controls $g_0(t)$ and $g_1(t)$, leads to significant cross-talk and degradation of the photons produced. Essentially, what happens

is that activating two couplings g_0 and g_1 at the same point and the same energy leads to population exchange between the emitters, even if these couplings have very different time profiles. The natural remedy for this issue is to separate the emitters in frequency space, thereby minimizing their interaction. This different approach introduces a new variant of multiplexing, termed frequency-type multiplexing, which is explored in the following section.

6.3 Frequency multiplexing

The second method for communication multiplexing discussed in this chapter uses the carrier frequency of the photon as an additional degree of freedom, it involves transmitting multiple qubits, with each qubit encoded onto a distinct photon characterized by its unique carrier frequency. In this section, we examine the efficacy of frequency multiplexing within microwave experiments that utilize microwave guides. The cutting-edge experiments guiding the analysis (see Refs. [KMW$^+$17, MSK$^+$20]) predominantly operate within the X-band, encompassing a bandwidth of 4 GHz (approximately 8-12 GHz). This bandwidth can accommodate several photons, each having a width of several MHz.

This setup features two nodes, each comprising a pair of frequency-matched qubits (cf. Fig. 6.1b). Qubits 1 and 2 are located at the first node, while qubits 3 and 4 are at the second node, with corresponding frequencies and resonator frequencies matched as follows: $\delta_1 = \omega_{R1} = \delta_3 = \omega_{R3}$, and $\delta_2 = \omega_{R2} = \delta_3 = \omega_{R3}$. The exact analysis concentrates on the subspaces for single and double excitations, adequately representing the state transfer capabilities for up to two qubits. The dynamics within these subspaces are precisely described by the wavefunctions for a single excitation, given by Eq. (3.1) and for 2 excitations, cf. Eq. (6.1).

The goal for the rest of the chapter is to analyze the errors arising from transmitting two qubits at different frequencies. Two primary types of errors are expected to appear in this scenario: one due to the indistinguishability of the photons associated with each qubit, and another stemming from the cross-talk between qubits and resonators operating at close frequencies. It is expected that these errors will diminish as the carrier frequency separation increases beyond the bandwidth of the individual photons, expressed as $\Delta_{12} \equiv |\delta_1 - \delta_2| \gg \kappa$. This intuition will lead us to use the control $g(t)$ derived for the single photon case to the multiplexed scenario. However, when the detuning Δ_{12} is small, we do not expect good fidelities employing the same control. This is why we will devote the following subsection to explore in some detail the physics of two excitations with small detuning. Once this is understood, the objective is to assess the fidelity of two-photon quantum state transfer and ultimately of the N-photon case.

6.3.1 Emitters cross-talk

When multiple qubits and filters are connected to the same environment, such as a waveguide, there exists a possibility that these quantum objects affect one another, even if their resonance frequencies are significantly different. This effect, commonly referred to as cross-talk, can manifest either as an actual transfer of energy—for example, an excitation located at qubit 1 might jump to site 2 and vice versa—or as alterations in the inherent properties of the emitters—such as the renormalization of their frequencies and decay rates.

A numerical exploration of the protocol at different detunings shows that the presence of multiple qubits and filters affects the intrinsic frequencies of all neighboring circuits. This influence can be summarized as a recalibration of the frequency of the resonators, a modification of the decay rates, and a coherent exchange of population between them.

Because all these effects occur only at the resonator-waveguide level, we chose to study them with an effective model ignoring the qubits. Also, for the sake of simplicity, we will drop the subindex R of the frequencies of the resonators throughout this subsection, and denote the waveguide frequencies as Ω_m. The Hamiltonian of such an effective model is

$$H = \sum_{i=1,2} \omega_i a_i^\dagger a_i + \sum_m \Omega_m b_m^\dagger b_m + \sum_{m,i=1,2} G_{m,i} \left(a_i^\dagger b_m + \text{H.c.} \right). \tag{6.13}$$

The calculation consists of two parts, first, departing from Eq. (6.13) and getting rid of the waveguide modes, the idea is to obtain an effective Hamiltonian for the resonators and a closed expression for the Lamb shift. Once with such Hamiltonian, the objective is to study how the exchange terms $a_i^\dagger a_j$ with $i \neq j$ affect perturbatively the energy of the resonators.

The first step is to move to an interaction picture that rotates with the free energies of resonator and waveguide modes, that way, Eq. (6.13) becomes

$$H^I = \sum_{m,i} G_{m,i} \left(a_i^\dagger b_m e^{+it(\omega_i - \Omega_m)} + a_i b_m^\dagger e^{-it(\omega_i - \Omega_m)} \right). \tag{6.14}$$

In this picture the equations of motion for the operators are

$$\begin{aligned}
\dot{a}_j &= i\left[H, a_j\right] = -i \sum_m G_{mj} b_m e^{+it(\omega_j - \Omega_m)}, \\
\dot{b}_m &= i\left[H, b_m\right] = -i \sum_j G_{mj} a_j e^{-it(\omega_j - \Omega_m)}, \quad \text{so that,} \\
b_m(t) &= b_m(0) - i \sum_j G_{mj} \int_0^t d\tau a_j(\tau) e^{-i\tau(\omega_j - \Omega_m)},
\end{aligned}$$

where we have changed the dummy index i by j for the sake of clarity. Substituting this formal solution for $b_m(t)$ in the Hamiltonian, and focusing now only on the first term yields

$$H^I = -i \sum_{i,j} a_i^\dagger e^{+it\omega_i} \int_0^t d\tau K(t-\tau) a_j(\tau) e^{-i\tau\omega_j} + \text{H.c.}\,; \tag{6.15}$$

$$\text{where} \quad K(t-\tau) = \sum_m G_{m,i} G_{m,j} e^{-i\Omega_m(t-\tau)}. \tag{6.16}$$

Recalling again the separation of time scales method introduced in Chapter 3 and exemplified by the expression Eq. (3.8). Separating the time evolution of the operator a as a slow contribution $a_j(t) = a_{j,slow}(t) e^{-i\omega_j' t} = a_{j,slow} e^{-i\omega_j t} e^{-i\omega_j' t}$ with an unknown frequency ω_j', and introducing $u = t - \tau$, the previous Hamiltonian becomes

$$H^I = -i \sum_{i,j} a_i^\dagger e^{+it\omega_i} a_{j,slow} e^{-it\omega_j} \int_0^{+\infty} du K(u) e^{i\omega_j' u} e^{-i\omega_j' t} + \text{H.c.} \tag{6.17}$$

Now, undoing the transformation to the interaction picture, using that $a_{j,slow} e^{-i\omega_j' t} = a_j$, and grouping terms appropriately leads to

$$H_{\text{eff}} = \sum_i (\omega_i + \delta\omega_i) a_i^\dagger a_i + \tilde{G} \left(a_1 a_2^\dagger + a_1^\dagger a_2 \right). \tag{6.18}$$

The Lamb shift and effective coupling are defined through

$$\delta\omega_i = \frac{1}{2\pi} \int_0^\infty \int J_i(\omega) e^{i(\omega_i' - \omega)u} d\omega du, \tag{6.19}$$

$$\tilde{G} = \frac{1}{2\pi}\int_0^\infty \int \sqrt{J_i(\omega)}\sqrt{J_j(\omega)}\, e^{i(\omega_i'-\omega)u} d\omega du, \quad \text{with} \tag{6.20}$$

$$J_i(\omega) = 2\pi \sum_m |G_{m,i}|^2 \delta(\omega - \Omega_m). \tag{6.21}$$

The obtainment of the expression (6.18) finishes the first part of the calculation and qualitatively explains the physics of the system in the region where the detuning is very small.

The Hamiltonian (6.18) illustrates two primary effects. The change of the natural frequency of the resonators, denoted by $\delta\omega_{Ri}$, and the emergence of a coherent coupling between these two resonators, represented by $\tilde{G}$. The resonator energy shift modifies the carrier frequency of the flying qubits, which, in turn, impacts the probability of successful absorption, and therefore, the state transfer fidelity. Additionally, the exchange term G opens up the transfer of energy between qubits 1 and 2, effectively scrambling the information being transmitted.

Further examination of Eq. (6.18) indicates that in the scenario where the separation between modes is less than the bandwidth of the filters, $|\omega_{R2} - \omega_{R1}| \ll \kappa$, the exchange terms $a_i a_j^\dagger$ predominantly govern the dynamics. Notably, in this context, the infidelity of photon emission/absorption can be approximated by considering the frequency overlap of the produced wavepackets. This overlap reflects the frequency indistinguishability, which correlates with the probability of photons from one resonator entering into the adjacent resonator. A detailed assessment of this process, underpinned by numerical simulations, is presented in Section 6.3.3.

Intuitively, one expects frequency multiplexing to become more accurate when the emitters and resonators are well separated in energy space. This question may be formally analyzed as a perturbative limit of the previous model in the limit of large detuning $|\omega_{R2} - \omega_{R1}| \ll \kappa$, using a Magnus expansion [Mag54, BCOR98] of the Hamiltonian (6.18). Moving once more to an interaction picture, rotating at the dressed frequencies of the resonators $\omega_i^D = \omega_i + \delta\omega_i$, the expression (6.18) transforms to

$$H_{\text{eff}} = \sum_i \omega_i^D a_i^\dagger a_i + \tilde{G}\left(a_1 a_2^\dagger + a_1^\dagger a_2\right) \longrightarrow$$

$$H_{\text{eff}}^I = \tilde{G}\left(a_1 a_2^\dagger e^{+it(\omega_2^D - \omega_1^D)} + a_1^\dagger a_2 e^{-it(\omega_2^D - \omega_1^D)}\right). \tag{6.22}$$

Given that ω_2^D and ω_1^D are sufficiently far apart, a second-order Magnus expansion is utilized to explore potential new renormalizations of frequencies.

The second order of the Magnus expansion is

$$M_2(t) = \frac{1}{2}\int_0^t dt_1 \int_0^{t_1} dt_2 \left[H_{\text{eff}}^I(t_1), H_{\text{eff}}^I(t_2)\right]. \tag{6.23}$$

The integral coming from explicitly computing the commutators of the first term yields

$$\frac{1}{2}\tilde{G}\left(-a_1^\dagger a_1 + a_2^\dagger a_2\right)\int_0^t dt_1 \int_0^{t_1} dt_2 e^{+it_1(\omega_2^D - \omega_1^D)} e^{-it_2(\omega_2^D - \omega_1^D)} = \tag{6.24}$$

$$\frac{1}{2}\tilde{G}\left(-a_1^\dagger a_1 + a_2^\dagger a_2\right)\int_0^t dt_1 \frac{i}{\omega_2^D - \omega_1^D}\left(1 - e^{+it_1(\omega_2^D - \omega_1^D)}\right) = \tag{6.25}$$

$$= -i\frac{1}{2}\frac{\tilde{G}^2}{\omega_2^D - \omega_1^D}\left(a_1^\dagger a_1 + (-a_2^\dagger a_2)\right)t + (\text{terms} \not\propto t). \tag{6.26}$$

A minus sign from the exponential cancels out with the minus sign in the second commutator, giving the same result, and therefore adding up. Taking all this into account, the

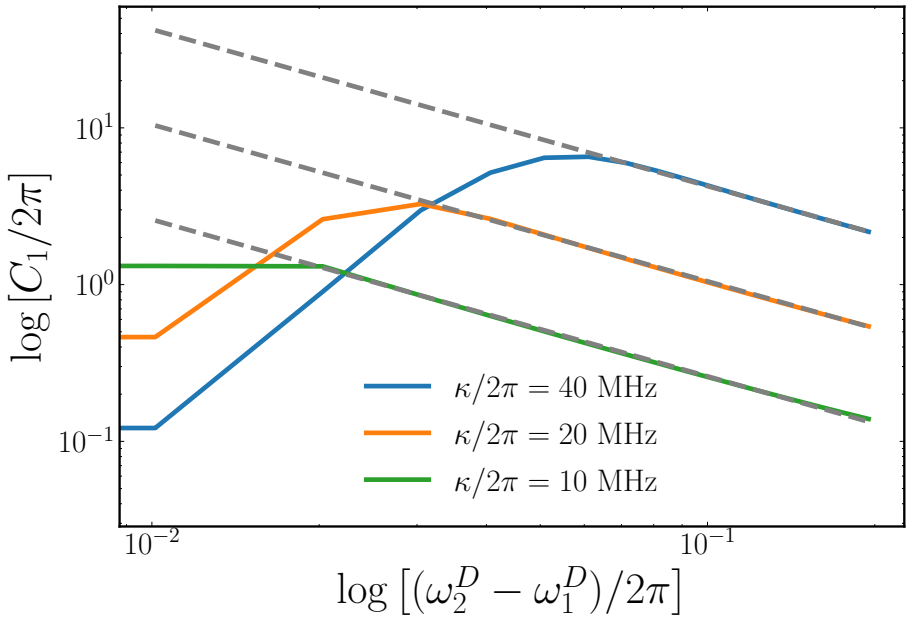

Figure 6.5: Frequency shift of the resonator 1 (arbitrary labeling) induced by the presence of the physically identical resonator 2 for three different values of the κ. We can estimate the value of $\tilde{G}^2$ from the slope of the dashed lines. The parameters of the simulation are $l = 30$m to avoid discrimination of the mode structure of the waveguide by any of the three resonator widths. We do spectroscopy of the resonator with a depletion experiment using as our control $g(t) = \kappa_{\text{eff}}/2 \operatorname{sech}(t\kappa_{\text{eff}}/2)$, where $\kappa_{\text{eff}} = \kappa$.

final Hamiltonian up to second order in the Magnus expansion has the simple form

$$\tilde{H}_{\text{eff}} = \sum_i C_i a_i^\dagger a_i, \text{ with } C_i = (-1)^{i+1} \frac{\tilde{G}^2}{\omega_2^D - \omega_1^D}. \tag{6.27}$$

The perturbative Hamiltonian (6.27) reveals the transformation of cross-talk into a Stark shift that moves the resonator frequencies up or down, depending on the location of its neighboring circuits, note that this shift is different from the Lamb shift, which is already taken into account in the definition of the dressed frequencies ω_i^D.

The presence of these effective Stark shifts is confirmed by accurate simulations of a 2+2 resonator and qubit system, starting with an excitation in qubit 1 and depleting it. The data shown in Fig. 6.5 represents the value of the coefficient C_1, starting in a regime where the physics is dominated by exchange terms and depletion spectroscopy is ineffective. However, as the condition $(\omega_2^D - \omega_1^D) \approx 2\kappa$ is met, the observed frequency shift aligns well with the predictions made by the effective Hamiltonian (6.22), as depicted by the straight dashed lines. This agreement is very informative because the effective model was derived considering only the resonators, while the numerical results in Fig. 6.5 utilize the complete Hamiltonian, including qubits and time-dependent controls $g(t)$. It indeed confirms our hypothesis that the effects of cross-talk can be analyzed by studying the only objects that couple to a common bath, namely the waveguide.

The study of qubit depletion experiments provides information not only about the resonator's energy shifts but also on changes in the resonator's effective bandwidth, κ, a value that must be very accurately calibrated to achieve the highest state transfer fidelity possible. We show, in Fig. 6.6, a depletion experiment in which we compare the values of the frequency and effective decay rate between a situation with two resonators (blue lines) and one with a single resonator (pink line). The y-axis represents the level of depletion of

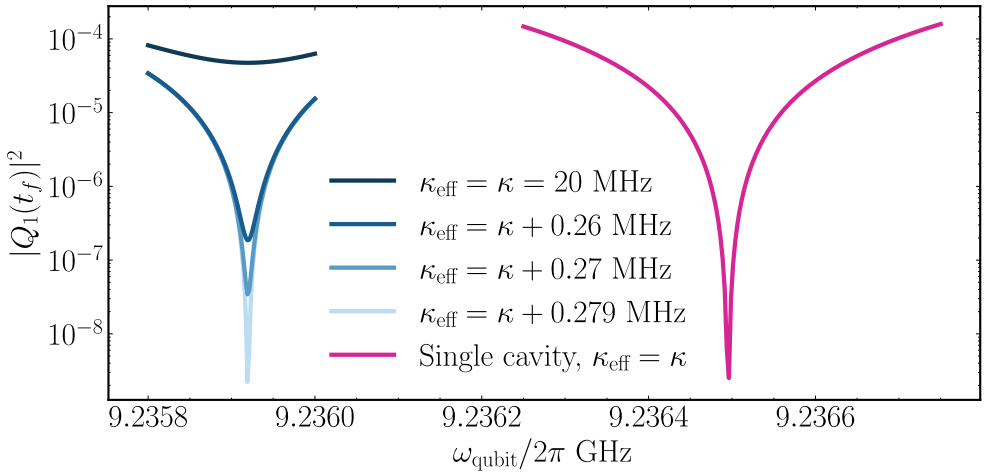

Figure 6.6: Depletion of qubit 1 (arbitrary labeling) when there is only one resonator connected at node 1 (pink line) versus when there are two (blue lines). In all cases with two resonators, they are connected at the same spacial points but with a large detuning of $(\omega_1 - \omega_2) = 2\pi \times 200$ MHz, or around 20κ. We run a qubit depletion experiment using as our control $g(t) = \kappa_{\text{eff}}/2 \text{ sech}(t\kappa_{\text{eff}}/2)$. This is all computed after the $\delta\omega$ has already been optimized. Numerical: $l = 30$ m, $N_{\text{modes}} = 390$.

the qubit. The numerical experiment shows that first, the frequency of the qubit has to be changed between one situation to the other, i.e., $\delta\omega$ changes when introducing an extra resonator. Second, the value of κ also has to be finely tuned. Once the qubit is rightly placed in frequency, keeping the width of the control κ_{eff} equal to the decay of the bare resonator κ leads to a depletion of only 10^{-4} (dark blue line). On the other hand, adding corrections to this parameter improves the depletion by over 4 orders of magnitude (pale blue line). As demonstrated in Fig. 6.6, even a slight misalignment in this parameter, about 1%, can result in a five-orders-of-magnitude reduction in depletion efficiency.

The process depicted in Fig. 6.6 is important, and it is a necessary first step for all state transfer experiments done in the following section. Because the inclusion of extra qubits and resonators affects the frequencies and decays, before running a state transfer experiment we perform a calibration procedure. This essentially consists of using the control $g_1(t) = \kappa_{\text{eff}}/2 \text{ sech}(\kappa_{\text{eff}}t/2)$ over a qubit with an initial frequency δ_1, and run many instances varying both κ_{eff} and δ_1 until we achieve good enough depletion. In this particular case, the optimizer is set to stop at a depletion value of $|q_1(t_f)| = 10^{-9}$. For the sake of simplicity, Fig. 6.6 shows a sweep over the values of κ_{eff} once the frequency has already been optimized. In practice, however, the optimization is done over both parameters simultaneously.

The outcomes of this section are promising. First, the application of the spectroscopy method enables the identification of the dressed properties of the cavity. Second, despite these properties being influenced by cross-talk, the simulations demonstrate that almost perfect depletion can still be achieved by adjusting the control parameters $g_i(t)$ to adapt to the altered conditions of the flying qubits. A significant question that remains is whether these effective renormalizations accurately represent the dynamics when multiple flying qubits are involved. To answer this, the next subsection is devoted to careful two-photon state transfer simulations.

6.3.2 Multiplexed state transfer tomography

The most basic configuration for investigating frequency multiplexing, illustrated in Fig. 6.1b, involves two sets of qubits, with each set containing resonant pairs. Qubits 1 and 2 are located at node A, while qubits 3 and 4 are at node B, and their frequencies are set according to $\delta_1 = \delta_3$ and $\delta_2 = \delta_4$. Ideally, the state transfer mechanism, represented by the unitary U_{ideal}, would map any state of each qubit at node A to its counterpart at node B in such a way that

$$\begin{aligned} &U_{\text{ideal}}\left[(\alpha\left|0\right\rangle_1 + \beta\left|1\right\rangle_1)(\delta\left|0\right\rangle_2 + \gamma\left|1\right\rangle_2) \otimes \left|0\right\rangle_3\left|0\right\rangle_4 \otimes \left|\mathbf{0}\right\rangle\right] \\ &\quad = \left|0\right\rangle_1\left|0\right\rangle_2 \otimes (\alpha\left|0\right\rangle_3 + \beta\left|1\right\rangle_3)(\delta\left|0\right\rangle_4 + \gamma\left|1\right\rangle_4) \otimes \left|\mathbf{0}\right\rangle. \end{aligned} \tag{6.28}$$

Each coefficient $\alpha, \beta, \gamma, \delta$ adheres to the normalization conditions $|\alpha|^2+|\beta|^2 = |\gamma|^2+|\delta|^2 = 1$. The first four indices refer to the qubits, with the final, bold index indicating the bosonic modes, which are consistently in the vacuum state at the start and conclusion of the process.

A protocol that fulfills this equation completely maps the information stored in the $d = 4$ states of the first node's computational basis $|i, A\rangle \in \{|00\ 00\ \mathbf{0}\rangle, |01\ 00\ \mathbf{0}\rangle, |10\ 00\ \mathbf{0}\rangle, |11\ 00\ \mathbf{0}\rangle\}$, to the four corresponding computational states of the second node $|i, B\rangle \in \{|00\ 00\ \mathbf{0}\rangle,\ |00\ 01\ \mathbf{0}\rangle,\ |00\ 10\ \mathbf{0}\rangle,\ |00\ 11\ \mathbf{0}\rangle\}$. The following isometry captures this ideal transformation

$$U_{\text{ideal}} = \sum_{i=1}^{d} |i, B\rangle\langle i, A|. \tag{6.29}$$

To characterize the experimental setup, we only need to reconstruct the isometry that maps the four input states $|i, A\rangle$ to other states of the quantum links and nodes

$$U_{\text{real}} = \sum_{i,j=1}^{d} \chi_{i,j}\, |i, B\rangle\langle j, A| + \Upsilon. \tag{6.30}$$

The coefficients $\chi_{i,j}$ will not be the identity. There is leakage to other states in the Hilbert space—e.g., photons that are not absorbed in the receiver qubits and wander through the waveguide or return to the original station, as well as imperfections in the emission process that leave the emitting qubit with a residual population. The additional term Υ represents the aggregate of all these effects. In particular, $\Upsilon = \sum_{i,j,x\notin B} \upsilon_{i,j}\, |i, x\rangle\, \langle j, A|$, where $|i, x \notin B\rangle$ spans all states containing at least one excitation in an element outside the qubits at node B, i.e. in any waveguide mode, resonator or in any qubit at node A.

Errors in state transfer can be quantified using either entanglement fidelity $\mathcal{F}_{\text{ST}}^{(e)}$ or average fidelity $\bar{\mathcal{F}}_{\text{ST}}$. These metrics are defined as follows [Nie02, PMM07]:

$$\begin{aligned} \mathcal{F}_{\text{ST}}^{(e)} &= \left|\frac{1}{d}\text{Tr}\left(U_{\text{ideal}}^{\dagger} U_{\text{real}}\right)\right|^2 = \frac{1}{d^2}\left|\sum_{i=1}^{d} \langle i, A|U_{\text{ideal}}^{\dagger} U_{\text{real}}|i, A\rangle\right|^2, \\ \bar{\mathcal{F}}_{\text{ST}} &= \frac{d\mathcal{F}_{\text{ST}}^{(e)} + 1}{d+1}, \end{aligned} \tag{6.31}$$

where the dimension of the computational input and output spaces is $d = 4$. The focus will be on using the entanglement fidelity $\mathcal{F}_{\text{ST}}^{(e)}$.

In numerical simulations, the fidelities of state transfer exhibit an oscillating behavior as a function of the frequency detuning between qubits 1 and 2. This behavior can be explained by dynamical phases acquired by the different states in the computational basis due to the frequency difference among those states. However, these are phases that can be compensated for by applying local rotations on the individual qubits, either before or

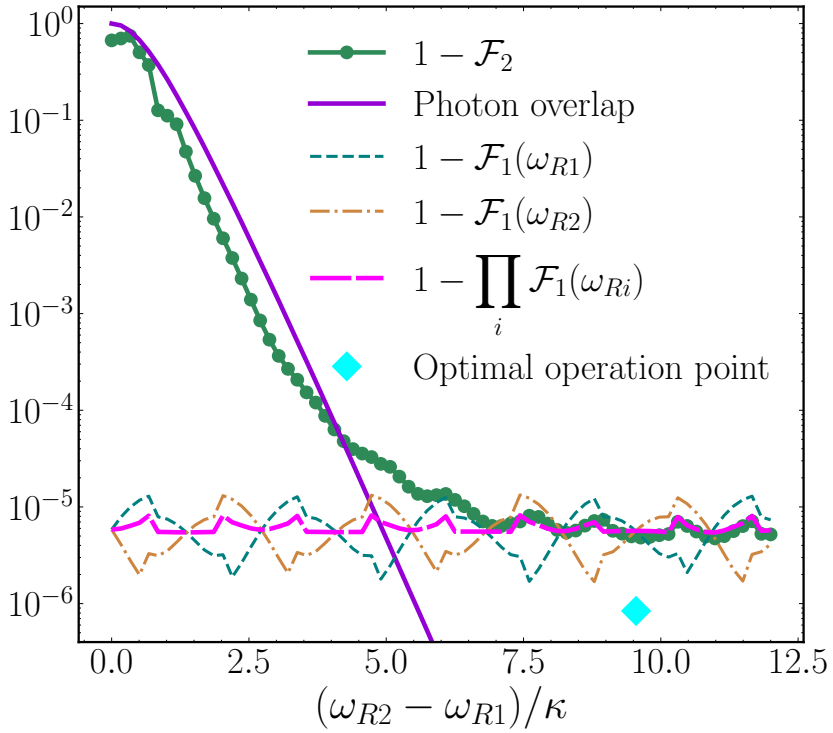

Figure 6.7: Quantum state transfer protocol errors for two emitters as a function of their frequency separation. We plot the actual infidelity from Eq. (6.32) (solid-dot) for multiplexed transfer; the single qubit infidelities for each emitter separately $1-\mathcal{F}(\omega_{R1,R2})$ (dashed and dot-dashed), and the lower bound for the multiplexed infidelity $1 - \mathcal{F}(\omega_{R1})\mathcal{F}(\omega_{R2})$ (long dash). As an illustration, we also plot the optimized infidelity of multiplexed state transfer (big light-blue diamond) for a particular frequency separation. The solid line is a visual guide given by the photon wavepacket overlap, that is, by Eq. (6.33). Qubit frequencies are symmetrically placed around $(\omega_{R1} + \omega_{R2})/2 = 2\pi \times 8.9$ GHz. The simulations were performed using $N_{\rm WG} = 500$ modes, a $l_{\rm WG} = 15$ m long waveguide, a resonator bare decay rates of $\kappa = 2\pi \times 10$ MHz, a hyperbolic secant control $g(t) = \kappa_{\rm eff}/2{\rm sech}(\kappa_{\rm eff}t/2)$ and a protocol duration $t \in (-35/\kappa, +35/\kappa)$.

after the state transfer. Hence, we introduce the corrected two-photon fidelities as those resulting from the maximization over those corrections

$$\mathcal{F}_2 = \max_{\phi_0,\phi_1,\phi_2} \mathcal{F}^{(e)}_{\rm ST}\left[e^{i\phi_0 + i\phi_1\sigma_1^z + i\phi_2\sigma_2^z}U_{\rm real}\right]. \tag{6.32}$$

Fortunately, this optimization is trivially performed by inferring the effective single- and two-qubit phases from $\chi_{i,j}$.

The study of the next subsection aims to assess the accuracy of multiplexed two-qubit state transfer as well as the fidelity of single-qubit processes. Additionally, it will evaluate the performance of systems that consider more than two flying qubits. The fidelity of state transfer involving one emitter on each side will be represented by $\mathcal{F}_1(\omega)$.

6.3.3 Two-photon state transfer performance

As in the mode multiplexing case, the simplest problem in which one may test the frequency multiplexing method consists of two nodes with 2+2 emitter and receiver qubits. This model can be simulated accurately with the ansatz (6.1) presented at the beginning of the chapter. The analysis will focus on a waveguide of $l_{\rm WG} = 15$ meters, which

utilizes $N_{\mathrm{WG}} = 500$ frequency modes. The analysis explores how the fidelity improves with the frequency separation of the flying qubits, starting from a resonant case $\omega_1 = \omega_2$ until their separation significantly exceeds the bandwidth $|\omega_1 - \omega_2| = 12\kappa$. The intrinsic frequencies of the qubits and filters that generate these photons are set to $\delta_i, \omega_{Ri} \in (2\pi \times 8.84,\ 2\pi \times 8.96)\,\mathrm{GHz}$, with a bare decay rate for the resonators of $\kappa_i = 2\pi \times 10$ MHz.

As commented previously, the simulations establish the frequency of the bare resonators ω_{Ri} and employ spectroscopy techniques to adjust the renormalized frequency and the effective decay rate $\kappa_{\mathrm{eff,\,i}}$. This closely resembles the calibration procedure that has to be done in the experiment once all the components are connected. Subsequently, these calibrated values are utilized to precisely position the emitter qubit $\delta_i = \omega_i^D$ and to engineer the photon shaping control $g_i(t)$. It is important to note that, although the modifications to the baseline figures are minor—approximately 10^2 kHz as shown in the previous section's Fig. 6.6—, they significantly affect the fidelity of state transfer.

We display, in Fig. 6.7, the fidelity of the quantum state transfer operation as the separation between the filter frequencies increases from 0 to 12κ. A first region is observed where there is significant population exchange between emitters, occurring when $\Delta_{12} \leq 5\kappa$. Following this, there is a plateau where the behavior effectively simplifies to two independent single-photon state transfer operations.

In the scenario where the detuning between emitters is minimal, the infidelity of the state transfer process is largely attributable to the indistinguishability of the emitted photons. By defining the overlap between two multiplexed modes, which are centered around distinct carrier frequencies ω_1 and ω_2—represented as $\xi(\omega_1)$ and $\xi(\omega_2)$, respectively—we introduce the following equation,

$$\mathcal{I}_{\mathrm{overlap}}(\omega_1, \omega_2) = \left|\langle \xi(\omega_1) |\, \xi(\omega_2)\rangle\right|^2 . \tag{6.33}$$

As supported by numerical simulations (cf. purple line in Fig. 6.7) the infidelity $1 - \mathcal{F}_{\mathrm{ST}}(\omega_{R1}, \omega_{R2})$[1] approximates $\mathcal{I}_{\mathrm{overlap}}(\omega_{R1}, \omega_{R2})$. Specifically, for sech-like photon profiles, the overlap decreases exponentially with the ratio $(\omega_{R1} - \omega_{R2})/\kappa$, which highlights the photon bandwidth as the crucial parameter for distinguishing between emitters.

As the detuning between wavepackets surpasses κ, the emission and absorption processes of the two flying qubits operate independently, returning to the behavior seen in the single excitation regime. Although the dressed frequencies of the cavities $\omega_{R1,R2}$ are not the same as in the single excitation case, the fine-tuning of δ_i through qubit-assisted spectroscopy maintains fidelities comparable with those found in single-qubit experiments. As depicted in Fig. 6.7, when the frequency difference exceeds 6κ, the fidelity of the two-qubit state transfer closely follows the product of the individual state transfer fidelities at ω_{R1} and ω_{R2}. This phenomenon includes oscillations that are inherent to the dynamics of single-photon state transfers (see $\mathcal{F}(\omega_{R1})$ and $\mathcal{F}(\omega_{R2})$ in Fig. 6.7). Specifically, within a 15-meter waveguide, a photon with a bandwidth of $\kappa \simeq 2\pi \times 10$ MHz is capable of discerning the mode structure of the quantum link. Optimal transfer occurs only when the filter frequency ω_R perfectly matches one of the waveguide modes. This is illustrated at the specific point in Fig. 6.7 highlighted as a blue diamond, where the positioning of all resonators with respect to a waveguide mode is optimal.

The numerical study, depicted in Fig. 6.7, identifies the different sources of imperfections in a two-photon scenario. The different regimes of operation impose different constraints, especially those arising from the crosstalk. The next subsection revolves around how to use these numerical results to develop a heuristic for the scaling of the fidelity.

[1] Throughout this and the following subsection, we denote functions defined over frequency space with a generic argument ω. To the contrary, ω_R refers to a specific evaluation at that particular frequency.

The objective is to infer how these multiple photon errors hinder the total information capacity of a given channel and bandwidth.

6.3.4 Scaling with N emitters

Exact numerical simulations for more than two excitations are extremely demanding. Because of this, the objective of the present subsection is to evaluate the state transfer fidelity of N qubits using the results from the previous section involving two quantum emitters. The deviation from the perfect single-photon state transfer is quantified by $G(\omega_i, \omega_j) = \mathcal{F}_2(\omega_i, \omega_j)/\mathcal{F}_1(\omega_i)\mathcal{F}_1(\omega_j)$. In a conservative upper limit, this factor accounts for the interference between all pairs of quantum emitters, thereby imposing $N(N-1)/2$ corrections to the single-photon state transfer across N qubits

$$\mathcal{F}_{\text{est}}(\omega_1, ..., \omega_N) = \prod_i \mathcal{F}_1(\omega_i) \times \prod_{i<j} G(\omega_i, \omega_j). \tag{6.34}$$

For an asymptotic approximation of the combined impact of these effects, note that the mode overlap $|\langle\xi(\omega_i)|\xi(\omega_j)\rangle|$ accounts for most of the factor $G(\omega_i, \omega_j)$, modifying (6.34) as

$$\tilde{\mathcal{F}}_{\text{est}}(\omega_1, ..., \omega_N) = \prod_i \mathcal{F}_1(\omega_i) \times \prod_{i<j} (1 - |\langle\xi(\omega_i)|\xi(\omega_j)\rangle|^2). \tag{6.35}$$

Despite the inclusion of $\mathcal{O}(N^2)$ factors, the photon overlap diminishes exponentially with the frequency separation $|\omega_{Ri} - \omega_{Rj}|/\kappa$, allowing for further simplifications, as shown below.

Both the upper bound $\mathcal{F}_{\text{est}}$ and the approximate asymptotic formula $\tilde{\mathcal{F}}_{\text{est}}$ can be derived from the simulation parameters discussed in Section 6.3.3. For this analysis, we will uniformly distribute the spacing between the emitters frequencies $\omega_{Ri+1} - \omega_{Ri} = \Delta$ around the original resonance. Numerical simulations of the two-photon state transfer are employed to determine the prefactor $G(\omega_i, \omega_j) \approx G(\omega_i - \omega_j) = G((j-i) \times \Delta)$ for all potential separations of N qubits.

A comparison of infidelity estimates across various frequency spacings, $\Delta/\kappa = 2, 3, 5$, and 6 is presented in Fig. 6.8. The infidelity calculations derived from simulations (6.34) display some fluctuations due to the position of the cavities with respect to the waveguide modes. Nonetheless, these values agree with those from the exponential approximations provided by the overlap calculations Eq. (6.35). In each scenario, whether considering upper bounds or overlap approximations, the fidelity decreases exponentially as the number of emitters increases. Notably, the rate of decline is proportional to N rather than N^2, suggesting that among the $N(N-1)/2$ possible interactions, only the nearest-neighbor effects are relevant, as denoted by

$$\tilde{\mathcal{F}}_{\text{est}} \approx \mathcal{F}_1^N \times (1 - \mathcal{I}_{\text{overlap}}(\Delta))^{N-1}.$$

As mode spacing widens, the fidelity curves gradually converge toward the asymptotic behavior of N independent state transfers, represented by the dash-dot line in Fig. 6.8. Particularly, at a mode spacing of $\Delta = 6\kappa$, the infidelity closely follows that of the ideal scenario.

From these curves, it is possible to determine the maximum number of qubits (N_{max}) that can be transmitted for a specific error threshold, ε. This determination is simplified by the straightforward behavior of $\tilde{\mathcal{F}}_{\text{est}}$, allowing an analytical estimation through the mode overlap equation

$$N_{\text{max}} = \frac{\log(1-\varepsilon)}{\log[\mathcal{F}_1(1 - \mathcal{I}_{\text{overlap}}(\Delta))]}, \tag{6.36}$$

where the total bandwidth requirement is $\Delta \times N_{\text{max}}$. For instance, in the 15 m waveguide illustrated in Fig. 6.8, a separation $\Delta > 6 \times \kappa$ closely approximates the single-photon

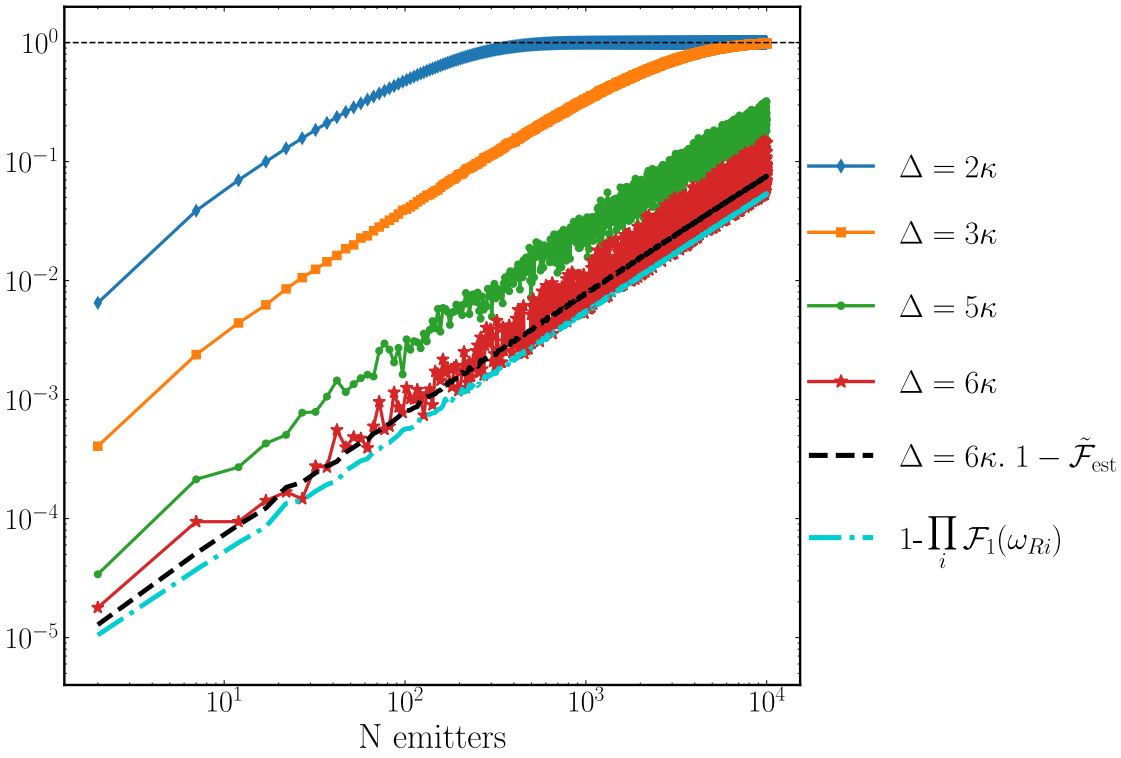

Figure 6.8: Heuristic infidelity scaling vs. number of transmitted qubits. We plot the estimates from Eq. (6.34), for multiplexed state transfer with frequency separations $\Delta = 2\kappa, 3\kappa, 5\kappa$ and 6κ. In the last case, we also plot the estimator Eq. (6.35) based on photon wavepacket overlap (dashed line). Note how, for sufficient frequency separation, the infidelity approaches the limit imposed by single-qubit state transfer (dot-dashed line), which scales as $\mathcal{F}_1^N$.

limit. Assuming no additional constraints, it is theoretically possible to transmit 500 qubits with an error below 10^{-3} over a bandwidth of $2\pi \times 5$ GHz. While these figures might be difficult to achieve experimentally, they underscore the potential of quantum links to serve as universal buses for quantum data transmission.

6.3.5 Transfer optimization

The main takeaway from the previous subsection is that the fidelity of individual qubits transmission, $\mathcal{F}_1(\omega)$, fundamentally limits the efficiency of multiplexed quantum state transfer. Given this, the goal now is to understand the actual information capacity of realistic waveguides.

Two primary factors contribute to the infidelity of single qubit state transfer. The deformation of the wavepacket due to propagation under non-linear dispersion relations, and Stark shifts resulting from the dynamic controls $g(t)$. To mitigate wavepacket distortion, one can adjust the phases in the emission and absorption controls $g(t)$, as was done in Chapter 5. Additionally, both issues can be mitigated by decreasing the photon bandwidth κ_{eff} and extending the duration of the state transfer, while considering the inherent decoherence and dephasing constraints of the emitters.

Another important factor is how the emitters are arranged relative to the resonances of the waveguide. This organization is especially significant when dealing with narrow-bandwidth photons and short waveguides, as the qubits resolve the mode structure of the waveguide. The placement of emitters in frequency space explains the fidelity fluctuations

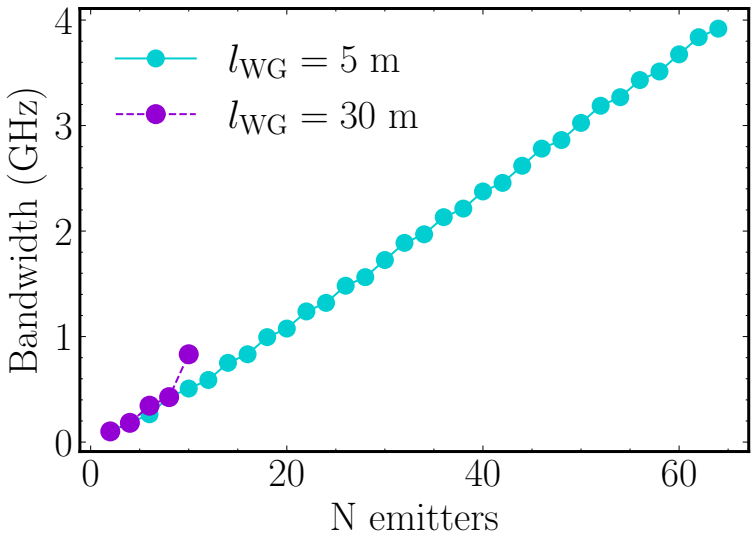

Figure 6.9: Bandwidth requirements to host a particular number of emitters with a given global tolerance of 10^{-4} for the N-photons state transfer operation. The graph shows data for two different waveguides of $l_{\mathrm{WG}} = 5$ m and $l_{\mathrm{WG}} = 30$m. The lines stop when increasing the bandwidth would not improve the fidelity, that is, when the value of the single independent processes is itself greater than the tolerance imposed for the global gate, $1 - \mathcal{F}(\omega_1)^N >$ Tol. These data have been obtained with the estimator $\tilde{\mathcal{F}}_{\mathrm{est}}$ defined by Eq. (6.35), unlike that of Fig. 6.8 which came from two-photon simulations.

observed in multiplexed state transfer for any number of qubits (cf. Figs. 6.7 and 6.8). A strategic placement of these emitters can markedly enhance the quality of the transfer, as evidenced by the diamond dot in Fig. 6.7. However, this placement affects the maximum channel capacity. If qubits must be placed close to resonant modes, the number of transmitted qubits per bandwidth will be limited by the waveguide's free spectral range.

We show, in Fig. 6.9, the physical requirements for setups in which the three optimizations—predistortion, wavepacket bandwidth, and emitter positioning—have been applied. The plot shows the number of qubits transmitted in waveguides of 5 and 30 meters, with a maximum error $\varepsilon = 10^{-4}$ estimated from $\mathcal{F}_{\mathrm{est}}$—which, as seen above, captures the overall scaling of resources very well. In both waveguides, the ultimate capacity is set by the single-qubit optimized infidelities $\mathcal{I}^1_{5\mathrm{m}} = 5 \cdot 10^{-7}$ and $\mathcal{I}^1_{30\mathrm{m}} = 10^{-5}$, as computed in previous chapters, with predistortion and optimal qubit positioning. These values already set a very stringent upper bound on the sequential and multiplexed transmission capacities. For instance, the 30 m waveguide only supports transmitting 10 qubits before the error exceeds the tolerance 10^{-4}. Furthermore, while shorter waveguides allow high-quality transmission of more qubits—e.g., over 60 qubits for the 5 m waveguide—the bandwidth requirement of over 4 GHz imposes challenging design restrictions in the emitters and filter designs. Under these conditions, it may be advantageous, from an engineering perspective, to use multiple separate physical channels.

6.4 Summary

In this chapter we have addressed the multiplexation of a microwave quantum link that connects $N + N$ qubits in two quantum nodes, inspired by setups from recent experiments [KMW$^+$17, MSK$^+$20, SSK$^+$23] in which 1 to 1 transmission has been demonstrated but whose generalization to more qubits seems feasible. Also, the tools that we have put

forward generalize to other waveguide-QED architectures.

The first important result is the demonstration that qubits can be transferred in different orthogonal modes by a suitable control of the interaction between the storage qubits and the quantum link. This required generalizing the methods for wavepacket engineering envisioned by [CZ95], and extended and implemented in various works [ELF$^+$12, PHE$^+$13, ZPB$^+$15, KMW$^+$17, BSZ$^+$19, MSK$^+$20, SSK$^+$23, QLN$^+$23, GYC$^+$24], arriving at close expressions for the controls to generate almost arbitrary wavepackets—under natural limitations of bandwidths set by the mediating cavities. As a particular case, the study demonstrates the accuracy of mode multiplexing for a family of sech-like pulses in a realistic setup.

The second relevant result stems from the study of frequency multiplexing for arbitrary numbers of qubits. An accurate analysis of the simultaneous transfer of two qubits identified cross-talk as the limiting factor to the fully coherent process fidelity. Detailed simulations with two qubits in generic waveguides enable extrapolating the fidelity of multiplexed state transfer to higher numbers of qubits, showing that the single-qubit state transfer fidelity and the overlap between neighboring photon wavepackets ultimately limit the overall fidelity. Using heuristic scaling in combination with the physical constraints of state-of-the-art superconducting circuit experiments, we estimated the practical capacity of microwave waveguides for a given error tolerance. For instance, we found that as many as 60 photons could be sent through a 5-meter waveguide with a global infidelity below the usual threshold for fault-tolerant computation 10^{-4}.

The next and last objective of the thesis is to use the techniques of wavepacket engineering to distribute entanglement deterministically across a network. The following chapter is devoted to that, and with it, we will have demonstrated the potential of quantum state transfer networks to work as fully operational distributed computers as they can send quantum states throughout the network as well as distribute entanglement.

Entanglement distribution in a quantum network via fractional state transfer

7

In Chapter 1 we argued for the proposal of a superconducting quantum state transfer network. We stated in that chapter that these kinds of networks were equal in capabilities to teleportation networks. This effectively means the ability to distribute arbitrary quantum states and, also, to distribute genuine multipartite entanglement across the different nodes. So far, we have devoted all our efforts to the task of transmitting quantum states and engineering distributed gates. This was the focus of Chapters 4, 5, and 6. The goal of this chapter is to apply the wavepacket engineering tools developed in Chapter 3 to propose a protocol for distributing genuine multipartite entanglement through *fractional quantum state transfer*. This will close up the content of this thesis, as it will show that state transfer networks can also distribute entanglement and, thus, implement all the protocols inherited from teleportation which need entanglement distribution as a first step. Critically, the method developed in this chapter achieves entanglement distribution without the need for measurements or the exchange of classical communication. Like all the other protocols developed throughout the thesis, it only makes use of finely tunable couplings and high-fidelity transmission of quantum information.

Genuine multipartite entangled states—those that are not separable under any bipartition of the N qubits—are of significant computational interest [HHHH09] due to their potential to provide quantum advantage [HBcvB99, BKB01, EKMB17, TA14]. In tripartite systems, there are two distinct families of entangled states: the Greenberger-Horne-Zeilinger (GHZ) and W states, both of which have been experimentally demonstrated on various platforms [SKK$^+$00, RNO$^+$00, RRH$^+$04, LKS$^+$05, HHR$^+$05]. The ability to control and generate entangled states is crucial for quantum-based technologies, including quantum key distribution [PAB$^+$20], quantum communication [Car15], quantum computation [NC00], and quantum metrology [Par09, GLM11]. In particular, W states find applications for random number generation [GHP$^+$14], quantum key distribution [ZXP15, JLJP02, JQC07], quantum teleportation [JPOK03, AP06] or even for quantum metrological purposes [NK14].

The *fractional quantum state transfer* scheme we propose relies on quantum communication through traveling single bosonic excitations. As we demonstrate, this method is especially well-suited for generating multipartite entanglement in the form of N-qubit W states across an arbitrary number of quantum registers. These registers can be separated by considerable distances, making the scheme highly relevant for quantum computation, communication, and other related tasks. The protocol provides fast operation times and can be adapted depending on the topology and connectivity of the quantum network, operating in either a sequential or a simultaneous fashion. We illustrate our scheme by detailed numerical simulations and show its robustness to the most pressing decoherence

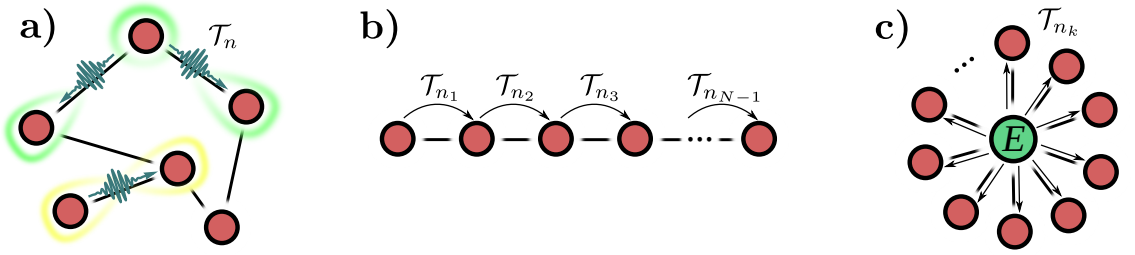

Figure 7.1: (a) Schematic illustration of a quantum network, where different nodes (circles) are connected via quantum communication channels (QCCs) (solid lines). Each node consists of a qubit and a resonator per QCC. By performing incomplete quantum state transfers $\mathcal{T}_n$ by transferring an excitation with a probability less than unity $n > 1$, different nodes can be entangled, leading to deterministic genuine multipartite entanglement across the network. (b) A linear quantum network where a sequential implementation of $\mathcal{T}_{n_k}$ leaves the N nodes in a W state. Other genuine multipartite entangled states can be prepared by different choices of n_k. The two families of multipartite entangled states can be obtained, although GHZ states require a further two-qubit gate (CNOT) which may be performed when qubits B and C are placed within the same node. (c) Extension to other geometries or connectivities in a quantum network, e.g. a simultaneous emission from qubit E to N nodes. See the main text for further details.

sources, namely, dephasing and qubit decay. The proposed protocols can be readily implemented in current setups, such as in the already cited experiments of superconducting networks [KMW$^+$17, MSK$^+$20, SSK$^+$23].

We choose to organize the chapter in the following four sections. Section 7.1 presents the primitive operation of fractional quantum state transfer. In Section 7.2 we explore how to engineer the specific controls for emitting these fractional excitations. This exploration follows the spirit of Chapter 3, in which different photon shapes are proposed in a variety of physical scenarios. Also, highlighting the important difference in this context between sending a fractional excitation in a 1-to-1, as depicted in Fig. 7.1b manner, or a 1-to-N, as in Fig. 7.1c. After that, Section 7.3 presents two different protocols for achieving entanglement distribution through fractional quantum state transfer. Subsection 7.3.1 focuses on a sequential protocol implemented in a linear topology, while 7.3.2 does so with a parallel protocol in an extended configuration. Finally, Section 7.4 revolves around numerical verification of the entanglement distribution protocols in real-world-inspired superconducting networks. We first present, in Subsection 7.4.1, results for the coherent case, and afterward, in Subsection 7.4.2 results considering decoherence and dephasing. In both scenarios, we study and compare the performance of the linear and extended networks.

7.1 Fractional quantum state transfer

The main goal of this chapter is to develop a protocol that spreads a single photon among multiple nodes of an arbitrary network, thus creating W-like states. Such vision is depicted schematically in Fig. 7.1a. The idea we put forward to achieve such a goal is that of *fractional quantum state transfer*, which consists of engineering a control $g(t)$ such that it does not inject a whole wavepacket into the waveguide, but only a fraction of it. The hypothesis is that by designing such control and tailoring its corresponding absorption, one can start with a network in a product state and drive it to a W-like state deterministically and without measurements. Furthermore, we envisioned protocols for wavepacket

generation that would apply to 1-D configurations—Fig. 7.1b—, and to extended 1-to-N-types—Fig. 7.1c. We believe that by combining these two methods, we can engineer entangled states across arbitrary networks.

The incomplete quantum state transfer protocol among two spatially separated qubits, denoted as $\mathcal{T}_n$, generalizes the original quantum state transfer proposal [CZKM96]. Initially, one qubit is prepared in a general state $|\psi\rangle = \alpha|0\rangle + \beta|1\rangle$, with $|\alpha|^2 + |\beta|^2 = 1$. The operation $\mathcal{T}_n$ can be split into two stages: First, the emission of a fraction $1/n$ of the qubit excitation $|1\rangle$, with $n \geq 1$, mapping it onto a flying qubit through the quantum communication channel that travels until it reaches the second qubit. The second stage of $\mathcal{T}_n$ demands that the receiver qubit, initially in the state $|0\rangle$, absorbs the incoming excitation. In this manner, the operation $\mathcal{T}_n$ can be written as (up to local phases)

$$(\alpha|0\rangle + \beta|1\rangle) \otimes |0\rangle \xrightarrow{\mathcal{T}_n} \alpha|00\rangle + \beta\sqrt{\frac{n-1}{n}}|10\rangle + \frac{\beta}{\sqrt{n}}|01\rangle . \tag{7.1}$$

A standard quantum state transfer protocol is realized setting $n = 1$, where the excitation of the first qubit is completely exhausted (see for example Refs. [KMW+17, MSK+20] or the thorough analysis made in Chapter 3), resulting in the transfer of the state $(\alpha|0\rangle + \beta|1\rangle)$ to the second qubit.

Importantly, in contrast to standard quantum state transfer, $\mathcal{T}_{n>1}$ directly enables a deterministic preparation of entangled states between the two connected qubits [CZN+18, ABP+18, BSZ+19, LLC+19, ZCB+21]. In particular, one obtains a maximal entangled state when $\alpha = 0$ and $n = 2$ in Eq. (7.1). For $n \to \infty$ no excitation is transferred, and the initial state remains unchanged. The protocol $\mathcal{T}_n$ can be realized employing wavepacket shaping techniques in different architectures, as we detail in the following. The techniques used throughout this whole chapter are very similar to those outlined in Chapter 3 but with the necessary changes to accommodate fractions of excitations.

One of the main ideas of this chapter is that emitting a fraction $1/n$ of a photon can achieve incomplete quantum state transfer, as described by Eq. (7.1). The additional requirement, besides the ones of speed and bandwidth utilization (cf. Sec. 3.2.2 of Chapter 3), is that the norm of the emitted packet must be

$$\int_{-\infty}^{\infty} dt|\xi(t)|^2 = n^{-1}, \text{ with } n \geq 1, \tag{7.2}$$

which is to say that the photon was emitted with a probability of $1/n$. This will be the core ingredient of the entanglement distribution operation.

The challenge is to find the emission and absorption controls that will enable the operation (7.1). For that, we need to engineer the couplings $g(t)$ such that the initial state

$$|\psi(t \to -\infty)\rangle = |1\rangle_q |0\rangle_r |0\rangle_{qcc}$$

is brought to

$$|\psi(t \to \infty)\rangle = \sqrt{\frac{n-1}{n}}|1\rangle_q |0\rangle_r |0\rangle_{qcc} + \frac{e^{i\phi}}{\sqrt{n}}|0\rangle_q |0\rangle_r |1\rangle_{qcc} .$$

The relative phase ϕ has two independent contributions, the accumulated phase during the protocol and the constant phase that can be imprinted in the control $g(t; n)$. Here $|1\rangle_q$, $|1\rangle_r$ and $|1\rangle_{qcc}$ denote a single excitation state in the qubit, resonator, and quantum communication channel or quantum link, respectively.

What we found when tackling this problem is that for the emission part, it suffices to impose the condition (7.2) on the proposed wavepacket and reverse engineer the equations of motion to obtain $g(t)_{\text{emission}}$. Much in the same way it was done in Chapter 3. However,

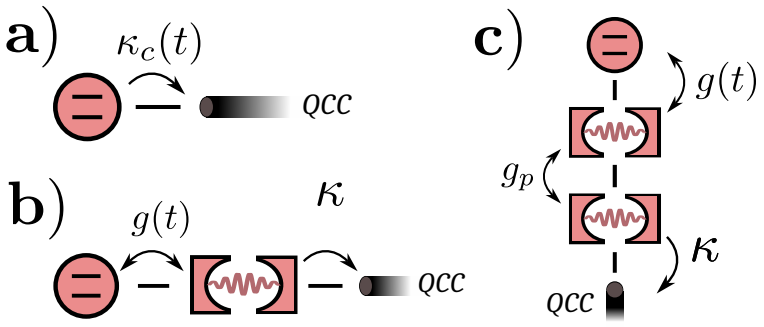

Figure 7.2: The three different coupling situations considered originally in Chapter 3 when studying wavepacket engineering and brought back here in the context of entanglement distribution. Panel a) illustrates the case of a qubit directly coupled to a waveguide, in which the decay rate itself has to be tuned. Panel b) shows the most explored scheme in this thesis (and also in this chapter) in which a qubit is dynamically coupled to a cavity, which leaks into the waveguide at a rate κ. Panel c) shows the case in which a second cavity, acting as a Purcell filter, is placed between the first one and the waveguide. It is important to consider these filters when interested in performing measurements and the dispersive regime in general.

for the absorption control, something quite different happens. For the fractional state transfer protocol $\mathcal{T}_{n>1}$ to succeed $g(t)_{\text{absorption}}$ has to be designed taking into account the whole excitation, and not just a part of it as in Eq. (7.2). This is crucial for the correct implementation of the protocol, and it means that the emission and absorption controls are not time-reversed of each other, in fact, depending on the value of n they can be dramatically different.

The two primitives—fractional emission and fractional absorption—and the fractional transfer that results can be utilized in various ways. Their versatility enables control over how much of a photon is transferred, allows for the selection of different network topologies, and permits the application of the same operation either sequentially or in parallel, and potentially multiple times. All of these possibilities will be discussed in detail in later sections. The following section will demonstrate how different wavepacket shapes can be emitted fractionally in various scenarios. We consider this important to cover in detail here, as we believe one of the key strengths of this method lies in its versatility.

7.2 Controls for fractional quantum state transfer

The protocol of entanglement distribution by incomplete quantum state transfer is, in principle, independent of the coupling scheme one chooses to use. Because of that, it is illustrative to consider different physical situations as well as different photon shapes. In the following subsections we will study the photon emission controls for the three different situations depicted in Fig. 7.2, first for a qubit directly coupled to a waveguide (Panel 7.2a), then for qubit-cavity node (Panel 7.2b), and finally for a qubit-cavity-Purcell filter configuration (Panel 7.2c).

In deriving the controls for entanglement distribution, it became clear that they could be adapted to different coupling schemes. The following subsections outline the methods and functional forms of these controls for three distinct coupling regimes. This approach closely mirrors the procedure discussed in Chapter 3, but here it is applied to fractional excitations rather than complete ones.

7.2.1 Qubit directly coupled to the waveguide

We start by considering the simplest case, where a qubit is directly coupled to the bosonic media through which an engineered boson propagates, as depicted in Fig. 7.2a. This was considered and experimentally realized in Ref. [BSZ+19]. We will consider two different situations, one in which a fraction of excitation is shared through a single channel and in which it is distributed in a 1-to-N manner.

7.2.1.1 1-to-1 channel

In this simplified model in which there is no filtering element between the emitter and the waveguide, the equation for the qubit takes the form

$$\dot{q}(t) = -\kappa(t)q(t)/2, \tag{7.3}$$

where now photon shaping requires a time-dependent decaying rate $\kappa(t)$. Making now use, as in Chapter 3 of the input-output relation for the wavepacket $\xi(t) = \sqrt{\kappa(t)}q(t)$, we obtain

$$\dot{\kappa}(t) = \kappa^2(t) + 2\kappa(t)\frac{\dot{\xi}(t;n)}{\xi(t;n)}. \tag{7.4}$$

It is quite straightforward to propose a photon with a hyperbolic secant shape that fulfills the fractional condition (7.2). Because we already know the normalization constant, it suffices to divide it by $\sqrt{n}$, which amounts to

$$|\xi(t;n)| = \sqrt{\frac{\kappa}{4n}}\mathrm{sech}(\kappa t/2). \tag{7.5}$$

For this specific wavepacket shape, the time-dependent decay rate adopts the form

$$\kappa(t;n) = \frac{\kappa_p \mathrm{sech}^2(\kappa_p t/2)}{4n - 2\tanh(\kappa_p t/2) - 2} \tag{7.6}$$

upon imposing that $\lim_{t\to-\infty}|q(t)|^2 = 1$ and $\lim_{t\to\infty}|q(t)|^2 = (n-1)/n$, and where κ_p refers to the frequency width of the injected photon.

If we allow for a frequency chirp, $\xi(t) = f(t)e^{-i\delta t}$, then the frequency of the qubit must be varied accordingly, namely, we find $\Delta(t) = -\delta t$, and $\kappa(t)$ still obeys Eq. (7.4).

7.2.1.2 1-to-N channel

In this case, the topology of the network resembles that of a star, cf. Fig. 7.1c, and the equation of motion for the qubit changes. In this case, the emitter decays into N quantum communication channels and this has to be captured in the equations. Assuming a decay rate $\kappa_{c,j}(t)$ for each of the j channels, the equation in the rotating frame corresponds to

$$\dot{q}_E(t) = -\sum_{j=1}^{N}\kappa_{c,j}(t)q_E(t)/2. \tag{7.7}$$

Employing the same sech-like wavepacket $\xi_j(t)$ with bandwidth κ_j, and making use of the input-output relation $|\xi_j(t)| = \sqrt{\kappa_{c,j}(t)}|q_E(t)|$, one can manipulate the equations of motion to find a close expression for $\dot{\kappa}_{c,1}(t)$ in terms of $f_j(t) = \sqrt{\xi_j(t)/\xi_1(t)}$,

$$\dot{\kappa}_{c,1}(t) = \left[\sum_{k=1}^{N} f_k^2(t)\right]\kappa_{c,1}^2(t) + 2\kappa_{c,1}(t)\frac{\dot{\xi}_1(t)}{\xi_1(t)}, \tag{7.8}$$

while $\kappa_{c,j}(t) = f_j^2(t)\kappa_{c,1}(t)$. For simplicity, we just provide here the expression when all bandwidths are equal, $\kappa_j = \kappa\ \forall j$, which becomes

$$\kappa_{c,j}(t) = \frac{\kappa \mathrm{sech}^2(\kappa t/2)}{2n_j(2-(1-\tanh(\kappa t/2))\sum_{k=1}^{N} n_k^{-1})}. \tag{7.9}$$

For $n_j \to \infty$, $\kappa_{c,j}(t) = 0$ and no excitation is injected into the jth quantum communication channel. Again, if an excitation fraction is emitted only through a unique channel, then the star topology becomes a 1-D network, and Eq. (7.9) reduces to Eq. (7.6).

7.2.2 Qubit-resonator node

This setup is the one described by the Hamiltonian (2.35). It is the most used throughout the thesis, and it is also the one in which we will implement the numerical simulations. For this reason, we will devote more space to it and will study how to create more photon shapes, as this can give rise to interesting applications.

7.2.2.1 1-to-1 channel

As in the previous Subsection 7.2.1, we will first write down the equations for nodes in 1-D configuration cf. Fig. 7.1b, and after that, consider the case with the emitter connected to N quantum communication channels. In the 1-to-1 topology, the equations are the same as the ones considered in Chapter 3, Section 3.2.2. For that reason, we will take that part of the derivation for granted and explore different wavepacket shapes.

Hyperbolic secant-shaped photon

Considering as a first example the fractional sech photon $|\xi(t)| = \sqrt{\frac{\kappa}{4n}}\mathrm{sech}(\kappa t/2)$, we take this wavepacket shape and use the standard procedure outlined in Chapter 3, that is, relating the outcoming field using input-output relations, and the integration of the equations we arrive at the following control

$$|g_{\mathrm{sech}}(t;n)| = \frac{e^{\kappa t/2}\kappa}{(1+e^{\kappa t})\sqrt{(n-1)(1+e^{\kappa t})^2+1}}. \tag{7.10}$$

Under the previous control $g_{\mathrm{sech}}(t;n)$ the qubit remains excited with a probability $|q(t\to\infty)|^2 = (n-1)/n$. For $n=1$, we recover the standard form $g_{\mathrm{sech}}(t;1) = \kappa/2\mathrm{sech}(\kappa t/2)$, as expected, and the qubit excitation is exhausted. Note that for any $n>1$, the control is modified in a non-trivial fashion compared to $g(t;1)$: For $\kappa t \gg 1$, $g_{\mathrm{sech}}(t;n>1)$ decays faster than $g_{\mathrm{sech}}(t;n=1)$, while the maximum scales as $\max_t g_{\mathrm{sech}}(t;n) \approx \kappa/\sqrt{9n}$ for $n \gg 1$ (see Fig. 7.3a for an illustration of $g_{\mathrm{sech}}(t;n)$).

Lorentzian-shaped photon

The previous procedure can be applied to other photon shapes, as long as they obey the speed condition (3.26). We now propose a Lorentzian-shaped photon with an adjusted normalization constant such that it fulfills Eq. (7.2)

$$|\xi(t;n)| = \left(\frac{\kappa}{n\pi(1+\kappa^2t^2)}\right)^{1/2}. \tag{7.11}$$

This photon shape leads to the control,

$$|g_{\mathrm{Lorentz}}(t;n)| = \frac{\kappa(\kappa t-1)^2}{(1+\kappa^2t^2)\sqrt{(4n-2)\pi(1+\kappa^2t^2)-4(1+\kappa^2t^2)\mathrm{atan}(\kappa t)-4}}, \tag{7.12}$$

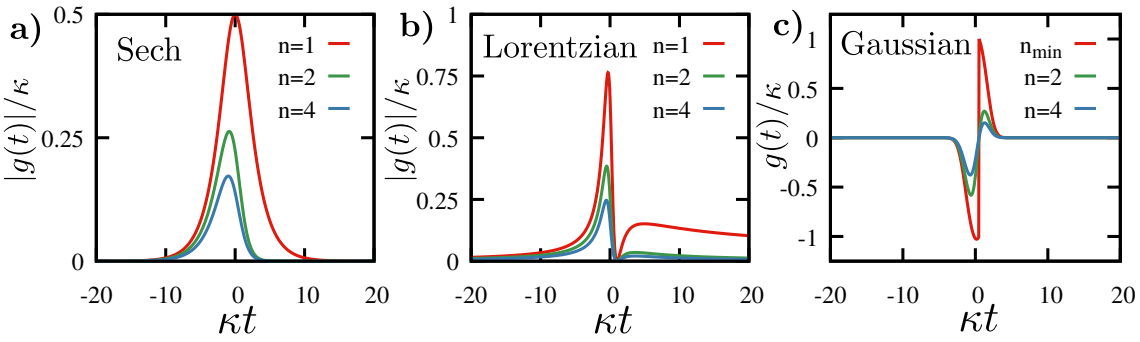

Figure 7.3: Time-dependent control $g(t;n)$ for different targeted photon shapes, sech-like photon $|\xi(t;n)| = \sqrt{\kappa/(4n)}\text{sech}(\kappa t/2)$ (a), Lorentzian $|\xi(t;n) = (\kappa/(n\pi(1+\kappa^2t^2)))^{1/2}$ (b) and Gaussian $|\xi(t;n)| = \sqrt{\kappa/\pi^{1/2}n}e^{-\kappa^2t^2/2}$ (c), and for different values of the transferred fraction n. Note that a Gaussian photon can only be emitted with a probability smaller than $1/n_{\text{min}} \approx 0.83$.

which leads to non-negative values of $|q(t)|^2$ for all κ and $n \geq 1$. See Fig. 7.3b for an illustration of this derived pulse $g_{\text{Lorentz}}(t;n)$.

Gaussian-shaped photon

A very interesting and somewhat surprising consequence of emitting fractions of excitations is the possibility of engineering Gaussian profiles. Recall, from Chapter 3, that emitting a photon $\propto e^{-\kappa^2t^2}$ violated the condition imposed on the logarithmic derivative. As we will show now, this is not the case anymore when n is big enough. The fraction of a Gaussian-shaped photon that we are proposing is

$$|\xi(t;n)| = \sqrt{\frac{\kappa}{\pi^{1/2}n}}e^{-\kappa^2t^2/2}. \tag{7.13}$$

Following the same steps we arrive to

$$|q(t)|^2 = \frac{1}{2n}\left(2n - 1 - \frac{2e^{-\kappa^2t^2}}{\sqrt{\pi}} - \text{erf}(\kappa t)\right) \tag{7.14}$$

where $\text{erf}(x) = \frac{2}{\pi^{1/2}}\int_0^x dt\ e^{-t^2}$ is the error function. The previous equation is non-physical for $n = 1$ since $|q(t)|^2 < 0$ for some t. The minimum value of $|q(t)|^2$ takes place at $2\kappa t = 1$, and therefore it is easy to find that the condition in Eq. (7.14) is fulfilled as long as $n \geq n_{min}$, with

$$n_{\text{min}} = \frac{1}{2}\left(1 + \frac{2}{e^{1/4}\sqrt{\pi}} + \text{erf}(1/2)\right) \approx 1.2 \tag{7.15}$$

For $n \geq n_{\text{min}}$ the control pulse reads as

$$g_{\text{Gauss}}(t;n) = \frac{\kappa e^{-\kappa^2t^2/2}(2\kappa t - 1)}{\sqrt{2\pi^{1/2}(2n - 1 - \text{erf}(\kappa t)) - 4e^{-\kappa^2t^2}}}. \tag{7.16}$$

Note that this control is negative in the range $t \in [-\infty, 1/2\kappa)$ (see Fig. 7.3c). A Gaussian-shaped photon can be emitted with a probability smaller than $1/n_{\text{min}} \approx 0.83$. Yet, the traveling excitation cannot be fully absorbed at the other end since it requires $n = 1$, which makes Gaussian protocols not suitable for this task.

Reduced bandwidth sech-shaped photons

In certain circumstances, it may be more convenient to inject photons with a narrower bandwidth. This can reduce potential distortion effects introduced by the propagation medium, as was explored in Chapter 4. For that, we introduce the following photon shape

$$|\xi(t,\eta;n)| = \sqrt{\frac{\kappa}{4\eta n}} sech\left(\frac{\kappa t}{2\eta}\right), \tag{7.17}$$

so that $\int_{-\infty}^{\infty} dt|\xi(t,\eta;n)|^2 = n^{-1}$, and whose bandwidth κ/η is reduced by a factor $\eta > 1$ for the usual sech-photon at the expense of a longer protocol duration. Following the previous steps, we find

$$|g(t,\eta;n)| = \frac{(\kappa/\eta n)^{3/2} n sech(\kappa t/(2\eta))(\eta - \tanh(\kappa t/(2\eta)))}{2\sqrt{\frac{2\eta(2n-1-\tanh(\kappa t/(2\eta)))-sech^2(\kappa t/(2\eta)}{\eta n}}}. \tag{7.18}$$

The derivation of these controls relies on the utilization of the simplified Markovian model with a qubit and a cavity, such as that defined by Eq. (3.20).

7.2.2.2 1-to-N channel

Let us now consider the 1-to-N scenario in the case of nodes made of qubit plus transfer resonators. In this network configuration, the emitter consists of a qubit plus N transfer resonators, each decaying with rate κ_j into the jth quantum communication channel, while the receiver nodes are as depicted in Fig. 7.2b. The equations of motion in the rotating frame (assuming again resonant elements) read as

$$\dot{q}_E(t) = -i\sum_{j=1}^{N} g_j(t) r_j(t) \tag{7.19}$$

$$\dot{r}_j(t) = -ig_j^*(t) q_E(t) - \kappa_j r_j(t)/2, \tag{7.20}$$

where $q_E(t)$ and $r_j(t)$ denote the amplitude of having an excitation in the emitter and the jth resonator, respectively. Considering again a sech-like wavepacket, but now transferring a $1/n_j$ excitation through each of the N QCCs, we have $\xi_j(t) = \sqrt{\kappa_j/(4n_j)}\text{sech}(\kappa_j t/2)$. Since

$$\frac{d}{dt}(|q(t)|^2 + \sum_{j=1}^{N}|r_j(t)|^2) = -\sum_{j=1}^{N}\kappa_j|r_j(t)|^2,$$

solving the equations of motion backward, one gets to

$$g_j(t;\mathbf{n}) = \frac{e^{\kappa_j t/2}\kappa_j}{(1+e^{\kappa_j t})^2\left[n_j(1-\sum_{k=1}^{N}\mathcal{K}_k(t))\right]^{1/2}} \tag{7.21}$$

with

$$\mathcal{K}_k(t) = [2 + \text{sech}^2(\kappa_k t/2) + 2\tanh(\kappa_k t/2)]/(4n_k),$$

and $\mathbf{n} = (n_1, n_2, \ldots, n_N)$, such that $\sum_{k=1}^{N} n_k^{-1} \leq 1$. If no excitation is transferred through the jth QCC, $n_j \to \infty$, which implies $\mathcal{K}_j(t) = 0$ as well as $g_j(t;\mathbf{n}) = 0$, as expected. Moreover, if only an excitation fraction is transferred through the jth QCC ($n_{k\neq j} \to \infty$, so $\mathcal{K}_{k\neq j}(t) = 0$), one falls back to the scenario discussed in Section 7.2, and accordingly $g_j(t;\mathbf{n})$ in Eq. (7.21) simply reduces to Eq. (7.10).

7.2.3 Qubit-resonator-Purcell filter node

For the sake of generality, we are also going to explore what control would one use for producing fractions of excitations in the presence of a Purcell filter. For that, we will proceed as done in Chapter 3, and will propose a sech-shaped photon and apply Eqs. (3.34).

The fractional hyperbolic secant photon is the same as before, $\xi(t;n) = \sqrt{\kappa/(4n)}\mathrm{sech}(\kappa t/2)$, but the control now has an extra parameter g_p that accounts for the coupling between the transfer and filter resonators. Besides this extra parameter, and analogous to Chapter 3, there are new restrictions on how fast the photon can be transmitted, which have to do with the fact that all populations $|q(t)|^2$ (qubit), $|c(t)|^2$ (transfer resonator), $|d(t)|^2$ (Purcell filter) must be positive at all times. From the fact that $0 \leq c^2(t) \leq 1$ we arrive at the inequality that sets a constraint between κ, g_p and n

$$\kappa \leq \frac{16 g_p \sqrt{n}}{3}. \tag{7.22}$$

On the other hand, the condition for the qubit population, $0 \leq q^2(t) \leq 1$, leads to a somewhat intricate relation between κ, g_p, and n

$$0 \leq q^2(t) = 1 - \frac{e^{\kappa t}((1+e^{\kappa t})^2(2+e^{\kappa t})g_p^2 + \kappa^2}{(1+e^{\kappa t})^4 g_p^2 n} \geq 1. \tag{7.23}$$

The first thing to observe is that by setting $n = 1$ we arrive at the same condition already found in Chapter 3

$$\kappa \leq 2g_p. \tag{7.24}$$

For $n > 1$, the physical constraint leads to a quite complicated expression relating κ and g_p, yet, it can be shown that Eq. (7.24) is more restrictive than the one resulting for $n > 1$ and the condition in Eq. (7.22). For example, for $n = 2$, we find $\kappa \lesssim 3.8 g_p$. What this means in practice is that once g_p is set, and the fraction n is chosen, then the maximum value of κ is given by Eq. (7.23). Keep in mind that this restriction in κ ultimately sets a constraint on the maximum bandwidth of the photon, and therefore in the speed at which it can be emitted.

Finally, we can obtain the control from $g(t) = -\dot{q}(t)/d(t)$ (up to phase factors), so that

$$g(t;n) = \frac{e^{\kappa t}(2(1+e^{\kappa t})^2 g_p^2 + (1-3e^{\kappa t})\kappa^2)\cosh(\kappa t/2)}{(1+e^{\kappa t})^4 g_p \sqrt{n - \frac{e^{\kappa t}((1+e^{\kappa t})^2(2+e^{\kappa t})g_p^2+\kappa^2)}{(1+e^{\kappa t})^4 g_p^2}}}, \tag{7.25}$$

where again, the factor n appears in a non-trivial manner in the control.

After having laid out the different fractions of excitations that can be engineered in a variety of physical setups, the following section is devoted to the design of entanglement distribution protocols. Section 7.3 explores two distinct approaches for distributing genuinely multipartite entanglement. Both make use of fractional state transfer, but one does it sequentially (cf. Subsection 7.3.1) while the other does it in parallel (cf. Subsection 7.3.2).

7.3 Generation of W states via fractional quantum state transfer composition

Let us show how the fractional state transfer primitive can be used to produce multipartite entangled states in various network topologies. In particular, we focus our attention on *linear sequential networks*, and *extended parallel networks*.

Fractional quantum state transfer, as defined by Eq. (7.1) allows for a direct and deterministic generation of Bell pairs among emitter and receiver qubits. Yet, we aim to extend this notion to a general quantum network comprising N nodes and distribute genuine multipartite entangled states in a deterministic fashion. In particular, we focus on the genuine multipartite entangled W state, which for N qubits can be written as

$$|W_N\rangle = \frac{1}{\sqrt{N}} \sum_{j=1}^{N} |1_j\rangle, \tag{7.26}$$

where $|1_j\rangle$ denotes a single excitation in the jth qubit, and $|0\rangle$ in the rest, i.e. $|1_j\rangle = \hat{\sigma}_j^+ |\text{vac}\rangle$, where $|\text{vac}\rangle$ is the vacuum state for all the system, and $\hat{\sigma}^+ = |1\rangle\langle 0|$ the raising operator. In the following, we detail how the state $|W_N\rangle$ can be obtained in two distinct quantum network topologies, namely, linear and star networks (cf. Fig. 5.4). Depending on the connectivity, multipartite entanglement can be distributed either by a sequential or simultaneous protocol. To derive the protocols, it is assumed that the underlying Hamiltonian $\hat{H}$ of the full system (nodes and QCCs) conserves the total number of excitations. This is indeed a good description in most parameter regimes of the mentioned realizations of quantum networks (see, for example, [KMW$^+$17, BSZ$^+$19, MSK$^+$20, SSK$^+$23, GYC$^+$24]).

7.3.1 Sequential protocol for 1-D networks

Let us consider a 1-D quantum network, where all the N nodes are connected via a unique path, as depicted in Fig. 7.1a. In this setting, we require the nodes between two different quantum communication channels to have the freedom to emit/absorb from the right or left channel. That is, for nodes made of a qubit interacting via controllable coupling $g(t)$ with transfer resonators (cf. Fig. 7.2b), there is a transfer resonator at either end, and the coupling between them and the qubit is defined as $g_{j,L}(t)$ and $g_{j,R}(t)$, where the subscript j denotes the jth qubit in the network. Similarly, for nodes where wavepacket shaping is done via a controllable qubit decay rate, we distinguish $\kappa_{cj,L}(t)$ and $\kappa_{cj,R}(t)$, depending on the side.

For simplicity, we assume that the quantum network is initially prepared (at time t_0) in a state containing a single excitation in the qubit at one of the ends, namely, $|\psi(t_0)\rangle = |1_1\rangle$. Ideally, for perfect emission and absorption protocols across the network, one can write the state at time t as

$$|\psi(t)\rangle = \sum_{j=1}^{N} q_j(t)|1_j\rangle, \tag{7.27}$$

since the number of excitations is conserved, and with a normalization $\sum_j |q_j(t)|^2 = 1$. Note that $q_1(t_0) = 1$ and $q_{j\neq 1}(t_0) = 0$.

Starting with the initial condition (7.27) it is possible to arrive at a W-state by composing of $N-1$ sequential fractional state transfer operations. We define the composition of these operations as

$$T(n_1, \ldots, n_j, \ldots, n_{N-1}) = \mathcal{T}_{n_1} \times \ldots \mathcal{T}_{n_j} \times \ldots \mathcal{T}_{n_{N-1}} \tag{7.28}$$

with $n_k = (N+1-k)/(N-k)$ and $k = 1, \ldots, N-1$. The idea, schematically depicted in Fig. 7.4a consists of taking the excitation housed initially in the first qubit and start sharing it among the other nodes, one after another. The further a given qubit is from the initial one, the smaller fraction of excitation will be shared with it, as n_j becomes bigger. However, as we will now show, and verify with numerical simulations in the following section, this mechanism of decrease sharing can make the final state a uniform

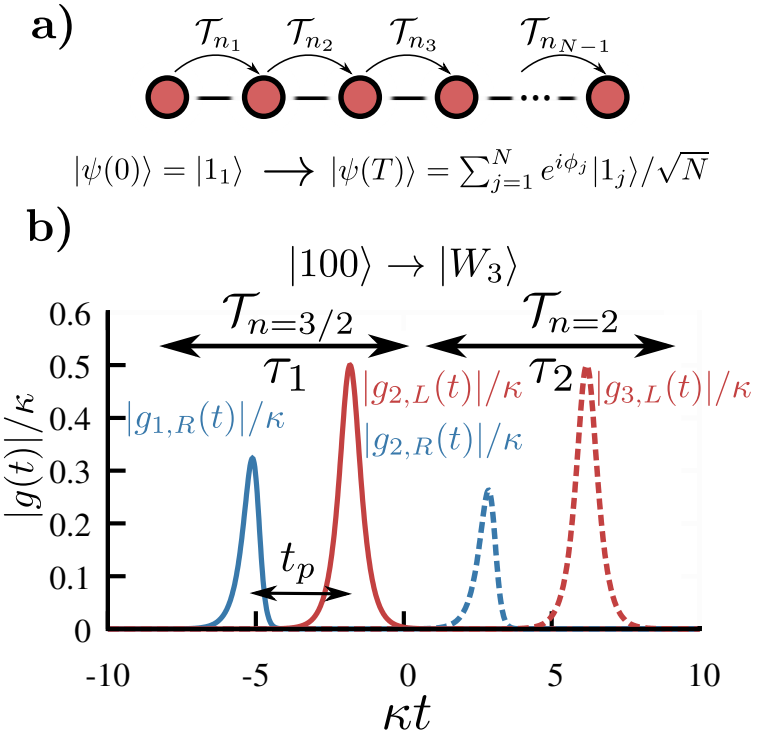

Figure 7.4: Sequential protocol to generate a $|W_3\rangle$ state starting from $|100\rangle$ (cf. Fig. 7.1b), assuming $\kappa_{1,2,3} = \kappa$ and equal propagation time between nodes. The initial excitation is transferred first to the second qubit (solid lines) through $\mathcal{T}_{n=3/2}$ taking a time τ_1 so that $|g_{1,R}(t)| = |g(t, n = 3/2)|$ performs the emission (blue) and $g_{2,L}(t) = g(-t + t_p; 1)$ the absorption (red). The second incomplete state transfer between qubit 2 and 3 is done by $\mathcal{T}_{n=2}$ (dashed lines) and takes a time τ_2, and similarly $|g_{2,R}(t)| = |g(t, n = 2)|$ (emission) and $|g_{3,L}(t)| = |g(-t + t_p; 1)$ (absorption)

superposition. Note that, by construction, $n_{k+1} > n_k > 1$ with $n_{N-1} = 2$, meaning that as we move along the quantum network, the fraction of the transferred excitation gets smaller. This designed protocol leaves the quantum network deterministically in a N-qubit W state, $|W_N\rangle$ (cf. Eq. (7.26)). Since it requires $N - 1$ incomplete quantum state transfers, $2(N - 1)$ processes of emission and absorption are needed.

Now, for qubit-transfer resonator nodes (cf. Fig. 7.2b), one chooses $g_{1,R}(t) = g(t; n_1)$ and $g_{2,L}(-t + t_{d,1}; 1)$ with $t_{d,1} = L_1/v_{g,1}$ the propagation time of the wavepacket through the first QCC of length L_1 and group velocity $v_{g,1}$.

Upon this first emission-absorption protocol that implements $\mathcal{T}_{n_1}$ among qubits 1 and 2, of duration τ_1 one finds the state $|\psi(\tau_1 + t_0)\rangle$ with coefficients

$$q_1(\tau_1 + t_0) = \sqrt{\frac{n_1 - 1}{n_1}}, \tag{7.29}$$

$$q_2(\tau_1 + t_0) = \frac{e^{i\phi_2}}{\sqrt{n_1}}, \tag{7.30}$$

$$q_{j>2}(\tau_1 + t_0) = 0. \tag{7.31}$$

Here ϕ_2 denotes the relative phase accumulated during the evolution.

Repeating the previous operation sequentially between neighboring nodes, i.e., performing $\mathcal{T}_{n_2}$ between node 2 and 3, and so on (cf. Fig. 7.1a), with $T = \sum_{j=1}^{N-1} \tau_j + t_0$ the

final time upon the protocol, one arrives at a state $|\psi(T)\rangle$ with coefficients

$$q_{j<N}(T) = e^{i\phi_j}\sqrt{n_j - 1}\prod_{k=1}^{j}\frac{1}{\sqrt{n_k}}, \tag{7.32}$$

$$q_N(T) = e^{i\phi_N}\prod_{k=1}^{N-1}\frac{1}{\sqrt{n_k}}. \tag{7.33}$$

Distinct choices of n_k and the phases determine different families of multipartite entangled states.

First, one can verify that for $n_1 = 2$ and $n_{j>1} = 1$, one prepares a Bell state among the first and last qubit in the linear quantum network, $|q_{1,N}| = 1/\sqrt{2}$ and $q_{j\neq 1,N} = 0$. This consists in transferring half excitation of the first qubit through the intermediate ones up to the last qubit so that the final state reads $|\psi(T)\rangle = \left(|10\ldots0\rangle + e^{i\phi_N}|0\ldots01\rangle\right)/\sqrt{2}$.

Second, a balanced superposition $|q_j| = 1/\sqrt{N}$ for $j = 1,\ldots,N$ can be achieved by $N-1$ incomplete quantum state transfers, namely,

$$\mathcal{T}_{n_1},\ldots,\mathcal{T}_{n_j},\ldots\mathcal{T}_{n_{N-1}} \quad \text{with} \quad n_k = (N+1-k)/(N-k)$$

Under ideal conditions and for the specific case of $N = 3$ qubits, an initial state $|\psi(0)\rangle = |100\rangle$ is brought to a three-qubit W state

$$|\psi(T)\rangle = \left(|100\rangle + e^{i\phi_2}|010\rangle + e^{i\phi_3}|001\rangle\right)/\sqrt{3}$$

using $n_k = (N+1-k)/(N-k)$ for $k = 1,2$, i.e. $n_1 = 3/2$ and $n_2 = 2$. Such state contains genuine tripartite entanglement, characterized by an entanglement of formation $E_{3\mathrm{F}} \approx 0.92$ where $E_{3\mathrm{F}} = \min\{S_1, S_2, S_3\}$ for pure states, and $S_j = -\mathrm{Tr}[\rho_j \log_2 \rho_j]$ the von Neumann entropy for the reduced state of the jth qubit [STF+20].

Finally, not all nodes need to be involved in the final quantum state. For example $N/2$-qubit W state for qubits placed at even sites, $|\psi(T)\rangle = \sqrt{2/N}\sum_{j=1}^{N/2} e^{i\phi_{2j}}|1_{2j}\rangle$, follows by alternating the transferred excitation fractions n_k at even and odd sites.

In Fig. 7.4b we show the example controls for a 3-node linear network. The excitation is first transferred from node one to node two, and then *sequentially* from node two to node three. The blue-colored controls correspond with the emission for $n = 3/2$, and $n = 2$, whereas the reception controls (red color) are perfect hyperbolic secant with $n = 1$. As previously discussed, the emission and absorption controls are not the time reverse of each other when the objective is to distribute entanglement.

7.3.2 Parallel protocol for 1-to-N networks

The previous sequential protocol is directly based on the fractional quantum state transfer among two spatially separated qubits. Although a sequential protocol suffices to distribute entanglement, other network architectures may grant larger connectivity, which can be harnessed to accelerate entanglement distribution across the network. As an example, we consider a star quantum network, as depicted in Fig. 7.1c, which consists of a central node linked to N different nodes via N quantum communication channels. In this situation, we require that the central node, denoted here as emitter (E), can address each of the N channels individually. Furthermore, it is assumed that distinct wavepackets can be injected through these waveguides simultaneously.

As anticipated, the simultaneous emission through independent quantum links leads to a non-trivial modification of the controls, given in Eqs. (7.21) and (7.9). Although they have been derived considering strictly simultaneous emission of wavepackets that

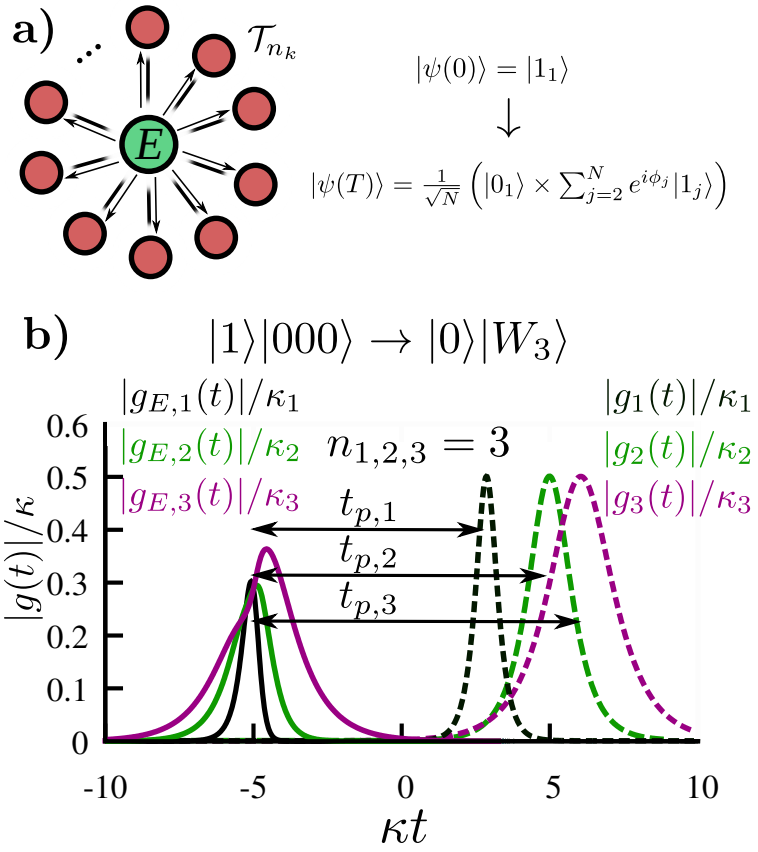

Figure 7.5: (b) Simultaneous emission from qubit E to $N = 3$ nodes (cf. Fig. 7.1c), preparing them in a $|W_3\rangle$ state. The pulses $g_{\mathrm{E},j}(t)$ denote the coupling between qubit E and the jth resonator (emission, solid lines) which then is routed towards the jth node, where $g_j(t)$ is tuned to absorb the incoming photon, i.e. $g_j(t) = g(-t+t_{p,j}, n = 1)$ (dashed lines). Here $g_{\mathrm{E},j}(t)$ follows from Eq. (7.21) with $n_1 = n_2 = n_3 = 3$ and $\kappa_j = \kappa/j$, and we have assumed different propagation times between E and the jth node $t_{p,j} = L_j/v_g$.

propagate through the quantum links, it is certainly possible to allow for arbitrary time delays among them.

We show, in Fig. 7.5b, the controls for a parallel protocol in which the excitation is transferred through three different channels, with different lengths and different decay rates of the resonators. In all three cases $n = 3$ for emission, while the absorption is done with $n = 1$, and therefore, all the absorption control are again hyperbolic secants.

The simultaneous emission from the emitter towards the N receiver nodes accelerates the protocol to distribute genuine multipartite entanglement, as will be shown with numerical simulations in the next section. Again, the absorption in the receiver nodes must be done according to the time-reversed controls as detailed in Sec. 7.1, namely, $g(-t+t_{d,j}; n = 1)$ and $\kappa_c(-t+t_{d,j}; n = 1)$ where $t_{d,j}$ refers to the propagation time through the jth QCC. The total protocol time is only limited by a single emission-absorption for the slowest QCC, and thus faster than the sequential scheme at the expense of requiring the synchronization among all nodes and careful simultaneous control on the emitter.

In particular, an initial state with $q_E(t_0) = 1$ and $q_{j\neq E}(t_0) = 0$, is mapped to

$$q_E(T) = (1 - \sum_{j=1}^{N} n_j^{-1})^{1/2} \quad \text{and} \quad q_j(T) = e^{i\phi_j}/\sqrt{n_j}. \tag{7.34}$$

The emission with $\sum_k n_k^{-1} = 1$ completely exhausts the emitter excitation, $q_E(T) = 0$. Moreover, setting $n_j = N\ \forall j \in \{1, N\}$, i.e. for each of the N emitted wavepackets, the final state upon absorption corresponds to a $|W_N\rangle$ among the N receiver nodes. For $n_j = N + 1\ \forall j \in \{1, N\}$, the emitter also participates in the entangled state, leading to a $|W_{N+1}\rangle$ state. Both options are interesting, but we will focus on the first in the numerical implementation, i.e., that which completely depletes the emitter qubit.

In the following, we focus on a particular setup to test the performance of the sequential and simultaneous protocols to prepare a genuine multipartite entangled state $|W_3\rangle$ for three qubits taking into account the dynamics of realistic waveguides. In addition, we detail the impact of the main pressing decoherence effects in these systems, namely, qubit decay and dephasing.

7.4 Numerical verification of W states creation

We will first, in Subsection 7.4.1 present explicitly the concrete models with their respective Hamiltonians for the linear and extended quantum networks. In this context, a proof of concept simulation is performed with a sequential protocol in the linear case and a parallel protocol in the extended one. These simulations show that the controls obtained in Section 7.3, applied to the Hamiltonians of the full problem, indeed transfer fractions of excitations and distribute genuine entanglement deterministically.

The second part of the section, i.e., Subsection 7.4.2, studies how much decoherence and dephasing ruin the protocols and offers quantitative measures for the quality of the obtained entanglement.

7.4.1 Coherent model

To illustrate the performance of the general framework put forward in the previous subsections, we consider two distinct quantum networks made of qubits coupled to transfer resonators operating in the microwave regime, close to the experimental setups reported in [KMW$^+$17, MSK$^+$20, SSK$^+$23]. In this case, the quantum communication channels are embodied by waveguides at cryogenic temperatures that allow for the exchange of itinerant single microwave photons with minimal losses.

7.4.1.1 Linear quantum network

We first consider a linear quantum network comprising three nodes, similar to the illustration in Fig. 5.4a. The Hamiltonian H_l, where the subscript l stands for linear quantum network, can be written as

$$H_l = \sum_{i=1}^{3} H_{n,i} + \sum_{i=1,2} H_{qcc,i} + \sum_{i=1,2} H_{n-qcc,i}, \tag{7.35}$$

being $H_{n,i}$ the local Hamiltonian for each node, $H_{qcc,i}$ the Hamiltonian for each QCC and $H_{n-qcc,i}$ the interaction between nodes and QCCs. The Hamiltonian for the nodes 1 and 3, i.e. $H_{n,1}$ and $H_{n,3}$, read as

$$H_{n,i} = \delta_i \sigma_i^+ \sigma_i^- + \omega_i a_i^\dagger a_i + g_i(t)(\sigma_i^+ a_i + \text{H.}c.) \quad i = 1, 3 \tag{7.36}$$

where σ^+ and σ^- are the usual raising and lowering spin operators, while $a^\dagger$ and a the bosonic creation and annihilation operators, such that $[a, a^\dagger] = 1$, and $g_i(t)$ is the tunable coupling between the ith qubit an its transfer resonator. Recall that the couplings are

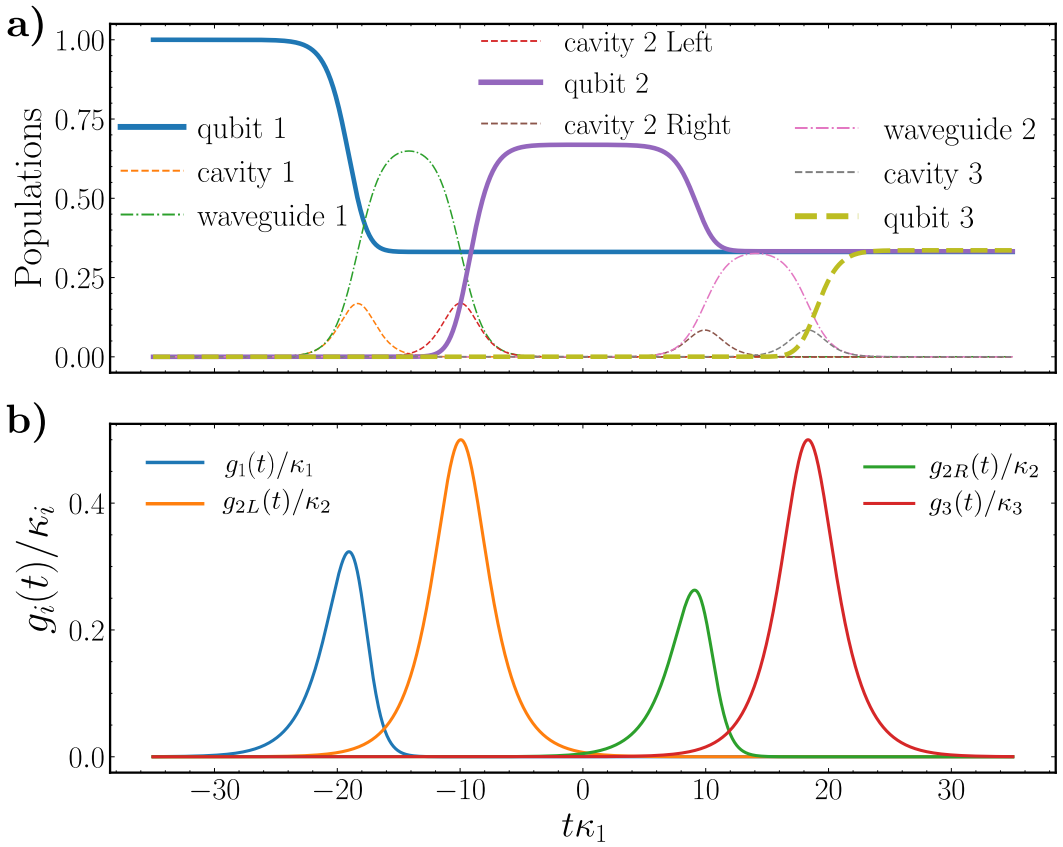

Figure 7.6: Proof-of-concept simulation of a sequential protocol for creating a $|W_3\rangle$ state implemented in a linear three nodes network. All components have been kept equal for the sake of simplicity. $l_{\mathrm{WG1}} = l_{\mathrm{WG2}} = 5\mathrm{m}$. The decay rates of all four cavities are $\kappa = 2\pi \times 10$ MHz. The resonant frequencies of all qubits and cavities $\delta_i = \omega_i = 2\pi \times 8.407$ GHz. Panel a) shows the occupations of the different elements of the network. The target state of this protocol is $|W_3\rangle$, and whereas the fidelity can not be assessed directly from the occupations, we see that the necessary condition that $|q_1(T)|^2 = |q_2(T)|^2 = |q_3(T)|^2 = 1/3$ is fulfilled. Precise measures of the fidelity and entanglement of the target state will be given when presenting the realistic simulations with noise. Panel b) shows the controls employed for the protocol, as the name states, they are applied sequentially.

assumed to be real. The central node containing qubit 2, is coupled to left and right transfer resonators, namely,

$$H_{n,2} = \delta_2 \sigma_2^+ \sigma_2^- + \sum_{s=L,R} \left(\omega_{2,s} a_{2,s}^\dagger a_{2,s} + g_{2,s}(t)(\sigma_2^+ a_{2,s} + \mathrm{H.}c) \right). \tag{7.37}$$

The QCCs connecting qubit 1 with 2, and qubit 2 with 3, are represented by a collection of N bosonic modes,

$$H_{qcc,i} = \sum_k \Omega_k b_{k,i}^\dagger b_{k,i}, \tag{7.38}$$

fulfilling also $[b_k, b_{k'}^\dagger] = \delta_{k,k'}$, while the interaction is given by

$$H_{n-qcc,1} = \sum_k G_k \left(b_{k,1}^\dagger a_1 + (-1)^k b_{k,1}^\dagger a_{2,L} + \mathrm{H.}c. \right) \tag{7.39}$$

$$H_{n-qcc,2} = \sum_k G_k \left(b_{k,2}^\dagger a_{2,R} + (-1)^k b_{k,2}^\dagger a_3 + \mathrm{H.}c. \right). \tag{7.40}$$

For the couplings G_k and the dispersion relation Ω_k, we once again use the models discussed in Chapter 2. For simplicity, we assume resonant elements and equal decay rates of the resonators, $\delta_i = \omega_i = \omega$, $\kappa = \kappa_i$ for $i = 1, 2$ and 3. In this manner, the couplings read $G_k = \sqrt{\kappa v_g \Omega_k/(2\omega L)}$ as customary in the Ohmic regime [Rip22], where v_g is the group velocity and L is the length of the waveguide.

The numerical simulations take advantage of the conservation of the total excitation of H_l. Considering an initial state containing a single excitation in the qubit 1, one can exactly simulate the coherent dynamics relying on the Wigner-Weisskopf ansatz.

This ansatz leads to the set of coupled differential equations in terms of the coefficients, $\frac{d}{dt}|\Psi_l(t)\rangle = -iH_l|\Psi_l(t)\rangle$, where the initial condition is $q_1(t_0) = 1$, and the rest of the coefficients set to zero.

A fully coherent, proof-of-concept simulation of a three-node linear network in which a sequential protocol is shown in Fig. 7.6. Panel a) depicts the different populations of all the elements of the network throughout the protocol. It can be seen that at the end the populations of all three qubits is $|q_1(T)|^2 = |q_2(T)|^2 = |q_3(T)|^2 = 1/3$. Although this alone is not proof of having obtained the W-state, it is a necessary condition. In the next section, we will provide precise measures of the fidelity and entanglement of formation, including the effects of dephasing and decoherence. In Fig. 7.6b we show the controls applied at each node, as mentioned before, the emitting controls significantly differ from the absorption ones. It is required to always set $n = 1$ for absorption since the success of the protocol depends on the node absorbing all the field that it receives.

7.4.1.2 Star-like quantum network

The second model we consider is a star-like quantum network, cf. Fig. 5.4b, consisting of four nodes, i.e. a central emitter plus three nodes. The Hamiltonian of this star network, H_s, can be written as

$$H_s = H_E + \sum_{i=1}^{3} \left(H_{n,i} + H_{qcc,i} + H_{n-qcc,i}\right). \tag{7.41}$$

The Hamiltonian of the emitter H_E reads as

$$H_E = \delta_E \sigma_E^+ \sigma_E^- + \sum_{i=1}^{3} \omega_{E,i} a_{E,i}^\dagger a_{E,i} + \sum_{i=1}^{3} g_{E,i}(t)(\sigma_E^+ a_{E,i} + \text{H.}c), \tag{7.42}$$

while the receiver nodes are described by $H_{n,i}$ as given in Eq. (7.36) for $i = 1, 2$ and 3, and similarly for $H_{qcc,i}$ (cf. Eq. (7.38)). The interaction between the QCCs, emitter, and receiver nodes is given by

$$H_{n-qcc,i} = \sum_k G_k \left(b_{k,i}^\dagger a_{E,i} + (-1)^k b_{k,i}^\dagger a_i + \text{H.}c.\right). \tag{7.43}$$

As in the previous case, we assume resonant elements so that the frequency of qubits and resonators is set to ω, as well as an equal decay rate κ. The dispersion relation of the QCCs and the corresponding couplings is taken as for H_l given above.

Note that in both cases, the counter-rotating terms in the interaction Hamiltonians have been neglected under the rotating-wave approximation. This is a good approximation in this setup as the frequencies (ω and Ω_k) are typically two orders of magnitude larger than the coupling strength (G_k and $g(t)$).

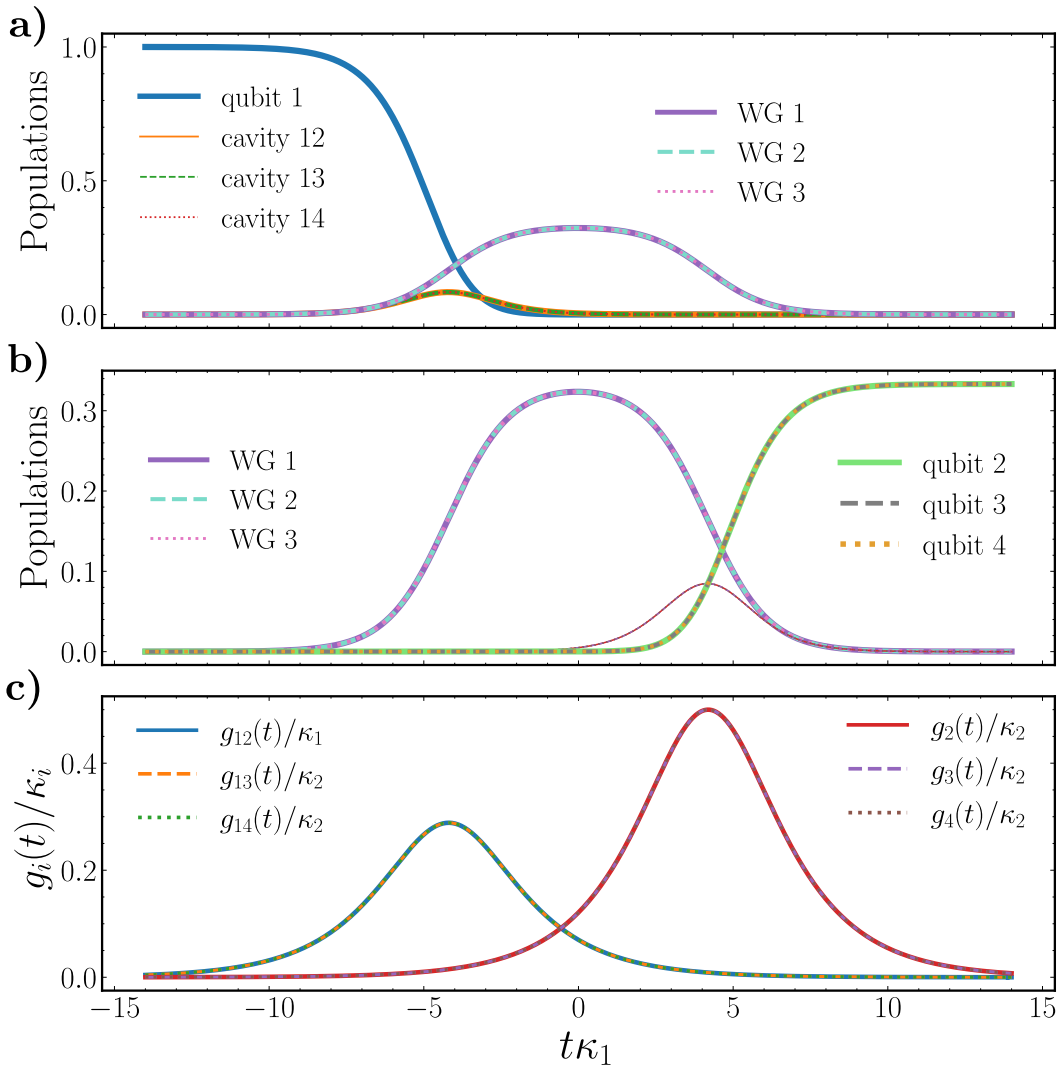

Figure 7.7: Proof-of-concept simulation of a parallel protocol for creating a $|W_3\rangle$ state implemented in a four nodes star-like network. All components have been kept equal for the sake of simplicity. $l_{\mathrm{WG1}} = l_{\mathrm{WG2}} = l_{\mathrm{WG3}} = 5\mathrm{m}$. The decay rates of all four cavities are $\kappa = 2\pi \times 10$ MHz. The resonant frequencies of all qubits and cavities $\delta_i = \omega_i = 2\pi \times 8.407$ GHz. Panel a) shows the occupations of the different elements at the emission point, where it can be seen that the emitting qubit (solid blue line) gets completely depleted. Panel b) shows the occupations at the different reception points. As in the sequential protocol, the target state is $|W_3\rangle$, and the condition that $|q_1(T)|^2 = |q_2(T)|^2 = |q_3(T)|^2 = 1/3$ is fulfilled. Panel b) shows the controls employed for the protocol. There are six controls in total, three employed for emission in parallel at the same node, and three for reception at each of the three nodes also in a simultaneous fashion.

In this case of the star quantum network, the single excitation wave function at all times is

$$|\Psi_s(t)\rangle = \Big[q_E(t)\sigma_E^+ + \sum_{i=1}^{3} q_i(t)\sigma_i^+ + \sum_{i=1}^{3}(c_{E,i}(t)a_{E,i}^\dagger + c_i(t)a_i^\dagger) + \sum_k \sum_{i=1}^{3} \psi_{k,i}(t)b_{k,i}^\dagger\Big]|\text{vac}\rangle\,. \tag{7.44}$$

This ansatz leads to the set of coupled differential equations in terms of the coefficients, $\frac{d}{dt}|\Psi_s(t)\rangle = -iH_s|\Psi_s(t)\rangle$, where the initial condition is $q_E(t_0) = 1$, and the rest of the coefficients set to zero.

We show, in Fig. 7.7, a full coherent, proof of concept simulation of a four-node extended network in which the parallel protocol is applied. Panels a) and b) depict the different populations of all the elements of the network throughout the protocol. Analogously to the linear case of the previous subsection, the final populations of all receiving qubits are $|q_2(T)|^2 = |q_3(T)|^2 = |q_4(T)|^2 = 1/3$. In Fig. 7.7c we show the controls applied at each node. In this case, contrary to the previous proposal, all emitting controls $g_{12}(t), g_{13}(t), g_{14}(t)$ are applied simultaneously to the qubit 1, and also the receiving controls are applied synchronously to each receiving qubit. Note, finally, that the whole protocol is much faster in this case than in the sequential one, ranging from $t \in (-14\kappa, +14\kappa)$ instead of the sequential time of $t \in (-35\kappa, +35\kappa)$.

7.4.2 Effects of decoherence and dephasing

We benchmark the generation of a genuine multipartite entangled state W employing an incomplete quantum state transfer, performing numerical simulations in the two quantum networks discussed above. In particular, we perform a sequential protocol for the linear quantum network, while the star network allows for simultaneous control. In both cases, we aim at preparing a three-qubit W state, i.e., $|W_3\rangle$.

We incorporate the impact of decoherence effects taking into account the most relevant sources in this setup, namely, qubit dephasing and spontaneous decay. We model qubit dephasing as a random uncertainty in each of the qubit frequencies obeying a Gaussian distribution. For a single realization, the frequency of the ith qubit is shifted according to $\delta_i \to \delta_i + \delta\omega_i$ with

$$p(\delta\omega) = \frac{1}{\sqrt{2\pi}\sigma} e^{-\delta\omega^2/(2\sigma^2)}. \tag{7.45}$$

The dephasing time is related to the standard deviation of the Gaussian distribution as $\sigma = \sqrt{2}/T_2$. Assuming an equal T_2 for all the qubits, this results in an independent and identically distributed fluctuation $\delta\omega_i$ for all qubits in the network.

The impact of spontaneous decay is included by integrating the population of each of the qubits during the time of the protocol, $\tau_i = \int dt|q_i(t)|^2$, and then reducing the amplitude of the corresponding qubit. That is, the population of the ith qubit decreases by a factor $e^{-\tau_i/T_1}$, which is brought to the vacuum state. Again, we consider equal T_1 times for all the qubits across the network. However, we anticipate that dephasing and spontaneous decay will have a different impact depending on the network configuration, i.e. depending on a sequential or simultaneous protocol. This is a direct consequence of both protocols having very different durations.

Averaging over many stochastic realizations for the dephasing noise, one obtains an ensemble $\overline{\rho}_T$. Since we are interested in the resulting state for the three qubits participating in the entangled state, all the other elements in the system are traced out, i.e. $\overline{\rho} = \text{Tr}_r[\overline{\rho}_T]$,

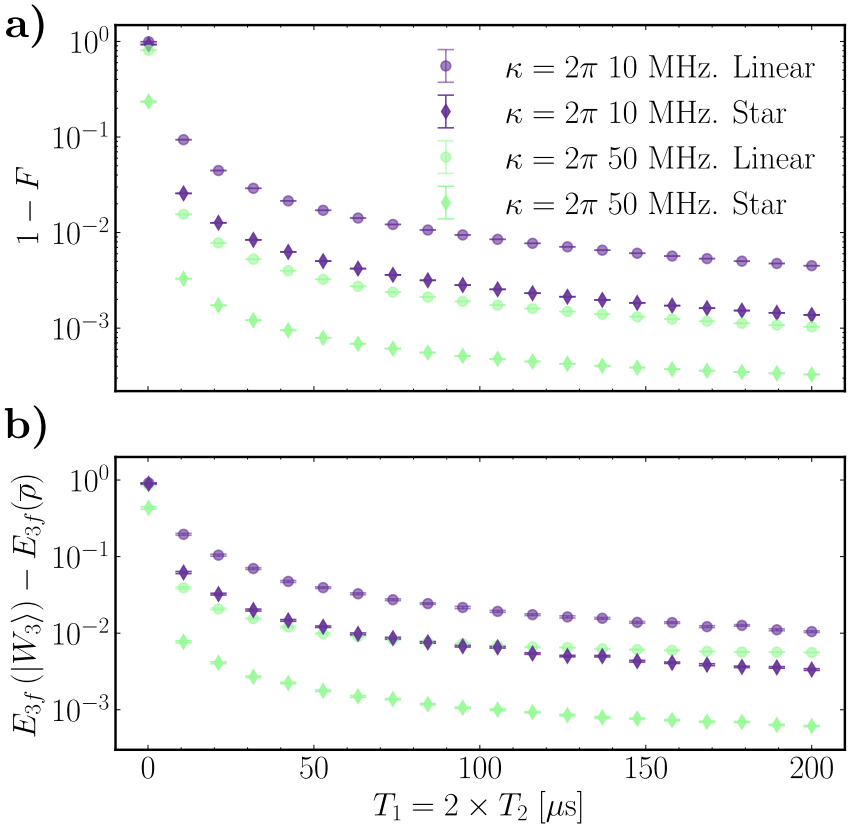

Figure 7.8: Performance of the generated genuine multipartite entangled state $|W_3\rangle$. Panel (a) shows the infidelity $\log_{10}(1-F)$ concerning the targeted state $|W_3\rangle$ for sequential (linear) and simultaneous (star) protocols as a function of T_2 and T_1, setting $T_1 = 2T_2$, and for two different decay rates κ. Panel (b) shows the entanglement of formation E_{3f} of the resulting state, in particular, the difference with the ideal value $E_{3f}(|W_3\rangle) \approx 0.918$, i.e. $\log_{10}(E_{3f}(|W_3\rangle) - E_{3f}(\overline{\rho}))$. In both panels, $\kappa = 2\pi \times 50$ MHz (green color) provides better results, as the protocol is faster than $\kappa = 2\pi \times 10$ MHz (violet color). Each of the points corresponds to 10^3 stochastic realization to correctly include dephasing noise. Error bars correspond to the standard deviation for each case performing bootstrapping. See the main text for details of the parameters.

so that $\overline{\rho}$ is the reduced state for three qubits. Note that, due to the nature of the process, only the states $|100\rangle$, $|010\rangle$, $|001\rangle$ and $|000\rangle$ will be relevant.

We numerically simulate the dynamics of the protocol to generate a $|W_3\rangle$ in these two networks, considering $\omega = 2\pi \times 8.407$ GHz for qubits and transfer resonators, $N = 100$ modes for each of the waveguides centered around the central frequency ω and a total length of $L = 5$ m. In addition, we introduce a correction on the qubit frequencies to account for the Lamb shift that stems from the interaction of the transfer resonators with the QCCs. Once again, as already done in previous chapters, we optimize the depletion of the qubit excitation and find $\delta_{LS} = 0.0065\kappa$ for each of the nodes so that $\delta \to \delta + \delta_{LS}$. To generate the $|W_3\rangle$ the time-dependent controls presented in Section 7.1 and Section 7.2 are used. In particular, for the linear network $g_1(t)$ follows $g(t;n)$ given in Eq. (7.21) with $n = 3/2$, $g_{2,L}(t)$ corresponds to $g(-t+t_d;1)$, while $g_{2,R}(t)$ again $g(t+t_s;n)$ with $n = 2$ and finally $g_3(t) = g(-t+t_d+t_s;1)$. Here t_s denotes the delay time of the emission protocol from qubit 2 to avoid an overlap with the absorption from qubit 1. For the star network, the emitter coupling $g_{E,i}(t)$ follows Eq. (7.21) with $\mathbf{n} = (3,3,3)$, while the receivers a set to $g(-t+t_d;1)$. We investigate the interplay of the decay rates, which also fixes the photon

bandwidth, namely $\kappa = 2\pi \times 10$ MHz and $2\pi \times 50$ MHz, with the coherence times T_1 and T_2 in the range of $\sim 1\mu$s to 100μs. The total duration of the sequential protocol is set to $35/\kappa$, while the simultaneous allows for a faster generation, $14/\kappa$.

We quantify the performance of the protocol in terms of the fidelity F for the target $|W_3\rangle$ and entanglement of formation E_{3f} [Woo98, Sza15]. The fidelity F is computed as $F = \max_{\phi_2,\phi_3} F(\phi_2, \phi_3)$ where $F(\phi_2, \phi_3) = \langle W_3'|\overline{\rho}|W_3'\rangle$ with $|W_3'\rangle = \frac{1}{\sqrt{3}}(|100\rangle + e^{i\phi_2}|010\rangle + e^{i\phi_3}|001\rangle)$, i.e. allowing for local phases. The entanglement of formation E_{3f} for a three-qubit pure state $|\psi\rangle$ is defined as $E_{3f}(|\psi\rangle) = \min\{S_1, S_2, S_3\}$ where S_j is the von Neumann entropy for the reduced state of the jth qubit, i.e. $S_j = -\mathrm{Tr}[\rho_j \log_2 \rho_j]$. For the $|W_3\rangle$, it follows $E_{3f}(|W_3\rangle) = \log_2(3) - 2/3 \approx 0.918$. For a mixed state ρ, however, the entanglement of formation is computed as the minimum over all possible ensemble decomposition of ρ, i.e. $E_{3f}(\rho) = \min \sum_i p_i E_{3f}(|\psi_i\rangle)$ where $\rho = \sum_i p_i |\psi_i\rangle\langle\psi_i|$ [Woo98, Sza15].

In Fig. 7.8 we show the numerical results for the infidelity (a) and the entanglement of formation (b) as a function of coherence times $T_2 = T_1/2$, and for the two networks with $\kappa = 2\pi \times 10$ MHz and $2\pi \times 50$ MHz. The results have obtained averaging 1000 stochastic realizations for the dephasing, while the error bars correspond to a standard deviation performing bootstrapping. As can be seen, the simultaneous protocol performed in the star network is more robust to decoherence than its linear counterpart. This is expected since the star network allows for a faster protocol to generate the genuine multipartite entangled state $|W_3\rangle$. In particular, we find good results for state-of-the-art coherence times, as evidenced by the entanglement of formation or the fidelity, $1 - F < 10^{-2}$ for $T_2 > 40\mu$s or even below 10^{-3} for the star network already for $T_2 \gtrsim 20\mu$s. In addition, it is worth mentioning that a fidelity $F > 2/3$ witnesses multipartite entanglement in the W class [WGE16]. This is achieved for very short coherence times ($T_2, T_1 \sim 5\mu$s).

7.5 Summary

In this chapter, we have introduced a fractional quantum state transfer protocol designed to generate entangled states across a quantum network. The protocol leverages wavepacket shaping to inject a traveling single photon through a quantum communication channel. We have first presented the mechanism between two quantum nodes, enabling the distribution of maximally-entangled states. We considered two key cases: (i) a node consisting of a qubit coupled to a transfer resonator with tunable control, and (ii) a qubit with a tunable, time-dependent decay rate into the quantum communication channel.

The protocol was then extended to N nodes, where a sequential application of incomplete quantum state transfers can generate a W multipartite entangled state. Additionally, we explored a scenario where the control allows for simultaneous emission, which accelerates the generation of W states. The general framework proposed in this chapter was tested numerically, considering both linear and extended network configurations. We included the primary sources of decoherence in these systems, namely, qubit dephasing and spontaneous decay. The numerical results demonstrated that multipartite entanglement can be successfully achieved in state-of-the-art setups, with fidelities in the range of $1 - F \approx 10^{-2}$ or better.

This work paves the way for exciting future developments in quantum networks, particularly for achieving deterministic and rapid operations between distant nodes without the need for measurements or the exchange of information through classical channels. Making use of multiple photonic excitations along with multiplexed quantum links could lead to new opportunities in quantum computation and communication.

8 Conclusions and Outlook

This thesis has addressed the challenge of building a comprehensive quantum optical modelization of a superconducting quantum state transfer network based on microwave links. The reason that drove us to face this task is the promise of a fully operational and scalable quantum computing architecture. With that goal in mind, we have proposed solutions to resolve some of the most pressing current limitations, such as cross-talk between emitters and size of the quantum computing chips [AAB+19, MMMJ20], and designed novel protocols to help increase the fidelity, speed, and computational capacity of quantum links that connect separated quantum processors.

In the last decade, mainly motivated by the high degree of control and astonishing gate fidelities that were being achieved with superconducting circuits, some experimental groups around the world started distributing the computations in a deterministic manner, by mapping the qubit states from the solid state transmons to flying microwave photons, first within the same refrigerators [KKT+18, ABP+18], and more recently, among different ones [MSK+20, SSK+23]. And thus the paradigm of state transfer networks began. Although this is a term that we have coined, the idea is by no means ours. It traces back to the original quantum state transfer proposal [CZKM96], and it refers to the general concept of mapping stationary qubits to flying ones in a way that enables their emission and retrieval. This protocol allows for entanglement distribution and enables multiqubit, non-local operations. It is within this context that this thesis falls.

The first original result of the present thesis is introduced in Chapter 3. It consists of the systematic use of input-output theory to obtain the specific functional form of the control $g(t)$ from the desired target wavepacket, which could be designed for emission or absorption. Through these quantum optics techniques, we discovered that the controls $g(t)$ vary significantly depending on specific hardware components, such as Purcell filters, which are commonly used to enhance qubit coherence. We integrated these previously overlooked details into our analysis, paving the way for employing time-dependent controls to tackle various challenges in the following chapters. Indeed, given the flexibility of the possible $g(t)$ controls and the generality of the paradigm, we believe their range of application extends far beyond what we explored in this thesis.

Once we established in detail the theory of wavepacket engineering, we studied, in Chapter 4, the most pressing sources of errors in superconducting quantum links to design two families of distributed and fully deterministic quantum gates. Within this exploration, we found an interesting side result, namely, that input-output theory describes the processes of scattering and wavepacket shaping faithfully even in limits in which the photon only interacts with very few waveguide modes. Building on this finding, we were able to show that wavepacket shaping, due to its speed, could outperform adiabatic protocols and overall increase the velocity of distributed protocols across quantum links. The results from this segment point towards the feasibility of quantum information processing based

on quantum links, and show that universal distributed gates based on wavepacket shaping and state transfer are ready for implementation with promising fidelity values.

As the technology advances towards faster protocols and better overall fidelities, two issues are becoming more relevant in the realm of microwave quantum links, these are wavepacket distortion by propagation and non-Markovian effects. We proposed in Chapter 5 a method for mitigating distortion by designing and engineering a wavepacket with a phase profile opposed to the one acquired by propagation. This proposal is very flexible and it could be used essentially for any distortion method that changes the wavepacket profile, such as scattering or change of physical medium. On top of this, we refined the theory for wavepacket shaping proposed in Chapter 3, including second-order corrections to the Markov approximation. As we identified, this is essential for a precise chirping of the controls and also for engineering faster pulses.

Another very important issue to address in the quest for distributed quantum computing via deterministic quantum links is that of information multiplexing. It is necessary to be able to send multiqubit states through the quantum link to allow for real and practical scalability. In Chapter 6 we turned our attention to this problem and proposed two complementary ways to increase the information capabilities of the waveguide. First, through spatio-temporal wavepacket multiplexing, we designed a family of mutually orthogonal wavepackets that can be selectively emitted and absorbed. Secondly, we performed a thorough study of the bandwidth capabilities of the waveguide and determined that, with enough qubits at the end of the quantum link, hundreds of quantum states could be sent simultaneously with very good fidelities. The requirement is that the carrier frequencies of the photons are sufficiently far apart, but this restriction is easy to circumvent as the overlap infidelity decreases exponentially, and the available bandwidths are large.

Finally, in Chapter 7 we shifted our attention towards another critical issue for distributed quantum computing, namely, the generation of entanglement. We envisioned a protocol, based on the emission of fractions of excitations, that deterministically generates entanglement across an arbitrary number of nodes. More specifically, our fractional state transfer method transforms an initial product state into a many-node W-state without needing measurements. We showed that the method is flexible and can be adapted to many experimental configurations—qubits directly coupled to the waveguide, cavities and frequency filters, one-to-one fractional states, one-to-N, etc. Each particular instance needs a different control $g(t)$, but the underlying mechanism is equivalent in any configuration.

Overall, this thesis advocates for a distributed architecture based on superconducting microwave quantum links as a viable alternative for scaling up quantum computing systems. Building on the very well-established theory of quantum optics [SZ97, Nav22, Rip22], and motivated by several ground-breaking experiments [KKT$^+$18, ABP$^+$18, MSK$^+$20, SSK$^+$23], we argue in favor of the all-microwave fully cryogenic distributed quantum computer.

Throughout the whole work, we have proposed solutions for some of the most acute sources of errors in these systems. We have also designed protocols that advance quantum information science by leveraging the best attributes of superconducting circuits, namely, their fast execution times and strong light-matter couplings. The general results of the exploration are positive. We believe that the full flexibility of the controls $g(t)$ has not yet been exhausted and that there is plenty of room for improvement. Some issues within this paradigm remain unaddressed in the present thesis, such as achieving longer coherence times for qubits—an ongoing engineering challenge—and improving measurement times and fidelities, which is an active area of research. However, substantial progress is being made in both of these areas, as well as with the limitations we did explore in detail.

Our analytical and numerical explorations showed that the full bandwidth of the available quantum links is far from being used. This makes it an appealing road for scaling

quantum processors. Furthermore, the fractional state transfer protocol that we proposed enables the creation of fast deterministic genuine multipartite entanglement with very little resource overhead, and with current technology. For all these reasons, this thesis adds another brick of evidence to the already quite robust building of superconducting circuits for quantum information processing. It points towards the convenience of supporting this architecture as a viable candidate for a fully scalable distributed quantum computer.

Although the vision of an extensive superconducting quantum network operating entirely with microwaves at cryogenic temperatures might seem distant, it is important to remember that connecting different cryostats via microwave waveguides seemed unthinkable just some years ago. Today, however, there are experiments already working based on this concept [MSK$^+$20, SSK$^+$23]. A complementary approach to the one explored in this thesis, and one to which many of our techniques could be applied is microwave-to-optical transduction [LSB$^+$20]. In this scenario, a small-scale local superconducting state transfer network would first be used to leverage the strong light-matter couplings available in circuit QED for mapping stationary qubits to propagating ones. Once the qubit state is mapped to a propagating microwave photon, it would then be transduced into an optical photon [LRSS20, SHR$^+$22], which could travel through an optical fiber. The appeal of this approach lies in the fact that photons in the THz regime experience minimal distortions and thermal fluctuations, as the density of thermal photons at such high energies is negligible. After traveling a considerable distance, the optical photon can be transduced back to a microwave photon and reabsorbed by a solid-state qubit at another local superconducting network. This concept could potentially enable the long-sought goal of an inter-city quantum internet [Kim08, MRR$^+$14, WEH18]. The main challenge facing this paradigm today is the transduction process, which is inherently noisy. Preserving quantum coherence during transduction is both crucial and extremely challenging [MSKP20, BKU$^+$22, SHR$^+$22, KSS$^+$23, WDB$^+$24]. Nonetheless, this remains an exciting and rapidly advancing area of research.

On top of all this, it is important to state that there remain big challenges and unresolved problems in the field, many of which were only partially addressed in the current work. The main issue that this thesis leaves open is the construction of a complete quantum optical theory of state transfer. We have made several incremental contributions and addressed the problem in different situations. However, we believe it should be possible to construct a general framework in which to relate the quantum states of the emitters, the controls $g(t)$, and the state of general bosonic media. A formalism that works backward and forward, for emission and absorption, and that is exempt from all artificial restrictions such as that of temporal inversion.

Besides this big challenge, many other, less ambitious research lines depart from this work. For instance, the convergence of the Lamb shift as defined in Chapter 3 when applied to the model constructed in Chapter 2 is far from obvious. The study of this problem already gave rise to a master thesis, and a publication on the issue is in progress. On a more applied front, the correction strategies conceived in Chapter 5 only work up to second-order on the dispersion relation. This limits their applicability, and there is no reason to think why phase profiles that encompass the full complexity of an arbitrary $\omega(k)$ can not be designed. Along the same lines, our correction to the Markovian approximation also admits generalization. It would be desirable, and in principle doable, to incorporate into the model more details and advance beyond the first-order correction. Ultimately, this objective overlaps with the more ambitious one of a general quantum optical framework for quantum state transfer.

Another quite direct continuation of this work is to explore the potential of the orthogonal wavepackets proposed in Chapter 6 to construct complex highly entangled photonic states [FKB$^+$24]. Moreover, the combination of the two multiplexing strategies proposed

could lead to an even larger exploitation of the available bandwidth. Finally, Chapter 7 opens up the way for many potential applications, we focused almost exclusively on the design and numerical benchmarking of the method, but transmission of fractional excitations can lead to other interesting applications. This intuition builds, for instance, on the fact that one can design fractions with shapes that are not allowed for whole excitations, such as Gaussian ones. Also, the possibility of combining fractional quantum state transfer with other known methods such as entangling two qubit gates at specific nodes seems exciting.

In summary, this thesis leads to optimistic conclusions and positive results regarding the utilization of superconducting quantum links for quantum computing tasks, while opening several interesting research paths that hopefully someone will walk.

Acknowledgements

I want to begin by thanking my parents. You have given me so much and have always been incredibly generous.

Mom, thank you for being the way you are, for teaching me the true meaning of strength, and for being so empathetic, sensitive, and caring. Not too long ago, I believed that strength was about being unshaken, about hiding weakness. But you have shown me otherwise. I deeply admire the way you face challenges—how no obstacle ever seems too great for you, and how you have always protected both your loved ones and yourself. What stands out most to me is how you have done all of this with so much joy and enthusiasm. You live life with an intensity and passion that I truly admire, and without a doubt, that is one of the most important lessons you have taught me. I aspire to enjoy life in my thirties as fully as you do now in your sixties. Finally, I believe you are the person who best embodies the balance between cherishing heritage and tradition while being open-minded and enthusiastic about the future. It is likely the migrant spirit that shapes this in you. *Amoriñas das silveiras/ que eu lle daba ó meu amor/ camininños entre o millo/ ¡adiós para sempre adios!*

Dad, thank you so much for everything you have taught me—especially for inculcating in me the passion for knowledge. Your boundless curiosity and love for exploring the unknown have been so inspiring. I am also deeply grateful for the countless breakfasts you prepared for me at 7 AM, every day for 15 years, without fail. Thank you for teaching me the value of discipline, hard work, and the importance of putting love into everything you do. I hope some of that shines through in this thesis.

To my siblings. Marina, thank you so much for always being there with such a strong presence and incredible willpower. It really feels so safe to be by your side. You make all problems seem small, handling difficulties with such ease, calm, and determination. I am hoping one day to carry myself with the same sense of security and confidence that you possess. Bruno, I never imagined you would ever become an adult—I thought you would remain the cutest 5-year-old in the world forever. Yet, you certainly have, and in doing so, you've made an incredible impact on me. You have taught me a lot about how to deal with myself. You have shown how one can be intelligent, thoughtful, and self-reflective, all while remaining relaxed and happy. I really admire the way you handle anxiety, and, especially, social interactions, how you always seem comfortable in any situation and offer support to everyone around you.

To my grandma Emilia, one of the most important people in my childhood, such an impactful presence in my life. You implanted in me a love for reading, and for many years, I eagerly awaited Friday evenings so I could spend the night at your house while you read Lorca to me. *El lagarto está llorando/ la lagarta está llorando/ el lagarto y la lagarta / con delantalitos blancos.* Also, of quite some relevance to the present document, you were the first person who ever mentioned derivatives to me. You have songs for literally everything, and differential calculus is no exception. I remember as if it were yesterday

that *la derivada de una función/ es el cociente o la relación/ entre el incremento de la variable/ y el incremento de la razón.*

To my grandpa Federico, another person who lives intensely, who loves knowledge and life above everything else. Definitely one of the reasons why I studied physics was a book you gave me when I was 13: *Una breve historia de casi todo.* To my grandma Viví, who taught me the value of a good story and the importance of memory—thank you for being the best storyteller in the entire northwest.

To my cousin Mario, thank you for showing me different parts of myself and helping me avoid over-rationalizing everything. Andrea, you are the first doctor in the family—thank you for paving the way and for supporting me through so many steps in my teenage years. Adrián, you have always been such a great support. You know me better than most and are someone I turn to when I need help. Thank you. To the rest of my cousins—Iria, Alejandra, Ana, César, Álvaro, Diego, Xaquín, María, Cecilia, and Manu—you are all amazing, and I am so grateful to have you in my life.

And then my friends, the family that one makes along the way. Thank you to my friends from Fuente el saz, Prieto, Juanen, Kike, Zapa, Inés y María. I grew up with you, life is not easy when you are a teenager, everything is so intense and emotional when you are a bag of hormones with an adult brain wandering around. However, it is a lot easier when you have people to share it with, people who love you and care about you.

Thank you so much to my *Dutch* friends—Lior, Nick, and Tifany. It was during my Erasmus in Groningen that I truly decided to pursue a PhD, something which felt so natural being by your side. You make me feel secure and loved, being with you feels like being at home. Although we don't see each other often, you are very important to me.

Silvia, it was with you that I transitioned from child to adult, and you were the most important person in that process. Thank you for your time, for your patience, and for understanding me the way you did. You were my biggest support for many years, and I would not be the person I am today without you. I remember very vividly how we learned by heart all songs in *Searching for Sugar Man.* We were so little and innocent, but the world was ours, *cause how many times can you wake up in this comic book and plant flowers?* I learned so much from you—the appreciation for detail, the anticipation, the humility. I loved the way you let your intelligence shine almost effortlessly, without intention, without condescension. Well, I didn't quite learn that last trait :), but I deeply admired it.

Marco, thank you for teaching me so much and for showing me time and again that everything can be viewed from a new perspective. That other ways of life and worlds are possible. You have made me question many things, and by doing so, you have undoubtedly influenced the content of this thesis. It's not easy to find a physicist who believes in magic, and what an extraordinary experience that has been. Jaime, thank you for teaching me peace. For showing me that you can have an extremely active life, full of milestones and achievements, and still chill. I admire you so much in general, but in particular, I appreciate that ability to make everyone around you happy. That balance that allows you to express disagreement and fight intellectually, always with such softness and kindness. I just wish you would lose some of those discussions occasionally! You really are one of my intellectual gold standards, and when you back any of my ideas, that makes me feel so sure about it. It's amazing to have you as a friend. David, we have gone through so much together, we have lived in the same house, traveled, written books, discussed so much science and politics, cried, laughed... You have been such a big support of mine, I am not sure I would have finished this thesis without you. Thank you so much for your love and your strength. To me, you seem like a giant—invincible, unbeatable. Having you by my side really feels like everything is going to turn out well, like nothing can deeply hurt. Emma, you met me at a very low point and took care of me amazingly. Thank you very

much for being the best flatmate one could have had at that moment, and for looking at life that way. Never stop writing, your texts give so more much joy to the world than this thesis :). Valentina, you have been an amazing support in the last half of this process. You brought me so much energy and inspiration. I am so grateful to know you and to be able to see a bit of the world through your eyes. You possess a very special look and have the ability to make every little thing seem amazing.

Thank you very much to all the friends I made during this thesis. Carlos, you have entered my life in a very special way, thank you for your kindness, your softness, your emotional intelligence, and your math classes. You are exceptional, when I grow up I want to be someone who communicates emotions the way you do. Gabriel, thank you for these years sharing working space, the amazing *Gazpacho*. You have been a very special presence, I never met someone who could be interested and talented at so many different things at once. Jan, also a huge support in the last half of this thesis, I will never be grateful enough for having taught me how delicious coffee can be, it really is amazing to be surprised in such a deep way by a substance you have been years and years drinking. I admire your attention to detail and the passion and effort you put into even the smallest things. Your love for knowledge is contagious. María, we started in this together, and have been such a big support for each other, the activities at *semana de la ciencia*, the talks in high schools, the QUTYR conference, and all the outreach we have done in general would have never been the same without you. Thanks also to Paula, Cristián, Pablo, Luciano, Alberto, Tomás, Álvaro, and the whole QUINFOG family in general.

And finally, a big thank you to my thesis advisors, without which this work would not have been possible. Ricardo, thank you very much for your kindness and your warmth, it has been a pleasure to work with and learn from you. You have made many moments and challenges of this thesis way easier than they would have been otherwise. Juanjo, thank you very much for everything you have taught me, it never ceases to amaze me how someone can know so many things with such a level of depth. It is really very comforting for a PhD student to sense that his director is an absolute reference on the field and that almost anything that passes his filter will be valued and accepted. Thank you for the spot-on critiques and corrections, they constitute an integral part of this thesis.

And finally finally, many thanks to the European Union, to the amazing idea of a united Europe that transcends linguistic and cultural differences and works together towards common prosperity. We still have a long way to go, but we are hopefully on the right track. Let us plead that science, with its universal language, can continue to bring people together as it has in the past. The research presented in this thesis was funded almost entirely by the European program SuperQuLAN, a collaborative effort between Spanish, Austrian, Swiss, and German laboratories.

Bibliography

[AAB+19] F. Arute, K. Arya, R. Babbush, D. Bacon, J. C. Bardin, R. Barends, R. Biswas, S. Boixo, F. G. S. L. Brandao, D. A. Buell, B. Burkett, Y. Chen, Z. Chen, B. Chiaro, R. Collins, W. Courtney, A. Dunsworth, E. Farhi, B. Foxen, A. Fowler, C. Gidney, M. Giustina, R. Graff, K. Guerin, S. Habegger, M. P. Harrigan, M. J. Hartmann, A. Ho, M. Hoffmann, T. Huang, T. S. Humble, S. V. Isakov, E. Jeffrey, Z. Jiang, D. Kafri, K. Kechedzhi, J. Kelly, P. V. Klimov, S. Knysh, A. Korotkov, F. Kostritsa, D. Landhuis, M. Lindmark, E. Lucero, D. Lyakh, S. Mandrà, J. R. McClean, M. McEwen, A. Megrant, X. Mi, K. Michielsen, M. Mohseni, J. Mutus, O. Naaman, M. Neeley, C. Neill, M. Y. Niu, E. Ostby, A. Petukhov, J. C. Platt, C. Quintana, E. G. Rieffel, P. Roushan, N. C. Rubin, D. Sank, K. J. Satzinger, V. Smelyanskiy, K. J. Sung, M. D. Trevithick, A. Vainsencher, B. Villalonga, T. White, Z. J. Yao, P. Yeh, A. Zalcman, H. Neven, and J. M. Martinis, *Quantum supremacy using a programmable superconducting processor*, Nature 2019 574:7779 **574** (2019), no. 7779, 505–510.

[AB95] M. Alexanian and S. K. Bose, *Unitary transformation and the dynamics of a three-level atom interacting with two quantized field modes*, Physical Review A **52** (1995), no. 3, 2218–2224.

[ABP+18] C. J. Axline, L. D. Burkhart, W. Pfaff, M. Zhang, K. Chou, P. Campagne-Ibarcq, P. Reinhold, L. Frunzio, S. M. Girvin, L. Jiang, M. H. Devoret, and R. J. Schoelkopf, *On-demand quantum state transfer and entanglement between remote microwave cavity memories*, Nat. Phys. **14** (2018), no. 7, 705–710.

[ACAS16] G. M. A. Almeida, F. Ciccarello, T. J. G. Apollaro, and A. M. C. Souza, *Quantum-state transfer in staggered coupled-cavity arrays*, Physical Review A **93** (2016), no. 3, 032310.

[AH11] A. H. Al-Mohy and N. J. Higham, *Computing the Action of the Matrix Exponential, with an Application to Exponential Integrators*, SIAM Journal on Scientific Computing **33** (2011), no. 2, 488–511.

[AP06] P. Agrawal and A. Pati, *Perfect teleportation and superdense coding with W states*, Physical Review A **74** (2006), no. 6, 062320.

[BB84] C. H. Bennett and G. Brassard, *Quantum cryptography: Public key distribution and coin tossing*, Theoretical Computer Science **560** (1984), 7–11.

[BBC+93] C. H. Bennett, G. Brassard, C. Crépeau, R. Jozsa, A. Peres, and W. K. Wootters, *Teleporting an unknown quantum state via dual classical and Einstein-*

Podolsky-Rosen channels, Physical Review Letters **70** (1993), no. 13, 1895–1899.

[BBMC20] B. Bauer, S. Bravyi, M. Motta, and G. K.-L. Chan, *Quantum Algorithms for Quantum Chemistry and Quantum Materials Science*, Chemical Reviews **120** (2020), no. 22, 12685–12717.

[BBP+96] C. H. Bennett, G. Brassard, S. Popescu, B. Schumacher, J. A. Smolin, and W. K. Wootters, *Purification of Noisy Entanglement and Faithful Teleportation via Noisy Channels*, Physical Review Letters **76** (1996), no. 5, 722–725.

[BBPS96] C. H. Bennett, H. J. Bernstein, S. Popescu, and B. Schumacher, *Concentrating partial entanglement by local operations*, Physical Review A **53** (1996), no. 4, 2046–2052.

[BCMS19] C. D. Bruzewicz, J. Chiaverini, R. McConnell, and J. M. Sage, *Trapped-ion quantum computing: Progress and challenges*, Applied Physics Reviews **6** (2019), no. 2, 021314.

[BCOR98] S. Blanes, F. Casas, J. A. Oteo, and J. Ros, *Magnus and Fer expansions for matrix differential equations: The convergence problem*, Journal of Physics A: Mathematical and General **31** (1998), no. 1, 259.

[BCS+04] M. D. Barrett, J. Chiaverini, T. Schaetz, J. Britton, W. M. Itano, J. D. Jost, E. Knill, C. Langer, D. Leibfried, R. Ozeri, and D. J. Wineland, *Deterministic quantum teleportation of atomic qubits*, Nature **429** (2004), no. 6993, 737–739.

[BDL11] S. Bravyi, D. P. DiVincenzo, and D. Loss, *Schrieffer–Wolff transformation for quantum many-body systems*, Annals of Physics **326** (2011), no. 10, 2793–2826.

[BDSW96] C. H. Bennett, D. P. DiVincenzo, J. A. Smolin, and W. K. Wootters, *Mixed-state entanglement and quantum error correction*, Physical Review A **54** (1996), no. 5, 3824–3851.

[BGB09] M. Boissonneault, J. M. Gambetta, and A. Blais, *Dispersive regime of circuit qed: Photon-dependent qubit dephasing and relaxation rates*, Phys. Rev. A **79** (2009), 013819.

[BGC+18] J. C. Besse, S. Gasparinetti, M. C. Collodo, T. Walter, P. Kurpiers, M. Pechal, C. Eichler, and A. Wallraff, *Single-Shot Quantum Nondemolition Detection of Individual Itinerant Microwave Photons*, Phys. Rev. X **8** (2018), no. 2, 21003.

[BGGW21] A. Blais, A. L. Grimsmo, S. M. Girvin, and A. Wallraff, *Circuit quantum electrodynamics*, Rev. Mod. Phys. **93** (2021), 025005.

[BGL+21] A. Barman, G. Gubbiotti, S. Ladak, A. O. Adeyeye, M. Krawczyk, J. Gräfe, C. Adelmann, S. Cotofana, A. Naeemi, V. I. Vasyuchka, B. Hillebrands, S. A. Nikitov, H. Yu, D. Grundler, A. V. Sadovnikov, A. A. Grachev, S. E. Sheshukova, J.-Y. Duquesne, M. Marangolo, G. Csaba, W. Porod, V. E. Demidov, S. Urazhdin, S. O. Demokritov, E. Albisetti, D. Petti, R. Bertacco, H. Schultheiss, V. V. Kruglyak, V. D. Poimanov, S. Sahoo, J. Sinha, H. Yang, M. Münzenberg, T. Moriyama, S. Mizukami, P. Landeros, R. A. Gallardo, G. Carlotti, J.-V. Kim, R. L. Stamps, R. E. Camley, B. Rana, Y. Otani, W. Yu,

T. Yu, G. E. W. Bauer, C. Back, G. S. Uhrig, O. V. Dobrovolskiy, B. Budinska, H. Qin, S. van Dijken, A. V. Chumak, A. Khitun, D. E. Nikonov, I. A. Young, B. W. Zingsem, and M. Winklhofer, *The 2021 Magnonics Roadmap*, Journal of Physics: Condensed Matter **33** (2021), no. 41, 413001.

[BHW+04] A. Blais, R.-S. Huang, A. Wallraff, S. M. Girvin, and R. J. Schoelkopf, *Cavity quantum electrodynamics for superconducting electrical circuits: An architecture for quantum computation*, Physical Review A **69** (2004), no. 6, 062320.

[BKB01] M. Bourennane, A. Karlsson, and G. Björk, *Quantum key distribution using multilevel encoding*, Phys. Rev. A **64** (2001), 012306.

[BKK21] M. Butt, S. Khonina, and N. Kazanskiy, *Recent advances in photonic crystal optical devices: A review*, Optics & Laser Technology **142** (2021), 107265.

[BKU+22] B. M. Brubaker, J. M. Kindem, M. D. Urmey, S. Mittal, R. D. Delaney, P. S. Burns, M. R. Vissers, K. W. Lehnert, and C. A. Regal, *Optomechanical Ground-State Cooling in a Continuous and Efficient Electro-Optic Transducer*, Physical Review X **12** (2022), no. 2, 021062.

[BPM+97] D. Bouwmeester, J.-W. Pan, K. Mattle, M. Eibl, H. Weinfurter, and A. Zeilinger, *Experimental quantum teleportation*, Nature **390** (1997), no. 6660, 575–579.

[BSZ+19] A. Bienfait, K. J. Satzinger, Y. P. Zhong, H. S. Chang, M. H. Chou, C. R. Conner, Dumur, J. Grebel, G. A. Peairs, R. G. Povey, and A. N. Cleland, *Phonon-mediated quantum state transfer and remote qubit entanglement*, Science **364** (2019), no. 6438, 368–371.

[BTZ+21] L. D. Burkhart, J. D. Teoh, Y. Zhang, C. J. Axline, L. Frunzio, M. Devoret, L. Jiang, S. Girvin, and R. Schoelkopf, *Error-Detected State Transfer and Entanglement in a Superconducting Quantum Network*, PRX Quantum **2** (2021), no. 3, 030321.

[BV97] E. Bernstein and U. Vazirani, *Quantum Complexity Theory*, SIAM Journal on Computing **26** (1997), no. 5, 1411–1473.

[BVJ+98] V. Bouchiat, D. Vion, P. Joyez, D. Esteve, and M. H. Devoret, *Quantum coherence with a single Cooper pair*, Physica Scripta **1998** (1998), no. T76, 165.

[Car15] G. Cariolaro, *Quantum communications*, Springer, 2015.

[CCCR16] G. Calajó, F. Ciccarello, D. Chang, and P. Rabl, *Atom-field dressed states in slow-light waveguide qed*, Phys. Rev. A **93** (2016), 033833.

[CDG+10] A. A. Clerk, M. H. Devoret, S. M. Girvin, F. Marquardt, and R. J. Schoelkopf, *Introduction to quantum noise, measurement, and amplification*, Reviews of Modern Physics **82** (2010), no. 2, 1155–1208.

[CEHM99] J. I. Cirac, A. K. Ekert, S. F. Huelga, and C. Macchiavello, *Distributed quantum computation over noisy channels*, Phys. Rev. A **59** (1999), no. 6, 4249–4254.

[CGBM+21] S. Casulleras, C. Gonzalez-Ballestero, P. Maurer, J. J. García-Ripoll, and O. Romero-Isart, *Remote individual addressing of quantum emitters with chirped pulses*, Phys. Rev. Lett. **126** (2021), 103602.

[CKJ+20] A. D. Córcoles, A. Kandala, A. Javadi-Abhari, D. T. McClure, A. W. Cross, K. Temme, P. D. Nation, M. Steffen, and J. M. Gambetta, *Challenges and Opportunities of Near-Term Quantum Computing Systems*, Proceedings of the IEEE **108** (2020), no. 8, 1338–1352.

[CKSG91] D. A. Cardimona, V. Kovanis, M. P. Sharma, and A. Gavrielides, *Quantum collapses and revivals in a nonlinear Jaynes-Cummings model*, Physical Review A **43** (1991), no. 7, 3710–3723.

[CKW+22] S. Casulleras, S. Knauer, Q. Wang, O. Romero-Isart, A. V. Chumak, and C. Gonzalez-Ballestero, *Generation of spin-wave pulses by inverse design*, arXiv:2209.06608 (2022).

[Cla14] B. D. Clader, *Quantum networking of microwave photons using optical fibers*, Phys. Rev. A **90** (2014), 012324.

[CNR+14] Y. Chen, C. Neill, P. Roushan, N. Leung, M. Fang, R. Barends, J. Kelly, B. Campbell, Z. Chen, B. Chiaro, A. Dunsworth, E. Jeffrey, A. Megrant, J. Y. Mutus, P. J. J. O'Malley, C. M. Quintana, D. Sank, A. Vainsencher, J. Wenner, T. C. White, M. R. Geller, A. N. Cleland, and J. M. Martinis, *Qubit Architecture with High Coherence and Fast Tunable Coupling*, Physical Review Letters **113** (2014), no. 22, 220502.

[CSP+19] G. Calajó, M. J. A. Schuetz, H. Pichler, M. D. Lukin, P. Schneeweiss, J. Volz, and P. Rabl, *Quantum acousto-optic control of light-matter interactions in nanophotonic networks*, Phys. Rev. A **99** (2019), 053852.

[CYL+07] L.-B. Chen, M.-Y. Ye, G.-W. Lin, Q.-H. Du, and X.-M. Lin, *Generation of entanglement via adiabatic passage*, Phys. Rev. A **76** (2007), no. 6, 062304.

[CZ95] J. I. Cirac and P. Zoller, *Quantum Computations with Cold Trapped Ions*, Tech. report, 1995.

[CZB+20] H.-S. Chang, Y. P. Zhong, A. Bienfait, M.-H. Chou, C. R. Conner, E. Dumur, J. Grebel, G. A. Peairs, R. G. Povey, K. J. Satzinger, and A. N. Cleland, *Remote entanglement via adiabatic passage using a tunably dissipative quantum communication system*, Phys. Rev. Lett. **124** (2020), 240502.

[CZKM96] J. I. Cirac, P. Zoller, H. J. Kimble, and H. Mabuchi, *Quantum state transfer and entanglement distribution among distant nodes in a quantum network*, Phys. Rev. Lett. **78** (1996), no. 16, 3221–3224.

[CZN+18] P. Campagne-Ibarcq, E. Zalys-Geller, A. Narla, S. Shankar, P. Reinhold, L. Burkhart, C. Axline, W. Pfaff, L. Frunzio, R. J. Schoelkopf, and M. H. Devoret, *Deterministic Remote Entanglement of Superconducting Circuits through Microwave Two-Photon Transitions*, Physical Review Letters **120** (2018), no. 20, 200501.

[dA17] I. de Vega and D. Alonso, *Dynamics of non-Markovian open quantum systems*, Reviews of Modern Physics **89** (2017), no. 1, 015001.

[Dav12] David M. Pozar, *Microwave Engineering*, John Wiley & Sons, 2012.

[DCPGR15] G. Díaz-Camacho, D. Porras, and J. J. García-Ripoll, *Photon-mediated qubit interactions in one-dimensional discrete and continuous models*, Phys. Rev. A **91** (2015), 063828.

[DiV00] D. P. DiVincenzo, *The Physical Implementation of Quantum Computation*, Fortschritte der Physik **48** (2000), no. 9-11, 771–783.

[DK04] L.-M. Duan and H. J. Kimble, *Scalable photonic quantum computation through cavity-assisted interactions*, Phys. Rev. Lett. **92** (2004), 127902.

[DMD+13] M. W. Doherty, N. B. Manson, P. Delaney, F. Jelezko, J. Wrachtrup, and L. C. L. Hollenberg, *The nitrogen-vacancy colour centre in diamond*, Physics Reports **528** (2013), no. 1, 1–45.

[EKMB17] M. Epping, H. Kampermann, C. Macchiavello, and D. Bruß, *Multi-partite entanglement can speed up quantum key distribution in networks*, New J. Phys. **19** (2017), no. 9, 093012.

[ELF+12] C. Eichler, C. Lang, J. M. Fink, J. Govenius, S. Filipp, and A. Wallraff, *Observation of Entanglement between Itinerant Microwave Photons and a Superconducting Qubit*, Phys. Rev. Lett. **109** (2012), no. 24, 240501.

[EPR35] A. Einstein, B. Podolsky, and N. Rosen, *Can quantum-mechanical description of physical reality be considered complete?*, Phys. Rev. **47** (1935), 777–780.

[ESK+24] A. M. Eriksson, T. Sépulcre, M. Kervinen, T. Hillmann, M. Kudra, S. Dupouy, Y. Lu, M. Khanahmadi, J. Yang, C. Castillo-Moreno, P. Delsing, and S. Gasparinetti, *Universal control of a bosonic mode via drive-activated native cubic interactions*, Nature Communications **15** (2024), no. 1, 2512.

[Fey82] R. P. Feynman, *Simulating physics with computers*, International Journal of Theoretical Physics **21** (1982), no. 6, 467–488.

[FKB+22] V. S. Ferreira, G. Kim, A. Butler, H. Pichler, and O. Painter, *Deterministic generation of multidimensional photonic cluster states with a single quantum emitter*, arXiv:2206.10076 (2022).

[FKB+24] V. S. Ferreira, G. Kim, A. Butler, H. Pichler, and O. Painter, *Deterministic generation of multidimensional photonic cluster states with a single quantum emitter*, Nature Physics **20** (2024), no. 5, 865–870.

[FLM+10] P. Forn-Díaz, J. Lisenfeld, D. Marcos, J. J. García-Ripoll, E. Solano, C. J. P. M. Harmans, and J. E. Mooij, *Observation of the Bloch-Siegert Shift in a Qubit-Oscillator System in the Ultrastrong Coupling Regime*, Physical Review Letters **105** (2010), no. 23, 237001.

[FMMC12] A. G. Fowler, M. Mariantoni, J. M. Martinis, and A. N. Cleland, *Surface codes: Towards practical large-scale quantum computation*, Physical Review A **86** (2012), no. 3, 032324.

[FSS18] F. Flamini, N. Spagnolo, and F. Sciarrino, *Photonic quantum information processing: A review*, Reports on Progress in Physics **82** (2018), no. 1, 016001.

[FWC+17] P. Forn-Díaz, C. W. Warren, C. W. S. Chang, A. M. Vadiraj, and C. M. Wilson, *On-Demand Microwave Generator of Shaped Single Photons*, Physical Review Applied **8** (2017), no. 5, 054015.

[FWS+05] L. Frunzio, A. Wallraff, D. Schuster, J. Majer, and R. Schoelkopf, *Fabrication and characterization of superconducting circuit qed devices for quantum computation*, IEEE Transactions on Applied Superconductivity **15** (2005), no. 2, 860–863.

[GC85] C. W. Gardiner and M. J. Collett, *Input and output in damped quantum systems: Quantum stochastic differential equations and the master equation*, Physical Review A **31** (1985), no. 6, 3761.

[GE90] C. C. Gerry and J. H. Eberly, *Dynamics of a Raman coupled model interacting with two quantized cavity fields*, Physical Review A **42** (1990), no. 11, 6805.

[GFB+08] M. Göppl, A. Fragner, M. Baur, R. Bianchetti, S. Filipp, J. M. Fink, P. J. Leek, G. Puebla, L. Steffen, and A. Wallraff, *Coplanar waveguide resonators for circuit quantum electrodynamics*, Journal of Applied Physics **104** (2008), no. 11, 113904.

[GHP+14] M. Gräfe, R. Heilmann, A. Perez-Leija, R. Keil, F. Dreisow, M. Heinrich, H. Moya-Cessa, S. Nolte, D. N. Christodoulides, and A. Szameit, *On-chip generation of high-order single-photon W-states*, Nature Photonics **8** (2014), no. 10, 791–795.

[GLM11] V. Giovannetti, S. Lloyd, and L. Maccone, *Advances in quantum metrology*, Nat. Phot. **5** (2011), no. 4, 222–229.

[Got98] D. Gottesman, *Theory of fault-tolerant quantum computation*, Physical Review A **57** (1998), no. 1, 127–137.

[GPRB+17] M. F. Gely, A. Parra-Rodriguez, D. Bothner, Y. M. Blanter, S. J. Bosman, E. Solano, and G. A. Steele, *Convergence of the multimode quantum rabi model of circuit quantum electrodynamics*, Physical Review B **95** (2017), 245115.

[GTK+21] F. P. García de Arquer, D. V. Talapin, V. I. Klimov, Y. Arakawa, M. Bayer, and E. H. Sargent, *Semiconductor quantum dots: Technological progress and future challenges*, Science **373** (2021), no. 6555, eaaz8541.

[GYC+24] J. Grebel, H. Yan, M.-H. Chou, G. Andersson, C. R. Conner, Y. J. Joshi, J. M. Miller, R. G. Povey, H. Qiao, X. Wu, and A. N. Cleland, *Bidirectional multiphoton communication between remote superconducting nodes*, Phys. Rev. Lett. **132** (2024), 047001.

[GZ15] C. Gardiner and P. Zoller, World Scientific, 2015.

[HA10] N. J. Higham and A. H. Al-Mohy, *Computing Matrix Functions*, Acta Numerica **19** (2010), 159–208.

[Har13] S. Haroche, *Nobel Lecture: Controlling photons in a box and exploring the quantum to classical boundary*, Reviews of Modern Physics **85** (2013), no. 3, 1083–1102.

[HBcvB99] M. Hillery, V. Bužek, and A. Berthiaume, *Quantum secret sharing*, Phys. Rev. A **59** (1999), 1829–1834.

[HHHH09] R. Horodecki, P. Horodecki, M. Horodecki, and K. Horodecki, *Quantum entanglement*, Rev. Mod. Phys. **81** (2009), 865–942.

[HHR+05] H. Häffner, W. Hänsel, C. F. Roos, J. Benhelm, D. Chek-al kar, M. Chwalla, T. Körber, U. D. Rapol, M. Riebe, P. O. Schmidt, C. Becher, O. Gühne, W. Dür, and R. Blatt, *Scalable multiparticle entanglement of trapped ions*, Nature **438** (2005), no. 7068, 643–646.

[HPB+22] S. L. N. Hermans, M. Pompili, H. K. C. Beukers, S. Baier, J. Borregaard, and R. Hanson, *Qubit teleportation between non-neighbouring nodes in a quantum network*, Nature **605** (2022), no. 7911, 663–668.

[JC63] E. Jaynes and F. Cummings, *Comparison of quantum and semiclassical radiation theories with application to the beam maser*, Proceedings of the IEEE **51** (1963), no. 1, 89–109.

[JLJP02] J. Joo, J. Lee, J. Jang, and Y.-J. Park, *Quantum Secure Communication with W States*, August 2002.

[JPOK03] J. Joo, Y.-J. Park, S. Oh, and J. Kim, *Quantum teleportation via a W state*, New Journal of Physics **5** (2003), no. 1, 136.

[JQC07] W. Jian, Z. Quan, and T. Chao-Jing, *Quantum Secure Communication Scheme with W State*, Communications in Theoretical Physics **48** (2007), no. 4, 637.

[JSM+14] E. Jeffrey, D. Sank, J. Y. Mutus, T. C. White, J. Kelly, R. Barends, Y. Chen, Z. Chen, B. Chiaro, A. Dunsworth, A. Megrant, P. J. J. O'Malley, C. Neill, P. Roushan, A. Vainsencher, J. Wenner, A. N. Cleland, and J. M. Martinis, *Fast accurate state measurement with superconducting qubits*, Phys. Rev. Lett. **112** (2014), 190504.

[KAS+23] B. Kannan, A. Almanakly, Y. Sung, A. Di Paolo, D. A. Rower, J. Braumüller, A. Melville, B. M. Niedzielski, A. Karamlou, K. Serniak, A. Vepsäläinen, M. E. Schwartz, J. L. Yoder, R. Winik, J. I.-J. Wang, T. P. Orlando, S. Gustavsson, J. A. Grover, and W. D. Oliver, *On-demand directional microwave photon emission using waveguide quantum electrodynamics*, Nature Physics **19** (2023), no. 3, 394–400.

[Kim98] H. J. Kimble, *Strong interactions of single atoms and photons in cavity QED*, Physica Scripta **1998** (1998), no. T76, 127.

[Kim08] H. J. Kimble, *The quantum internet*, Nature **453** (2008), no. 7198, 1023–1030.

[KKT+18] S. Kono, K. Koshino, Y. Tabuchi, A. Noguchi, and Y. Nakamura, *Quantum non-demolition detection of an itinerant microwave photon*, Nat. Phys. **14** (2018), no. 6, 546–549.

[KM19] A. H. Kiilerich and K. Mølmer, *Input-Output Theory with Quantum Pulses*, Physical Review Letters **123** (2019), no. 12, 123604.

[KMW+17] P. Kurpiers, P. Magnard, T. Walter, B. Royer, M. Pechal, J. Heinsoo, Y. Salathé, A. Akin, S. Storz, J.-C. Besse, S. Gasparinetti, A. Blais, and A. Wallraff, *Deterministic Quantum State Transfer and Generation of Remote Entanglement using Microwave Photons*, Nature **558** (2017), no. 7709, 264–267.

[KMW+18] P. Kurpiers, P. Magnard, T. Walter, B. Royer, M. Pechal, J. Heinsoo, Y. Salathé, A. Akin, S. Storz, J.-C. Besse, S. Gasparinetti, A. Blais, and A. Wallraff, *Deterministic quantum state transfer and remote entanglement using microwave photons*, Nature **558** (2018), no. 7709, 264–267.

[KSS+23] A. Kumar, A. Suleymanzade, M. Stone, L. Taneja, A. Anferov, D. I. Schuster, and J. Simon, *Quantum-enabled millimetre wave to optical transduction using neutral atoms*, Nature **615** (2023), no. 7953, 614–619.

[Kur19] P. Kurpiers, *Quantum Networks with Superconducting Circuits*, Doctoral Thesis, ETH Zurich, 2019.

[KW19] W. Kozlowski and S. Wehner, *Towards Large-Scale Quantum Networks*, Proceedings of the Sixth Annual ACM International Conference on Nanoscale Computing and Communication (New York, NY, USA), NANOCOM '19, Association for Computing Machinery, September 2019, pp. 1–7.

[KYG+07] J. Koch, T. M. Yu, J. Gambetta, A. A. Houck, D. I. Schuster, J. Majer, A. Blais, M. H. Devoret, S. M. Girvin, and R. J. Schoelkopf, *Charge-insensitive qubit design derived from the Cooper pair box*, Physical Review A **76** (2007), no. 4, 042319.

[LBS+03] K. W. Lehnert, K. Bladh, L. F. Spietz, D. Gunnarsson, D. I. Schuster, P. Delsing, and R. J. Schoelkopf, *Measurement of the Excited-State Lifetime of a Microelectronic Circuit*, Physical Review Letters **90** (2003), no. 2, 027002.

[LCD+87] A. J. Leggett, S. Chakravarty, A. T. Dorsey, M. P. A. Fisher, A. Garg, and W. Zwerger, *Dynamics of the dissipative two-state system*, Reviews of Modern Physics **59** (1987), no. 1, 1–85.

[LH17] Y. Liu and A. A. Houck, *Quantum electrodynamics near a photonic bandgap*, Nat. Phys. **13** (2017), no. 1, 48–52.

[LKS+05] D. Leibfried, E. Knill, S. Seidelin, J. Britton, R. B. Blakestad, J. Chiaverini, D. B. Hume, W. M. Itano, J. D. Jost, C. Langer, R. Ozeri, R. Reichle, and D. J. Wineland, *Creation of a six-atom 'Schrödinger cat' state*, Nature **438** (2005), no. 7068, 639–642.

[LLC+19] N. Leung, Y. Lu, S. Chakram, R. K. Naik, N. Earnest, R. Ma, K. Jacobs, A. N. Cleland, and D. I. Schuster, *Deterministic bidirectional communication and remote entanglement generation between superconducting qubits*, npj Quantum Information **5** (2019), no. 1, 1–5.

[LPB10] E.-M. Laine, J. Piilo, and H.-P. Breuer, *Measure for the non-markovianity of quantum processes*, Phys. Rev. A **81** (2010), 062115.

[LR47] W. E. Lamb and R. C. Retherford, *Fine Structure of the Hydrogen Atom by a Microwave Method*, Physical Review **72** (1947), no. 3, 241–243.

[LRSS20] N. J. Lambert, A. Rueda, F. Sedlmeir, and H. G. L. Schwefel, *Coherent Conversion Between Microwave and Optical Photons—An Overview of Physical Implementations*, Advanced Quantum Technologies **3** (2020), no. 1, 1900077.

[LSB+20] N. Lauk, N. Sinclair, S. Barzanjeh, J. P. Covey, M. Saffman, M. Spiropulu, and C. Simon, *Perspectives on quantum transduction*, Quantum Science and Technology **5** (2020), no. 2, 020501.

[Mag54] W. Magnus, *On the exponential solution of differential equations for a linear operator*, Communications on Pure and Applied Mathematics **7** (1954), no. 4, 649–673.

[Mag21] P. Magnard, *Meter-scale Microwave Quantum Networks for Superconducting Circuits*, Doctoral Thesis, ETH Zurich, 2021.

[MD02] H. Mabuchi and A. C. Doherty, *Cavity Quantum Electrodynamics: Coherence in Context*, Science **298** (2002), no. 5597, 1372–1377.

[MEA+20] S. McArdle, S. Endo, A. Aspuru-Guzik, S. C. Benjamin, and X. Yuan, *Quantum computational chemistry*, Reviews of Modern Physics **92** (2020), no. 1, 015003.

[MKLR19] O. Morin, M. Körber, S. Langenfeld, and G. Rempe, *Deterministic shaping and reshaping of single-photon temporal wave functions*, Phys. Rev. Lett. **123** (2019), 133602.

[MMMJ20] P. Murali, D. C. Mckay, M. Martonosi, and A. Javadi-Abhari, *Software Mitigation of Crosstalk on Noisy Intermediate-Scale Quantum Computers*, Proceedings of the Twenty-Fifth International Conference on Architectural Support for Programming Languages and Operating Systems (New York, NY, USA), ASPLOS '20, Association for Computing Machinery, March 2020, pp. 1001–1016.

[MRR+14] C. Monroe, R. Raussendorf, A. Ruthven, K. R. Brown, P. Maunz, L.-M. Duan, and J. Kim, *Large-scale modular quantum-computer architecture with atomic memory and photonic interconnects*, Physical Review A **89** (2014), no. 2, 022317.

[MSK+20] P. Magnard, S. Storz, P. Kurpiers, J. Schär, F. Marxer, J. Lütolf, T. Walter, J.-C. Besse, M. Gabureac, K. Reuer, A. Akin, B. Royer, A. Blais, and A. Wallraff, *Microwave Quantum Link between Superconducting Circuits Housed in Spatially Separated Cryogenic Systems*, Phys. Rev. Lett. **125** (2020), no. 26, 260502.

[MSKP20] M. Mirhosseini, A. Sipahigil, M. Kalaee, and O. Painter, *Quantum transduction of optical photons from a superconducting qubit*.

[Nav22] C. Navarrete-Benlloch, *Introduction to Quantum Optics*, March 2022.

[NC00] M. A. Nielsen and I. L. Chuang, *Quantum computation and quantum information*, Cambridge University Press, Cambridge, England, 2000.

[NDH+10] T. Niemczyk, F. Deppe, H. Huebl, E. P. Menzel, F. Hocke, M. J. Schwarz, J. J. Garcia-Ripoll, D. Zueco, T. Hümmer, E. Solano, A. Marx, and R. Gross, *Circuit quantum electrodynamics in the ultrastrong-coupling regime*, Nature Physics **6** (2010), no. 10, 772–776.

[Nie02] M. A. Nielsen, *A simple formula for the average gate fidelity of a quantum dynamical operation*, Physics Letters A **303** (2002), 249–252.

[NK14] H. T. Ng and K. Kim, *Quantum estimation of magnetic-field gradient using W-state*, Optics Communications **331** (2014), 353–358.

[NPT99] Y. Nakamura, Y. A. Pashkin, and J. S. Tsai, *Coherent control of macroscopic quantum states in a single-Cooper-pair box*, Nature **398** (1999), no. 6730, 786–788.

[OFV09] J. L. O'Brien, A. Furusawa, and J. Vučković, *Photonic quantum technologies*, Nature Photonics **3** (2009), no. 12, 687–695.

[OPA+19] T. Ozawa, H. M. Price, A. Amo, N. Goldman, M. Hafezi, L. Lu, M. C. Rechtsman, D. Schuster, J. Simon, O. Zilberberg, and I. Carusotto, *Topological photonics*, Reviews of Modern Physics **91** (2019), no. 1, 015006.

[PAB+20] S. Pirandola, U. L. Andersen, L. Banchi, M. Berta, D. Bunandar, R. Colbeck, D. Englund, T. Gehring, C. Lupo, C. Ottaviani, J. L. Pereira, M. Razavi, J. S. Shaari, M. Tomamichel, V. C. Usenko, G. Vallone, P. Villoresi, and P. Wallden, *Advances in quantum cryptography*, Adv. Opt. Photon. **12** (2020), no. 4, 1012–1236.

[Par09] M. G. A. Paris, *Quantum estimation for quantum technology*, Int. J. Quant. Inf. **7** (2009), no. supp01, 125–137.

[PCZL17] H. Pichler, S. Choi, P. Zoller, and M. D. Lukin, *Universal photonic quantum computation via time-delayed feedback*, PNAS **114** (2017), no. 43, 11362–11367.

[Pel97] T. Pellizzari, *Quantum Networking with Optical Fibres*, Phys. Rev. Lett. **79** (1997), no. 26, 5242–5245.

[PEW+15] S. Pirandola, J. Eisert, C. Weedbrook, A. Furusawa, and S. L. Braunstein, *Advances in quantum teleportation*, Nature Photonics **9** (2015), no. 10, 641–652.

[PHB+14] W. Pfaff, B. J. Hensen, H. Bernien, S. B. van Dam, M. S. Blok, T. H. Taminiau, M. J. Tiggelman, R. N. Schouten, M. Markham, D. J. Twitchen, and R. Hanson, *Unconditional quantum teleportation between distant solid-state quantum bits*, Science **345** (2014), no. 6196, 532–535.

[PHE+13] M. Pechal, L. Huthmacher, C. Eichler, S. Zeytinoglu, A. A. Abdumalikov Jr., S. Berger, A. Wallraff, and S. Filipp, *Microwave-controlled generation of shaped single photons in circuit quantum electrodynamics*, Physical Review X **4** (2013), no. 4.

[PHE+14] M. Pechal, L. Huthmacher, C. Eichler, S. Zeytinoğlu, A. A. Abdumalikov, S. Berger, A. Wallraff, and S. Filipp, *Microwave-controlled generation of shaped single photons in circuit quantum electrodynamics*, Phys. Rev. X **4** (2014), 041010.

[PMM07] L. H. Pedersen, N. M. Møller, and K. Mølmer, *Fidelity of quantum operations*, Physics Letters A **367** (2007), 47–51.

[PnPR+22] G. F. Peñas, R. Puebla, T. Ramos, P. Rabl, and J. J. García-Ripoll, *Universal deterministic quantum operations in microwave quantum links*, Phys. Rev. Applied **17** (2022), 054038.

[PPGR23] G. F. Peñas, R. Puebla, and J. J. García-Ripoll, *Improving quantum state transfer: correcting non-markovian and distortion effects*, Quantum Sci. Technol. **8** (2023), no. 4, 045026.

[Pre18] J. Preskill, *Quantum Computing in the NISQ era and beyond*, Quantum **2** (2018), 79.

[QLN+23] J. Qiu, Y. Liu, J. Niu, L. Hu, Y. Wu, L. Zhang, W. Huang, Y. Chen, J. Li, S. Liu, Y. Zhong, L. Duan, and D. Yu, *Deterministic quantum teleportation between distant superconducting chips*, arXiv:2302.08756 (2023).

[Rab37] I. I. Rabi, *Space Quantization in a Gyrating Magnetic Field*, Physical Review **51** (1937), no. 8, 652–654.

[RBH01] J. M. Raimond, M. Brune, and S. Haroche, *Manipulating quantum entanglement with atoms and photons in a cavity*, Reviews of Modern Physics **73** (2001), no. 3, 565–582.

[RHR+04] M. Riebe, H. Häffner, C. F. Roos, W. Hänsel, J. Benhelm, G. P. T. Lancaster, T. W. Körber, C. Becher, F. Schmidt-Kaler, D. F. V. James, and R. Blatt, *Deterministic quantum teleportation with atoms*, Nature **429** (2004), no. 6993, 734–737.

[Rip22] J. J. G. Ripoll, *Quantum information and quantum optics with superconducting circuits*, Cambridge University Press, 2022.

[RNH+12] S. Ritter, C. Nölleke, C. Hahn, A. Reiserer, A. Neuzner, M. Uphoff, M. Mücke, E. Figueroa, J. Bochmann, and G. Rempe, *An Elementary Quantum Network of Single Atoms in Optical Cavities*, Nature **484** (2012), no. 7393, 195–200.

[RNO+00] A. Rauschenbeutel, G. Nogues, S. Osnaghi, P. Bertet, M. Brune, J.-M. Raimond, and S. Haroche, *Step-by-Step Engineered Multiparticle Entanglement*, Science **288** (2000), no. 5473, 2024–2028.

[RPA+16] M. Reagor, W. Pfaff, C. Axline, R. W. Heeres, N. Ofek, K. Sliwa, E. Holland, C. Wang, J. Blumoff, K. Chou, M. J. Hatridge, L. Frunzio, M. H. Devoret, L. Jiang, and R. J. Schoelkopf, *Quantum memory with millisecond coherence in circuit QED*, Physical Review B **94** (2016), no. 1, 014506.

[RRH+04] C. F. Roos, M. Riebe, H. Häffner, W. Hänsel, J. Benhelm, G. P. T. Lancaster, C. Becher, F. Schmidt-Kaler, and R. Blatt, *Control and Measurement of Three-Qubit Entangled States*, Science **304** (2004), no. 5676, 1478–1480.

[RSA78] R. L. Rivest, A. Shamir, and L. Adleman, *A method for obtaining digital signatures and public-key cryptosystems*, Communications of the ACM **21** (1978), no. 2, 120–126.

[RSM+14] N. Roch, M. E. Schwartz, F. Motzoi, C. Macklin, R. Vijay, A. W. Eddins, A. N. Korotkov, K. B. Whaley, M. Sarovar, and I. Siddiqi, *Observation of Measurement-Induced Entanglement and Quantum Trajectories of Remote Superconducting Qubits*, Physical Review Letters **112** (2014), no. 17, 170501.

[RVH+16] T. Ramos, B. Vermersch, P. Hauke, H. Pichler, and P. Zoller, *Non-markovian dynamics in chiral quantum networks with spins and photons*, Phys. Rev. A **93** (2016), 062104.

[SCC+22] M. Scigliuzzo, G. Calajò, F. Ciccarello, D. Perez Lozano, A. Bengtsson, P. Scarlino, A. Wallraff, D. Chang, P. Delsing, and S. Gasparinetti, *Controlling Atom-Photon Bound States in an Array of Josephson-Junction Resonators*, Physical Review X **12** (2022), no. 3, 031036.

[SCS+16] I. Schwartz, D. Cogan, E. R. Schmidgall, Y. Don, L. Gantz, O. Kenneth, N. H. Lindner, and D. Gershoni, *Deterministic generation of a cluster state of entangled photons*, Science **354** (2016), no. 6311, 434–437.

[SHK+08] J. A. Schreier, A. A. Houck, J. Koch, D. I. Schuster, B. R. Johnson, J. M. Chow, J. M. Gambetta, J. Majer, L. Frunzio, M. H. Devoret, S. M. Girvin, and R. J. Schoelkopf, *Suppressing charge noise decoherence in superconducting charge qubits*, Physical Review B **77** (2008), no. 18, 180502.

[Sho94] P. W. Shor, *Algorithms for Quantum Computation: Discrete Logarithms and Factoring*, Proceedings 35th Annual Symposium on Foundations of Computer Science. IEEE Comput. Soc. Press (1994), 124–undefined.

[Sho95] P. W. Shor, *Scheme for reducing decoherence in quantum computer memory*, Physical Review A **52** (1995), no. 4, R2493–R2496.

[Sho96] P. Shor, *Fault-tolerant quantum computation*, Proceedings of 37th Conference on Foundations of Computer Science, October 1996, pp. 56–65.

[SHR+22] R. Sahu, W. Hease, A. Rueda, G. Arnold, L. Qiu, and J. M. Fink, *Quantum-enabled operation of a microwave-optical interface*, Nature Communications **13** (2022), no. 1, 1276.

[SKK+00] C. A. Sackett, D. Kielpinski, B. E. King, C. Langer, V. Meyer, C. J. Myatt, M. Rowe, Q. A. Turchette, W. M. Itano, D. J. Wineland, and C. Monroe, *Experimental entanglement of four particles*, Nature **404** (2000), no. 6775, 256–259.

[SKO+06] J. F. Sherson, H. Krauter, R. K. Olsson, B. Julsgaard, K. Hammerer, I. Cirac, and E. S. Polzik, *Quantum teleportation between light and matter*, Nature **443** (2006), no. 7111, 557–560.

[SLZ+19] N. M. Sundaresan, R. Lundgren, G. Zhu, A. V. Gorshkov, and A. A. Houck, *Interacting qubit-photon bound states with superconducting circuits*, Phys. Rev. X **9** (2019), 011021.

[SMB06] A. Serafini, S. Mancini, and S. Bose, *Distributed quantum computation via optical fibers*, Phys. Rev. Lett. **96** (2006), 010503.

[SMK15] E. A. Sete, J. M. Martinis, and A. N. Korotkov, *Quantum theory of a bandpass purcell filter for qubit readout*, Phys. Rev. A **92** (2015), 012325.

[SRS+10] K. Stannigel, P. Rabl, A. S. Sørensen, P. Zoller, and M. D. Lukin, *Optomechanical transducers for long-distance quantum communication*, Phys. Rev. Lett. **105** (2010), 220501.

[SRS+11] K. Stannigel, P. Rabl, A. S. Sørensen, M. D. Lukin, and P. Zoller, *Optomechanical transducers for quantum-information processing*, Phys. Rev. A **84** (2011), 042341.

[SSK+23] S. Storz, J. Schär, A. Kulikov, P. Magnard, P. Kurpiers, J. Lütolf, T. Walter, A. Copetudo, K. Reuer, A. Akin, J.-C. Besse, M. Gabureac, G. J. Norris, A. Rosario, F. Martin, J. Martinez, W. Amaya, M. W. Mitchell, C. Abellan, J.-D. Bancal, N. Sangouard, B. Royer, A. Blais, and A. Wallraff, *Loophole-free bell inequality violation with superconducting circuits*, Nature **617** (2023), no. 7960, 265–270.

[STF+20] J. Schneeloch, C. C. Tison, M. L. Fanto, S. Ray, and P. M. Alsing, *Quantifying tripartite entanglement with entropic correlations*, Phys. Rev. Research **2** (2020), 043152.

[SW66] J. R. Schrieffer and P. A. Wolff, *Relation between the Anderson and Kondo Hamiltonians*, Physical Review **149** (1966), no. 2, 491–492.

[SWB+05] D. I. Schuster, A. Wallraff, A. Blais, L. Frunzio, R.-S. Huang, J. Majer, S. M. Girvin, and R. J. Schoelkopf, *Ac Stark Shift and Dephasing of a Superconducting Qubit Strongly Coupled to a Cavity Field*, Physical Review Letters **94** (2005), no. 12, 123602.

[SZ97] M. O. Scully and M. S. Zubairy, *Quantum Optics*, Cambridge University Press, Cambridge, 1997.

[Sza15] S. Szalay, *Multipartite entanglement measures*, Phys. Rev. A **92** (2015), 042329.

[TA14] G. Tóth and I. Apellaniz, *Quantum metrology from a quantum information science perspective*, J. Phys. A: Math. Theor. **47** (2014), no. 42, 424006.

[Ter15] B. M. Terhal, *Quantum error correction for quantum memories*, Reviews of Modern Physics **87** (2015), no. 2, 307–346.

[Tia12] L. Tian, *Adiabatic State Conversion and Pulse Transmission in Optomechanical Systems*, Phys. Rev. Lett. **108** (2012), no. 15, 153604.

[TKC14] T. Tufarelli, M. S. Kim, and F. Ciccarello, *Non-markovianity of a quantum emitter in front of a mirror*, Phys. Rev. A **90** (2014), 012113.

[TKK+19] K. Tsurumoto, R. Kuroiwa, H. Kano, Y. Sekiguchi, and H. Kosaka, *Quantum teleportation-based state transfer of photon polarization into a carbon spin in diamond*, Communications Physics **2** (2019), no. 1, 1–6.

[VAC+02] D. Vion, A. Aassime, A. Cottet, P. Joyez, H. Pothier, C. Urbina, D. Esteve, and M. H. Devoret, *Manipulating the Quantum State of an Electrical Circuit*, Science **296** (2002), no. 5569, 886–889.

[von45] J. von Neumann, *First draft of a report on the EDVAC*, IEEE Annals of the History of Computing **15** (1945), no. 4, 27–75.

[VRSB17] N. V. Vitanov, A. A. Rangelov, B. W. Shore, and K. Bergmann, *Stimulated raman adiabatic passage in physics, chemistry, and beyond*, Rev. Mod. Phys. **89** (2017), 015006.

[VS97] N. V. Vitanov and S. Stenholm, *Analytic properties and effective two-level problems in stimulated raman adiabatic passage*, Phys. Rev. A **55** (1997), 648–660.

[VVN+17] B. Vogell, B. Vermersch, T. E. Northup, B. P. Lanyon, and C. A. Muschik, *Deterministic quantum state transfer between remote qubits in cavities*, Quantum Sci. Technol. **2** (2017), no. 4, 045003.

[WDB+24] M. J. Weaver, P. Duivestein, A. C. Bernasconi, S. Scharmer, M. Lemang, T. C. van Thiel, F. Hijazi, B. Hensen, S. Gröblacher, and R. Stockill, *An integrated microwave-to-optics interface for scalable quantum computing*, Nature Nanotechnology **19** (2024), no. 2, 166–172.

[WDE+23] K. Wintersperger, F. Dommert, T. Ehmer, A. Hoursanov, J. Klepsch, W. Mauerer, G. Reuber, T. Strohm, M. Yin, and S. Luber, *Neutral atom quantum computing hardware: Performance and end-user perspective*, EPJ Quantum Technology **10** (2023), no. 1, 1–26.

[WEH18] S. Wehner, D. Elkouss, and R. Hanson, *Quantum internet: A vision for the road ahead*, Science **362** (2018), no. 6412, eaam9288.

[WGE16] M. Walter, D. Gross, and J. Eisert, *Multipartite Entanglement*, Quantum Information, John Wiley & Sons, Ltd, 2016, pp. 293–330.

[WKG+17] T. Walter, P. Kurpiers, S. Gasparinetti, P. Magnard, A. Potočnik, Y. Salathé, M. Pechal, M. Mondal, M. Oppliger, C. Eichler, and A. Wallraff, *Rapid high-fidelity single-shot dispersive readout of superconducting qubits*, Phys. Rev. Applied **7** (2017), 054020.

[Woo98] W. K. Wootters, *Entanglement of Formation of an Arbitrary State of Two Qubits*, Physical Review Letters **80** (1998), no. 10, 2245–2248.

[WSB+04] A. Wallraff, D. I. Schuster, A. Blais, L. Frunzio, R.-S. Huang, J. Majer, S. Kumar, S. M. Girvin, and R. J. Schoelkopf, *Strong coupling of a single photon to a superconducting qubit using circuit quantum electrodynamics*, Nature **431** (2004), no. 7005, 162–167.

[WSB+05] A. Wallraff, D. I. Schuster, A. Blais, L. Frunzio, J. Majer, M. H. Devoret, S. M. Girvin, and R. J. Schoelkopf, *Approaching Unit Visibility for Control of a Superconducting Qubit with Dispersive Readout*, Physical Review Letters **95** (2005), no. 6, 060501.

[WSLT20] J. Wang, F. Sciarrino, A. Laing, and M. G. Thompson, *Integrated photonic quantum technologies*, Nature Photonics **14** (2020), no. 5, 273–284.

[Wu96] Y. Wu, *Effective Raman theory for a three-level atom in the lambda configuration*, Physical Review A **54** (1996), no. 2, 1586–1592.

[YEA+23] J. Yang, A. M. Eriksson, M. A. Aamir, I. Strandberg, C. Castillo-Moreno, D. P. Lozano, P. Persson, and S. Gasparinetti, *Deterministic generation of shaped single microwave photons using a parametrically driven coupler*, Phys. Rev. Appl. **20** (2023), no. 5, 054018.

[YFA+17] F. Yoshihara, T. Fuse, S. Ashhab, K. Kakuyanagi, S. Saito, and K. Semba, *Superconducting qubit–oscillator circuit beyond the ultrastrong-coupling regime*, Nature Physics **13** (2017), no. 1, 44–47.

[YMHK19] S.-P. Yu, J. A. Muniz, C.-L. Hung, and H. J. Kimble, *Two-dimensional photonic crystals for engineering atom–light interactions*, PNAS **116** (2019), no. 26, 12743–12751.

[Yur84] B. Yurke, *Use of cavities in squeezed-state generation*, Physical Review A **29** (1984), no. 1, 408–410.

[YZZ08] S.-Y. Ye, Z.-R. Zhong, and S.-B. Zheng, *Deterministic generation of three-dimensional entanglement for two atoms separately trapped in two optical cavities*, Phys. Rev. A **77** (2008), no. 1, 014303.

[ZCB+21] Y. Zhong, H.-S. Chang, A. Bienfait, É. Dumur, M.-H. Chou, C. R. Conner, J. Grebel, R. G. Povey, H. Yan, D. I. Schuster, and A. N. Cleland, *Deterministic multi-qubit entanglement in a quantum network*, Nature **590** (2021), no. 7847, 571–575.

[ZCS+19] Y. P. Zhong, H.-S. Chang, K. J. Satzinger, M.-H. Chou, A. Bienfait, C. R. Conner, É. Dumur, J. Grebel, G. A. Peairs, R. G. Povey, D. I. Schuster, and A. N. Cleland, *Violating Bell's inequality with remotely connected superconducting qubits*, Nature Physics **15** (2019), no. 8, 741–744.

[ZPB+15] S. Zeytinoglu, M. Pechal, S. Berger, A. A. Abdumalikov Jr., A. Wallraff, and S. Filipp, *Microwave-Induced Amplitude and Phase Tunable Qubit-Resonator Coupling in Circuit Quantum Electrodynamics*, Physical Review A - Atomic, Molecular, and Optical Physics **91** (2015), no. 4.

[ZXP15] C. Zhu, F. Xu, and C. Pei, *W-state Analyzer and Multi-party Measurement-device-independent Quantum Key Distribution*, Scientific Reports **5** (2015), no. 1, 17449.